

Robust Control for Maximum Power Point Tracking of Tidal Current Turbines

Xuhua Yan

A thesis submitted in partial fulfilment of the requirements for the degree of Doctor of Philosophy

School of Engineering

Newcastle University

November 2024

Abstract

In recent years, there has been a growing interest in tidal current energy as a potential source for predictable green electricity generation. Due to the harsh marine environment, the Tidal Current Turbine (TCT) system has to be designed to be robust and to work reliably to minimize the need for intervention. Faults may happen in the TCT system, particularly tidal current speed sensor faults, as this sensor is exposed directly to seawater and significant forces from the tidal current flow. Tidal current velocity sensor-less control strategies are needed to enable the TCT system to continue operating under the situation where the tidal current velocity sensor fails. This thesis presents two sensor-less control strategies: Perturb and Observe (P&O) control and Fuzzy Logic (FL) control. Models of a conventional grid-connected TCT and a stand-alone TCT generation system are presented. The P&O control is developed for both models and its performance analysed. FL control is then applied in the grid-connected TCT generation system model to compare the control performance.

The simulation results show that variable step size P&O can track the maximum power point (MPP) with fluctuations of +/- 2% around the desired value for both grid-connected and stand-alone systems. The grid-connected model was tested under both step and ramp changes of tidal current velocity to test the response to both sudden and continuous variation of input. The P&O control has reliability issues caused by the algorithm itself, however the FL control was able to solve this problem and can also track the MPP with less than 2% variation in generator speed around the required value. Both P&O control and FL control are tested with realistic tidal current velocity input for a tidal cycle (low tide-high tide-low tide), and multiple variable step size P&O control was developed and applied to solve tracking issues. The performance comparison of the two control strategies in terms of efficiency, turbine and generator power and generator reference speed ware analysed. The results show that the sensor less control strategies developed in this thesis can allow the TCT generation system to operate without the tidal current velocity sensor, thus improving the system robustness whilst reducing system maintenance and power generation cost.

Acknowledgments

Firstly, I would like to express my deepest appreciation to my parents Yu Tang and Chongxiang Yan for their unconditional love, support, understanding and encouragement. For both financially and spiritually, they give their best to me through my whole life. They guide me and encourage me with their love in each stage of my growth, without their help, I cannot come to Newcastle to start and finish my PhD work.

I would like to express my sincere gratitude to my primary supervisor Dr Rosemary Norman for her support, guidance, patience and encourage through my PhD journey. I really appreciate to her help, she always be there if I need any help, show me the research direction and encourage me to go overcome difficult problems. Her excellent knowledge in academic area and diligence in work are admirable, it has really been a wonderful experience to work with you.

I would also like to extend my grateful respect to my co-supervisor Dr Mohammed Elgendy for his kindness and help. I can not finish my first simulation model without his help. He can always give me some key suggestions during my research work with his serious working attitude and rich knowledge reserve.

I would like to thank all my friends who helped and cared me, they make I had a truly happy life in Newcastle, and they always at my side when I have any difficult in my life. Thank you for your help.

Finally, I would like to offer my special regards to all the staff of the Marine Technology Group at Newcastle.

Contents

Acknowledgments	iv
List of Figures	X
List of Tables	xvi
List of Abbreviations and Symbols	xvii
Abbreviations	xvii
Roman Symbols	xvii
Greek Symbols	xix
Other Symbols	XX
List of Publications	xxi
Chapter 1. Introduction	1
1.1 Background	1
1.2 Motivation	5
1.3 Aims and Objectives	7
1.5 Thesis Organisation	7
Chapter 2. Literature Review	9
2.1 Tidal Current Energy	9
2.2 Tidal Current Turbine System	10
2.3 Faults in Tidal Current Systems on the Electrical Side and Potential S	olutions 13
2.3.1 Tip-speed-ratio and power coefficient	15
2.3.2 Tidal current velocity sensor faults and potential solutions	16
2.3.3 Rotor speed sensor faults and potential solutions	20
2.3.4 Converter open circuit faults and potential solutions	25
2.4 Maximum Power Point Tracking	28
2.5 Summary	31
Chapter 3. Tidal Current Turbine System Modelling	33
3.1 Tidal Current Turbine Model	33
3.1.1 Evopod E35 tidal current turbine	33
3.1.2 Tip-speed ratio	35
3.1.3 Power coefficient	36
3.2 Resource Model	37
3.2.1 New location site	37
3.2.2 Resource Model	39
3.2.3 Tidal power and turbine performance	42
- · · · · · · · · · · · · · · · · · · ·	

3.4 Generator Side Convert Control Test Model	46
3.3.1 Power convertor	46
3.3.2 Axis reference frame transfer	47
3.3.3 Zero-d axis current (ZDC) control	49
3.3.4 Speed control	50
3.3.5 Evaluation of the generator side convertor control test model	51
3.4 Summary	54
Chapter 4. Tidal Current Speed Sensor-less MPPT Control with Perturb ar	
4.1 Maximum Power Point Tracking (MPPT)	56
4.2 Perturb and Observe Control (P&O)	
4.3 Typical P&O Control Model	
4.3.1 Stand-alone tidal current turbine system model	
4.3.2 Stand-alone system P&O control	
4.3.3 Results and discussion	
4.4 P&O Control Application in Conventional Model	
4.4.1 P&O control design	
4.4.2 Generator side connection with P&O control	
4.4.3 Grid side connection	
4.4.4 Complete system simulation	
4.5 Results and discussion	
4.5.1 Step size and step time	
4.5.2 Drift problem discussion	
4.5.3 Performance analysis	
4.6 Summary	
Chapter 5. Tidal current speed sensor-less MPPT control with Fuzzy Logic	
5.1 Fuzzy Logic Control	91
5.1.1 Fuzzification	92
5.1.2 Fuzzy Rules	93
5.1.3 Defuzzification	93
5.2 Fuzzy Logic Control Design	94
5.3 FL Control Application in Conventional Model	98
5.4 Results and discussion	100
5.4.1 MFs and Step time	101
5 1 2 Parformance analysis	102

5.5 Comparison of P&O and FL control for the Conventional TCT Model	111
5.5.1 Under step change tidal current velocity input	112
5.5.2 Under ramp change tidal current velocity input	115
5.5 Summary	118
Chapter 6. Long term simulation test based on P&O and Fuzzy Logic control stra	
6.1 Model adjustments and tidal current velocity data	
6.1.1 Model adjustments	
6.1.2 P&O control detailed model and average model comparison	
6.1.3 FL control detailed model and average model comparison	
6.1.4 Tidal current velocity data	
6.1.5 Control parameter tuning	130
6.2 Results and discussion	
6.2.1 Fuzzy Logic control results	132
6.2.2 Perturb and observe control results	135
6.2.3 Performance discussion	142
6.4 Extra long term simulation and energy production estimations	147
6.5 Summary	152
Chapter 7. Conclusions and Recommendations for Further Work	153
7.1 Conclusions	153
7.1.1 Comparison of P&O and FL under step change and ramp change input	153
7.1.2 Control performance with real tidal current velocity input	154
7.1.3 Discussion of wider issues	154
7.1.4 Generalisation and limitations of proposed control strategies	155
7.1.5 Thesis contributions	156
7.2 Recommendations for further work	156
Reference	158
Appendices	169
Appendix A	169
Appendix B	172
Appendix C	174
Annondiy D	177

List of Figures

Figure 1.1 AR1500 tidal turbine of Meygen project [10]	2
Figure 1.2 Orbital Marine Power O2 [13]	3
Figure 1.3 LHD tidal current turbine "Endeavour" [16]	3
Figure 2.1 OpenHydro tidal current turbine [65]	. 12
Figure 2.2 Conventional tidal current turbine generation system	. 13
Figure 2.3 O2 tidal system control structure [12]	. 13
Figure 2.4 Occurrence (%) of failures for Swedish wind power plants between 2000-2004	. 14
Figure 2.5 Tidal current turbine power coefficient vs the tip speed ratio	. 16
Figure 2.6 O2 tidal current turbine generator side control [12]	. 17
Figure 2.7 (a) MeyGen project maintenance [71], (b) O2 turbine maintenance mode [72]	. 17
Figure 2.8 PSF control block diagram	. 18
Figure 2.9 OT control block diagram	. 18
Figure 2.10 TCSE-based control diagram	. 19
Figure 2.11 DO control diagram	. 22
Figure 2.12 SMO control diagram	. 23
Figure 2.13 MRAS control diagram	. 23
Figure 2.14 SOSM converter structure and traditional converter structure	. 25
Figure 3.1 Evopod E35 general arrangement (figure from report [128])	. 34
Figure 3.2 deployment of the E35 at Sanda Sound at the mooring location [130]	. 35
Figure 3.3 Tidal current turbine power coefficient with respect to the tip speed ratio	. 36
Figure 3.4 Map of the north of Scotland showing the Inner Sound in the Pentland Firth (fig	gure
taken from [136])	. 38
Figure 3.5 the area of tidal current velocity data taken from CMEMS	. 39
Figure 3.6 (a) Tidal current velocity in Pentland Firth from 01/05/2022 to 01/05/2023; (b) Ti	idal
current velocity for a month	. 39
Figure 3.7 Evopod E35 profile (taken from [128])	. 40
Figure 3.8 Tidal current velocity profile	. 41
Figure 3.9 Spine interpolated tidal current velocity data verse original data	. 41
Figure 3.10 MATLAB/SIMULINK rectified input data	. 42
Figure 3.11 Evopod E35 turbine power verses tidal current velocity curve	. 43
Figure 3.12 PMSG <i>dq</i> equivalent circuit	. 44

Figure 3.13 generator side convertor topology	47
Figure 3.14 <i>abc/dq</i> transformation	47
Figure 3.15 The generator side control structure	50
Figure 3.16 Speed control block diagram	51
Figure 3.17 Speed control loop result	52
Figure 3.18 d-axis current control loop result	53
Figure 3.19 q-axis current control loop result	54
Figure 3.20 Load voltage control loop result	54
Figure 4.1 Tidal current turbine output power vs rotor speed under different tidal speed	57
Figure 4.2 P&O control searching process	58
Figure 4.3 P&O control flow chart	58
Figure 4.4 P&O control diagram	59
Figure 4.5 Stand-alone tidal current turbine system	60
Figure 4.6 Stand-alone system P&O control diagram	61
Figure 4.7 Stand-alone system P&O control flow chart	61
Figure 4.8 Stand-alone system P&O control block diagram	62
Figure 4.9 Generator rotational speed	63
Figure 4.10 Power coefficient	63
Figure 4.11 Root-Mean-Square (RMS error) of power coefficient	63
Figure 4.12 Load voltage control	64
Figure 4.13 P&O control model block diagram	65
Figure 4.14 Tidal current turbine generation system with P&O control	66
Figure 4.15 Fixe step size P&O control output generator reference speed	66
Figure 4.16 Generator rotor reference speed (output of P&O control)	68
Figure 4.17 Tidal current turbine power coefficient	68
Figure 4.18 Root-Mean-Square (RMS) error of power coefficient	68
Figure 4.19 Generator rotor speed	69
Figure 4.20 Zoomed in view of the generator rotor speed	70
Figure 4.21 DC-link voltage	70
Figure 4.22 Experimental results (a) tidal current velocity step change; (b) generator rotate	tiona
speed (figure from [153])	71
Figure 4.23 Experimental results DC-link voltage (figure from [153])	71
Figure 4.24 Topology of the back-to-back converter	72
Figure 4.25 Grid side converter control block diagram.	74

Figure 4.26 Conventional tidal current turbine system model with P&O control	75
Figure 4.27 P&O control output with different step size	77
Figure 4.28 P&O control output with different step time	77
Figure 4.29 P&O control instantaneous power efficiency with different step size und	ler step
change tidal current velocity input	79
Figure 4.30 P&O control instantaneous power efficiency with different step size under	er ramp
change tidal current velocity input	80
Figure 4.31 P&O control instantaneous power efficiency with different perturb time	e under
step change tidal current input	81
Figure 4.32 P&O instantaneous power efficiency with different perturb time under	r ramp
change tidal current input.	82
Figure 4.33 P&O control output generator reference speed with 0.3 step size and 1.7	'5s step
time	83
Figure 4.34 P&O control drift problem	84
Figure 4.35 Changes in power and speed with P&O control with 0.3 step size and 1.7	5s step
time	85
Figure 4.36 P&O control output generator reference speed under step change tidal	curren
velocity input.	86
Figure 4.37 Turbine output power and generator output power under step change tidal	curren
velocity input.	87
Figure 4.38 Active and reactive power under step change tidal current velocity input	87
Figure 4.39 P&O control generator reference speed under ramp change tidal current inp	out 88
Figure 4.40 Turbine output power and generator output power under ramp chang	ge tida
current velocity input	89
Figure 4.41 Active and reactive power under ramp change tidal current input	89
Figure 5.1 FL control diagram	92
Figure 5.2 Types of membership functions	93
Figure 5.3 FL control detect searching process	95
Figure 5.4 (a) MFs of FL input ΔP ; (b) MFs of FL input $\Delta \omega$; (c) MFs of FL output $\Delta \omega r$	ref.97
Figure 5.5 FL control block diagram	98
Figure 5.6 Conventional tidal current turbine system model with FL control	99
Figure 5.7 FL control output with different MFs	101
Figure 5.8 FL control output with different step time.	102
Figure 5.9 FL control instantaneous power efficiency with different MFs under step	change

tidal current input
Figure 5.10 FL control instantaneous power efficiency with different MFs under ramp change
tidal current input104
Figure 5.11 FL control instantaneous power efficiency with different perturb time under step
change tidal current input106
Figure 5.12 FL control instantaneous power efficiency with different perturb time under ramp
change tidal current input106
Figure 5.13 FL control generator output reference speed under step change tidal current
velocity input107
Figure 5.14 Turbine output power and generator output power under step change tidal current
velocity input
Figure 5.15 Active and reactive power under step change tidal current input109
Figure 5.16 FL control generator output reference speed under ramp change tidal current
velocity input110
Figure 5.17 Turbine output power and generator output power under ramp change tidal
current velocity input
Figure 5.18 Active and reactive power under ramp change tidal current input111
Figure 5.19 Generator reference speed of P&O control and FL control under step change tidal
current input
Figure 5.20 Instantaneous power efficiency of P&O and FL control under step change tidal
current input
Figure 5.21 Generator output power of P&O control and FL control under step change tidal
current velocity input
Figure 5.22 Active power of P&O control and FL control under step change tidal current
input114
Figure 5.23 Generator reference speed of P&O control and FL control under ramp change
tidal current input115
Figure 5.24 Instantaneous power efficiency of P&O and FL control under ramp change tidal
current input
Figure 5.25 Generator output power of P&O control and FL control under ramp change tidal
current velocity input116
Figure 5.26 Active power of P&O control and FL control under step change tidal current
input118
Figure 6.1 Block diagram of average model voltage source converter control

Figure 6.2 P&O control speed with detailed and average models under step input	. 123
Figure 6.3 P&O control active power with detailed and average models under step input	. 123
Figure 6.4 Differences in active power of P&O control under step input	. 124
Figure 6.5 P&O control speed with detailed and average models under ramp input	. 124
Figure 6.6 P&O control active power with detailed and average models under ramp input.	. 125
Figure 6.7 Differences in active power of P&O control under ramp input	. 125
Figure 6.8 FL control speed with detailed and average models under step input	. 126
Figure 6.9 FL control active power with detailed and average models under step input	. 127
Figure 6.10 Differences in active power of FL control under step input	. 127
Figure 6.11 FL control speed with detail and average model under ramp input	. 128
Figure 6.12 FL control active power with detail and average model under ramp input	. 128
Figure 6.13 Differences in active power of FL control under step input	. 129
Figure 6.14 Tidal current velocity input for average model (from CMEMS)	. 130
Figure 6.15 FL control active power with different step time	. 131
Figure 6.16 P&O control active power with different step time	. 132
Figure 6.17 Fuzzy Logic control output reference speed	. 133
Figure 6.18 Power of Fuzzy Logic control	. 134
Figure 6.19 Fuzzy Logic control power coefficient	. 135
Figure 6.20 Variable step size P&O output reference speed	. 136
Figure 6.21 Changes in power with same rotation speed change	. 137
Figure 6.22 Changes in power and speed of variable step size P&O control	. 138
Figure 6.23 Variable step size P&O output reference speed with decreasing tidal cur	rren
velocity	. 139
Figure 6.24 Perturb and observe multiple variable step size control output reference speed	140
Figure 6.25 Power of Perturb and Observe multiple variable step size control	. 141
Figure 6.26 Perturb and observe multiple variable step size control power coefficient	. 142
Figure 6.27 FL, P&O and sensor control output generator reference speed	. 144
Figure 6.28 FL, P&O and sensor control active power	. 144
Figure 6.29 Instantaneous power efficiency of FL and P&O control.	. 145
Figure 6.30 FL control and PO control generator output power	. 146
Figure 6.31 24 hour tidal current velocity input	. 147
Figure 6.32 P&O control output reference speed under 24 hour tidal input	. 148
Figure 6.33 P&O control active power under 24 hour tidal input	. 148
Figure 6.34 FL control output reference speed under 24 hour tidal input	. 149

Figure 6.35 FL control active power under 24 hour tidal in	out149
Figure 6.36 Estimated, P&O control and FL control active	power150

List of Tables

Table 2.1 Fault counts in wind farm in Tianjing China in 2019
Table 3.1 Evopod E35 specification of the 1/4 scale device (taken from [128] and [130]) 3:
Table 3.2 GDF-355L permanent magnet generator parameters
Table 4.1 Average efficiency of P&O control with different step size under ramp and step
change tidal current velocity input
Table 4.2 Average efficiency of P&O control with different perturb time under ramp and step
change tidal current velocity input
Table 5.1 FL control fuzzy rules
Table 5.2 Average power efficiency of FL control with different MFs under step and ram
change tidal current velocity input
Table 5.3 Average efficiency of FL control with different perturb time under step and ram
input
Table 5.4 Average power efficiency of P&O control and FL control
Table 6.1 Percentage Energy yield and energy production of FL and P&O control
Table 6.2 Energy yield and energy production for 24 hour tidal input

List of Abbreviations and Symbols

Abbreviations

AC alternating current

DC direct current

DFIG doubly fed induction generator

DO disturbance observers

FL fuzzy logic

GRBFN Gaussian radial basis function
IGBT insulated gate bipolar transistor

LQG linear quadratic Gaussian

M5P multivariate regression prediction
MPPT maximum power point tracking
MRAS model reference adaptive system
MTPA maximum torque per ampere

OT optimal torque

P&O perturb and observe

PID proportional integral derivative

PMSG permanent magnet synchronous generators

PSF power signal feedback

PV photovoltaics

PWM pulse-width modulation

RBF radial basis function

SMO sliding mode observers

SOSM second-order sliding mode

TCSE tidal current speed estimation

TCT tidal current turbines

TSR tip-speed ratio
UPF unity power factor
ZDC zero-d axis current

Roman Symbols

 A_i variable step size P&O control power change range

bias term between hidden and output layers

COG centre gravity

 C_p power coefficient

 C_{pmax} maximum power coefficient E_a induced electromotive force

 $egin{array}{ll} e & & ext{phase back EMF} \\ i & & ext{phase current} \\ i_{dc} & & ext{DC-link current} \\ \end{array}$

 i_{dg}, i_{qg} d-axis grid current, q-axis grid current

 i_{α}, i_{β} α -axis current, β -axis current K_{SMO} gain of the SMO observer

 K_{do} gain of DO observer

K_e back electromotive force (EMF) constant

 K_i variable step size P&O control adjustment constant

 L_{S} phase synchronous inductance

 L_g three-phase inductance

 P_e output power of three-phase generator P_g , Q_g system active and reactive power

 P_m tidal current turbine mechanical power

 P_{max} tidal current turbine theoretical calculated maximum power

 P_{out} tidal current turbine actual output power

 P_t turbine power

p number of pole pairs

R radius of the turbine blades

 R_{II}, L_{II} inductor impedance

 R_{II}, L_{IJ} transformer leakage impedance

 R_p phase resistance

 R_s rotor stator resistance

sgn sigmoid function

SAF variable step size P&O control slowdown adjustment factor

T_{eref} optimal electromagnetic torque

 T_m mechanical torque

 T_{opt} optimal torque

 V_T tidal current flow speed

v phase voltage

 v_d, v_q d-axis voltage, q-axis voltage

 v_{dc} DC-link voltage

 v_{dg}, v_{qg} d-axis grid voltage, q-axis grid voltage

 v_{di}, v_{qi} d-axis and q-axis grid side converter voltages

 v_{ds}, v_{qs} d-axis stator voltage, q-axis stator voltage

 v_j weight between the hidden and output layers

 v_{α}, v_{β} α -axis voltage, β -axis voltage

 x_i centre value of the membership functions

Greek Symbols

 α , β positive constant

 β pitch angle

 Γ_{M1} , Γ_{M2} upper bound of γ_1 and γ_2 Γ_{m1} , Γ_{m2} lower bound of γ_1 and γ_2

 Δd changes between duty cycle

 ΔP changes between power

 $\Delta\omega_r$ changes between rotor speed

 $\eta_{MPPT(average)}$ average MPPT tracking efficiency

 η_{MPPT} instant MPPT tracking efficiency

 θ_r rotor position angle

 λ tip-speed ratio

 λ_{opt} optimal tip-speed ratio

 $\lambda_{qs}, \lambda_{ds}$ d-axis stator flux, q-axis stator flux

 λ_r rotor (permanent magnet) flux

 $\lambda_{r\alpha}, \lambda_{r\beta}$ α -axis rotor flux linkage, β -axis rotor flux linkage

 $\lambda_{s\alpha}, \lambda_{s\beta}$ α -axis stator flux linkage, β -axis stator flux linkage

 $\lambda_{\alpha}, \lambda_{\beta}$ α -axis flux linkage, β -axis flux linkage

 μ_i membership value of the i_{th} rule in FL control

 ρ water density

 $\varphi_1, \varphi_2, \gamma_1, \gamma_2$ uncertain bounded functions ϕ_1, ϕ_2 Lower bound of φ_1 and φ_2

 ω_q dq-axes frame rotating angle speed

 ω_{mpp} rotor speed at MPP

 ω_r rotor speed (rad/s)

 ω_{ref} generator reference speed

Other Symbols

 $\hat{e}_{\alpha}, \hat{e}_{\beta}$ estimated α -axis back EMF, β -axis back EMF

 $\hat{\imath}_{\alpha}, \hat{\imath}_{\beta}$ estimated α -axis current, β -axis current

 $\hat{\theta}$ estimated rotor position angle

List of Publications

- 1. X. Yan, R. Norman, and M. A. Elgendy, "Fault Tolerant Control Design for a Tidal Current Turbine Generation System," in *The 30th International Ocean and Polar Engineering Conference*, 2020: OnePetro.
- X. Yan, R. Norman, and M. A. Elgendy, "Investigations Into Tidal Current Turbine System Faults and Fault Tolerant Control Strategies," in *International Conference on Offshore Mechanics and Arctic Engineering*, 2020, vol. 84416: American Society of Mechanical Engineers, p. V009T09A001

Chapter 1. Introduction

This chapter will introduce the background of tidal current turbine generation systems, motivations and aims and objectives of this thesis. The thesis structure is presented at the end of the chapter.

1.1 Background

The demand for energy has increased rapidly due to the development of global industry and the growth of the population [1]. However, the traditional energy resources face problems of exhaustion and, in addition, fossil energy such as oil and coal has also brought environmental issues. In recent years, across the world, many countries have modified their energy supply systems and developed research on renewable energy [2, 3]. Among the numerous renewable energy resources, tidal current energy is an endless supply of green energy with no significant harm to the environment [4]. For tidal current energy, the density of seawater in the tidal current is large and the current flow is stable [5]. Thus, tidal current energy is considered for renewable energy production, and can operate continuously all through the year [6].

Compared with other renewable energies, tidal current energy has some advantages, such as being easy to predict, and it has high power density and continuity. These advantages have promoted the development of controller design and grid connection, for this energy, considerably [7]. However, due to the harsh underwater environments, tidal current turbines are subjected to challenging conditions, and this brings high pressure to the maintenance work [8]. Thus, tidal current turbine (TCT) generation systems with high fault tolerance have become the main focus of research work [9].

In the UK, since 2010, the planning and development of the MeyGen tidal energy project, owned and run by SIMEC Atlantis Energy, has been taking place with the project officially operating since March 2018. Phase 1 of the MeyGen project was installed with a capacity of 6MW, delivered by four 1.5MW horizontal axis underwater tidal turbines. Figure 1.1 shows one of the four turbines, which is an AOU TTG AR1500 turbine supplied by Atlantis Operations UK. The AR1500 is a 1.5MW tidal turbine with 18m rotor diameter [10]. The Meygen project is located at the Pentland Firth, specifically the Inner Sound between the Island of Stroma and mainland Scotland. This is also the location for which tidal current velocity data has been used in this thesis, the details of which will be presented in Chapter 3. By December 2023, the MeyGen project had already generated 61GWh to the grid over 6

years, and it can be considered as the world's largest tidal current facility that is currently operational [11].



Figure 1.1 AR1500 tidal turbine of Meygen project [10]

In July 2021, the Orbital O2 tidal system was installed at the European Marine Energy Centre (EMEC) in Orkney. The EMEC grid-connected tidal test site is in a narrow channel between the Westray Firth and Stronasy Firth where the tidal current velocity can reach 3m/s. The O2 turbine comprises a 74m long cylindrical floating superstructure, with a total of 2MW of turbine capacity on two legs, each turbine is 1MW turbine with 20m diameter as shown in Figure 1.2 [12] [13]. The O2 has the potential to provide the electrical demand of about 2000 UK homes and offset approximately 2,200 tonnes of CO₂ production per year [14].



Figure 1.2 Orbital Marine Power O2 [13]

In February 2022, the tidal current energy unit "Endeavour" was launched on Xiushan Island, Zhoushan, Zhejiang, China. This is the world's largest single-capacity tidal current turbine device, rated at 1.6MW with a 28m diameter (as shown in Figure 1.3), and the total station capacity is planned to reach 3.3MW. After one month of operation, the Zhejiang Zhoushan tidal current energy power station was integrated into the national grid [15].

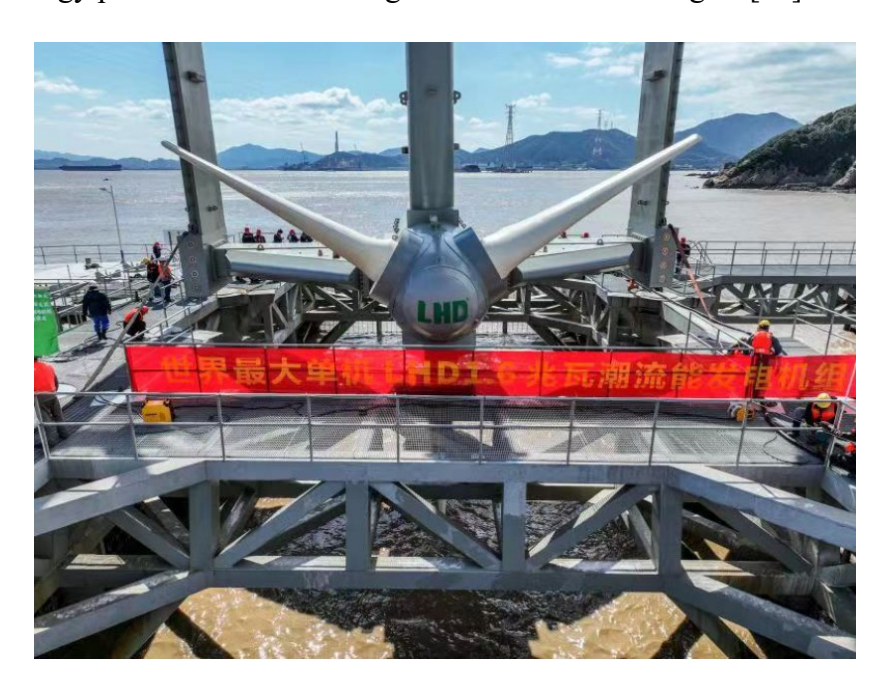


Figure 1.3 LHD tidal current turbine "Endeavour" [16]

In addition to the tidal current turbines mentioned above, there are many other tidal current turbine projects around the world, such as the Tocardo Tidal Project in Eastern Scheldt, Netherlands with the capacity of 1.25MW; the Water Wall Turbine Project in Dent Island,

Canada with the capacity of 1MW and the OceanQuest Project of HydroQuest in Pampol-Brehat, France with the capacity of 1MW [17, 18]. These have proved that the extraction of tidal current energy is developing very rapidly.

Tidal current turbines have similarities to wind turbines in many aspects, thus at first tidal current turbines were not considered as a new technology, since wind turbines had already been developed for a long time and been commercialized. Thus, the research, development and experimental work on tidal current turbines was mainly based on the experiences of wind turbines. Through analysis and data collection of wind turbine generation systems or wind turbine farms, the importance of availability and reliability of tidal current turbine generation systems has been emphasised [19]. In wind turbine systems, researchers have proved that among the failures, electrical and control system failures have the highest rate. In the year 2000, 50% of the wind turbine repairs were for failures of electrical and control systems [20], and that has continued with recent research, in 2019, from a wind farm showing that the failure of converter systems also has the highest rate [21]. However, in tidal current turbine systems, due to the high maintenance cost and site intervention requirements, it is not acceptable for TCT systems to tolerate high failure rates [19].

Furthermore, TCT generation systems face more challenges, such as immersion, offshore locations, and intervention weather-dependence, and a small failure can cause the interruption of the whole system operation. Repair and maintenance are highly dependent on the sea state, and this will increase the energy generation cost. Also the power quality will be affected by the discontinuity of energy transmission [22]. Thus, a fault tolerant or robust control strategy is essential in a TCT generation system to maintain continuous operation when one or more failures occur. Robust control can provide high reliability and strong fault tolerance for the TCT systems [23, 24].

For a horizontal-axis tidal current turbine, the power that it can extract from the tidal current is related to the turbine rotational speed and blade pitch angle. Generally in TCT systems, if the pitch angle is controlled by a mechanical control system, this will increase the TCT system complexity and the failure probability [25, 26], so the pitch angle is typically fixed, which means that the TCT system can only control the power by controlling the turbine rotational speed. In the speed control system, the control efficiency is dependent on sensor signals. These sensors can provide the tidal current speed signal, turbine rotational speed and generator rotor speed signal. When a sensor is damaged or lost, fault tolerant control can ensure continuous operation of the TCT system to maintain energy production [22].

In wind turbine generation systems, maximum power point tracking (MPPT) technology is required to capture maximum power from the wind. Due to the similarities between wind turbines and tidal current turbines, in TCT generation systems, MPPT is also needed to extract maximum power from the tidal current flow. The MPPT technology needs to be applied in fault tolerant control, in order to track the maximum power point under some fault conditions. Many studies in recent years have focused on the MPPT control in wind turbine systems. For example for wind turbine pitch control, in [27] PID control is applied, while in [28] linear quadratic Gaussian (LQG) is used and fuzzy logic (FL) control was implemented in [29]. These pitch angle control strategies in wind turbine systems can control the wind turbine system to track the maximum power point, while in tidal current turbine system, these control methods can be considered for application to control the tidal current turbine speed.

1.2 Motivation

Due to the high maintenance cost and the harsh environment that tidal current turbines are installed in [30], tidal current turbine generation systems face the risk of interruption caused by failures. Generally, if one failure in the electrical or control system occurs, the tidal current turbine system would have to be stopped for unscheduled maintenance, and the marine environment requires a long time planning in advance in order to make sure human intervention can be carried out [31]. This will lead to the system operation being interrupted and will cause serious consequences. Therefore, improving the reliability and robustness of the tidal current turbine generation system has raised the interest of engineers and researchers [24].

In this context, with the aim to increase the reliability and the continuous operation of the tidal current turbine system, fault tolerant control has been developed [32, 33]. Some studies have focused on fault tolerant control of wind turbine systems, such as in [34] where a new structure of inverter is implemented, while in [35] and [36] the studies are focused on the fault tolerant control of wind turbines with doubly fed induction generators.

Also, many studies have had an interest in multi-phase generators. Multiphase generators can provide additional degrees of freedom that can be used for fault tolerant control options, and can operate the remaining healthy phases under fault conditions [19, 37]. In [38], a fault tolerant controller was designed by Lagrangian formulation based on an optimal torque reference, and in [39], for both short circuit and open circuit faults in a dual stator based tenphase generator, a limitation torque control was designed according to the reference torque

commands.

Compared with the three-phase generators, the muti-phase generators have some advantages. They have higher torque density, higher reliability, smoother torque and can minimize the constraints on the converter switches by dividing power. However these advantages are limited to some specialized applications such as aerospace, automotive and ship propulsion applications [19]. Also, in general, the generators that are most commonly used in tidal current turbine generation systems are permanent magnet synchronous generators (PMSG). In fixed pitch tidal current turbine systems, the PMSG direct drive system has been found to be more reliable and economical [40].

In a conventional tidal current turbine generation system, the control of turbine speed is highly dependent on the tidal current speed sensor and generator speed sensor, and in the harsh underwater environment, the tidal current speed sensor faces the risk of damage or being lost altogether [8]. Furthermore, whilst many studies have investigated fault tolerance in mutiphase generator based tidal current turbine systems, relatively little research has been carried out to focus on fault tolerant control based on a conventional tidal current turbine generation system with a PMSG. Thus, this thesis focuses on the fault tolerant control of PMSG-based conventional tidal current turbine generations systems under tidal current speed sensor fault conditions, aiming to continue system operation without the tidal current speed sensor signal whilst tracking the maximum power point.

Similar to wind turbine systems, tidal current turbine generation systems generally have two types, the first of these is a stand-alone tidal current turbine generation system, which can connect to a device or an energy storage module (such as a battery). Paper [41] presented a stand-alone tidal current turbine generation system with MPPT controller, and [42] reported on a stand-alone wind turbine system. The other type is the conventional, grid-connected tidal current turbine generation system, which is based on the widely used wind turbine generation system. Paper [43] developed an extended Kalman filter and fuzzy logic control system based on the conventional system, while [24] compares three-phase and five-phase generators with second order sliding control based on the conventional type system. Generally, the conventional TCT system contains a turbine, generator, generator side converter and grid side converter, and the system is grid connected.

1.3 Aims and Objectives

Based on the stand-alone and conventional systems, this thesis aims to develop a sensor-less control strategy to deal with the tidal current speed sensor fault. The sensor-less control aims to ensure continuous system operation without the tidal current speed sensor data, whilst also implementing MPPT to maintain the tidal current turbine speed at or close to the maximum power point under different tidal current speeds.

In order to achieve the above aims, the main objectives of this thesis are as follows:

- 1. Review the literature about faults that may happen in the electrical side of tidal current turbine systems, the state-of-the-art of fault tolerant control system strategies and tidal current turbine generation system design.
- 2. Investigate the modelling of a stand-alone system with Perturb and Observe (P&O) control to track the maximum power point under step change tidal current velocity inputs.
- 3. Develop a model of a grid-connected conventional tidal current turbine generation system based on the generator side converter control of the stand-alone system together with the grid side converter control.
- 4. Implement the P&O control in the conventional tidal current turbine generation system model under both step change and ramp change tidal current velocity inputs, evaluate the performance of P&O control.
- 5. Investigate the application of Fuzzy Logic (FL) control in the conventional TCT system and evaluate its MPPT performance under the condition of loss of tidal current speed sensor signal, comparison of the P&O control and FL control application in the conventional model in terms of parameters such as the MPPT tracking efficiencies, generator reference speed, power generation.
- 6. Investigate the application of P&O control and FL control in the grid-connected conventional system model under realistic tidal current velocity input, evaluate the performance of P&O control and FL control.

1.5 Thesis Organisation

This thesis consists of seven chapters and is organised as follows:

Chapter 1 presents the introduction of this thesis. It provides a background on tidal current

energy and system. Then the research motivations are discussed and followed by the research aims and objectives.

Chapter 2 provides a review of tidal current energy, then gives a brief introduction to the tidal current turbine generation system, followed by the faults which might occur on the electrical side in tidal current turbine generation system and some potential solutions. Finally, a review of MMPT technology is provided.

Chapter 3 presents the tidal current turbine generation system modelling with a tidal current turbine model and a permanent magnet generator model simulated in MATLAB, as well as the tidal current sources. The generator side converter control strategy is presented, followed by results to evaluate the system operation.

Chapter 4 presents the design of a tidal current speed sensor-less control strategy based on the P&O control method. The basic theories of MPPT technology in a tidal current turbine system are introduced along with the principle of P&O control. Different P&O parameters are tested under different tidal current velocity inputs, the effects of different step size and step time of P&O control. The P&O control is applied in both stand-alone and grid connected systems. Finally, the results are discussed.

Chapter 5 introduces the design of a tidal current speed sensor-less control strategy based on the FL control method. A brief review of FL control application is provided, along with the principle of FL control. The FL control with different membership functions and step time are then tested under different tidal current speed inputs in the conventional tidal current turbine generation system. The results are discussed, as well as the comparisons with P&O control under the same conditions.

Chapter 6 presents the simulation of the grid-connected conventional system with both P&O and FL control under real tidal current velocity input for a tidal cycle (low tide-high tide-low tide). The detailed control performances are illustrated in terms of control output, power efficiency etc, as well as the comparison of two control methods.

Chapter 7 presents the conclusion of this thesis, discussions of P&O and FL based sensor-less control, advantages and disadvantages of P&O and FL control, as well as the proposed potential research direction of the future work.

Chapter 2. Literature Review

Chapter 1 introduced the background, motivation, aims and objectives of this thesis. The main aim of the thesis is to develop P&O control and FL control in a TCT system to realize the tidal current velocity sensor-less control, to operate the TCT system without a tidal current velocity sensor whilst tracking the MPP. In order to have a better understanding of P&O control and FL control applications in TCT systems, this chapter is presents a review of tidal current energy, giving a basic introduction to tidal current energy along with the tidal current turbines and the generation system. Some challenges that the tidal current generation system is facing and the issues and faults that may happen in the TCT generation system on the electrical side, such as tidal current velocity sensor faults are discussed. Also, potential control strategies that can deal with faults on the electrical side are discussed. The MPPT control is introduced, following with the use of P&O and FL control applications in wind turbine and photovoltaic (PV) systems along with the potential of P&O and FL control in TCT control systems.

2.1 Tidal Current Energy

The rapid exhaustion of the limited reserves of fossil fuel resources have promoted renewable energy development [44]. Renewable energy can be recreated or renewed by nature in a short period of time, the major types of renewable energy are solar, wind, geothermal, hydro, marine energy, biomass and biofuels [43]. Tidal current energy has been identified as a potential candidate resource due to the predictability and capacity of the tides [45, 46]. The position of tidal energy in the renewable energy mix has gradually increased with tidal current energy starting to make a contribution [23].

The study in [47] shows that around the world, the power that can be extracted from waves is about 2000 GW, and about 1000 GW from tidal currents. The research in [48] shows that in the US, 14 GW of instream hydrokinetic power can be extracted from rivers, and paper [49] predicts that about 18.6 GW could be extracted from offshore ocean currents. It has been reported that of the European tidal resource, 48% is in UK waters, 42% in France and 8% in Ireland [23, 50].

Paper [51] shows that around 75 GW power could be economically extracted from tidal current technologies worldwide, and of the 75 GW of power, around 11 GW would be in Europe, with 6 GW in the UK and 3.4 GW in France. Significant amounts of research work

have been done on tidal current turbines in recent years in different locations. The majority of this research work is still at an experimental stage, at locations such as the European Marine Energy Centre in Scotland [52] and the Fundy Ocean Research Centre for Energy in Canada [53].

Tidal current power is a predictable source of energy that oscillates on a known cycle, and research has forecast that tidal current turbine technology will be a huge percentage of UK's renewable electricity power in the future [54, 55]. Across the UK, there is approximately 308TWh per year electricity generated, and of this electric energy, 40% is from fossil fuels which accounts for 20% of the UK's annual greenhouse gas emissions [56]. The UK government legislated net-zero greenhouse gas emissions by 2050 in the year 2019, and the electricity demand is projected to increase to 680TWh by 2050. While wind and solar are expected to provide 515TWh per year, the rest of the demand is expected to be generated from tidal current energy [56]. Since 2008, the UK has installed 18 MW of tidal stream capacity, utilizing the energy of tides through turbines that typically feature horizontal axis rotors to power a generator. Of this capacity, 10.4 MW is currently in operation, while the remaining 7.7 MW has been decommissioned after completing its testing phase [57]. The UK tidal stream installed capacity is estimated to be 11.5GW by 2050 and in order to reach this goal, the installed capacity needs to reach 60MW before 2027 and 140MW before 2031. In 2021, three tidal stream projects were identified as eligible to participate in bidding: the Morlais project in Wales with a capacity of 14 MW, the Perpetuus Tidal Energy Centre (PTEC) in England with 30 MW, and MeyGen 1C in Scotland, which has a capacity of 80 MW. This means there is still a large gap which needs to be filled [56]. In [3], the authors suggested that tidal current turbines are likely to develop to surpass other offshore energy, primarily for mainland electrification.

Of the 11.5GW installed capacity by 2050, some 6GW is expected to be reached in the Pentland Firth; the MeyGen project has proved that the Pentland Firth has the potential to achieve this goal, and the tidal current velocity resource used in this thesis is from Pentland Firth, which will be illustrated in Chapter 3.

2.2 Tidal Current Turbine System

Tidal current conversion systems transform tidal current energy to electrical power. There are similarities between wind turbines and tidal current turbines, as they both capture energy from a mass flow [8, 58]. However the density is different between air and water, the water density

being about three times the order of magnitude of air [23], thus the tidal current turbines must withstand larger forces than the wind turbines.

Generally, in order to maximise the conversion of the available energy, the tidal current turbines are installed at locations with strong tidal current, and they are therefore subjected to large forces. These challenging locations require that the tidal current turbine system has to work reliably with high availability to minimise the need for intervention [8]. Due to the harsh marine environment, some small faults that happen in the tidal current turbine system may lead to the failure of the whole system, and will cause unplanned maintenance [22]. The tidal current turbine system maintenance operation may have to take place onshore, because of the limitations of working offshore in high sea states, and this will increase the cost of power generation [45].

In order to avoid expensive unscheduled maintenance service, a TCT system has to meet the requirement of high reliability and strong fault tolerance [23, 24], and fault tolerant control strategies can be applied to help to maintain the system's continuous operation. This will reduce the power generation cost and also improve the system robustness.

On the electrical side, layout and modelling approaches used in tidal current systems are similar to those used in onshore and offshore wind systems. The speed of wind is higher than the water current speed while the air density is lower than water density, so these lead to a result that the wind turbine operates at relatively high rotational speeds and low torque while the tidal current turbines operate at lower rotational speeds and higher torque [59].

The generators used in wind turbine systems are similar to those in the tidal current turbine systems, such as permanent magnet generators (PMG) and the doubly fed induction generator (DFIG). These two kinds of machines are mainly used in tidal current systems. In [60], the study of power system stability analysis has been illustrated, and the results show that for small signal stability, the PMGs has a better performance compared to the DFIG. Also due to the very difficult maintenance operations and the maintenance cost, the PMG has been found to have the advantages of self-excitation leading to higher efficiency and low maintenance cost.

Basically, the drivetrain technologies that are common for tidal current energy capture are similar to those used in wind turbine systems. There are two drivetrains typically designed for tidal current turbine system with PMGs: geared and direct drive drivetrains. In geared drivetrain systems, the efficiency of the drivetrain depends on the number of gear sets and the

efficiency of each gear set. Generally, muti-stage gear sets can have the efficiency of about 98% while the efficiency of planetary gear sets can even reach 99% [61]. The advantage of the multi-stage gear set (up to 1:5) drivetrains is that they are available in a wide range and at low costs, while planetary gear sets can have higher speed ratios (up to 1:12). Of the tidal current turbine devices that are mentioned in Chapter 1, the MeyGen project, uses a 1.5MW two stage planetary gear box, while the O2 project, uses a Superposition Gear which also contains two planetary gear sets. Direct drive systems with PMGs, such as the OpenHydro project shown in Figure 2.1, can have higher efficiency and can improve the reliability of the tidal current turbine system and reduce the maintenance cost but the direct drive generators are more expensive than generator systems with gearboxes [61, 62], and the competition between geared and direct drive drivetrains in tidal current turbine systems is still ongoing.

In general, three types of tidal current turbine have been designed to transfer tidal current energy to electrical power, they are horizontal axis turbines, oscillating hydrofoils and vertical axis turbines [63], and these turbines can be installed on the seabed, on the surface and in between [53]. Horizontal axis turbines are the most commonly used and more developed type, due to their large energy capture ability from tidal currents [64]. Considering the turbines that were introduced in Chapter 1, the AR1500 tidal current turbine of the MeyGen project is a horizontal axis turbine which was installed on the seabed, the O2 tidal current device is a floating horizontal axis tidal current turbine, while the "Endeavour" tidal current turbine is also a horizontal axis turbine that operates between the surface and seabed.

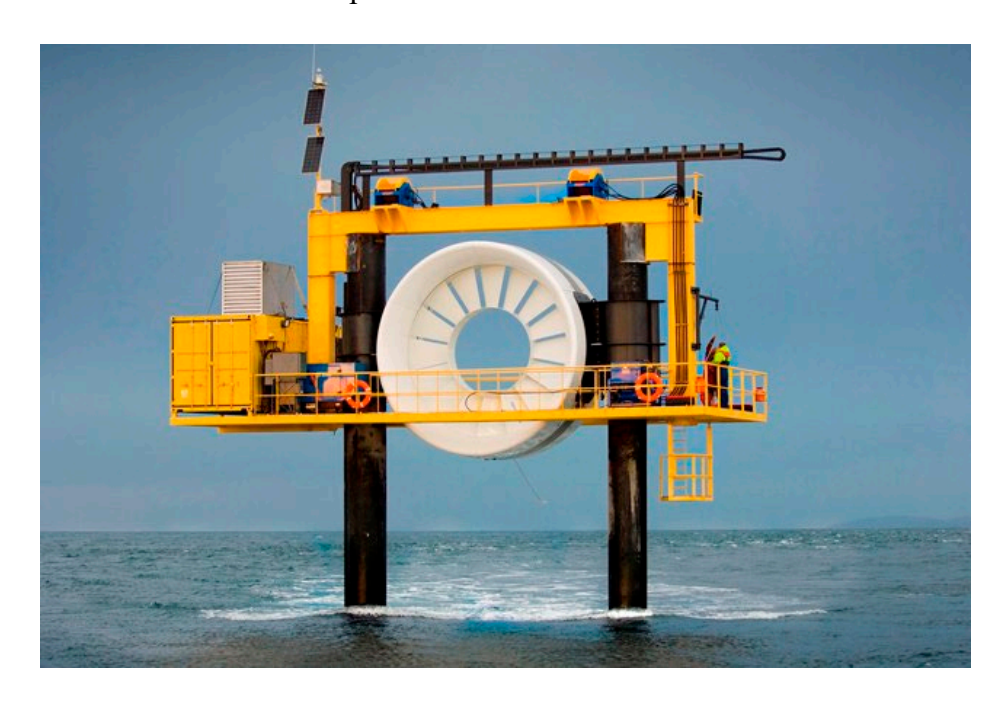


Figure 2.1 OpenHydro tidal current turbine [65]

Tidal current velocity sensor-less control strategies will be developed in this thesis based on a generic, typical tidal current turbine system. Figure 2.2 is the block diagram of a typical tidal current turbine generation system [24, 45]. The generator can be either a PMG or a DFIG. Generally, the system consists of the tidal turbine, generator, generator side converter, DC link and the grid side inverter connected to the grid. The controller here is used to control the speed of the generator, and the switching time of the converter and inverter. The detailed TCT generation system model design and MATLAB simulation model will be presented in Chapter 3. For example, the Orbital O2 tidal current turbine (mentioned in Chapter 1) control strategy is illustrated in Figure 2.3, which has the same structure as the conventional tidal current turbine generation system.

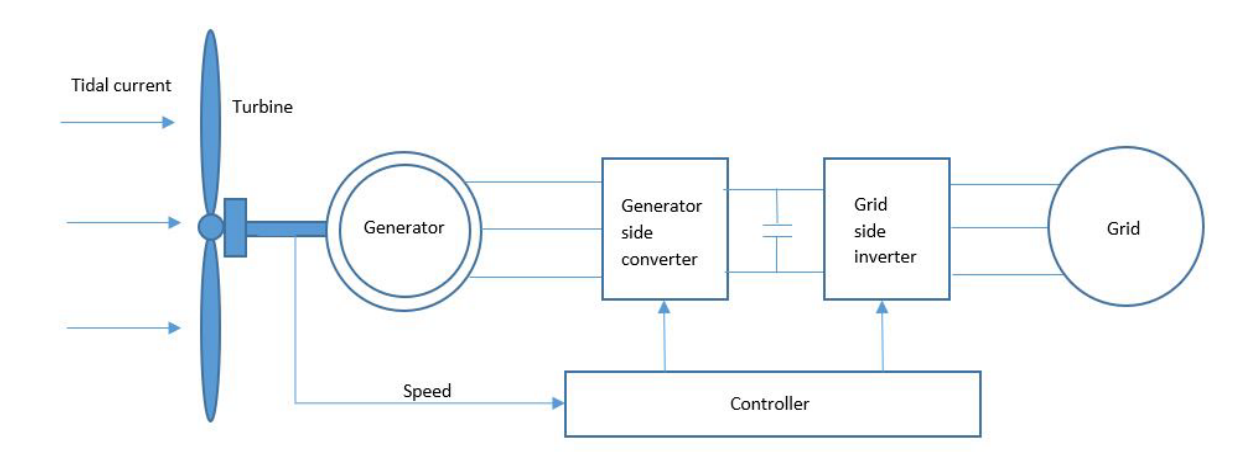


Figure 2.2 Conventional tidal current turbine generation system

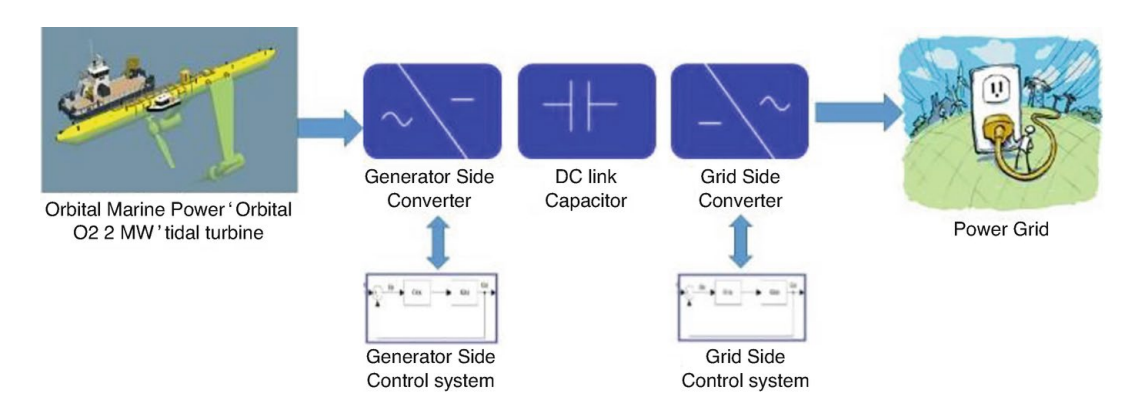


Figure 2.3 O2 tidal system control structure [12]

2.3 Faults in Tidal Current Systems on the Electrical Side and Potential Solutions

Tidal current sensors are often lost or degraded due to the underwater environment and the strong tidal current [22, 45]. Rotor speed/position sensors are generally installed on the rotor shaft; the accuracy of this kind of mechanical sensor will be influenced by environmental

factors, such as humidity, temperature and vibration, all of which will be significant in the underwater turbines and will potentially cause problems with the speed/position readings. Another issue with the environmental conditions is that a TCT system captures energy from the tidal current that will also have harmonic current speeds caused by swells and waves and these will lead to the degradation of performance of the various functional blocks of the system and an accelerated aging process, particularly with regard to the blades, the generator and the converters (short-circuit faults, open-circuit faults and intermittent gate misfiring faults) [66-68].

The electrical control system of tidal current turbines is sufficiently similar to that of a wind turbine, that the fault data in wind turbines can be considered as a reference for tidal current turbines. Figure 2.4 shows the percentage breakdown of failures that occurred during the period 2000-2004 in Swedish wind power plants, and from this figure it can be seen that the sensor faults account for 14.1%, faults in electric systems 17.5% and faults in the control system 12.9%; these are the most common faults that may happen in the electrical side of the system [20]. Also from [21], a set of data collected from 15 direct-drive wind turbines in a wind farm located in Tianjing, China in 2019 shows that the electrical converter system has the highest frequency of failure, then comes low yawing velocity and high temperature of the gearbox. These failures can be caused by a speed control fault or a power converter fault. This means that for the electrical control aspect, the wind turbine system faces high rates of failure. Table 2.1 illustrates the failure counts in [21].

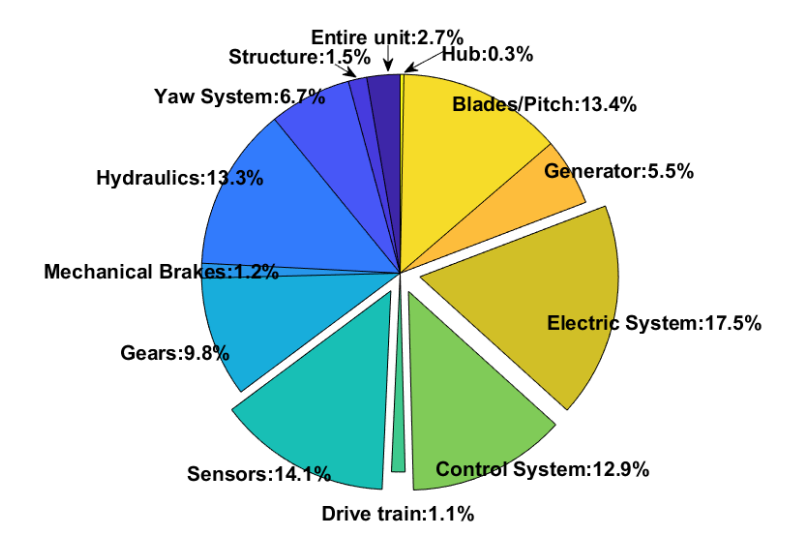


Figure 2.4 Occurrence (%) of failures for Swedish wind power plants between 2000-2004 (Data taken from [20])

Fault name	Total count
Failure of converter system	169
Low yawing velocity	127
High temperature of gearbox	96
High temperature of generator	79
Low pressure of hydraulic system	75
Emergency stop of cabin	63
Emergency stop of tower	58

Table 2.1 Fault counts in wind farm in Tianjing China in 2019.

(Data taken from [21])

2.3.1 Tip-speed-ratio and power coefficient

The tip-speed ratio λ is defined by

$$\lambda = \frac{\omega_t R}{V}$$
 Equation 2.1

where the ω_t is the rotational speed of the rotor (rad/s), R is the radius of the turbine blades (m) and V is the tidal current flow speed (m/s).

The amount of power that be captured from a tidal current turbine is governed as follow [69]:

$$P_t = \frac{1}{2}C_p(\lambda, \beta)\rho\pi R^2 V^3$$
 Equation 2.2

where the water density ρ (kg/m^3), the P_t is the turbine power (W), and C_p is the power coefficient, which is approximated as a function of the turbine blades' pitch angle β and the tip-speed ratio λ [70]. If the turbine is a fixed pitch device, the value of β is constant and equals zero.

The C_p against λ curve of a marine current turbine is typically of the form shown in Figure 2.5 (provided by Ocean Flow Energy, Evopod E35 turbine). The detailed relationship of tip-speed ratio and power coefficient of the turbine used in this thesis is illustrated in Chapter 3.

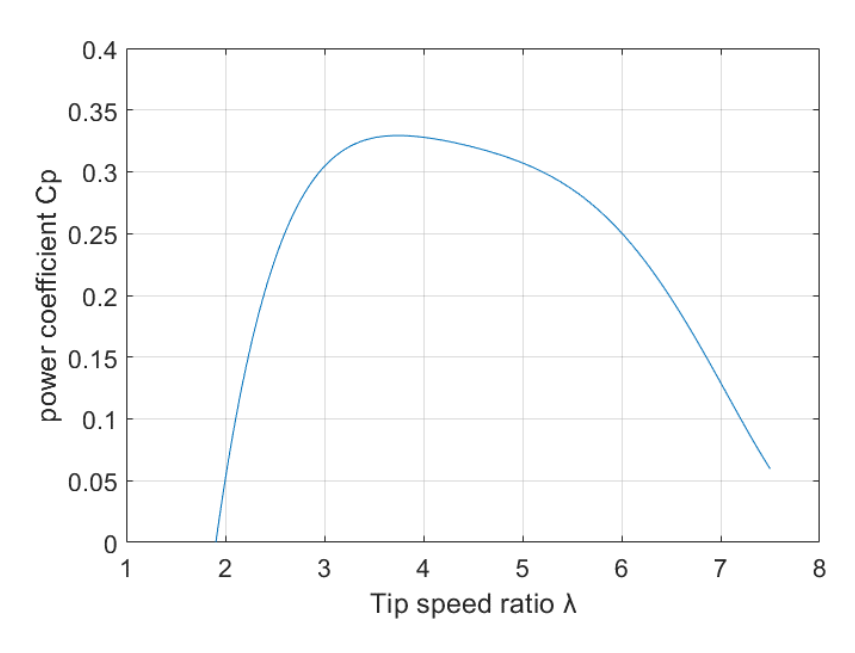


Figure 2.5 Tidal current turbine power coefficient vs the tip speed ratio

2.3.2 Tidal current velocity sensor faults and potential solutions

In order to extract the maximum power from the tidal current, the rotor speed needs to be adjusted to follow a reference speed, to make sure that the tip-speed ratio is at its optimal value. The reference speed is normally calculated from the tidal current velocity through a MPPT algorithm, and the tidal current velocity is measured by a tidal current velocity sensor (flow-meter). Due to the harsh environment, the tidal current velocity sensors are often lost or degraded, and in this situation, the control system still needs to make sure that the system continues operating [22, 45]. As shown in Figure 2.2, the generic tidal current velocity is provided by a tidal current velocity sensor to the controller to calculate the turbine and generator reference speed. This is the case also in the O2 project where the tidal current velocity signal is provided to calculate the Ω_{shaft_ref} in Figure 2.6. This means that in the conventional tidal current turbine system like in Figure 2.2 and Figure 2.3, if the tidal current velocity sensor is damaged, it will lead to the turbine operating away from the maximum power point, losing speed control or even working over the rated speed, and this may cause damage to the tidal current turbine and generator with maintenance work needed to solve the problem. For the MeyGen project, offshore maintenance work can be done by lifting the tidal current turbine up from the seabed and undertaking the maintenance work on the maintenance vessel, as shown in Figure 2.7 (a). For the O2 project, as it is a floating tidal current turbine system designed with two liftable legs (working mode is with the two legs down under sea surface), the maintenance work can be done by lifting the two legs up as shown in Figure 2.7 (b).

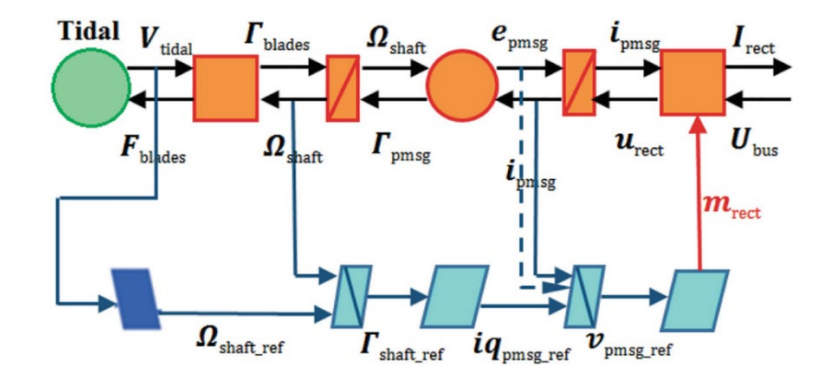


Figure 2.6 O2 tidal current turbine generator side control [12]

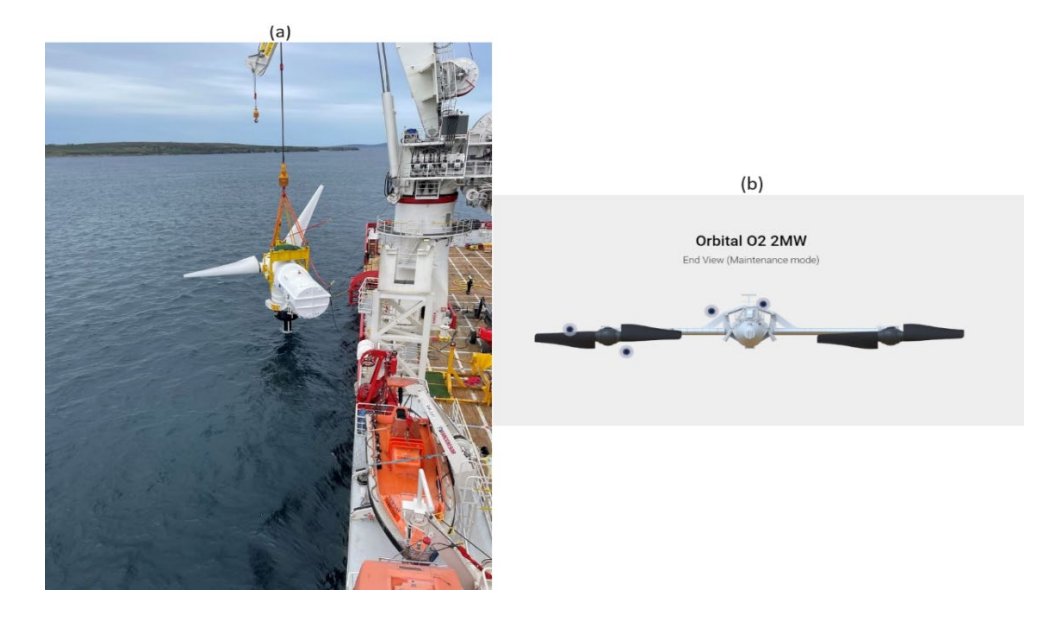


Figure 2.7 (a) MeyGen project maintenance [71], (b) O2 turbine maintenance mode [72]

This section will present some control methods that can deal with the tidal current velocity sensor fault, to make sure that the TCT system can still operate without the tidal current velocity sensor signal.

(1) Power Signal Feedback control

The maximum power that a tidal current turbine can extract from the tidal flow can be expressed by [73]:

$$P_{max} = \frac{C_{pmax}\rho\pi R^5}{2\lambda_{opt}^3}\omega_r^3 = K_{opt}\omega_r^3$$
 Equation 2.3

where C_{pmax} is the maximum power coefficient when the tip speed ratio is at its optimal value (λ_{opt}) . Thus the rotor speed reference can be calculated as follows [45] [22]:

$$\omega_r^* = \sqrt[3]{\frac{P_{max}}{K_{opt}}}$$
 Equation 2.4

The block diagram of the power signal feedback (PSF) control is shown in Figure 2.8. The rotor speed may be used to find the optimal power value through a power versus rotor speed curve, with the optimal power as a reference value to adjust the generated power until it converges to the optimal value. The speed calculated from Equation 2.4 is used as the reference speed for the speed control loop. Thus, the generated power and rotor speed converge towards the optimal value and the turbine is able to extract the maximum power from tidal current [22, 45].

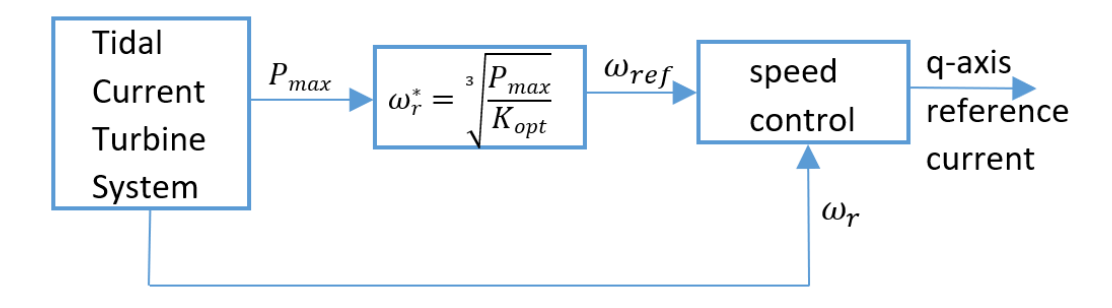


Figure 2.8 PSF control block diagram

(2) Optimal Torque control

The optimal torque (OT) control method needs the rotor speed to be controlled in torque control mode. The basic theory of OT control is similar to that of PSF control, with the purpose of ensuring that the turbine can extract the maximum power from the tidal current flow, as expressed by Equation 2.3. Since $P = \omega * T$, the optimal torque can be expressed as [73]:

$$T_{opt} = \frac{C_{pmax}\rho\pi R^5}{2\lambda_{opt}^3}\omega_r^2 = K_{opt}\omega_r^2$$
 Equation 2.5

The rotor speed is used to calculate the reference optimal torque which is used to adjust the turbine torque through an optimal torque curve. The schematic diagram of OT control is illustrated in Figure 2.9 [73].

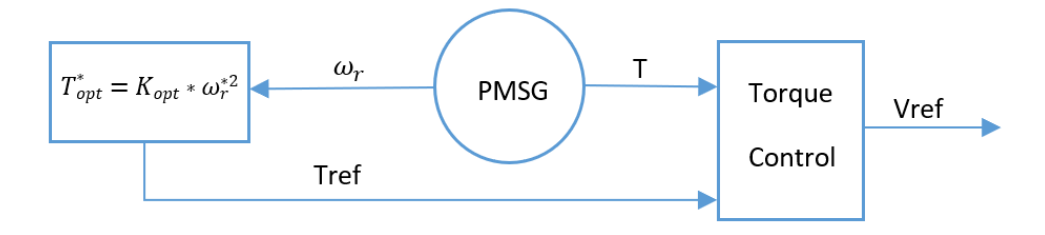


Figure 2.9 OT control block diagram

(3) Tidal current velocity estimation-based control

In a TCT system, the tidal current velocity can be estimated if the current sensor is damaged, and the estimated speed can be used in the traditional tip-speed ratio (TSR) control. According to [22, 45] and [73], one of the most widely used current speed estimation methods is the Gaussian radial basis function (GRBFN) in which the estimated speed is given by

$$\hat{V} = b + \sum_{j=1}^{h} v_j \exp\left[-\frac{\left\|x - C_j\right\|^2}{\sigma_j^2}\right]$$
 Equation 2.6

where $x = [P_m, \omega_r, \beta]$ is the input vector, $C_j \in R^n$ and $\sigma_j \in R$ are the centre and width of the jth radial basis function (RBF) unit in the hidden layer, h is the number of RBF units, b and v_j are the bias term and weight between the hidden and output layers respectively. \hat{V} is the estimated tidal current velocity, P_m is the turbine mechanical power, ω_r is the rotor speed, β is blade pitch angle, and if in a fixed speed case $\beta = 0$. The schematic diagram of the tidal current velocity estimation (TCSE) is shown in Figure 2.10. The parameters of the GRBFN are determined by an offline training process using the data from a conversion system dynamic model [22] [73].



Figure 2.10 TCSE-based control diagram

(4) Perturb and Observe control

Perturb and Observe (P&O) control is also known as hill climb search control. This method does not rely on the tidal current velocity information and TCT characteristics [74]. The basic theory of this method is one of creating changes in rotor speed and observing the corresponding changes in power. The P&O control will be introduced in detail in Chapter 4.

(4) Fuzzy Logic control

Fuzzy logic (FL) control is a control method that also does not need the knowledge of tidal current turbine and tidal current velocity [75], through three steps: fuzzification, fuzzy rules and defuzzification, the FL control can provide the desired generator speed value in a TCT system. The FL control will be introduced in detail in Chapter 5.

2.3.3 Rotor speed sensor faults and potential solutions

In order to deal with generator speed sensor failures, the control system needs to estimate the generator rotor speed. Generally, these control strategies can be divided into two categories: open-loop calculation and closed-loop observers. This section will give brief introductions to these control strategies.

(1) Open-loop calculation

The basic idea of open-loop calculation is to use other measured parameters such as flux linkage, EMF or winding inductance to calculate the rotor speed/position. These parameters are obtained from the dynamic model of the permanent magnet generator (PMG) which can run in parallel with the actual PMG. This section will introduce two kinds of open-loop calculation control methods.

For the flux linkage-based method, in the $\alpha\beta$ -axis, the voltage equations for the PMG are as follows [76]:

$$v_{\alpha} = R_{s}i_{\alpha} + \frac{d}{dt} \left[(L_{0} + L_{1}\cos(2\theta_{r}))i_{\alpha} + L_{1}\sin(2\theta_{r})i_{\beta} \right] + \frac{d}{dt} (K_{e}\cos\theta_{r}) \quad \text{Equation 2.7}$$

$$v_{\beta} = R_s i_{\beta} + \frac{d}{dt} \left[L_1 \sin(2\theta_r) i_{\alpha} + (L_0 - L_1 \cos(2\theta_r)) i_{\beta} \right] + \frac{d}{dt} (K_e \sin \theta_r) \quad \text{Equation 2.8}$$

Where $L_0 = (L_d + L_q)/2$ and $L_1 = (L_d - L_q)/2$. For a non-salient PMSG the $L_d = L_q$, then $L_1 = 0$. Substituting these into Equations 2.7 and 2.8 gives

$$v_{\alpha} = R_{s}i_{\alpha} + L_{q}\frac{di_{\alpha}}{dt} - K_{e}\omega\sin\theta_{r}$$
 Equation 2.9

$$v_{\beta} = R_{s}i_{\beta} + L_{q}\frac{di_{\beta}}{dt} + K_{e}\omega\cos\theta_{r}$$
 Equation 2.10

If the rotor has salient poles, then this method will be complex. When a PMSG is operating in the steady state, the stator and rotor flux vectors rotate synchronously, then $di_{\alpha}/d_{t} \approx 0$ and $di_{\beta}/d_{t} \approx 0$. Because the rotor flux angle is the same as the stator flux angle in the steady state, thus if the stator flux position angle can be calculated then the rotor flux angle can be estimated [73].

When the PMSG is operating at medium-high speed, the flux linkage can be expressed as:

$$\begin{cases} \lambda_{\alpha} = K_e \cos \theta_r \\ \lambda_{\beta} = K_e \sin \theta_r \end{cases}$$
 Equation 2.11

Differentiating Equation 2.11 gives the back EMF in the $\alpha\beta$ -axis:

$$\begin{cases} E_{\alpha} = \frac{d}{dt} K_{e} = -\omega K_{e} \sin \theta_{r} \\ E_{\beta} = \frac{d}{dt} = \omega K_{e} \cos \theta_{r} \end{cases}$$
 Equation 2.12

Substituting Equations 2.9 and 2.10 into 2.12 gives the stator flux linkage:

$$\begin{cases} \lambda_{s\alpha} = \int (v_{\alpha} - R_{s}i_{\alpha})dt \\ \lambda_{s\beta} = \int (v_{\alpha} - R_{s}i_{\beta})dt \end{cases}$$
 Equation 2.13

The rotor flux linkage is as follows:

$$\begin{cases} \lambda_{r\alpha} = \lambda_{s\alpha} - L_0 i_{\alpha} \\ \lambda_{r\beta} = \lambda_{s\beta} - L_0 i_{\beta} \end{cases}$$
 Equation 2.14

Thus, the rotor position can be calculated by $\hat{\theta} = \tan^{-1}(\lambda_{r\alpha}/\lambda_{r\beta})$.

The inductance-based method on the other hand can deal with a PMG that has a high saliency ratio, such as $L_q/L_d > 2.5$, and the performance will be poor for a non-salient PMG. The accuracy of this method is highly dependent on the quality and accuracy of the voltage and current measurements [77]. The basic principle of this method is the spatial distribution of the phase inductance of a PMG, using the measured voltage and current to calculate the phase inductance, then estimating the rotor position through a lookup table. When the switching frequency is high, for example over 10kHz, the phase inductance and back EMF can be considered as constant during the switching period [73]. Under this situation the voltage of a single phase is as follows:

$$v = R_p i + L_s \frac{di_a}{dt} + e$$
 Equation 2.15

where R_p is the phase resistance, i is the phase current, i_a is the phase A current, L_S is the phase synchronous inductance, e is the phase back EMF. The inductance can be re-written as:

$$L_S = \frac{v - R_p i - e}{\frac{di_a}{dt}}$$
 Equation 2.16

The back EMF in Equation 2.16 can be evaluated using the calculated rotor position in the previous two cycles by $e(k) = K_e[\theta_r(k) - \theta_r(k-1)]/\Delta t$, where K_e is the back EMF constant. Using the calculated phase inductance L_S the corresponding rotor position can be

found through a lookup table [73] [77].

(2) Close-loop calculation

The closed-loop observer uses tracking errors as the input to an observer. Thus, the estimated value will converge to the actual value, so the rotor speed and position information will be more accurate. Closed-loop observers have good disturbance rejection and can improve the robustness of the TCT system to the variations of PMG parameters and current/voltage measurements [73]. In this section, the disturbance observers will be introduced.

Disturbance Observers (DO) can be used to estimate back EMF and the rotor position is calculated as follows [78]:

$$\hat{\theta} = \tan^{-1} \left(-\frac{\hat{e}_{\alpha}}{\hat{e}_{\beta}} \right)$$
 Equation 2.17

This observer is generally designed based on the dynamic model of a PMSG in the $\alpha\beta$ -axis, and the observer is designed as follows:

$$\frac{d}{dt} \begin{bmatrix} \hat{i}_{\alpha} \\ \hat{i}_{\beta} \end{bmatrix} = \begin{bmatrix} -\frac{R_s}{L} & 0 \\ 0 & -\frac{R_s}{L} \end{bmatrix} \times \begin{bmatrix} i_{\alpha} \\ i_{\beta} \end{bmatrix} + \frac{1}{L} \left(\begin{bmatrix} v_{\alpha} \\ v_{\beta} \end{bmatrix} - \begin{bmatrix} \hat{e}_{\alpha} \\ \hat{e}_{\beta} \end{bmatrix} \right)$$
Equation 2.18

$$\frac{d}{dt} \begin{bmatrix} \hat{e}_{\alpha} \\ \hat{e}_{\beta} \end{bmatrix} = K_{do} \cdot \frac{d}{dt} \begin{bmatrix} \hat{\iota}_{\alpha} - i_{\alpha} \\ \hat{\iota}_{\beta} - i_{\beta} \end{bmatrix}$$
 Equation 2.19

where $\hat{\iota}_{\alpha}$, $\hat{\iota}_{\beta}$, \hat{e}_{α} , \hat{e}_{β} are the estimated values and K_{do} is the gain of the observer, which can be designed using a pole assignment scheme. The schematic diagram is shown in Figure 2.11.

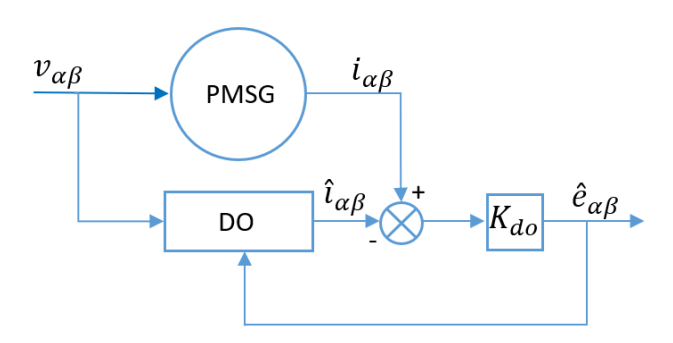


Figure 2.11 DO control diagram

The Sliding Mode Observers (SMO) can also be used for the calculation of the generator rotor speed. The inputs of SMO are discontinuous functions of error between the estimated and measured system states. Similar to DO control, the SMO also estimates the back EMF and

uses it to calculate the rotor position. The back EMF is estimated as follows [79]:

$$\begin{bmatrix} \hat{e}_{\alpha} \\ \hat{e}_{\beta} \end{bmatrix} = K_{SMO} sgn \begin{bmatrix} \hat{\iota}_{\alpha} - i_{\alpha} \\ \hat{\iota}_{\beta} - i_{\beta} \end{bmatrix}$$
 Equation 2.20

where K_{SMO} is the gain of the SMO observer, and sgn is the sigmoid function, which is given by:

$$sgn(x) = \frac{2}{1 + e^{-ax}} - 1$$
 Equation 2.21

The rotor position can be calculated using Equation 2.17, and the schematic diagram of the SMO is illustrated in Figure 2.12.

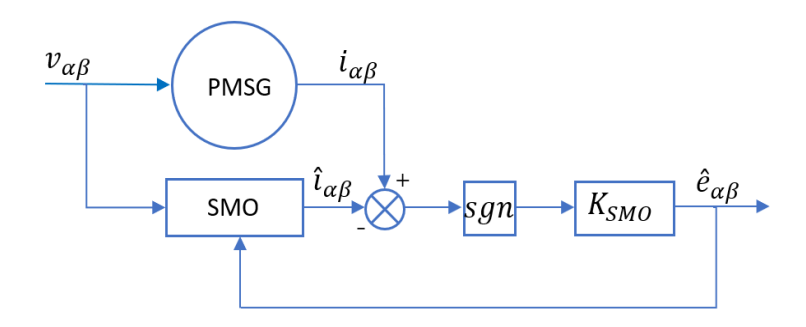


Figure 2.12 SMO control diagram

Another method that can calculate the generator rotor speed is the Model Reference Adaptive System (MRAS) for which the control diagram is shown in Figure 2.13. As shown in Figure 2.13, MRAS contains a reference model and an adjustable model connected in parallel. The error between the outputs of the two models is used to estimate the rotor speed, and the output of the adjustable model is expected to converge to the output of the reference model by using an adaptive mechanism [22, 73].

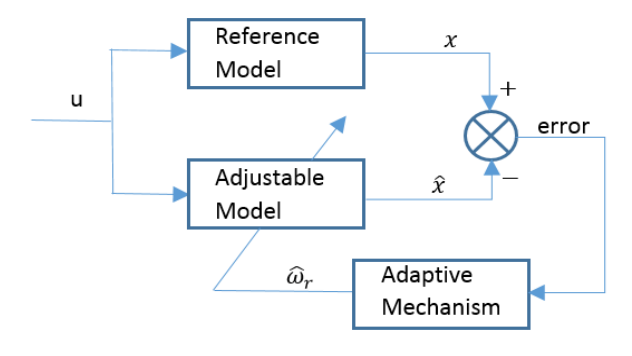


Figure 2.13 MRAS control diagram

The reference model can be designed as follow:

$$\frac{d}{dt}x = A \cdot x = u$$
 Equation 2.22

where

$$x = \begin{bmatrix} x_1 \\ x_2 \end{bmatrix} = \begin{bmatrix} i_d + \frac{\lambda_r}{L_d} \\ i_q \end{bmatrix}$$
 Equation 2.23

$$u = \begin{bmatrix} u_1 \\ u_2 \end{bmatrix} = \begin{bmatrix} \frac{v_d L_d + \lambda_r}{L_d^2} \\ \frac{v_q}{L_q} \end{bmatrix}$$
 Equation 2.24

$$A = \begin{bmatrix} -\frac{R_s}{L_d} & \frac{L_q \omega_r}{L_d} \\ -\frac{L_d \omega_r}{L_q} & -\frac{R_s}{L_q} \end{bmatrix}$$
 Equation 2.25

The adjustable model can be designed as:

$$\frac{d}{dt}\hat{x} = \hat{A} \cdot \hat{x} = u$$
 Equation 2.26

where

$$\hat{x} = \begin{bmatrix} \hat{x}_1 \\ \hat{x}_2 \end{bmatrix} = \begin{bmatrix} i_d + \frac{\lambda_r}{L_d} \\ i_q \end{bmatrix}$$
 Equation 2.27

$$u = \begin{bmatrix} u_1 \\ u_2 \end{bmatrix} = \begin{bmatrix} \frac{v_d L_d + \lambda_r}{L_d^2} \\ \frac{v_q}{L_a} \end{bmatrix}$$
 Equation 2.28

$$\hat{A} = \begin{bmatrix} -\frac{R_s}{L_d} & \frac{L_q \hat{\omega}_r}{L_d} \\ -\frac{L_d \hat{\omega}_r}{L_q} & -\frac{R_s}{L_q} \end{bmatrix}$$
 Equation 2.29

The matrix \hat{A} in the adjustable model is corrected by the estimated speed $\hat{\omega}_r$, and the $\hat{\omega}_r$ can be expressed by an adaptive mechanism:

$$\widehat{\omega}_{r} = \int_{0}^{t} k_{1} \left[i_{d} \widehat{\iota}_{q} - i_{q} \widehat{\iota}_{d} - \frac{\lambda_{r} \left(i_{q} - \widehat{\iota}_{q} \right)}{L_{d}} \right] dt + k_{2} \left[i_{d} \widehat{\iota}_{q} - i_{q} \widehat{\iota}_{d} - \frac{\lambda_{r} \left(i_{q} - \widehat{\iota}_{q} \right)}{L_{d}} \right] + \omega_{r}(0)$$
Equation 2.30

where k_1 and k_2 are the PI regulator coefficients. The error between the reference model and the adjustable model is the input to the adaptive mechanism to modify the parameters of the

adaptive model to make state \hat{x} approach state x quickly and in a stable manner and the error approaches zero [80].

2.3.4 Converter open circuit faults and potential solutions

Power converters are often exposed to high stresses and several failures such as power switch open-circuit faults [81] may occur. Open-circuit faults are usually linked to the loss of bonding wires of the control signal or to a short-circuit fault causing rupture of the transistor [66, 67]. In the event of such a fault, the converter cannot synthesize the desired output voltage and it provides a large torque ripple and increase in harmonic components in the current [82]. Thus, fault tolerant control is needed which can be provided by, for example, a high order sliding mode control. This section will introduce the Second-Order Sliding Mode (SOSM) control.

Ideally the structure of the converter needs to be designed with minimum hardware modifications from the conventional circuit whilst allowing bypassing of the affected components to minimise the impact of an open-circuit fault. In [68], a circuit structure was presented that added extra bidirectional switches to bypass a faulty IGBT. This structure added three Triacs (pairs of back-to-back thyristors) in series with the three-phase generator and connected to the mid-point of the split DC bus capacitor link. Figure 2.14 illustrates the new converter structure on the right with the traditional converter structure on the left-hand side.

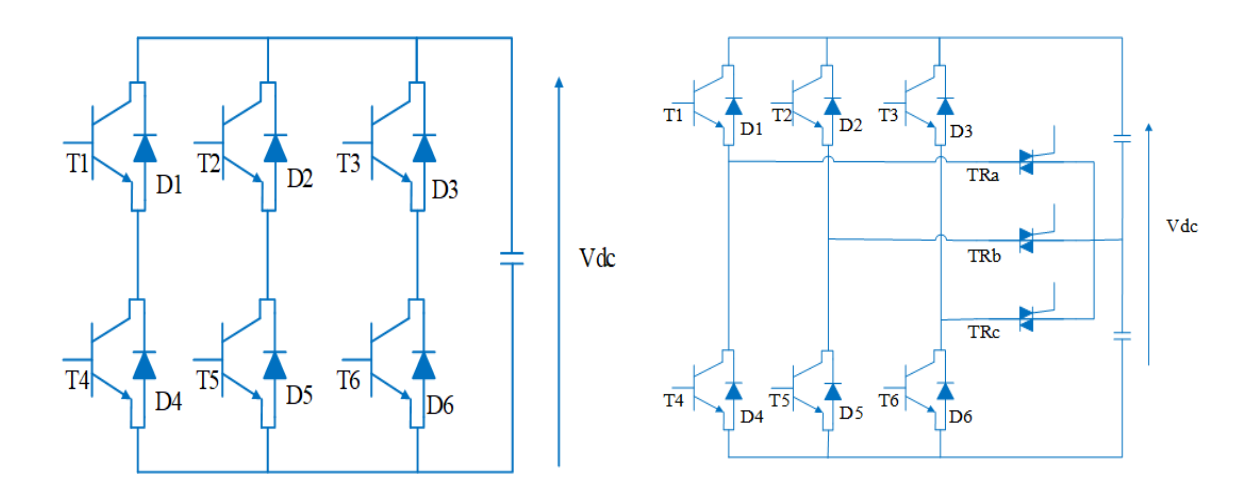


Figure 2.14 SOSM converter structure and traditional converter structure

The SOSM control can be developed through five steps [68, 83]:

(1) The speed reference ω_{ref} is given by the MPPT control

(2) To make sure that the rotor speed converges to ω_{ref} , an optimal electromagnetic torque is given as follows:

$$T_{eref} = T_m + f\omega_r - \alpha(\omega_r - \omega_{ref}) + J\dot{\omega}_{ref}$$
 Equation 2.31

where α is a positive constant. In order to make the PMSG torque converge to the optimal torque, the current equations are as follows:

$$\begin{cases} i_{ds-ref} = 0\\ i_{qs-ref} = \frac{2T_e}{3p\lambda_r} \end{cases}$$
 Equation 2.32

(3) The second-order sliding mode is defined to make the currents converge to the reference values:

$$\begin{cases}
S_1 = i_{ds} - i_{ds-ref} \\
S_2 = i_{as} - i_{as-ref}
\end{cases}$$
 Equation 2.33

it follows that

$$\begin{cases} \dot{S}_1 = \dot{i}_{ds} - \dot{i}_{ds-ref} \\ \ddot{S}_1 = \varphi_1(t, x) + \gamma_1(t, x) v_{ds} \end{cases}$$
 Equation 2.34

$$\begin{cases} \dot{S}_2 = \dot{i_{qs}} - \dot{i_{qs-ref}} \\ \ddot{S}_1 = \varphi_2(t, x) + \gamma_2(t, x)v_{qs} \end{cases}$$
 Equation 2.35

where $\varphi_1(t, x)$, $\varphi_2(t, x)$, $\gamma_1(t, x)$ and $\gamma_2(t, x)$ are uncertain bounded functions that satisfy:

$$\begin{cases} \varphi_1 > 0; \ |\varphi_1| > \varphi_1; 0 < \Gamma_{m1} < \gamma_1 < \Gamma_{M1} \\ \varphi_2 > 0; \ |\varphi_2| > \varphi_2; 0 < \Gamma_{m2} < \gamma_1 < \Gamma_{M2} \end{cases}$$
 Equation 2.36

where ϕ is the lower bound of φ , Γ_m and Γ_M are the lower bound and upper bound of γ respectly.

(4) The super-twisting algorithm [83] is used to design the second-order sliding mode controller and it contains two parts:

$$\begin{cases} v_{ds} = u_1 + u_2 \\ v_{qs} = w_1 + w_2 \end{cases}$$
 Equation 2.37

$$\begin{cases} \dot{u}_1 = -\alpha_1 sign(S_1) \\ u_2 = -\beta_1 |S_1|^p sign(S_1) \end{cases}$$
 Equation 2.38

$$\begin{cases} \dot{w}_1 = -\alpha_2 sign(S_2) \\ w = -\beta_2 |S_2|^p sign(S_2) \end{cases}$$
 Equation 2.39

where α and β are positive constants.

(5) In order to make the convergence of sliding manifolds equal to zero in finite time, the gains can be chosen as follows:

$$\begin{cases} \alpha_{i} > \frac{\phi_{i}}{\Gamma_{mi}} \\ \beta_{i}^{2} \geq 4 \frac{\phi_{i}}{\Gamma_{mi}^{2}} \frac{\Gamma_{Mi}}{\Gamma_{mi}} \frac{(\alpha_{i} + \phi_{i})}{(\alpha_{i} - \phi_{i})} \\ 0 Equation 2.40$$

The PSF control requires the turbine power versus shaft speed curve and estimate the shaft speed to get the optimal power reference, and the OT control required the system operating under torque control mode, and also need the turbine torque versus shaft speed curve to implement. While for the TCSE control, the parameters of the GRBFN are obtained through an offline training process, which is using a training data set that provided by the TCSE dynamic characteristics [84].

The open-loop control is easy to implement, however there are limits to the numerical resolutions. The open-loop control is highly dependent on the system sampling frequency and control loop frequency. In the closed-loop control, the stability of DO control is guaranteed by the appropriate observer gains and the machine parameters are needed in the observer model. For the SMO control, in some practical applications, if the system is operating under a low sampling ratio and control loop frequency, the robustness and load variations will be affected. In [85], the SMO has a worse performance without oversampling. The SOSM control requires the new structure of the converters, which will increase the power generation cost.

The fault tolerant control strategies discussed in this section can deal with different failures in TCT generation on the electrical side. For the generator rotor speed sensor fault and converter open-circuit fault, there is no further investigation in this thesis. The main research direction of this thesis will be focus on the MPPT control of TCT generation systems to deal with tidal current velocity sensor faults. As mentioned above, the PSF control, OT control and TCSE control have some disadvantages. The P&O control and FL control will be the main methods used in this thesis. The aim is to use P&O control and FL technology to implement the MPPT control without a tidal current velocity sensor.

2.4 Maximum Power Point Tracking

The tidal current generation system generally consists of a turbine to transfer tidal current energy to mechanical power, a generator to transfer the mechanical power to electrical power, and through power converters to realize power flow control and the grid connection. The maximum power will vary according to changes in the tidal current velocity, thus the tidal current generation system needs MPPT control to maintain maximum output power under different tidal current velocity. Therefore, the tidal current turbine generation system needs the tidal current velocity signal that would normally be provided by the tidal current velocity sensor. Generally, for wind turbine systems and tidal current turbine systems, the MPPT technologies include optimum tip speed ratio control, MPPT control with a look-up table or perturb and observe control [86].

Optimum tip speed ratio control is widely used in wind turbine and tidal current turbine generation systems. This control method requires the wind or tidal current velocity signal which is used to keep the tip speed ratio at its optimal value to make sure the turbine system can extract the maximum power from the wind or tidal current flows [87]. MPPT control with a look-up table needs a table to be created that provides the maximum power curve which is related to the speed reference under certain wind or tidal current velocity conditions and this requires experiments or simulations to establish the look-up table [88]. The optimum tip speed ratio MPPT control and MPPT with loop-up table method need the wind or tidal current velocity signal and the turbine characteristics, which means that the wind or tidal current velocity sensor is needed. Tidal current velocity sensors are expensive and due to the locations where the turbines are installed, the sensors may not provide accurate tidal current velocity signals [86]. Furthermore, the harsh environment may damage the speed sensors. This will lead to differences between feedback values and designed values, and cause a decrease in the MPPT performance.

The P&O control does not require the wind or tidal current velocity signal. It will detect changes in the output power and provide a corresponding reference speed signal to control the system and maintain operation at the maximum power point [88]. The basic principle of the P&O control method in PV systems is to calculate the PV generation power through the PV voltage and current, compare the present power and voltage with previous values, then adjust the duty cycle of power converter to control the PV system. The advantage of using P&O control in PV systems is that it is easy to implement and low cost [89], but also there will be some problems, for example: the long tracking time and big oscillation near the maximum

power point under fast changing irradiation conditions [90] which will cause low tracking efficiency on cloudy days [91].

Generally, in PV systems, the P&O control application is one of two types: reference value perturbation or duty cycle perturbation. Paper [92] shows the use of P&O control with reference value perturbation. In this paper, the P&O control provides the reference voltage value directly to the control system by detecting the changes in generation power, and the step size of P&O control should be considered to find the balance between response time and steady state stability. Paper [93] presents the use of P&O control in PV systems with duty cycle perturbation. In this paper, the P&O control is used to provide the duty cycle signal directly to the control system, and the output of the P&O control depends on the PWM frequency and analogue-to digital conversion rate. According to [93], the P&O control has a fast response and low fluctuation, but under high perturbation rates, due to noise, the P&O control will face significant impacts on the tracking performance.

The use of P&O control in wind turbine generation systems can also track the maximum power point without knowledge of the wind turbine characteristics. The P&O control can provide the local maximal point for a given function [94]. However, under rapid changes in wind speed, similar to the PV system, the P&O control will sometimes give the wrong direction of output signal in attempting to achieve the most significant power point [95]. In [96] and [97], a modified P&O control was presented which can avoid the wrong direction of output problem under sudden changes in wind speed by adding more control modes in the P&O control algorithm.

The use of P&O control in PV and wind turbine generation systems will have problems due to the rapid change of solar radiation and wind speed respectively. This will reduce the tracking performance. However in tidal current turbine generation systems, the tidal current velocity does not have quick changes and flows with a fairly constant cycle, thus, P&O control will be a good candidate for the tidal current turbine generation system tidal current velocity sensor less control [86].

Another control method that can be used in tidal current turbine generation systems is fuzzy logic control (FL). FL control has also been widely used in wind turbine generation and PV systems. FL control transfers the input values to fuzzy rules, and through fuzzy inference gets output values, and this make it is possible to deal with nonlinear perturbations caused by the fluctuations in wind speed [98]. In [99, 100] and [101] the fuzzy rules in the FL control

applied in wind turbine generation systems have been modified variously by human experience, intuition, wind range classification and deductive reasoning.

Basically, the FL control has two groups of input values, one is the error of controlled values, the other is the error in the error of controlled values, and there is one output value which is the desired value [102]. In wind turbine systems, the output of FL control is generally set as pitch angle. The inputs of FL control have some different options depending on the design thoughts. From [103-107], the set of FL control input values are the active power errors and the error of active power errors, whilst in [108, 109] and [110] the generator rotor speed errors and the error of generator rotor speed errors were used as the FL control input values. The inputs of FL control can also be errors of different controlled values, such as in [111] where the FL control inputs are the error of active power and generator rotor speed. Sometimes three inputs can also be set for FL control. In [112], the error of generator power, the variation of power error (compared with the previous step power error) and error of generator rotor speed are used as the inputs. The inputs of FL control do not all need to be all error values, for example, paper [113] used the wind speed and the error of generator rotor speed as the inputs, while in [114] the voltage and error of voltage are the inputs of FL control. All of these FL control methods have achieved the control aims, and all the FL control applications have better performance than a PID controller.

FL control has been considered to be the most powerful control method in PV systems, as FL control has quick tracking speed and small variations near the maximum power points [115] [116]. Similar to the FL applications in wind turbine systems, FL control in PV systems also does not require training data, and this will make it is suitable for serval PV systems that have the same MPPT design. However under rapid changes in irradiance, FL control will face drift problems [117, 118].

Some research has been done to try to solve the drift problem. In [119], a particle swarm optimisation algorithm was used in a PV system. When the solar irradiance changes quickly, this algorithm can adjust the duty cycle to avoid the drift problem. In [120], a gain controller was designed based on the FL control, and this controller can adjust the traditional FL control step size online. Meanwhile, for a stand-alone PV system, paper [121] implemented a new FL control method which is based on P&O control. In [122], a fuzzy cognitive network was added to the conventional FL control to solve the drift problem. These papers solved the FL control drift problem in PV systems, but these solutions need more control modules, and this will make the whole system highly complex.

In order to avoid the drift problem in PV systems and not add more control units, some papers have presented improved conventional FL control methods by upgrading the membership functions of the FL control. For example in [123], for an FL control that had already been designed, a genetic algorithm was used to optimize the membership functions. In [124], in order to reduce the processing time of FL control, a new structure of FL control was proposed based on an asymmetrical fuzzy functions process. Also in [125], a Multivariate Regression prediction (M5P) model tree was used to model the FL control to track the maximum power point. Paper [126] provided a new membership function tunning method, the traditional trial-and-error method was replaced by a Hopfield neural network. An improved FL control was designed in [127], which is based on indirect fuzzy logic. From [123-127], these researchers have proved that the optimization of FL control algorithm can solve the drift problem in PV systems, with fast tracking speed and small fluctuations.

The MPPT control algorithm is an important part of wind turbine and PV systems, and in tidal current turbine systems, MPPT is indispensable. Due to the similarities between wind turbine systems and tidal current turbine systems, most of the MPPT control applications that have been used in wind turbine systems could also be implemented in tidal current turbine systems. In order to maintain the system operation when the tidal current velocity sensor is damaged or lost, MPPT control algorithms which do not require the system characteristics are considered to be candidates to approach as the control strategy in tidal current turbine systems, such as the P&O control and FL control mentioned above.

In TCT generation system, MPPT control is necessary, and the traditional MPPT control requires the signal/data from a tidal current velocity sensor, but under the tidal current velocity sensor damage condition, the traditional MPPT control will not work, and the system operation will be interrupted. The work in this thesis with P&O and FL technology based MPPT control can continue the TCT generation system operation without the tidal current velocity sensor signal.

2.5 Summary

This chapter gives a brief introduction to tidal current energy which has high energy capacity and has been considered in recent years for development in many countries to generate significant amounts of electrical power. In order to extract the maximum power from the tidal current energy, MPPT technology is necessary in a tidal current turbine generation system. MPPT technology is widely used in wind turbine and PV systems, and due to the similarities

between tidal current turbines and wind turbine systems, the MPPT technologies used in wind turbines can be implemented in tidal current turbine systems.

In conventional tidal current turbine systems, the approach of MPPT requires the signal from a tidal current velocity sensor. However due to the harsh underwater environment, and the fact that the tidal current velocity sensor is exposed directly to the seawater, they may suffer from the tidal current forces and erosion by seawater. In order to avoid high-cost maintenance and improve the system robustness, a TCT system that can operate with the elimination of tidal current velocity sensor can be considered as a solution, of which the control system can enable continuous system operation, tracking the maximum power. In this thesis, P&O control and FL control will be implemented in a conventional tidal current turbine generation system to be developed as sensor-less control.

The next chapter will present the modelling of a tidal current turbine, generator, the tidal current resource, as well as the generator side converter control, which can be used as the basic model to develop a conventional TCT system and to apply the P&O control and FL control on it.

Chapter 3. Tidal Current Turbine System Modelling

This chapter deals with the model development of a tidal current turbine system based on MATLAB/SIMULINK. The overall system includes the resource model, turbine model and generator model, and the location site will be briefly introduced as well. The turbine model is developed based on the EVOPOD project, with the turbine model parameters the same as in the project device. The generator model is developed from a manufacturer from China, whose permanent magnet generator can be produced and customized to meet the users' requirements, and it is chosen in this case based on the EVOPOD project turbine. The location site is chosen as the Pentland Firth, which has high tidal current flow velocities. A basic tidal current turbine system will be illustrated together with results and discussions. This model will be the fundamental model to allow control strategies, grid connection control and a long-term simulation to be developed and evaluated.

3.1 Tidal Current Turbine Model

The electrical layout and modelling approaches used in tidal current systems are similar to those used in onshore and offshore wind systems. The speed of wind is higher than the water current speed while the air density is lower than water density, so these lead to a result that the wind turbine operates at higher rotational speeds and lower torque while the tidal current turbines operate at lower rotational speeds and high torque [59].

The generators used in wind turbine systems are similar to those in tidal current turbine systems, such as permanent magnet synchronous generators (PMSG) and doubly fed induction generators (DFIG) [60]. A fixed pitch wind turbine with a PMSG direct drive system has been found to be more reliable and economical, because the elimination of the pitch variation mechanism simplifies the system's operation and decreases its downtime due to failure [40]. The tidal current turbine used in this thesis is a fixed pitch turbine, which will be introduced in the following sections.

3.1.1 Evopod E35 tidal current turbine

The tidal current turbine model used in this thesis is the Evopod E35, which is a ¼ scale turbine from Ocean Flow Energy Ltd. and was tested in the sea from third quarter 2014 at a nearshore site in Sanda Sound, Argyll & Bute. The Evopod E35 is a 4.5m diameter horizontal axis tidal current turbine, mounted on a semi-submerged floating platform, the rated output power is 35kW [128]. Before the Evopod E35 was tested in the sea, a 1/40th experimental

scale Evopod turbine model was tested in the combined wave, wind and current tank in Newcastle University, with the performance tested under both current and wave conditions [129]. From reports [128] and [129], the turbine parameters can be obtained, and based on these parameters, a MATLAB/SIMULINK model was developed.

Figure 3.1 shows the general arrangement of the Evopod E35 turbine, while Figure 3.2 illustrates the deployment of E35 in the sea. There is a navigation light and a yellow St Andrews Cross on its mast, to make sure that vessels can pass the turbine units like they would pass a navigation buoy. It was deployed from 7th August 2014 to 7th September 2015 and the trials proved that the Evopod E35 has low levels of motion and is robust in the moderately fast flowing tidal site. The streamlined surface-piercing struts and turret mooring of the floating platform make sure that the device always faces into the tidal current direction [130, 131].



Figure 3.1 Evopod E35 general arrangement (figure from report [128])



Figure 3.2 deployment of the E35 at Sanda Sound at the mooring location [130]

Value	
4	
4.5	
13	
8	
0.7	
2.4	
35	
3.2	
	4 4.5 13 8 0.7 2.4 35

Table 3.1 Evopod E35 specification of the ½ scale device (taken from [128] and [130])

Table 3.1 gives the parameters of the Evopod E35 turbine from which, together with knowledge of tip-speed ratio and power coefficient, the tidal current turbine model can be developed in MATLAB/SIMULINK. The specific details of tip-speed ratio, power coefficient and the model build are explained in the following sections.

3.1.2 Tip-speed ratio

As discussed in Section 2.3.1, and repeated here for convenience, the tip-speed ratio λ is defined by Equation 2.1, the amount of power that be captured from a tidal current turbine can be expressed by Equation 2.2. As in this thesis, the turbine Evopod E35 is a fixed pitch device,

thus the value of β is constant and equals 0.

The C_p against λ curve of a marine current turbine is typically of the form shown in Figure 3.1. From Equation 2.2 it can be seen that the power P_t is proportional to the power coefficient C_p , and from Equation 2.1 the tip-speed ratio λ is proportional to rotor speed ω_t . In order to get the maximum power from the turbine, from Figure 3.1 it can be seen that only one value of λ makes C_p a maximum. This means, that to improve the power capture from the turbine, the rotor speed must be adjusted in a range to make sure that C_p can reach the maximum value range. For different marine current turbine systems, the values of C_p and λ are different but Figure 3.1 is representative of a typical characteristic.

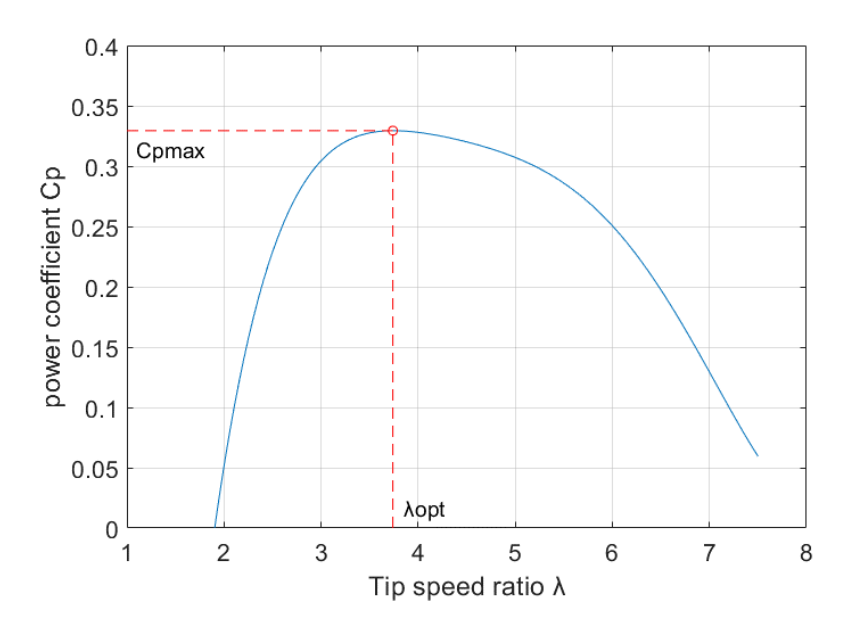


Figure 3.3 Tidal current turbine power coefficient with respect to the tip speed ratio

3.1.3 Power coefficient

From the above, it can be seen that in order to capture the maximum power from the tidal current turbine, the tip speed ratio must be kept within a specific range, thus speed control is the basic control requirement of the tidal current turbine system. The purpose of turbine control is to adjust the rotor speed to follow a reference to keep the tip speed ratio at its optimum value [45].

Based on the power coefficient versus tip speed ratio (Figure 3.3) and turbine power extraction (Equation 2.2), the relationship between the power coefficient C_p and tip speed ratio λ can be defined as follows (note that this is specific to this particular curve):

$$C_p = 0.001161 \lambda^5 - 0.030582 \lambda^4 + 0.3139 \lambda^3 - 1.5888 \lambda^2 + 3.976 \lambda - 3.6047$$
 Equation 3.1

When $\frac{dC_p}{d\lambda} = 0$, the power that the turbine captures is the maximum value; from the calculation, $C_{pmax} = 0.3294$ and $\lambda_{opt} = 3.774$.

Thus, in the tidal current turbine generation system, the power coefficient should be held near to 0.3294, so that the system can extract maximum power from the tidal current. From the parameters above and Equation 3.1 a model can be built relating C_p and λ , and the simulation model in MATLAB is shown in Appendix A.1.

The turbine model was built using the power coefficient C_p and tip-speed-ratio λ relations from Equations 2.1 and 2.2, with the input of the turbine model being tidal current velocity, and the output of the turbine model as the torque. The simulation model is illustrated in Appendix A.2. In this turbine simulation model, according to the generator parameters, the gear ratio is calculated to match the rated power of the turbine and generator, the calculation process will be presented in Section 3.2.

3.2 Resource Model

According to report [128], the Evopod E35 device was operating at Sanda Sound, which is located at the South-Eastern end of the Mull of Kintyre, between the mainland and Sanda Island. At this site, the strong tidal currents can robustly test the performance and survivability of the device. The tidal current velocity can be up to 5 knots (2.572m/s) in the deeper channel of Sanda Sound, while the maximum spring tide at the device installation site is 4 knots (2.0578m/s). However, due to a cable problem, the data that from the test could not be obtained, so in this thesis, it was necessary to get new tidal current velocity data to test the control strategy performance.

As mentioned above and the data from Table 3.1, it can be seen that turbine installation location needs to have strong tidal currents, of up to at least 2.3m/s, to allow the device to extract maximum power from the tidal current flow. A 2.3m/s tidal current velocity would enable the device to reach its rated power state, otherwise the turbine and generator will be unable to operate at the rated condition.

3.2.1 New location site

In this thesis, the tidal current velocity data from the Pentland Firth is used as the input for the system model to test the performance of the control strategies. The Pentland Firth is located at the northern tip of Scotland separating the Orkney Islands from the mainland to the south [132]. This is the strait connecting the Atlantic Ocean to the North Sea between mainland

Scotland and the Orkney Isles [133]. Figure 3.4 shows the location of Pentland Firth. Scotland is well known for marine renewable energy, it has 16500km of coastline and a population density of 64/km², and is in a strong position to use its wave and tidal resources to generate meaningful levels of electrical power [134, 135]. Pentland Firth has very high average kinetic power density (power per unit area of the sea floor), approximately 170W/m² over an area of 50km² [136] and paper [132] mentioned that the Inner Sound can provide capacity for 85MW of tidal arrays but this may affect natural patterns of sediment migration.

In 2021, the O2 tidal current turbine was installed in the Fall of Warness off the Orkney islands. This is a 2MW tidal current turbine, and it's now generating electricity via the grid in Orkney, capable of powering approximately 4000 UK homes and is also being used to produce green hydrogen energy. The O2 is an upgrade of the SR2000, both developed by Orbital Marine Power (formerly Scotrenewables). The SR2000 was tested by the European Maring Energy Centre (EMEC), showing that it can regularly generate the equivalent of 7% of Orkney's electricity demand [137].

Essentially, Pentland Firth has high power density, strong tidal current flow, and has the potential for subsequent development of tidal current turbines[132].

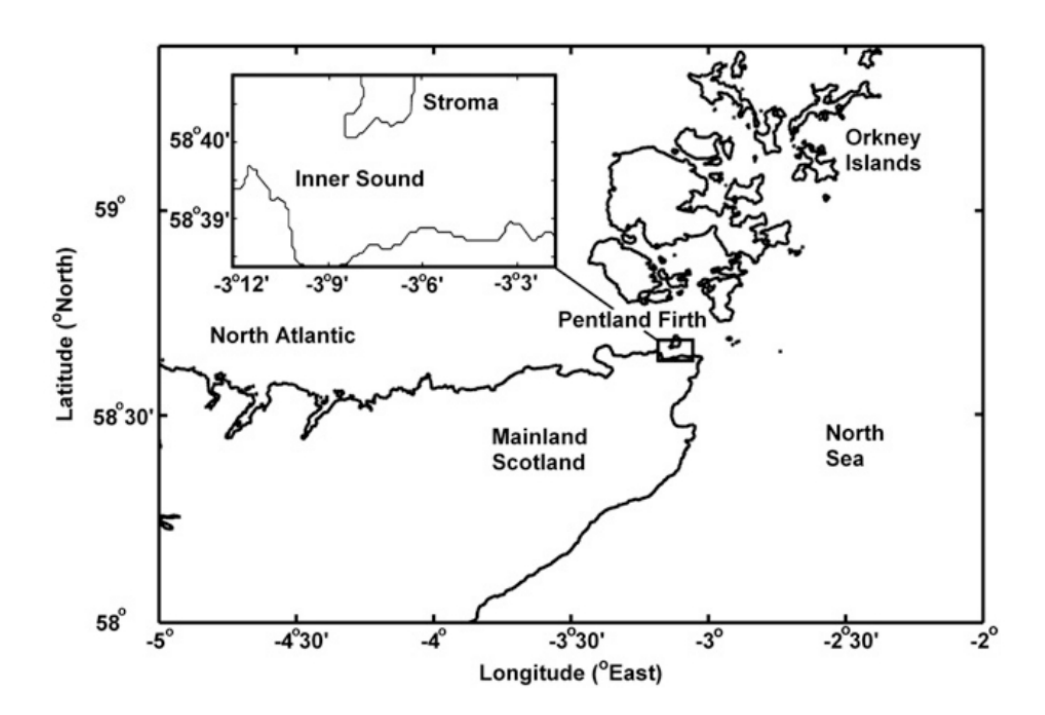


Figure 3.4 Map of the north of Scotland showing the Inner Sound in the Pentland Firth (figure taken from [136])

3.2.2 Resource Model

Tidal current velocity data for Pentland Firth are taken from the E.U. Copernicus Marine Service (CMEMS). Figure 3.5 presents the data area and the data period, it can be seen that the data are from 01/05/2022 to 01/05/2023 [138].



Figure 3.5 the area of tidal current velocity data taken from CMEMS

Figure 3.6 illustrates the tidal current velocity in Pentland Firth from May 2022 to May 2023. From this figure it can be seen that the maximum tidal current velocity can reach 4m/s, which is enough to allow the Evopod E35 turbine to reach its rated power.

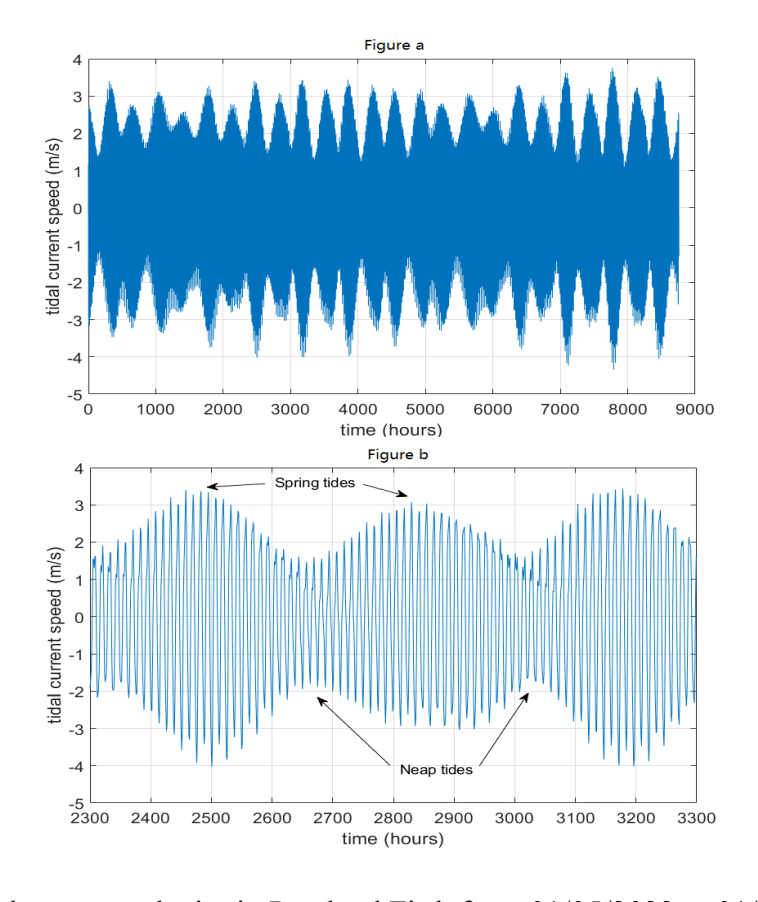


Figure 3.6 (a) Tidal current velocity in Pentland Firth from 01/05/2022 to 01/05/2023; (b) Tidal current velocity for a month

It should be noted that the data taken from CMEMS is the tidal current velocity at -0.5m depth below the surface, but according to [128] Evopod E35 was installed to operate at about -5m depth below the sea surface, as shown in Figure 3.7.

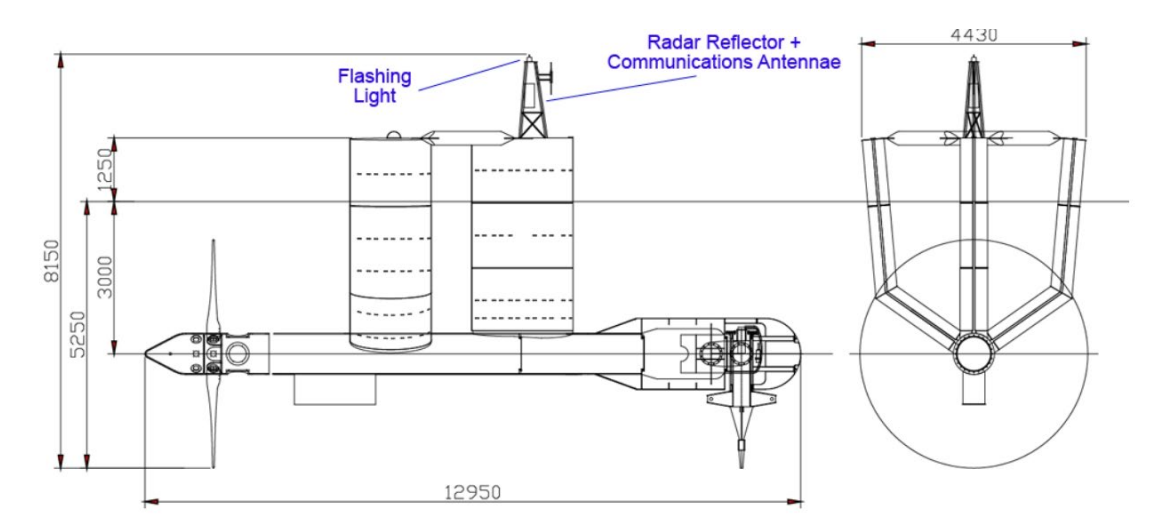


Figure 3.7 Evopod E35 profile (taken from [128])

In order to get more specific performance of the system model, the speed at -5m below the sea surface needs to be calculated. The tidal current velocity profile can be used to calculate the speed at a specific depth where the profile can be expressed as [139, 140]:

$$U_Z = U_0 \left(\frac{d-z}{d}\right)^{\left(\frac{1}{\alpha_{pl}}\right)}$$
 Equation 3.2

where U_0 is the tidal current velocity at the sea surface, U_Z is the tidal current velocity at height z above the seabed, α_{pl} is a power law, and d is the total height that from seabed to sea surface. Considering the Pentland Firth as a tidal stream energy site, the power law can be considered to be 7 [141], and the total depth is 35m, so substituting the tidal current velocity data into Equation 3.2, the tidal current velocity profile can be obtained. Figure 3.8 shows the tidal current velocity profile. Taking the data at point 2508 in Figure 3.6 as an example, it can be seen that, at point 2508, the tidal current velocity at -5m below the surface is about 3.14m/s, which is lower than the speed at -0.5m depth.

The data above are a whole year of tidal current velocity, with the interval of 1 hour per point, and in order to get a smoother input, spline interpolation was used. Spline interpolation can ensure that the new data contains the original data but can increase the number of points with smooth changes, this will lead to a more realistic performance compared with the sudden changes between two points during an hour in the original data set. Figure 3.9 shows the interpolated data set compared with the original data set. It is obvious that the interpolated

data has a smoother change than the original data set. Also, in order to use these data as the input of the tidal current turbine generation system model in MATLAB/SIMULINK, the interpolated data are rectified, as shown in Figure 3.10, this will avoid having a negative power input when running the simulation model.

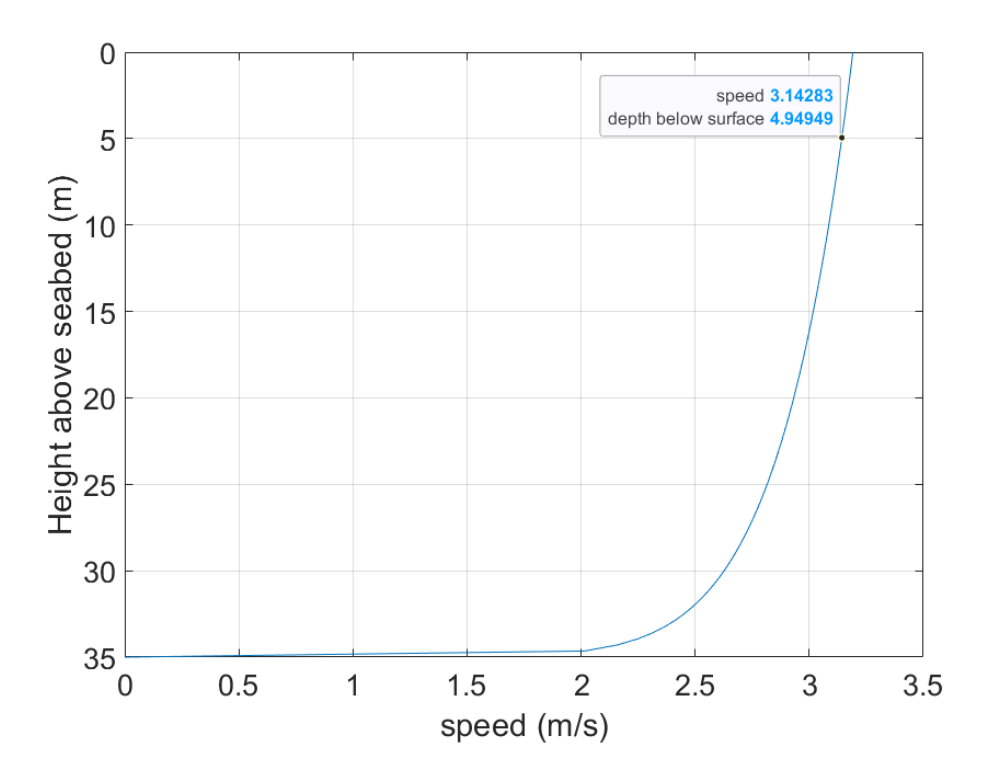


Figure 3.8 Tidal current velocity profile

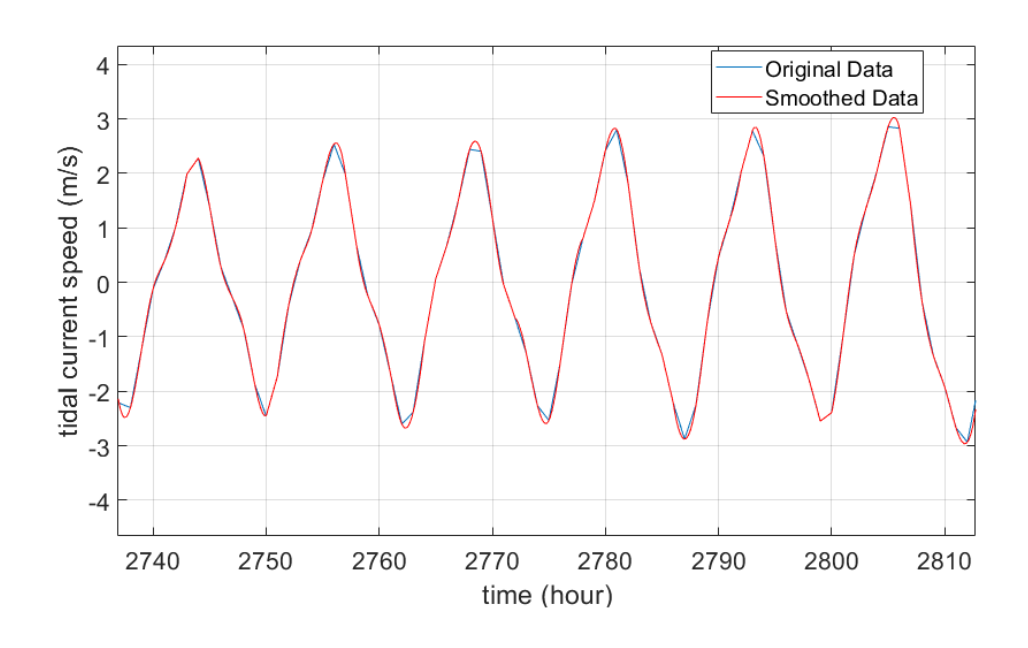


Figure 3.9 Spine interpolated tidal current velocity data verse original data

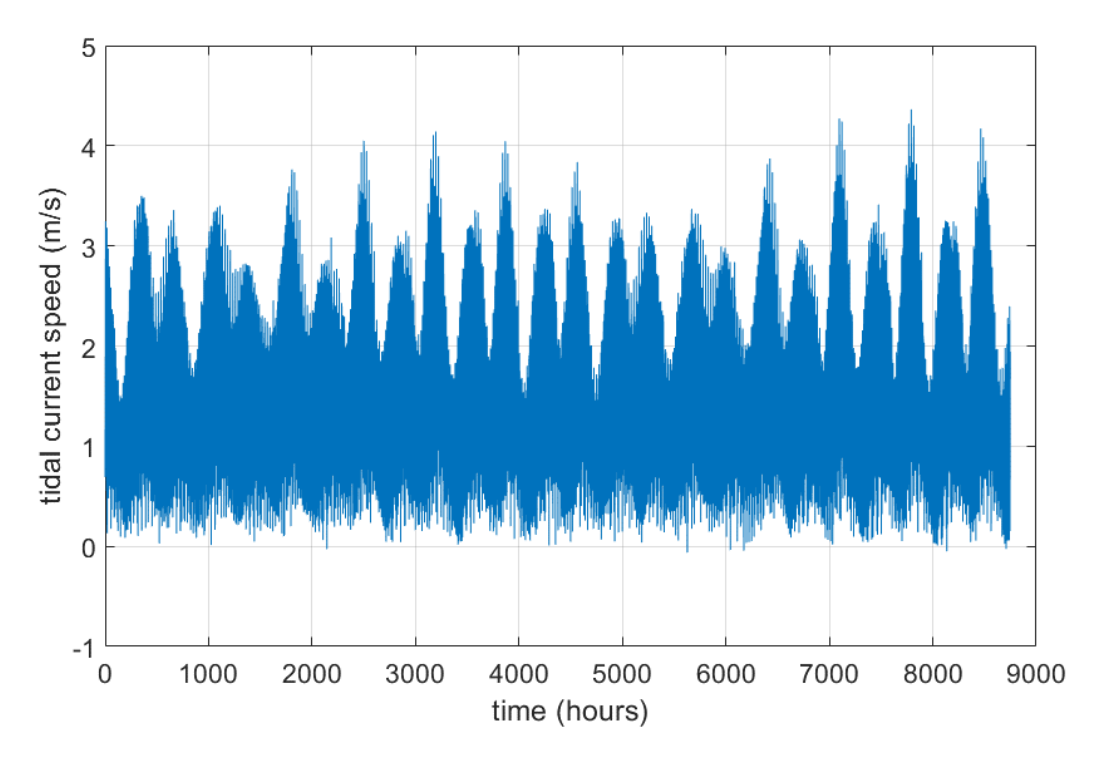


Figure 3.10 MATLAB/SIMULINK rectified input data

3.2.3 Tidal power and turbine performance

In order to describe a tidal current turbine specification, a power curve is needed. The power curve can present the relationship between tidal current velocity and the generator electrical output power. The power that a tidal current turbine can extract from the tidal current flow can be expressed by [142]:

$$P_{t} = \begin{cases} 0 & if \ V_{T} < V_{cut-in} \\ \frac{1}{2} C_{p} \rho \pi R^{2} V_{T}^{3} & if \ V_{cut-in} < V_{T} < V_{rated} \\ P_{t-rated} & if \ V_{rated} < V_{T} < V_{cut-out} \end{cases}$$
Equation 3.3

where V_{cut-in} and $V_{cut-out}$ are the cut-in and cur-out tidal current velocity (m/s) respectively, V_{rated} is the rated tidal current velocity, and $P_{t-rated}$ is the rated output power of tidal current turbine.

The cut-in tidal current velocity, V_{cut-in} , is the minimum speed at which the turbine can generate enough power to overcome all the of the losses in the system. When the tidal current velocity is lower than the cut-in speed, the power extracted from tidal flow is not enough to overcome the turbine drive train friction. Even if it can drive the turbine and generator rotation, the generator output power may still not be enough to overcome the electrical power transformation to the grid, so the active power to the grid may be zero while the generator is driven by the turbine under cut-in speed.

Between the cut-in speed and the rated tidal current velocity, V_{rated} , the output power generated from the turbine and generator increases in proportion to the tidal current velocity. When tidal current reaches the rated speed, the turbine and generator produce rated power which is the rated operating state that they are designed for, and when tidal current velocity goes over rated speed, an approach needs to be taken to limit the turbine and generator rotating speed, such as active pitch control or brake, otherwise, the generator will be damaged by working for an extended time over its rated state.

When the tidal current increases, the forces on the turbine increase and it may exceed the tidal turbine design limit or cut-out speed, $V_{cut-out}$. This means that the turbine must be shut down to avoid turbine system being damaged. Under this situation, the output power from the turbine and generator will be zero [143].

Figure 3.11 illustrates the Evopod E35 turbine output power verses tidal current velocity curve. It can be seen from this figure that when the tidal current is higher than cut-in speed, the turbine output starts to increase following Equation 2.2, when it reaches the rated speed, the output power is equal to the rated power, and once the speed is over cut-out speed, the turbine is shut down and output power then become zero. The black line in this figure is the power defined from Equation 3.3.

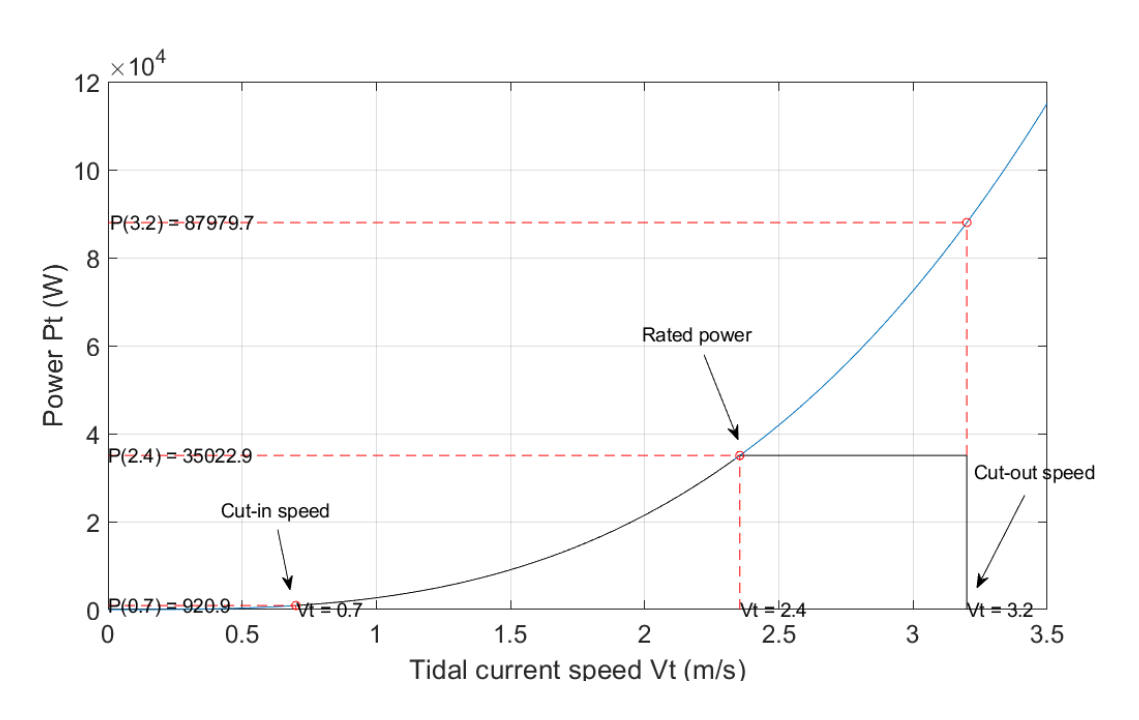


Figure 3.11 Evopod E35 turbine power verses tidal current velocity curve

3.3 Generator Model

This section will present the dynamic model of the PMSG. The model of the PMSG in a dq-axis equivalent circuit form is shown in Figure 3.12 [144].

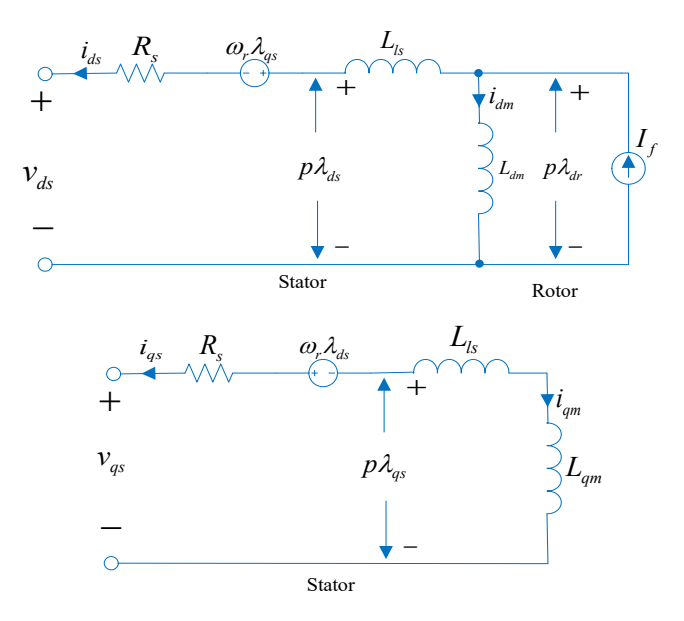


Figure 3.12 PMSG dq equivalent circuit

From the equivalent circuit, the voltage equations of the PMSG in the dq-axis can be expressed as follows [144]:

$$v_{ds} = -R_s i_{ds} - \omega_r \lambda_{qs} + \frac{d\lambda_{ds}}{dt}$$
 Equation 3.4

$$v_{qs} = -R_s i_{qs} + \omega_r \lambda_{ds} + \frac{d\lambda_{qs}}{dt}$$
 Equation 3.5

where i_{ds} is d-axis stator current, i_{qs} is q-axis stator current, v_{ds} is d-axis stator voltage, v_{qs} is q-axis stator voltage, v_{qs} is the winding (stator) resistance (Ω) , ω_r is the electrical rotational speed (rad/s), v_{qs} and v_{qs} are $v_{$

$$\lambda_{ds} = -L_d i_{ds} + \lambda_r$$
 Equation 3.6

$$\lambda_{qs} = -L_q i_{qs}$$
 Equation 3.7

where L_d and L_q are the winding (stator) inductance (H), λ_r is the rotor (permanent magnet) flux (Wb). Substituting Equations 3.6 and 3.7 into 3.4 and 3.5 gives:

$$v_{ds} = -R_s i_{ds} + \omega_r L_q i_{qs} - L_d \frac{di_{ds}}{dt}$$
 Equation 3.8

$$v_{qs} = -R_s i_{qs} - \omega_r L_d i_{ds} - L_q \frac{di_{qs}}{dt} + w_r \lambda_r$$
 Equation 3.9

Rearranging the dq-axis voltage Equations 3.8 and 3.9 gives the dq-axis current equations:

$$\frac{di_{ds}}{dt} = -\frac{R_s}{L_d} + \frac{L_q}{L_d} \omega_r i_{qs} + \frac{v_{ds}}{L_d}$$
 Equation 3.10

$$\frac{di_{qs}}{dt} = -\frac{R_s}{L_q}i_{qs} - \frac{1}{L_q}\omega_r(L_di_{ds} + \lambda_r) + \frac{v_{qs}}{L_q}$$
 Equation 3.11

The electromagnetic torque is then given by:

$$T_e = \frac{3}{2}p(i_{qs}\lambda_{ds} - i_{ds}\lambda_{qs})$$
 Equation 3.12

where p is the number of pole pairs. Substituting Equations 3.6 and 3.7 into 3.12 gives:

$$T_e = \frac{3}{2}p[i_{qs}\lambda_r - (L_d - L_q)i_{ds}i_{qs}]$$
 Equation 3.13

No specific generator data was available for the Evopod E35 therefore, in this thesis, a generator which could match the E35 turbine requirements was chosen. After consulting with several manufacturers, the Qingdao Greef New Energy Equipment Co. Ltd (https://www.greefenergy.com/) were able to provide permanent magnet generators which can meet the requirements of the E35 turbine, and were able to provide detailed generator parameters. The model they can provide is GDF-355L, which is a 60rpm, 35kW permanent magnet generator. Table 3.2 illustrates the main electrical parameters of GDF-355L.

This generator's rated power is 35kW, which matches the rated power of the E35 turbine. This means that when the turbine is operating at its rated condition, the generator is also at rated state, this will not waste energy that is captured by the turbine.

From Section 3.1.3, the optimal value of power coefficient C_{pmax} and tip speed ratio λ_{opt} of the E35 turbine model respectively are 0.3294 and 3.774, and substituting these into Equation 2.1, shows that when the E35 turbine is operating under rated conditions, the rotational speed will be 3.948rad/s which is approximately 37.72rpm. Hence when the E35 rotates at 37.72rpm, it can provide 35kW output power. The GDF-355L generator's rated rotational speed is 60rpm, thus in order to match this with the turbine, a gear box is needed, and the gear ratio is 1:1.6. The use of gear boxes is common in tidal current turbine systems. As discussed in Chapter 2 the MeyGen project and O2 project both have gear boxes in the system. Generally the efficiency of gear boxes will is 98%-99% [61], which means that in the system simulation, this will not affect the turbine and generator output significantly. With the aim to simplify the simulation model, the inertia of the gear box is added to the generator inertia, which can

simulate the dynamics of the drive train system.

Parameters	Value
Rated power (kW)	35
Rated rotate speed (rpm)	60
Rated voltage (Vac)	380
Rated current (A)	53.2
Start torque (N.m)	113.1
Rated torque (N.m)	5655.7
Number of poles	40
Stator phase resistance (Ohm)	0.481
Inductances (H)	Ld=0.0087; Lq=0.01031
Torque Constant (N.m/A_peak)	82
Flux linkage (Wb)	2.733
Inertia (kg.m²)	15.05
Viscous damping properties (N.m/rad)	0.886652

Table 3.2 GDF-355L permanent magnet generator parameters

3.4 Generator Side Convert Control Test Model

3.3.1 Power convertor

Power convertors are widely used in wind turbine generation systems, and given the similarity of the power conversion system, the tidal current turbine generation system also needs power convertors. The power convertors can control the generator rotation speed at a desired value, and during this control process can ensure that the turbine captures power from the tidal current flow efficiently. Generally, in the generation system with a PMSG as the generator, the full power rating back-to-back convertor will be chosen. The back-to-back convertors can decouple the generator from the grid, control the generator rotation speed, and can also control the active and reactive power to improve the power quality [145, 146]. This section will present the generator side convertor control strategy. This is the basic control method of a tidal current turbine generation system for both stand-alone system and grid connection system. The grid side convertor control will be illustrated in Chapter 4.

On the generator side, the convertor can transfer the PMSG three-phase AC current to DC current. In order to maintain the DC link voltage at a constant value, the control method needs to use the dq-axis current to control the speed and output power to create firing angle times for each switching device. The control strategies are introduced in the following sub-sections

[146]. Figure 3.13 shows the generator side convertor topology.

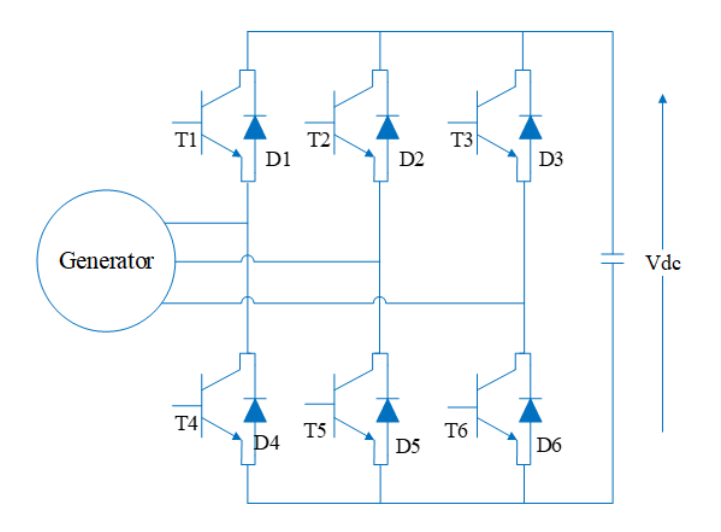


Figure 3.13 generator side convertor topology

3.3.2 Axis reference frame transfer

(1) abc/dq transformation

The axis reference frame transformation can simplify the machine analysis and relevant control strategies in simulations. The most commonly used are abc/dq transformations and $abc/a\beta$ transformations [144]. Figure 3.14 shows the axis reference frame transformation for abc/dq. For a space vector \vec{x} in the abc-axis reference frame, if \vec{x} rotates with the speed ω the value of each phase can be calculated by projection of space vector \vec{x} to the abc-axis, such as in Figure 3.14 the components on abc-axis respectively are x_a , x_b and x_c .

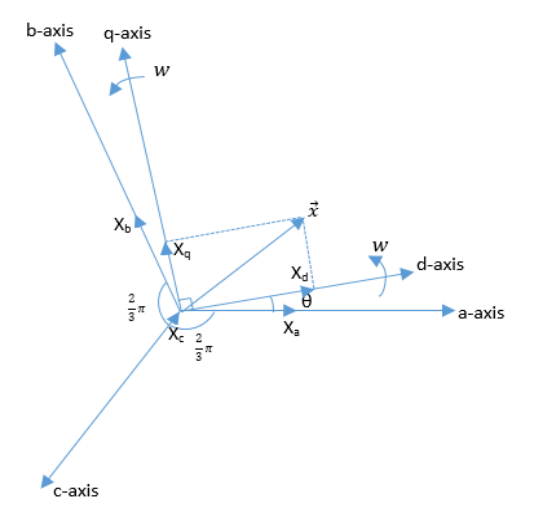


Figure 3.14 *abc/dq* transformation

For the rotating dq-aixs reference frame, if the dq-axis reference frame rotates with the speed

 ω , and the angle between the *a*-axis and *d*-axis is θ , then the relationship between speed ω and angle θ is $\omega = \frac{d\theta}{dt}$. Using trigonometric functions, the rectangular projection of x_a , x_b and x_c on the dq-axis can be obtained. For x_d :

$$x_d = x_a \cos \theta + x_b \cos \left(\frac{2}{3}\pi - \theta\right) + x_c \cos \left(\frac{4}{3}\pi - \theta\right)$$
 Equation 3.14

Thus, the function of the transfer from the *abc*-axis to *dq*-axis is as follows:

$$\begin{bmatrix} x_d \\ x_q \end{bmatrix} = \frac{2}{3} \begin{bmatrix} \cos \theta & \cos \left(\theta - \frac{2}{3}\pi\right) & \cos \left(\theta + \frac{2}{3}\pi\right) \\ -\sin \theta & -\sin \left(\theta - \frac{2}{3}\pi\right) & -\sin \left(\theta + \frac{2}{3}\pi\right) \end{bmatrix} \begin{bmatrix} x_a \\ x_b \\ x_c \end{bmatrix}$$
 Equation 3.15

And using Equation 3.15 an *abc/dq* transformation module can be created in the MATLAB simulation, which is illustrated in Appendix A.3.

By using matrix operations, the dq/abc axis transformation function can be written as:

$$\begin{bmatrix} x_a \\ x_b \\ x_c \end{bmatrix} = \begin{bmatrix} \cos \theta & -\sin \theta \\ \cos \left(\theta - \frac{2}{3}\pi\right) & -\sin \left(\theta - \frac{2}{3}\pi\right) \\ \cos \left(\theta + \frac{2}{3}\pi\right) & -\sin \left(\theta + \frac{2}{3}\pi\right) \end{bmatrix} \begin{bmatrix} x_d \\ x_q \end{bmatrix}$$
 Equation 3.16

The simulation module in MATLAB is shown in Appendix A.4

(2) abc/αβ transformation

The $\alpha\beta$ axis reference frame is stationary, thus making angle θ equal to zero in Equation 3.14 gives the $\alpha\beta$ axis and the function is:

$$\begin{bmatrix} x_{\alpha} \\ x_{\beta} \end{bmatrix} = \frac{2}{3} \begin{bmatrix} 1 & -\frac{1}{2} & -\frac{1}{2} \\ 0 & \frac{\sqrt{3}}{2} & \frac{\sqrt{3}}{2} \end{bmatrix} \begin{bmatrix} x_{a} \\ x_{b} \\ x_{c} \end{bmatrix}$$
 Equation 3.17

And from Equation 3.17 the $\alpha\beta/abc$ transformation function becomes:

$$\begin{bmatrix} x_a \\ x_b \\ x_c \end{bmatrix} = \begin{bmatrix} 1 & 0 \\ -\frac{1}{2} & \frac{\sqrt{3}}{2} \\ -\frac{1}{2} & \frac{\sqrt{3}}{2} \end{bmatrix} \begin{bmatrix} x_\alpha \\ x_\beta \end{bmatrix}$$
 Equation 3.18

From the abc/dq equations and $abc/\alpha\beta$ equations, the $dq/\alpha\beta$ transformation can be written as:

$$\begin{bmatrix} x_{\alpha} \\ x_{\beta} \end{bmatrix} = \begin{bmatrix} \cos \theta & -\sin \theta \\ \sin \theta & \cos \theta \end{bmatrix} \begin{bmatrix} x_{d} \\ x_{q} \end{bmatrix}$$
 Equation 3.19

And the simulation module in MATLAB is presented in Appendix A.5.

3.3.3 Zero-d axis current (ZDC) control

In this project, a current control method has been chosen which is Zero d-axis current control. The Zero d-axis current is widely used in industry, it can provide an efficient solution, and the control algorithm is simple, high efficiency and can decrease the system loss [147, 148].

After transfer from the abc-axis reference frame to the dq reference frame, the d-axis component, i_{ds} is controlled to zero. When the d-axis stator current equals zero, the PMSG stator current is equal to the q-axis component, i_{qs} . It can be illustrated in the following equations [144]:

$$\begin{cases} \vec{l_s} = i_{ds} + ji_{qs} \\ i_s = \sqrt{i_{ds}^2 + i_{qs}^2} \end{cases}$$
 Equation 3.20

In Equation 3.20, if i_{ds} equals zero, then i_s will be equal to i_{qs} . Then the electromagnetic torque, Equation 3.13, can be simplified as:

$$T_e = \frac{3}{2}pi_{qs}\lambda_r$$
 Equation 3.21

From Equation 3.21, the generator electromagnetic torque is proportional to i_{qs} , and in the steady state, the electromagnetic torque is equal to the generator torque. The current i_{qs} can then be calculated by:

$$i_{qs} = \frac{2T_e}{3p\lambda_r}$$
 Equation 3.22

The diagram of zero d-axis control is shown in Figure 3.15, in which the PWM rectifier controls the active power of the system. This can be achieved by controlling the electromagnetic torque. The electromagnetic torque can be controlled by i_{qs} in Equations 3.21 and 3.22. The i_{qs} and i_{ds} current errors will be injected into the PI controllers to generate v_{qs} and v_{ds} by using current Equations 3.10 and 3.11, and then by using the dq/abc axis transformation, this will be passed to the PWM rectifier to generate the pulses to control the switches of the converter.

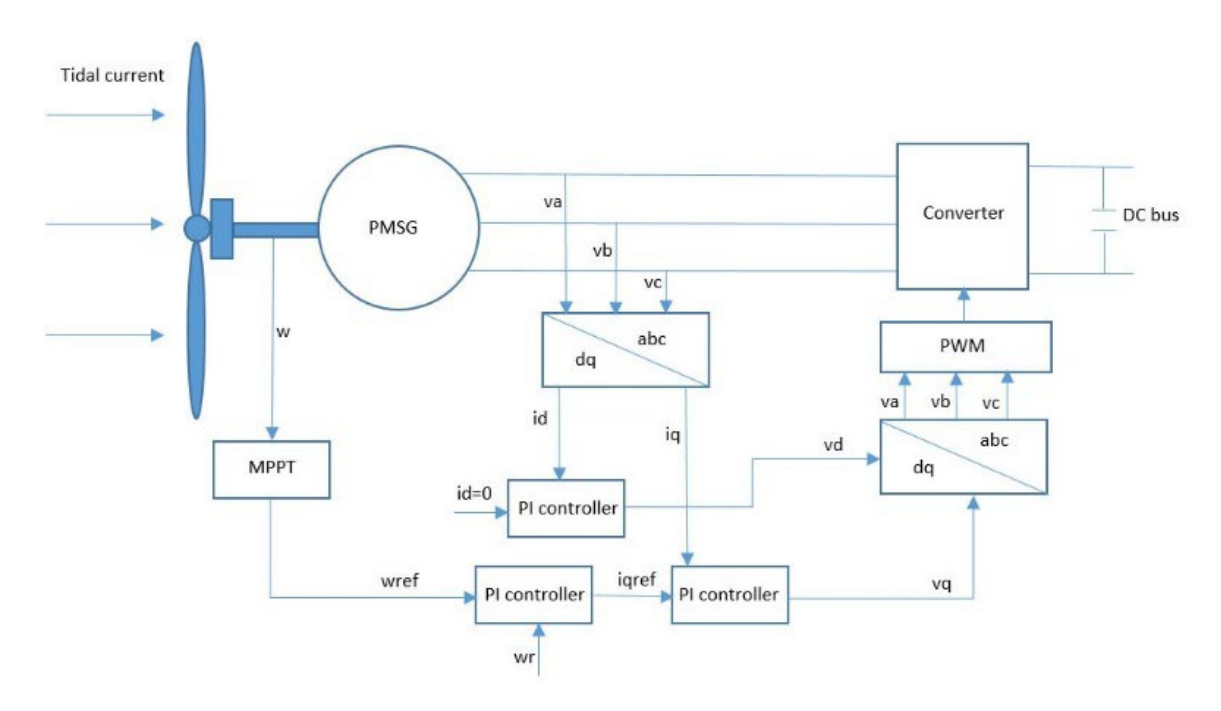


Figure 3.15 The generator side control structure

According to Figure 3.15 and Equations 3.10 and 3.11 the current control loop of the generator side converter can be built in MATLAB, and the current control loop model is shown in Appendix A.6. In the tidal current control loop, through two PI controllers, the real d-axis and q-axis current can be adjusted to follow the reference value, and the outputs of the PI controllers are used to calculate d-axis and q-axis voltage through Equations 3.10 and 3.11. The detailed model can be seen in Appendix A.6.

PI controllers are widely applied in tidal energy systems due to their ability to enhance stability and accuracy. Given the fluctuating nature of tidal flow, PI controllers can adjust system response to maintain steady generator power and frequency [149]. The proportional (P) part enables quick response, while the integral (I) part reduces steady state error, ensuring output despite tidal flow variability [150]. Thus, in this thesis, PI controllers are applied to control the speed, current and voltage.

3.3.4 Speed control

The speed control is the outer control loop. Injecting the error of the speed into the PI controller gives the torque demand and then by using Equation 3.22 the reference i_{qref} can be calculated. The block diagram of the speed control loop is shown in Figure 3.16.

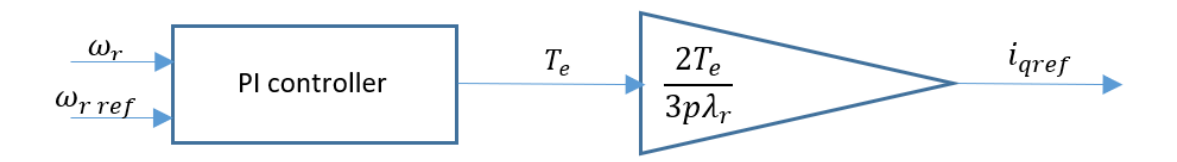


Figure 3.16 Speed control block diagram

The reference speed value can be calculated from the Maximum Power Point Tracking (MPPT). MPPT needs to be used in the control strategies of the tidal current turbines to maximise the power coefficient and hence energy captured. The principle of the MPPT algorithms is as follows:

$$\omega_{ref} = \frac{\lambda_{opt} V_T}{R}$$
 Equation 3.23

where λ_{opt} is the value of tip-ratio speed that maximises the coefficient C_p . The output of the MPPT block is used as the reference value for the rotor speed control [45].

The speed control loop model in MATLAB is illustrated in Appendix A.7. This model is built based on Figure 3.16and Equation 3.22. The speed loop provides the q-axis reference current that is used in the current control loop.

Based on Figure 3.15 and combining all the control loops together, the tidal current turbine system generator side control can be simulated in MATLAB. The model is illustrated in Appendix A.8. In this model, the input torque of the generator is set as a constant to test the system operation, the input torque is 5656 Nm, which is the rated torque of the generator. Also, there is a load control loop in this model, the aim of which is to control the load voltage, which can be seen as the DC link voltage. The DC link voltage needs to be controlled in the grid converter control part, so the load voltage control loop is to test whether the DC link voltage is controllable.

The load voltage is controlled by an IGBT switch, and the IGBT is controlled by a PWM signal provided by a PI controller. The actual load voltage is compared with the reference voltage and then the errors are injected into PI controller.

3.3.5 Evaluation of the generator side convertor control test model

Tests were carried out to evaluate the tidal current turbine system generator side converter control model. The operation of the converter control in terms of accuracy and speed of response was investigated.

Figure 3.17 shows the speed control loop performance. In this figure, the red line is the reference value which has been set as the rated speed of the generator (60 rpm), and the blue line is the actual value. It can be seen from this figure that the generator speed overshoots the demand at first, then converges to the reference speed and reaches the steady state after about 0.75s. During the steady state, the generator rotational speed is stable, and stays at the reference speed. This means that the speed control loop is working, has a fast response time and it is stable.

The PI tuning process was manual: first disable the integral parameter (set to zero), and start with a low proportional value, then observe the results, and increase the proportional value by doubling the value until the result oscillates, and then adjust the proportional value down by half of the value. Then start to adjust the integral parameter with a small value and increase it by doubling the value. When oscillation of the output occurs, the result is near the reference value. Finally, adjust both the proportional and integral values by small steps to get the desired performance. The tuning processes of the other two control loops (*d*-axis and *q*-axis control) are the same.

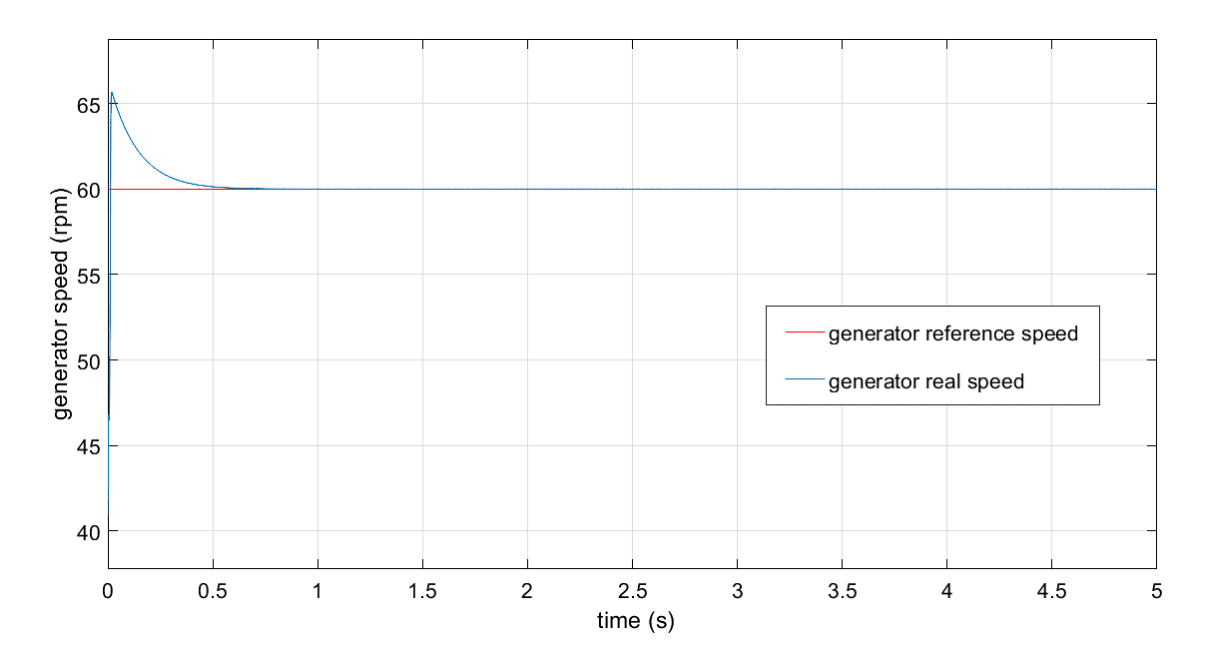


Figure 3.17 Speed control loop result

The current control loop results are shown in Figure 3.18 and Figure 3.19. As mentioned in Section 3.3.3, the aim of the *d*-axis current control loop is to regulate the *d*-axis current to zero. Figure 3.18 is the *d*-axis current, where the red line is the *d*-axis reference value which has been set as zero, and the blue line is the actual *d*-axis current. The actual value converges to the red line and fluctuates around the reference value after 0.75s, remaining stable after

reaching the steady state.

Figure 3.19 is the q-axis current control loop result, where again the red line is the q-axis reference current which is the output of the speed control loop, and the blue line is the q-axis current. It can be seen in this figure that the reference value changes rapidly before 0.75s, and at first, the error between the reference value and actual value is large, and the real value then converges to the reference value. When the error is reducing, the convergence trend is clear, and after 0.75s, the actual current reaches the reference value and remains stable during the steady state.

The load voltage is illustrated in Figure 3.20 where the red line is the reference value and is set as 605 V, to ensure that the converter can provide appropriate AC voltage. In the grid-connected system, with the aim to transfer the power to the grid (380V phase-phase voltage), the converter needs to provide at least the same peak voltage to the grid, which is $\left(\frac{380V}{\sqrt{3}}\right) \times \sqrt{2} \approx 310V$. Generally the DC-link voltage will be 1.5 to 2 times higher than the grid peak value, thus the range of DC-link voltage should be from 460V to 620V. The simulation grid side converter control will be presented in Chapter 4. The full grid-connected system simulation will finally decide the DC-link voltage. The blue line is the actual load voltage. In this figure, the actual voltage overshoots at first and then converges to the reference value. After about 0.75s it reaches the steady state and remains stable.

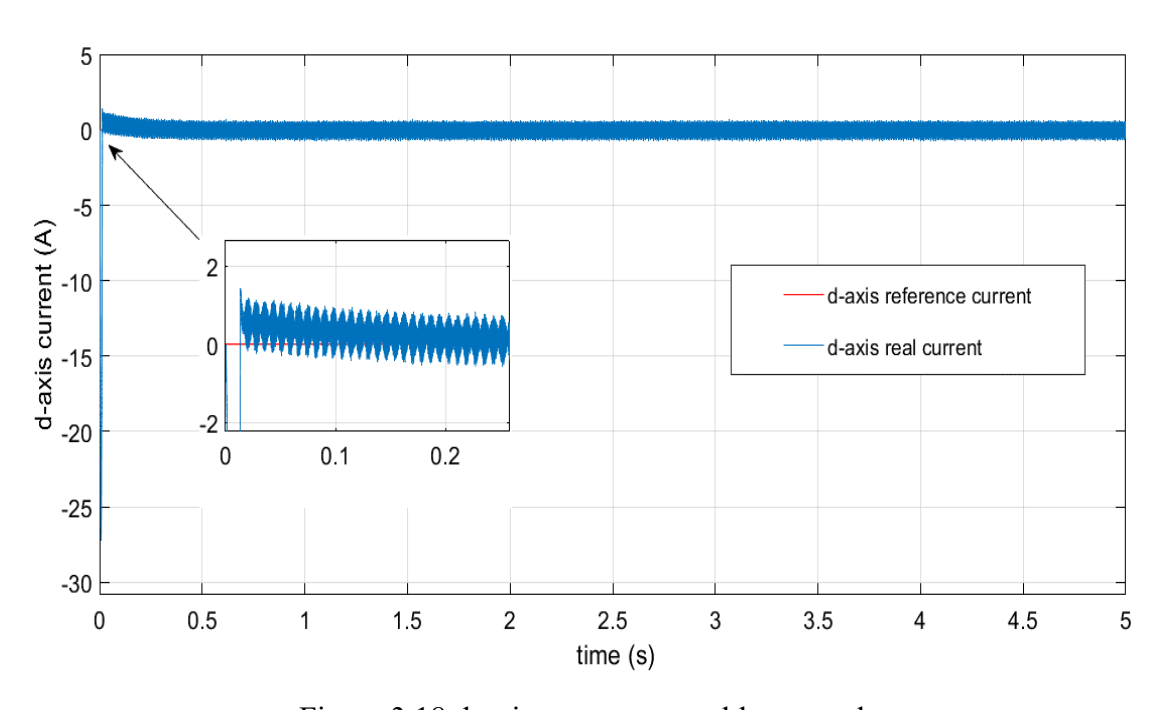


Figure 3.18 d-axis current control loop result

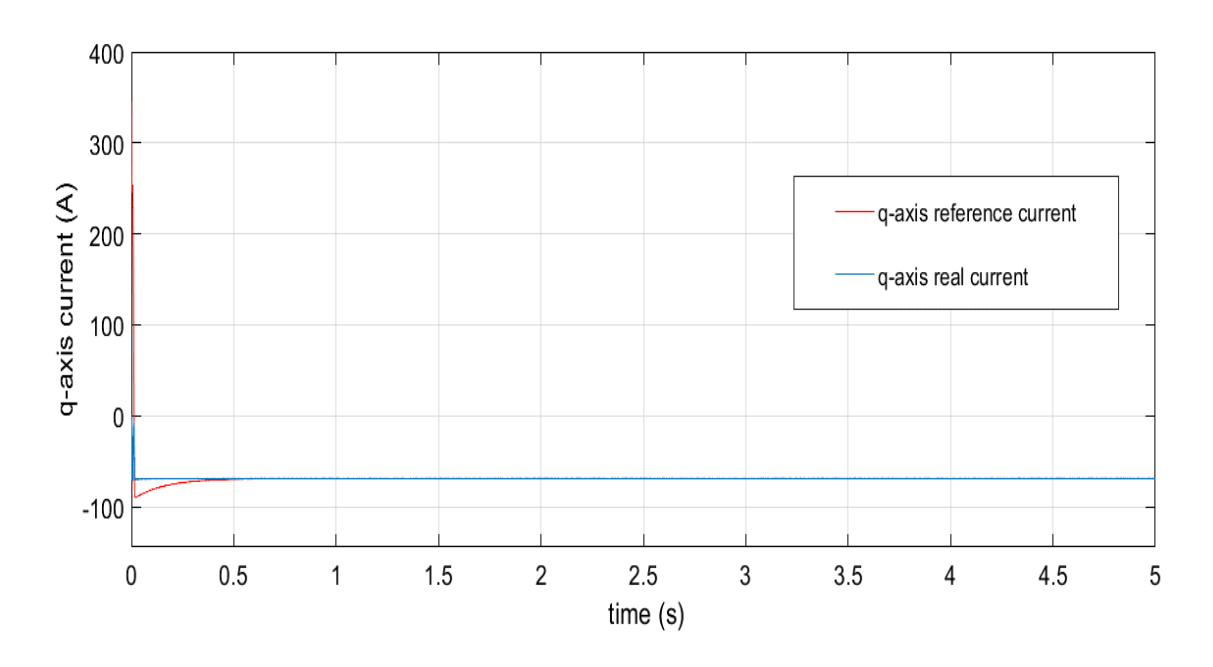


Figure 3.19 q-axis current control loop result

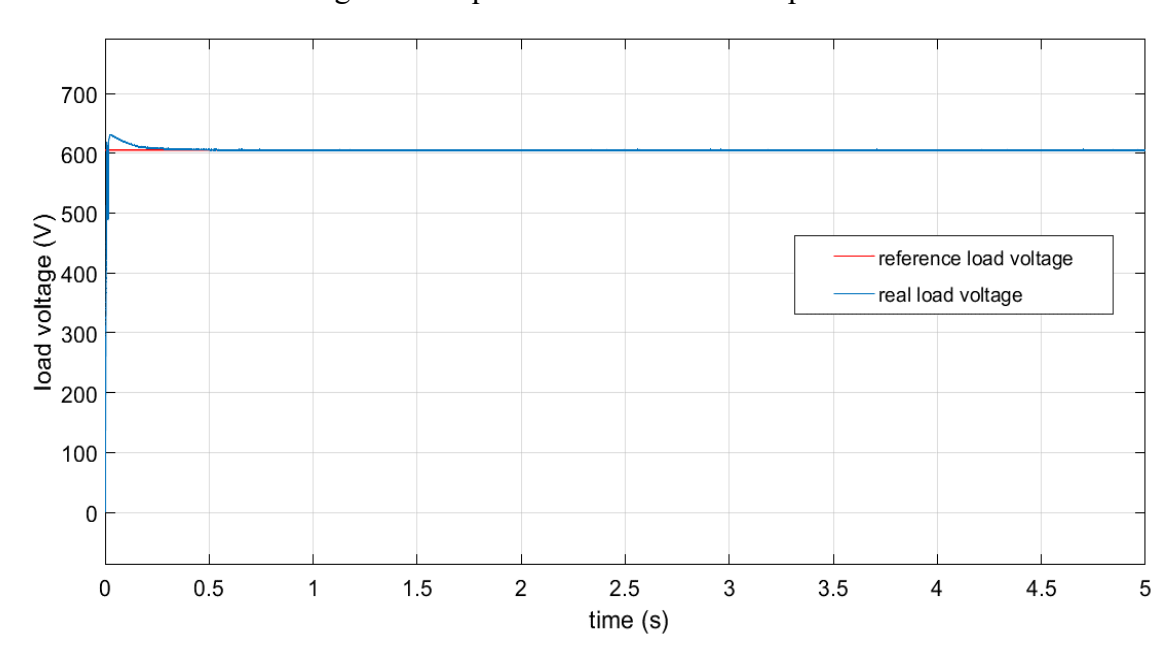


Figure 3.20 Load voltage control loop result

3.4 Summary

This chapter mainly discussed the tidal current turbine model development in MATLAB/SIMULINLK basic on the ¼ scale Evopod E35 turbine, and the generator model created based on the GDF-355L PMG. Also, it introduced the tidal current velocity data and the power that the turbine can extract form the tidal current flow. A test model of generator side converter is illustrated as well as the control strategies. Finally, some results of this test model are presented. From the results above, it can be seen that the tidal current turbine system generator side converter control is working correctly, and has a fast response time,

which can make the system reach steady state after 0.75s. The system is stable during the steady state, which can be seen from the generator rotational speed and load voltage, when the system reaches steady state, the value of generator speed and load voltage remain at the reference and rated values respectively. Also, the load voltage is controllable, it has been controlled at 605V, and thus this model can be connected with the grid side converter control model and transfer power to the grid.

Based on the model developed in this chapter, an energy storage module and a boost converter can be added to make a stand-alone system model. Also, the model in this chapter can be combined with a grid side converter to give a grid-connected system model and control strategies can then be applied in the complete grid-connected system to control the turbine and generator without tidal current velocity sensor. The detailed model development and results for both the stand-alone and grid connected systems with P&O control strategies are presented in the next chapter.

Chapter 4. Tidal Current Speed Sensor-less MPPT Control with

Perturb and Observe Methodology

Chapter 3 introduced the tidal current turbine and generator modelling and also tested the generator side convertor control. The models in Chapter 3 will be used as the basis for this chapter to develop the completed model and control strategy applications. In order for the system to operate without a tidal current velocity sensor, Perturb and Observe (P&O) control is developed as the control strategy in the models in this chapter. The P&O control can track the maximum power point without having a signal from the tidal current speed sensor, which means that the system can avoid the need for maintenance of the tidal current speed sensor if it becomes lost or damaged. In this chapter, based on the tested model in Chapter 3, two systems will be presented: one is a stand-alone tidal current turbine generation system in which the output of the tidal current turbine is directly connected to the load and an energy storage system to store the extra energy, while the other one is a grid connected system, combined with a grid side convertor model in which the output power is transferred to the power network via a grid side converter. The P&O control design for the stand-alone system and grid-connected system are illustrated, with the input of the stand-alone system as a step change to test the dynamic response of the P&O control; while the input of the conventional grid-connected system will be both a step change and a ramp change to test the P&O control performance under sudden and continuous changes. The results and discussion will be presented at the end of the chapter.

4.1 Maximum Power Point Tracking (MPPT)

Maximum Power Point Tracking (MPPT) is widely used in Photovoltaic (PV) energy systems and wind turbine generation systems in order to track the maximum power point of PV arrays and wind turbines [151].

For a given tidal current turbine, the power that is captured by the turbine varies with tidal current velocity. Equations 2.1 and 3.1 determine the variation of the turbine output power versus rotor speed and Figure 4.1 shows the relationship between power that the case study turbine can produce and the turbine rotor speed. It can be seen that for each tidal current speed, there is a corresponding rotor speed that maximises the turbine output power, and in this figure, the black line is the optimal power curve. The MPPT control aims to make the system operate at the speed matching the black line to get the maximum output power.

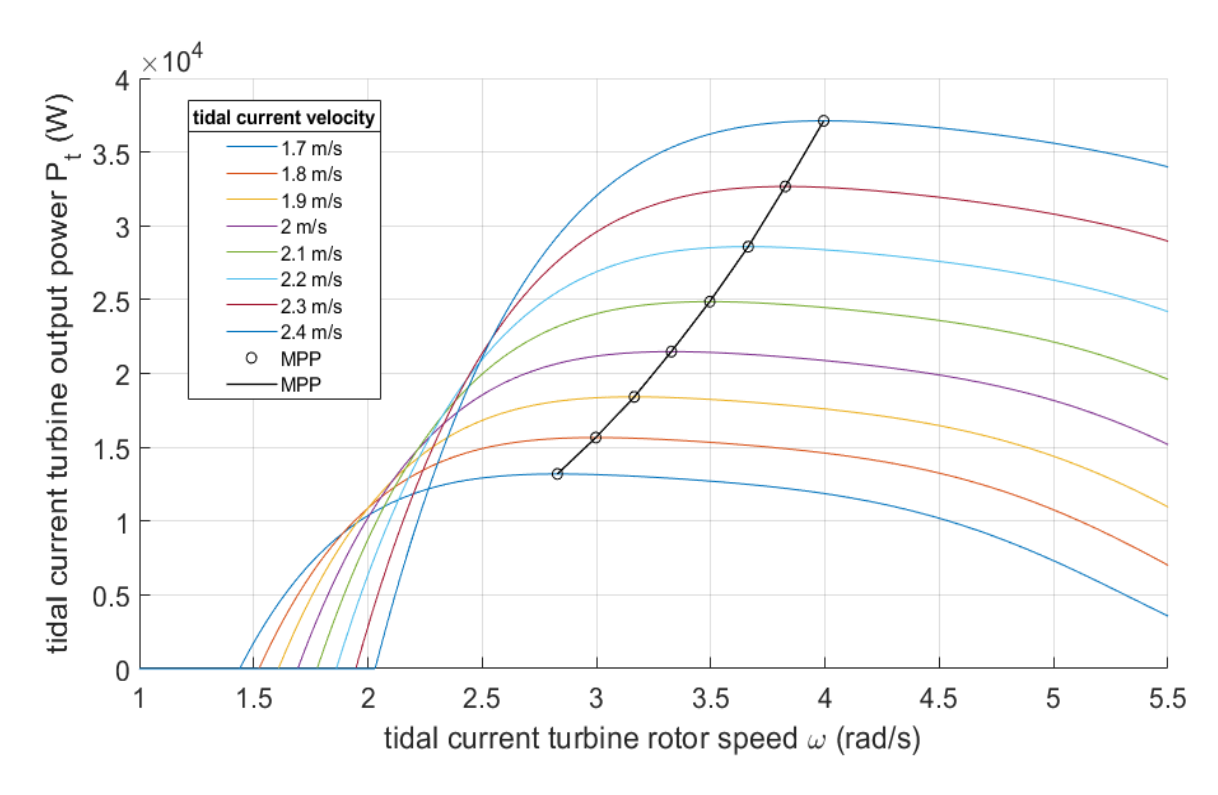


Figure 4.1 Tidal current turbine output power vs rotor speed under different tidal speed

4.2 Perturb and Observe Control (P&O)

Perturb and Observe (P&O) control does not rely on the turbine characteristics. This means that the tidal current speed sensor is not needed, which will reduce the failures that are caused by the loss of or damage to tidal current speed sensors.

P&O control is also known as hill climb search control. The basic theory of this method is one of creating changes in rotor speed and observing the corresponding changes in power. The searching process is illustrated in Figure 4.2, the control schematic diagram is shown in Figure 4.3, and the flow diagram is in Figure 4.4.

During the searching process, the P&O control continuously gives the generator a reference speed, and the control system adjusts the actual generator speed to follow this reference. The reference speed is increased or decreased by $\Delta\omega$ in each step. In the tidal current turbine generation system, the output voltage is proportional to the generator speed, so the change in generator speed leads to a change in output power by an amount, ΔP . If $\Delta P > 0$, the search direction in next step is the same, if $\Delta P < 0$, then the search direction is opposite [22, 73, 152].

Figure 4.2 illustrates the searching process. In the searching process, the generator is initially operating at a speed ω_n , and the corresponding power is P_n , then if the rotor speed is

increased by value $\Delta\omega$, the new rotor speed is $\omega_{(n+1)}$ and the new power is $P_{(n+1)}$. Comparing the new power $P_{(n+1)}$ and the previous power P_n , if $P_{(n+1)} > P_n$ then the method keeps increasing rotor speed by an increment $\Delta\omega$ until the power reaches the maximum value, otherwise it decreases the rotor speed by the increment $\Delta\omega$.

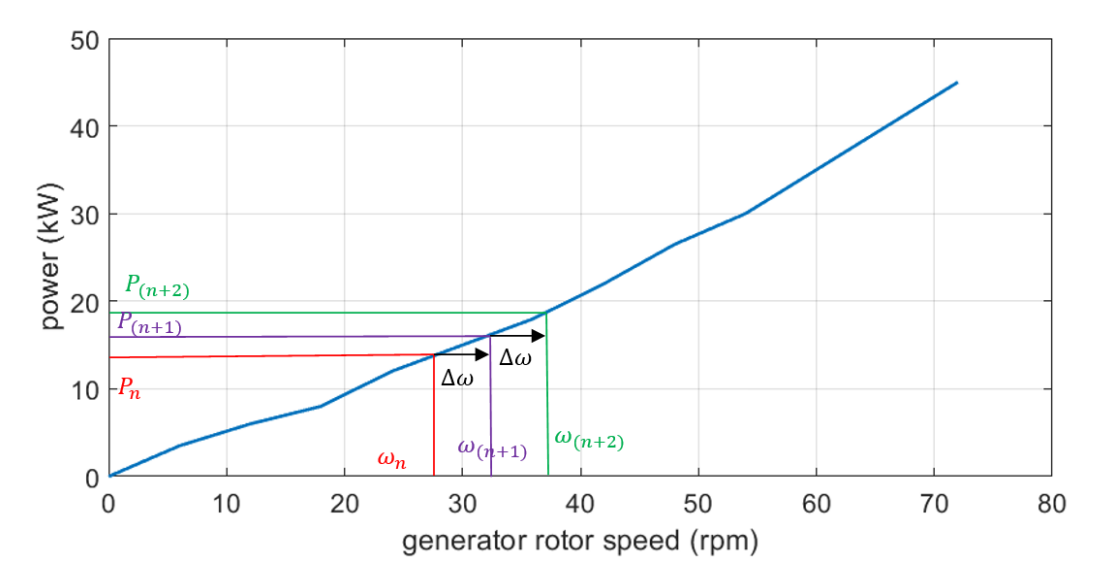


Figure 4.2 P&O control searching process

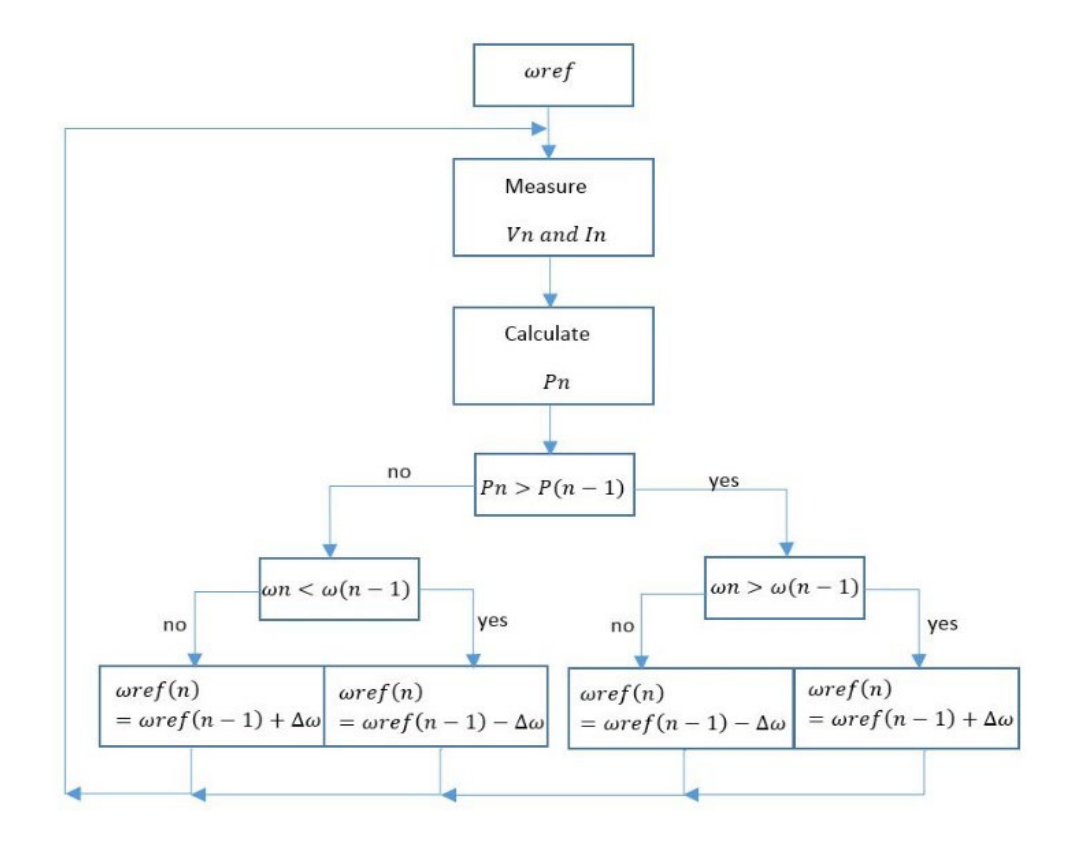


Figure 4.3 P&O control flow chart

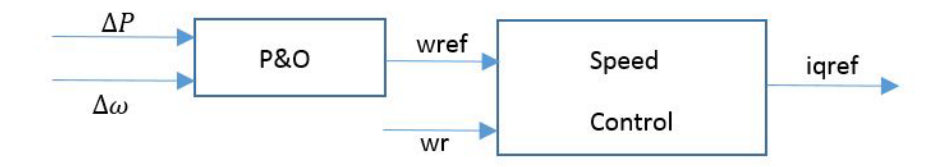


Figure 4.4 P&O control diagram

In the conventional searching process, the rotor speed is continuously adjusted by a constant increment or decrement of $\Delta\omega$ at each step. Figure 4.2 and Figure 4.3 can be used to design the P&O control code for a conventional tidal current turbine generation system.

4.3 Typical P&O Control Model

In tidal current turbines, like in wind turbines, a method has to be implemented to deal with fluid flow (tidal current or wind) speed sensors. Solutions to this have included P&O control. However, the systems that use P&O control are different from conventional tidal current turbine generation systems. This section will illustrate a typical model with P&O control applied.

4.3.1 Stand-alone tidal current turbine system model

Unlike the conventional model, the stand-alone model uses an uncontrolled rectifier to transfer the three-phase alternating current from the generator to direct current, while the conventional model uses a controllable generator side converter. In the stand-alone system, the output power transfer is controlled by a boost converter which increases the DC voltage.

Figure 4.5 shows the block diagram of the stand-alone system. In this figure, the tidal current turbine and generator are the same as those in the conventional model. The P&O control loop is used to provide the switch signal for the boost converter, and the output DC voltage and current are used to calculate the changes in the output power for the P&O control. Generally, the stand-alone system does not connect with the grid, usually it is connected directly to DC loads or an energy storage system (such as a battery). In this system, the output DC voltage of the uncontrolled rectifier varies following changes in the tidal current from which the output power of the generator is changed. A boost converter can be used to control the active power of the turbine. The power of the generator is proportional to rotor speed, so controlling the boost converter can control the generator speed, which in turn can control the turbine speed to make it work near the maximum power point. The energy storage can store the extra power that the turbine generates from the tidal current and can also balance the load voltage to ensure that the load voltage remains stable.

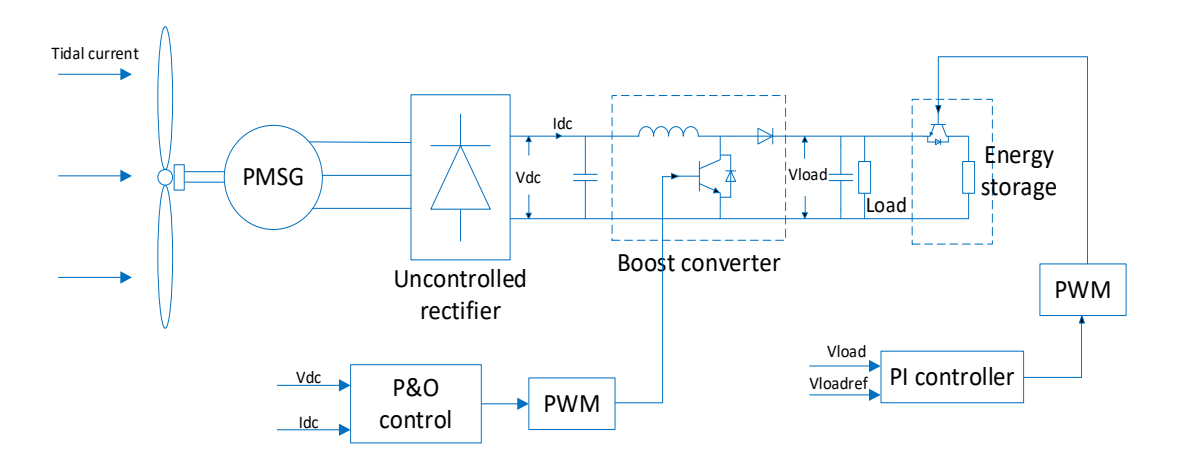


Figure 4.5 Stand-alone tidal current turbine system

4.3.2 Stand-alone system P&O control

The P&O control basic theory has been illustrated in section 4.2, and this section will show the P&O control that will be used in the stand-alone system. The control objectives and output of P&O in these two systems are different: in the conventional tidal current turbine system, the output of the P&O control is the generator reference speed whereas in the stand-alone system, the output of P&O control is the boost converter switch signal.

In a permanent magnet generator (PMG) based tidal current turbine system, the output electrical power of a three-phase generator can be expressed by [41]:

$$P_e = 3v_a i_a$$
 Equation 4.1

Where v_a is the phase voltage and i_a is the phase current, and the induced electromotive force is:

$$E_a = K_e \omega_r$$
 Equation 4.2

Where K_e is the induced electromotive force constant and ω_r is the rotor angular speed. Then the phase current i_a can be expressed as:

$$i_a = \frac{E_a - U_a}{R_a} = \frac{K_e \omega_r - v_a}{R_a}$$
 Equation 4.3

The electric power then can be obtained from:

$$P_e = \frac{3(K_e\omega_r - v_a)v_a}{R_a}$$
 Equation 4.4

For the three-phase generator, ignoring the voltage drop across the diodes, the relationship between phase voltage U_a and DC output voltage U_{dc} can be describe as:

$$U_{dc} = 2.34v_a$$
 Equation 4.5

Substituting Equation 4.5 into Equation 4.4 gives:

$$P_e = \frac{(2.34K\omega_r - U_{dc})U_{dc}}{1.83R_a}$$
 Equation 4.6

From Equation 4.6 it can be seen that when the rotor speed is specified as certain values, the maximum power point is at:

$$\frac{dP_e}{dU_{dc}} = 0$$
 Equation 4.7

Equation 4.7 means that by adjusting the DC voltage U_{dc} the maximum power point can be tracked. The searching process theory is the same as in the conventional system, which was illustrated in Figure 4.2. The control diagram figure and control flowchart however are different and are shown in Figure 4.6 and Figure 4.7 respectively.

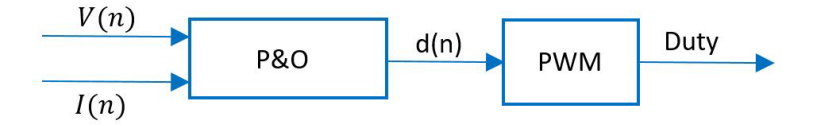


Figure 4.6 Stand-alone system P&O control diagram

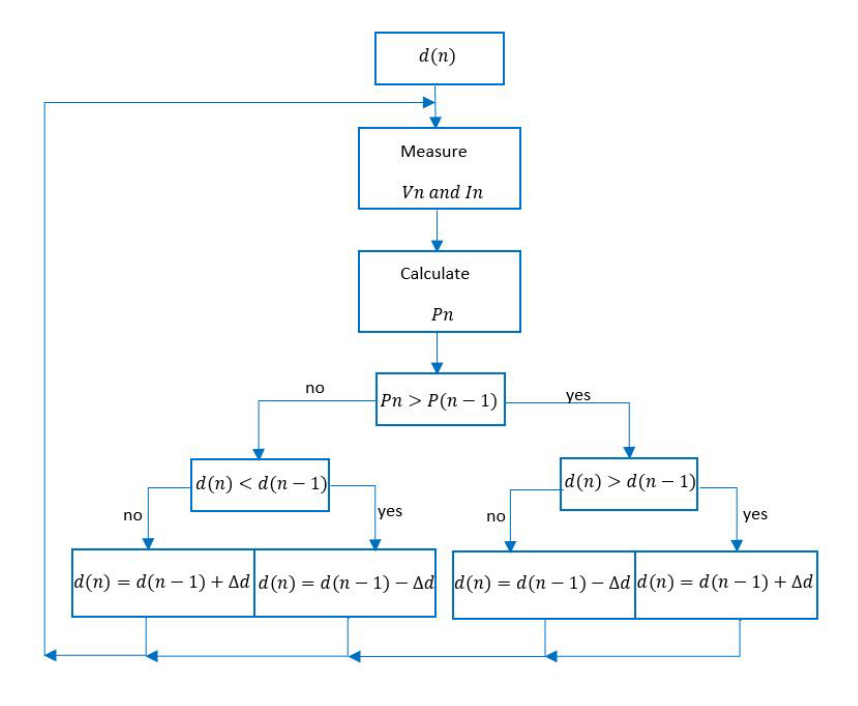


Figure 4.7 Stand-alone system P&O control flow chart

From Figure 4.2, Figure 4.6 and Figure 4.7 the P&O control system can be built in the simulation model.

The P&O control block diagram is shown in Figure 4.8, and the P&O control simulation model in MATLAB is in Appendix B.1. In Figure 4.8, it can be seen that P&O control does not require knowledge of the tidal current turbine generation system's characteristics, it only needs the DC side voltage and current as the input. Thus, the system can operate near the maximum power point without the readings of the tidal current speed sensor and the generator speed sensor.

After building the P&O control part, it was then integrated into the overall stand-alone system in MATLAB, and the simulation model is presented in Appendix B.2. In this figure, the input of the system is tidal current speed, the boost converter is controlled by the P&O control, and the energy storage module is controlled by an IGBT switch to control the load DC voltage.

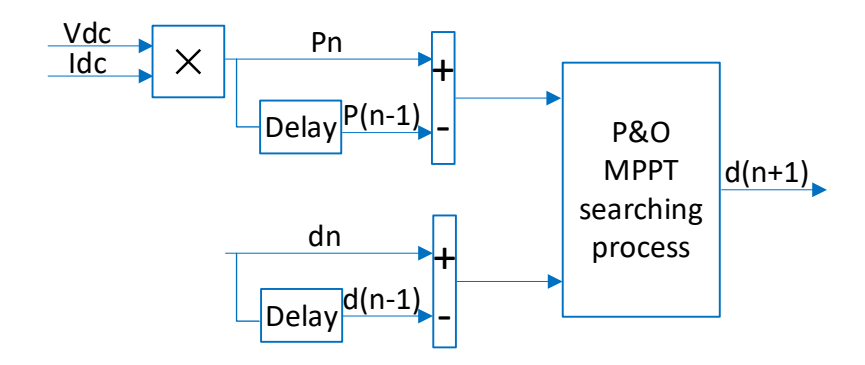


Figure 4.8 Stand-alone system P&O control block diagram

4.3.3 Results and discussion

Tidal current speed is the input of the whole system, and for the purposes of testing the dynamic response, there is a step change in tidal current velocity from 1.75m/s to 2.25m/s at 10s of the simulation time to demonstrate the control operation. Figure 4.9 shows the generator rotor speed result, where the red line is the optimal rotor speed, and the blue line is the real rotor speed. In this figure, it can be seen that the rotor speed converges to the optimal value in the first 5s and the real rotor speed then fluctuates around the optimal rotor speed value. After the step change in tidal current speed at 10s, the speed tracks the change in optimal value quickly. It should be noted that the system mechanical inertia is modelled within the generator block.

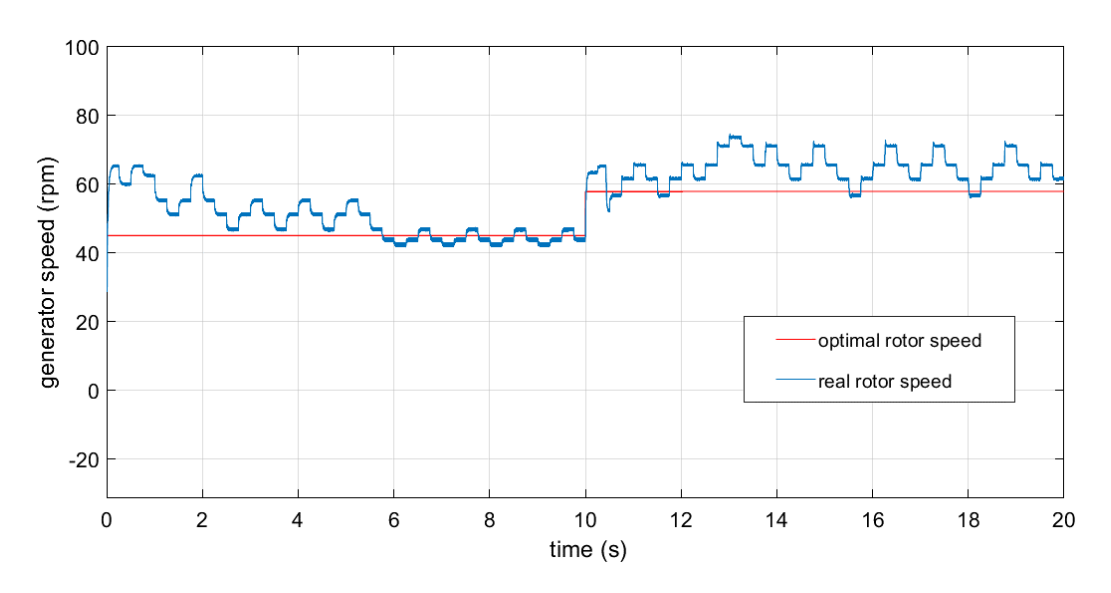


Figure 4.9 Generator rotational speed

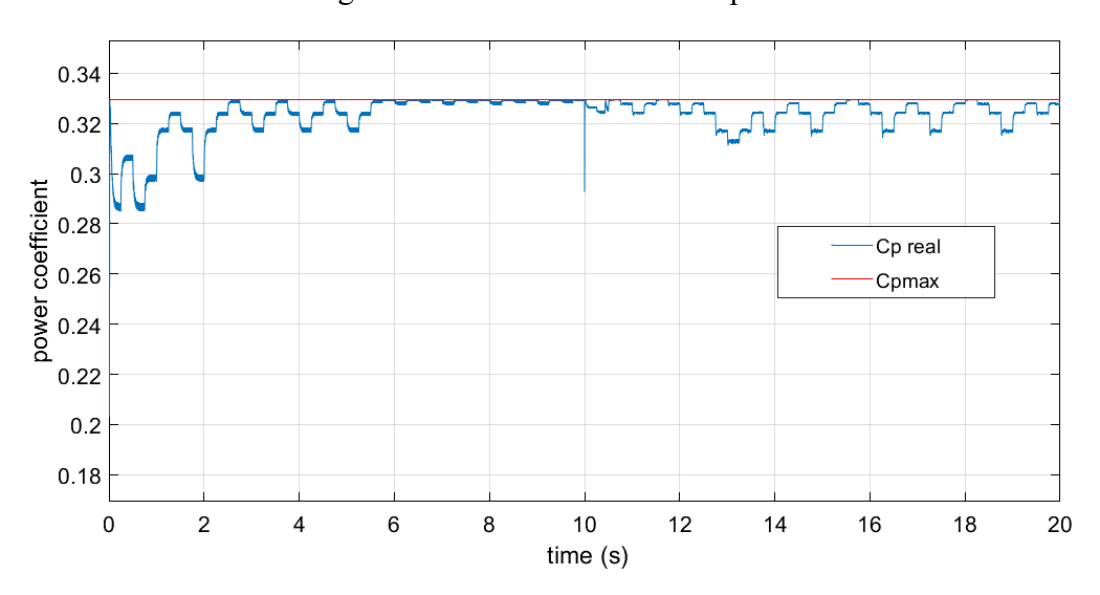


Figure 4.10 Power coefficient

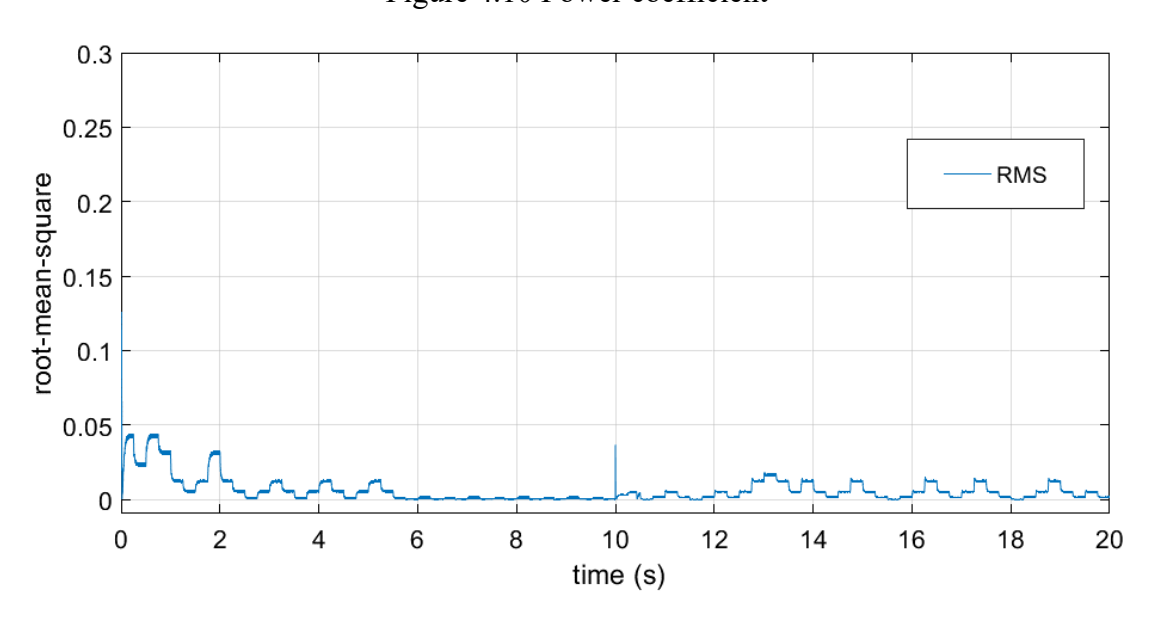


Figure 4.11 Root-Mean-Square (RMS error) of power coefficient

Figure 4.10 is the power coefficient curve. It is clear that the actual power coefficient is very close to the maximum value (0.3294) with only a small fluctuation. The Root-Mean-Square (RMS) error of the power coefficient is illustrated in Figure 4.11; after the system stabilises, the RMS value is less than 0.05 and in an acceptable range.

Figure 4.12 presents the load voltage; the load is connected in parallel with the energy storage module. The energy storage configuration is intended to emulate the function of a battery. There is an IGBT switch in the energy storage module, it is controlled by a PI controller and PWM generator so that the energy storage can balance the extra power that is captured by the turbine and control the load voltage to a constant value. In Figure 4.12 it can be seen that the voltage is controlled, and it is stable after 5s with less than 0.05% error. The furthermore P&O control test will be illustrated in the following sections.

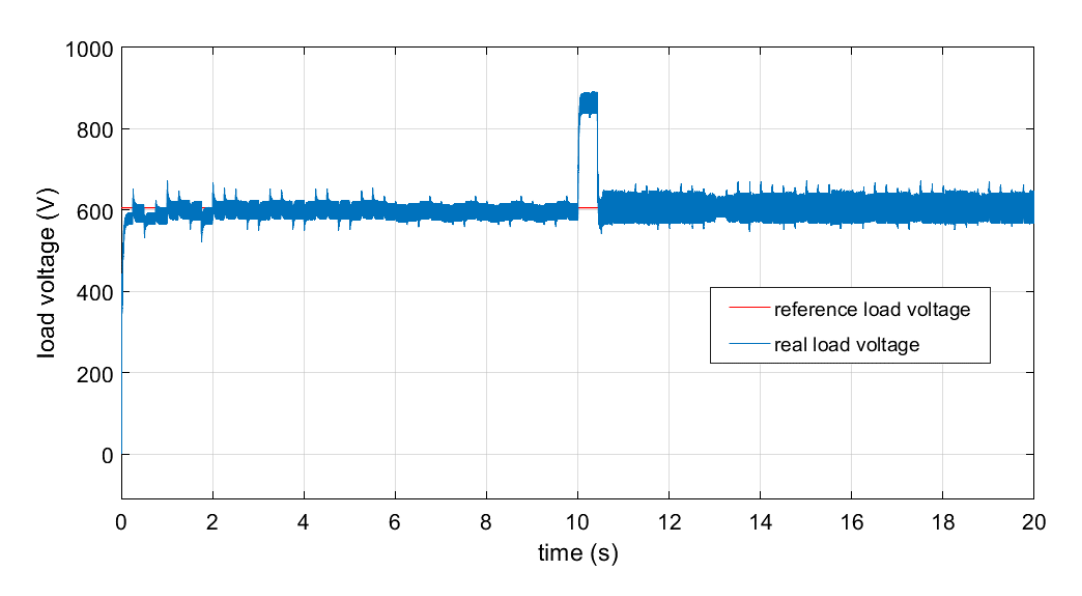


Figure 4.12 Load voltage control

4.4 P&O Control Application in Conventional Model

The sections above had presented the P&O control applied in a stand-alone tidal current turbine generation system to control the generator speed without the tidal current velocity sensor. Having demonstrated the principle, the P&O control can then be tested in the whole grid-connected model. Before connecting the grid side converter control loop to the test model presented in Chapter 3, the P&O control needed to be tested in the generator side converter model, as the output of the P&O control is different in this case. The output of P&O control in the stand-alone system model is the switch signal of the boost converter, while in the conventional grid-connected model, the output is designed to be the generator reference speed, which can be provided to the generator speed control loop. This section will introduce the P&O control design first, then present results of the control test on the generator side

converter model and finally the discussion will look at the grid-connected model with the P&O control to achieve the maximum power point tracking to extract the maximum power, and proportional integral regulators to control the speed and *dq*-axis current.

4.4.1 P&O control design

In the conventional tidal current turbine generation system, the whole system is connected to the grid, so the DC-link voltage is controlled by the grid side converter to maintain stability. Thus, in the conventional system, the DC-link voltage cannot be used in the P&O control, so the power of the system is used in the P&O control instead. Figure 4.13 shows the block diagram of the P&O control implemented in MATLAB, and the P&O control method model in MATLAB Simulink is illustrated in Appendix B.3.

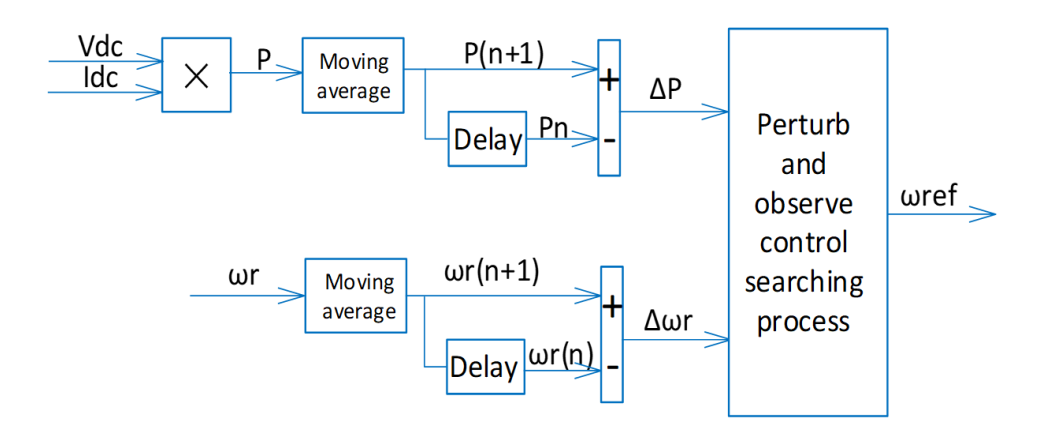


Figure 4.13 P&O control model block diagram

According to the generator side control test model and results in Chapter 3, a system with a P&O control model but without the grid side connection can be developed and is presented in this section. This model was built to check the P&O operation and Figure 4.14 shows the block diagram of the test model. Because in the full system model for a tidal current turbine the DC-link voltage is the input to a grid side converter which controls the power of the whole system, thus the IGBT switch in Figure 4.5 can control the DC-link voltage to be stable to simulate the DC-link voltage state when this model is connected to the grid.

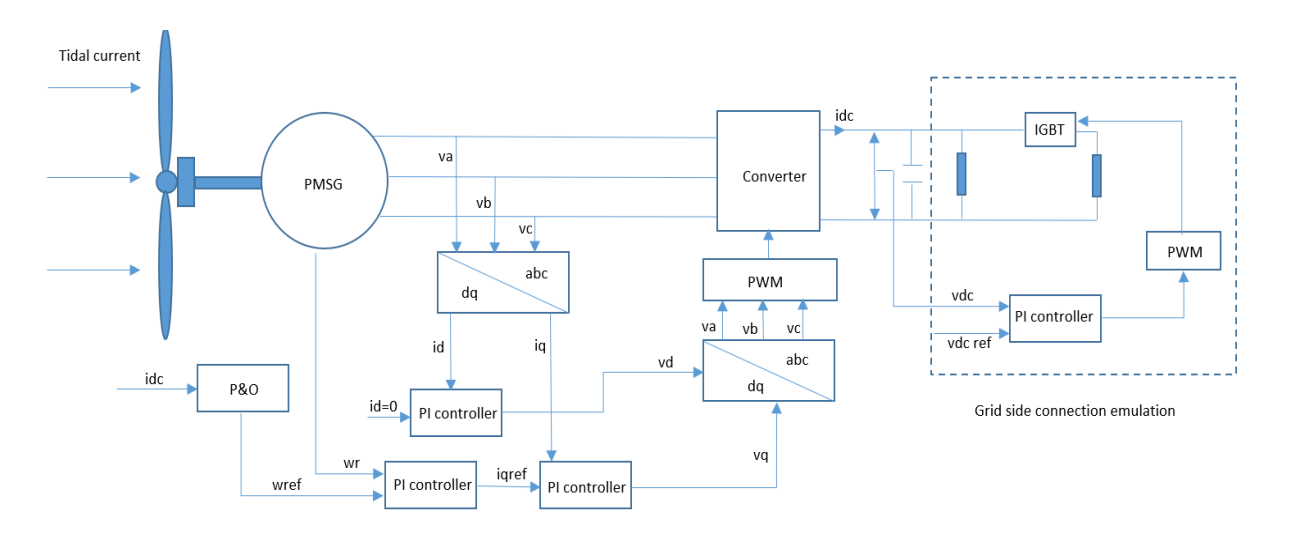


Figure 4.14 Tidal current turbine generation system with P&O control

The power signal goes into the P&O control algorithm together with the generator rotational speed signal and provides a reference generator speed signal as an output to let the speed control loop regulate the generator speed and ensure that the system operates in a desired state.

As mentioned in Section 4.3, the conventional P&O control which applied widely in PV system are fixed step size, while in tidal current turbine system, the results with fixed step size has disadvantages, for larger step size, the P&O control output value may go over the optimal reference speed and with large fluctuations, while small fixed step size may reach the optimal value after a long time, or potentially cannot reach the optimal speed before the tidal current velocity changes. In Figure 4.15, P&O control output generator reference speed with large and small fixed step size are illustrated, it can be seen that with 0.7rpm fixed step size, the P&O control overshoots the optimal value significantly while 0.2rpm fixed step size does not reach the optimal speed.

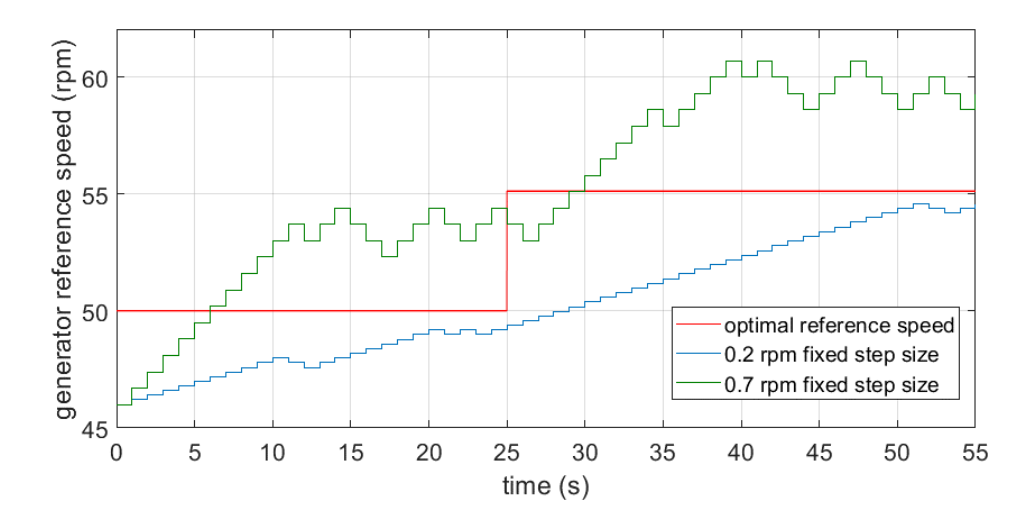


Figure 4.15 Fixe step size P&O control output generator reference speed

In order to have a more accurate output value, to make sure that P&O control can track the MPP efficiently, P&O control with variable step size can solve the problems in Figure 4.15. With an aim to give a variable step size to the P&O control output to compare to the fixed step size P&O control that is widely used in PV system and wind turbine system, together with the control flow chart of Figure 4.3, the P&O control output generator reference speed can be expressed as follows:

$$\omega_{ref} = -sign(\Delta P(n))K + \omega_{ref(n-1)}$$
 Equation 4.8

where K is the adjustment constant that can make the output of the P&O control vary depending on the magnitude of changes in the power, which means that when the changes in the power are small, the P&O control output generator reference speed change will also be small compared to the fixed step size, of which the changes of P&O control output will be the same value.

4.4.2 Generator side connection with P&O control

The results of the generator side connection model are presented in the following figures. Figure 4.16 shows the generator rotor reference speed which is also the output of the P&O control. The generator side converter control will regulate the generator rotor speed to follow the reference speed, so that the turbine will operate in the optimal tip-speed ratio range. It can be seen from Figure 4.16 that the P&O control is a three-level operation, and it is also a variable step size algorithm. The step size is smaller when the reference speed is nearer the optimal value than when it is in the searching process.

Figure 4.17 illustrates the tidal current turbine power coefficient value; the real power coefficient, is very close to the maximum value, and it is clear that the turbine coefficient is close to the maximum value and oscillates over a small range (less than 1% error) near the maximum value. This means that the power that is captured by the tidal current turbine is near the optimal value which is the aim of the MPPT algorithm.

In Figure 4.18 the Root-Mean-Square (RMS) error of the turbine power coefficient is presented and it can be seen that the error is very small and would be in an acceptable range.

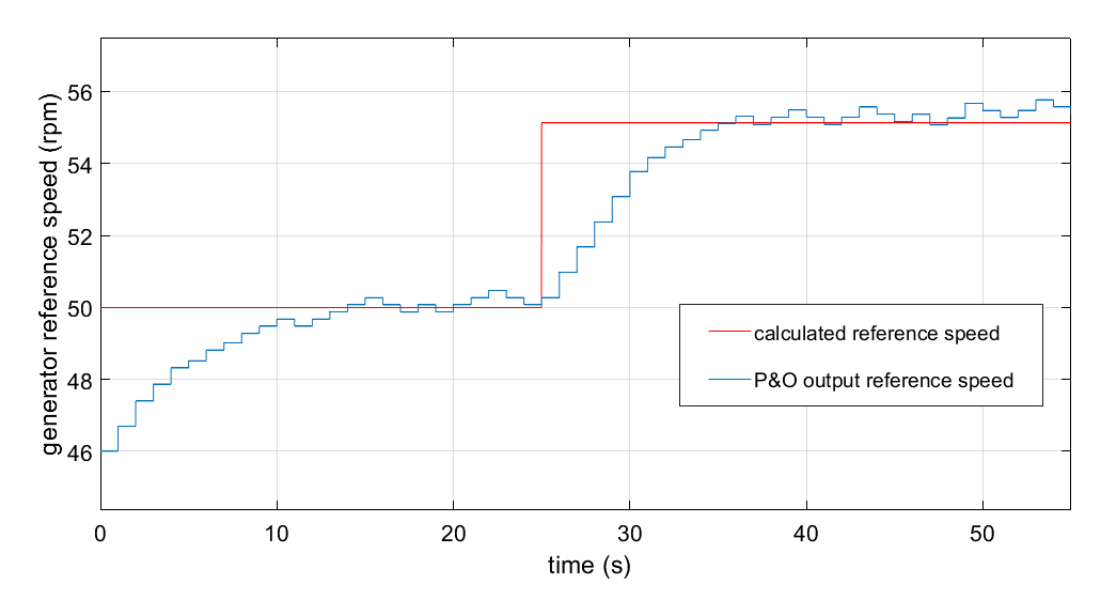


Figure 4.16 Generator rotor reference speed (output of P&O control)

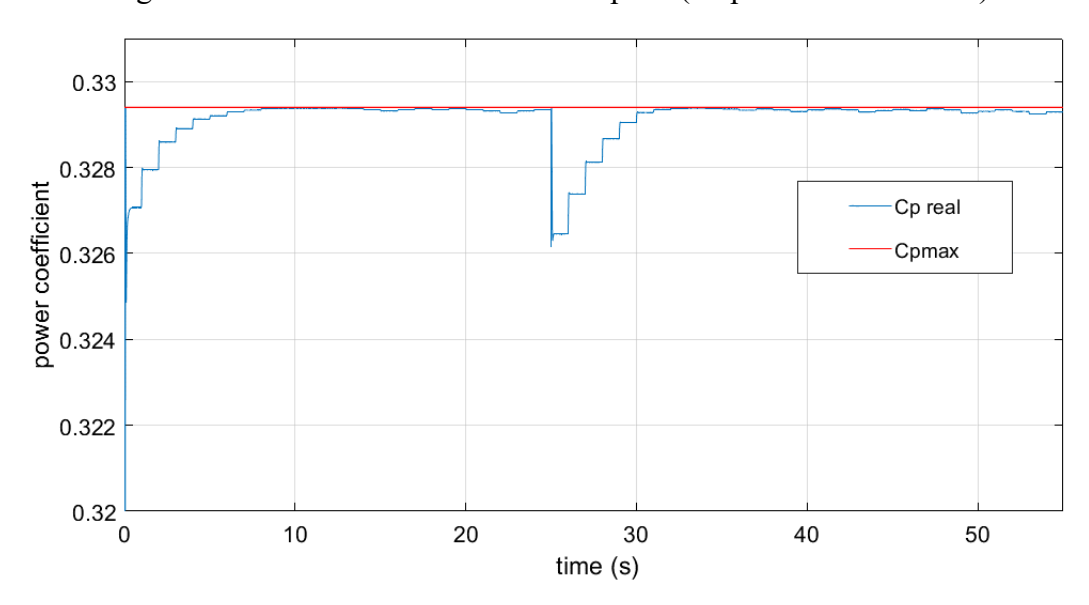


Figure 4.17 Tidal current turbine power coefficient

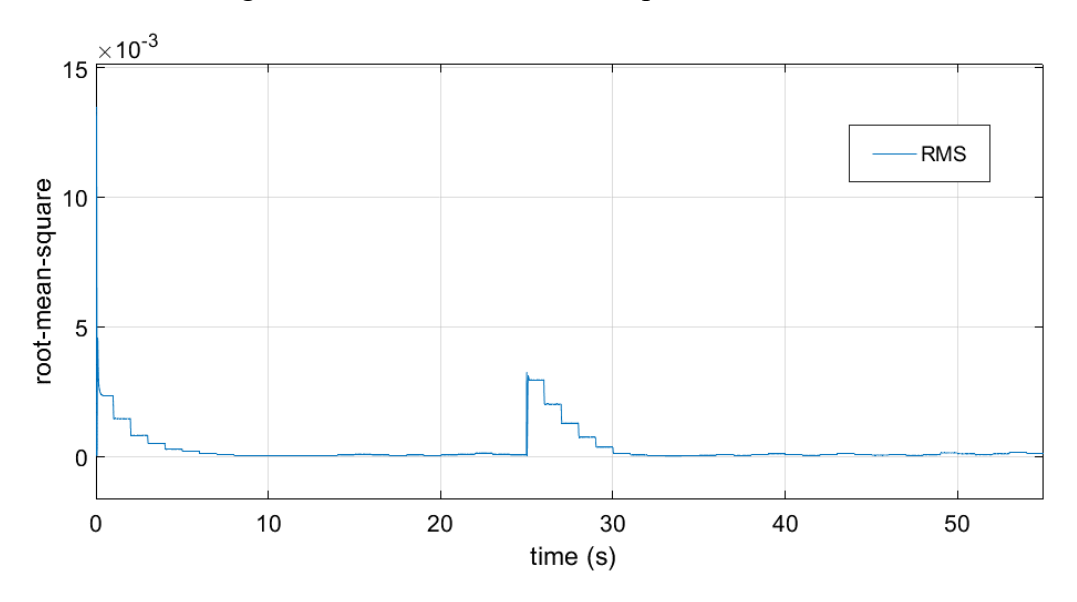


Figure 4.18 Root-Mean-Square (RMS) error of power coefficient

Figure 4.19 shows the generator rotor speed; as mentioned above, the generator rotor speed is controlled by the generator side convertor to converge to the generator reference speed. Figure 4.20 shows a zoomed in view of the rotor speed, demonstrating that the generator is able to follow the reference speed changes rapidly and it is stable during the steady state. This means that the P&O control step size and perturb time are acceptable for the system control strategy. Figure 4.21 illustrates the DC link voltage, which is controlled to be stable. The value of DC voltage depends on the load resistance value and the generator rated power. In Figure 4.21, the DC-link voltage is controlled to the desired value, which is the same as it in Chapter 3 (605V), also it can be seen that when the tidal current velocity increased at 25s, the DC voltage also increased, but that it can then be controlled back to the desired value. This also happened in Figure 4.19 where the generator speed overshot for a moment then recovered to follow the reference speed. The DC voltage could also be controlled by a grid side convertor, which means that this system can be used for grid connection.

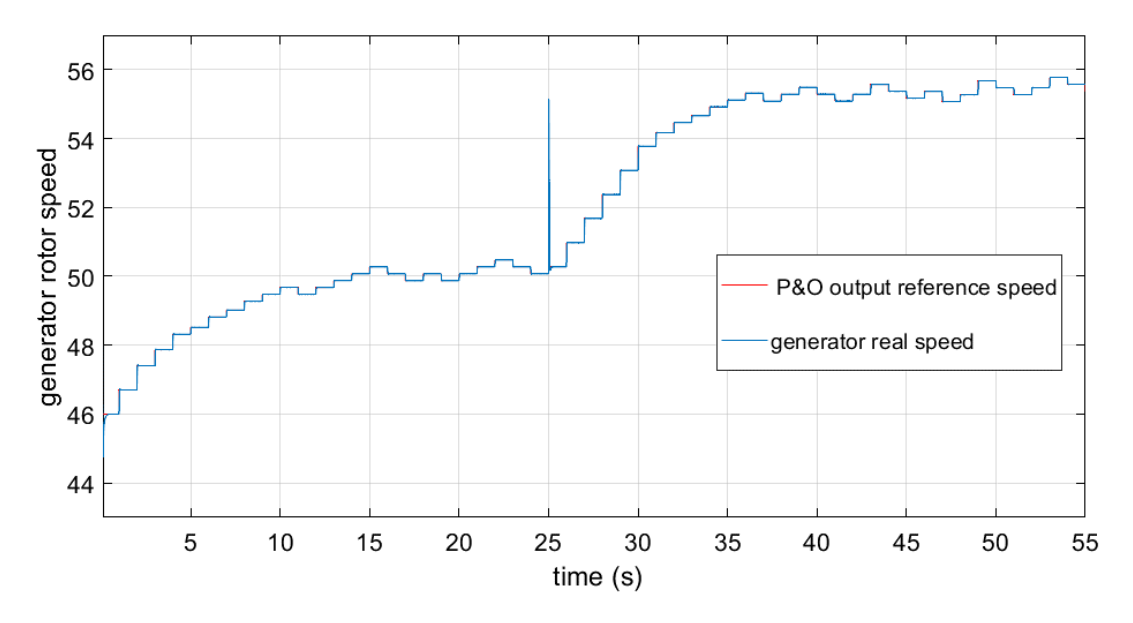


Figure 4.19 Generator rotor speed

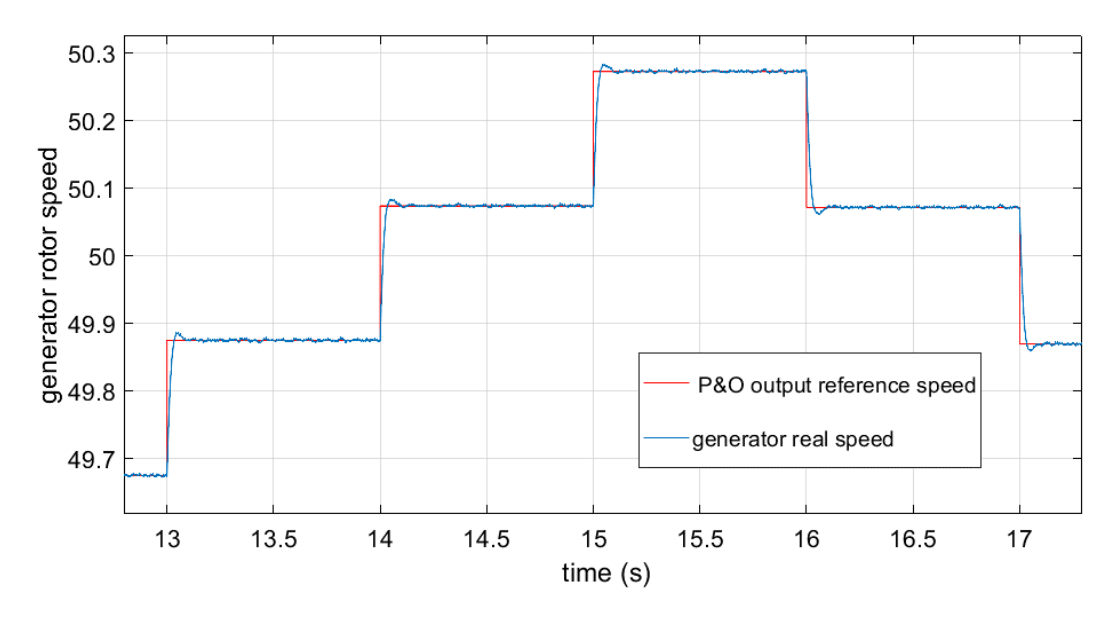


Figure 4.20 Zoomed in view of the generator rotor speed

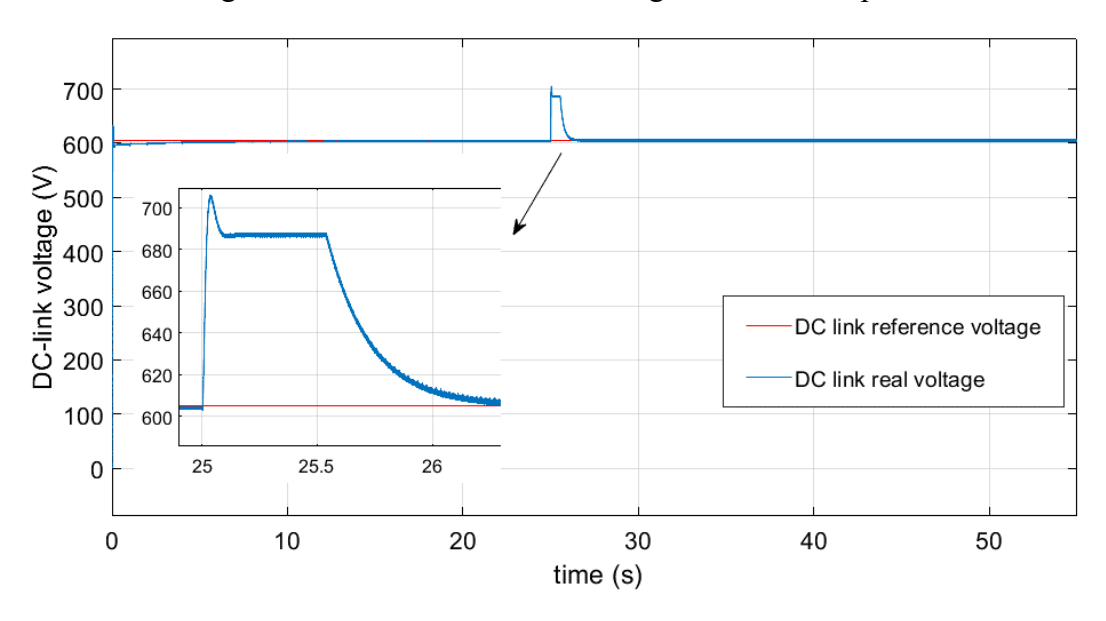


Figure 4.21 DC-link voltage

In paper [153], the basic control system of the tidal current turbine uses the same conventional system as in this thesis, but with different tidal current turbine and generator. The experimental results from [153] can provide a reference for accuracy of the simulation model developed in this thesis. Figure 4.22 shows the experimental results of step change tidal current velocity input and the corresponding generator rotor speed. If compared Figure 4.20 to Figure 4.22(b), if can be seen that the response of generator rotor speed is the same, both can reach the desired value after a few seconds, which has proved the model accuracy.

Another result from [153] is the DC-link voltage, which is illustrated in Figure 4.23, it can be seen that, the DC-link voltage maintains at the desired value with some oscillations when the tidal current input changes. In Figure 4.21 the voltage maintains the required value, and when

tidal current changes, it is controlled back to this value similar to the results of [153], again confirming the accuracy of the simulation model results.

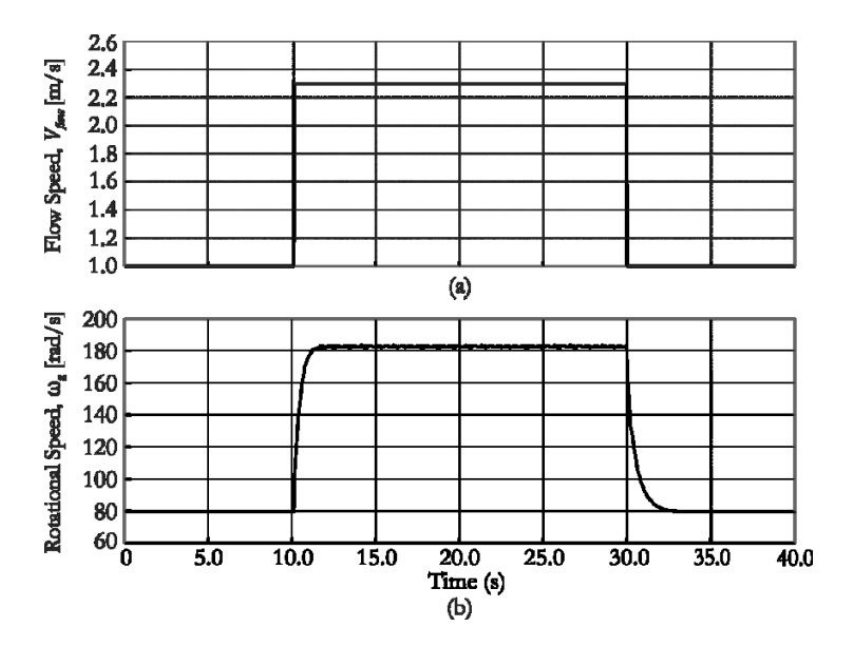


Figure 4.22 Experimental results (a) tidal current velocity step change; (b) generator rotational speed (figure from [153])

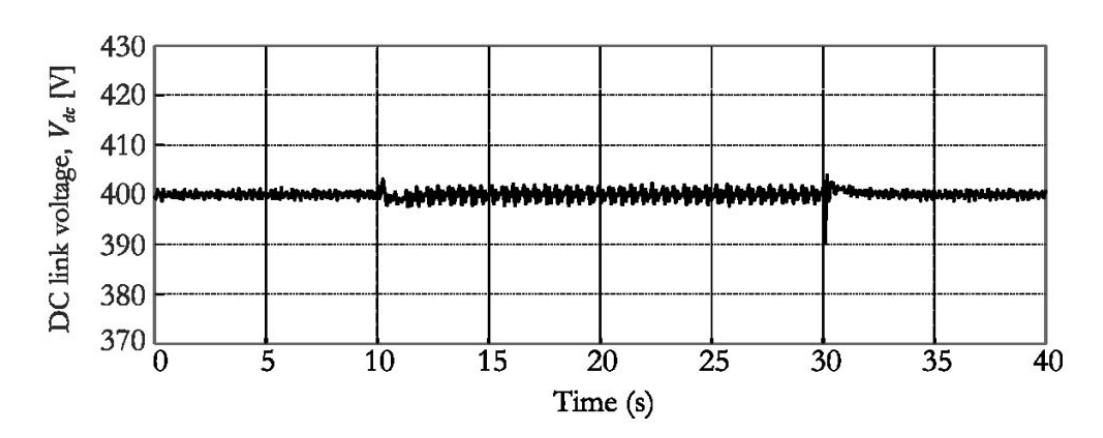


Figure 4.23 Experimental results DC-link voltage (figure from [153])

4.4.3 Grid side connection

In order to connect the tidal current turbine generation system to the grid, a grid side converter is needed in the model. The generator side converter can control the speed of the generator, while the grid side converter controls the DC-link voltage when controlling the active and reactive power transferred to the grid. In Section 3.3 the generator side converter is illustrated; the overall topology of the converter that is used in this model is a back-to-back converter, and the structure is shown in Figure 4.24 [144].

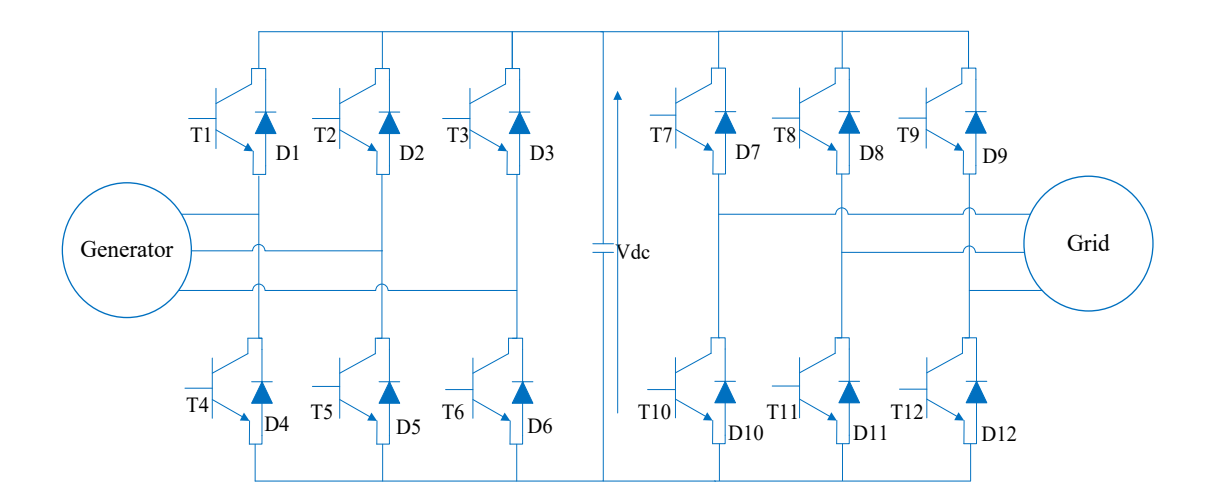


Figure 4.24 Topology of the back-to-back converter

The system active and reactive power can be expressed as follows [144]:

$$P_g = \frac{3}{2} \left(v_{dg} i_{dg} + v_{qg} i_{qg} \right)$$
 Equation 4.9

$$Q_g = \frac{3}{2} \left(v_{qg} i_{dg} - v_{dg} i_{qg} \right)$$
 Equation 4.10

where v_{dg} and v_{qg} are the grid voltages in dq-axes, i_{dg} and i_{qg} are the grid currents in dq-axes. The dynamic equations of the grid side in the synchronously rotating dq axes frame can be explained in the following equations:

$$\frac{di_{dg}}{d_t} = \frac{v_{dg} - v_{di} + \omega_g L_g i_{qg}}{L_g}$$
Equation 4.11

$$\frac{di_{qg}}{d_t} = \frac{v_{qg} - v_{qi} - \omega_g L_g i_{qg}}{L_g}$$
Equation 4.12

where v_{di} and v_{qi} are the grid side converter voltages, ω_g is the dq-axes frame rotating angle speed, L_g is the three-phase inductance. From the equations above, it can be seen that the derivative of d-axis current i_{dg} has relationships with both d-axis and q-axis components, and the derivative of q-axis is the same, which means that the control is cross coupling, this will make the control of the active and reactive powers complex. In this situation, field-oriented control is applied in the grid side control. If the grid voltage vector is aligned with the q-axis frame, then the q-axis voltage will be equal to the grid voltage which will be $v_{qg} = v_g$, and $v_{dg} = 0$, and substituting $v_{dg} = 0$ into equations 4.9 and 4.10, the active and reactive power will be:

$$P_g = \frac{3}{2} v_{qg} i_{qg}$$
 Equation 4.13

$$Q_g = \frac{3}{2} v_{qg} i_{dg}$$
 Equation 4.14

From Equations 4.13 and 4.14, the active and reactive power can then be controlled by the grid d-axis and q-axis current. The grid current component i_{dg} can be controlled to zero (then $Q_g = 0$) through a PI controller to make the system operate under unity power factor. Using another PI controller to control the DC-link voltage, the output of the PI controller can be used as the reference value of the q-axis current, which represents the active power of the system [144, 154]. When the grid side converter is operating in steady state, the converter DC side current will be constant, and the converter AC side power will be equal to the DC power, which can be expressed as:

$$P_g = \frac{3}{2} v_{qg} i_{qg} = \frac{3}{2} v_{dc} i_{dc}$$
 Equation 4.15

From Equations 4.11, 4.12, 4.13 and 4.14, the decoupled control strategy can then be explained as [144]:

$$v_{di} = -\left(k_1 + \frac{k_2}{S}\right)\Delta i_{dg} + \omega_g L_g i_{qg} + v_{dg}$$
 Equation 4.16

$$v_{qi} = -\left(k_1 + \frac{k_2}{S}\right)\Delta i_{qg} - \omega_g L_g i_{dg} + v_{qg}$$
 Equation 4.17

where $\left(k_1 + \frac{k_2}{S}\right)$ is the transfer function of the PI controller, and the model of the grid side converter control strategy can be developed according to Equations 4.16 and 4.17. Figure 4.25 is the block diagram of the decoupled control.

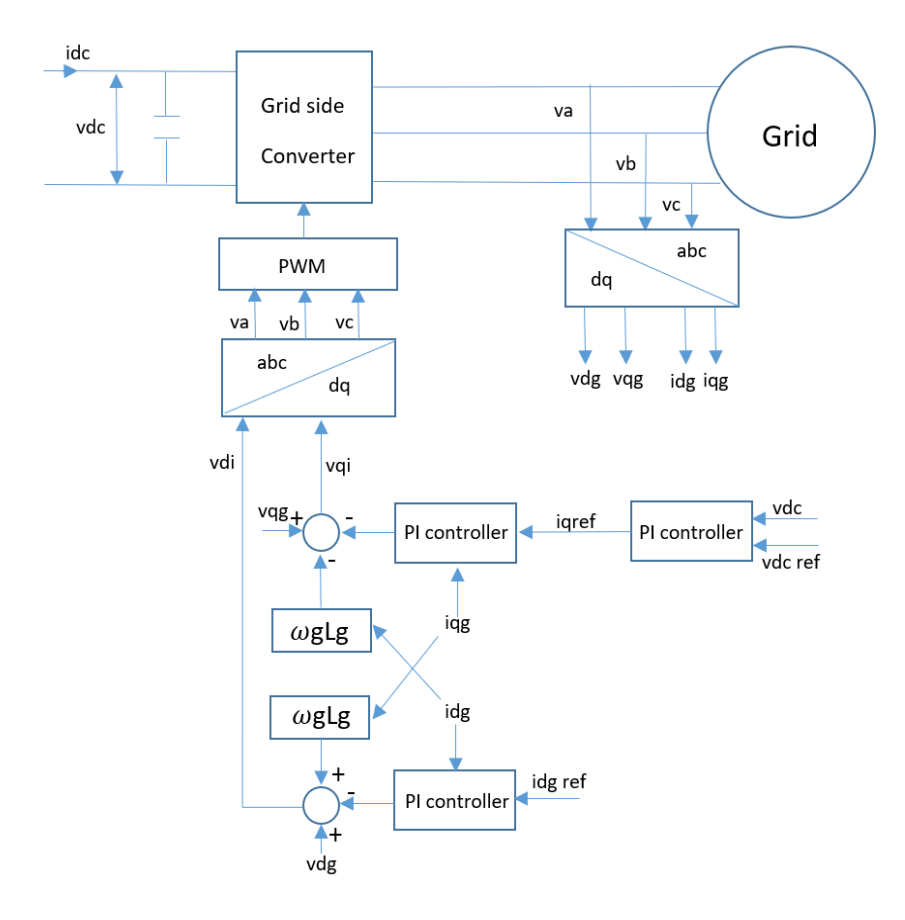


Figure 4.25 Grid side converter control block diagram

4.4.4 Complete system simulation

In this section, a complete tidal current turbine generation system with P&O control which combines the generator side control and grid side control together is illustrated. Figure 4.26 shows the overall system block diagram. In this system the P&O control replaces the traditional MPPT algorithm to allow the system to track the maximum power point without a tidal current speed sensor. The output power of the generator and generator rotor speed signals are used as the input to the P&O algorithm, and the P&O control output is the generator reference speed signal. This signal goes into a PI controller to control the system to operate at the reference generator speed, and through the two PI controllers on the generator side, the *q*-axis and *d*-axis voltages are provided and used to provide PWM to control the generator side converter switches.

On the grid connection side, the DC-link voltage is used to compare with a reference value through a PI controller to provide q-axis current. Also through two PI controllers on the grid side, the *d*-axis and *q*-axis voltages are created, and the PWM control signal is generated to control the grid side converter switches. The simulation model in MATLAB is illustrated in Appendix B.

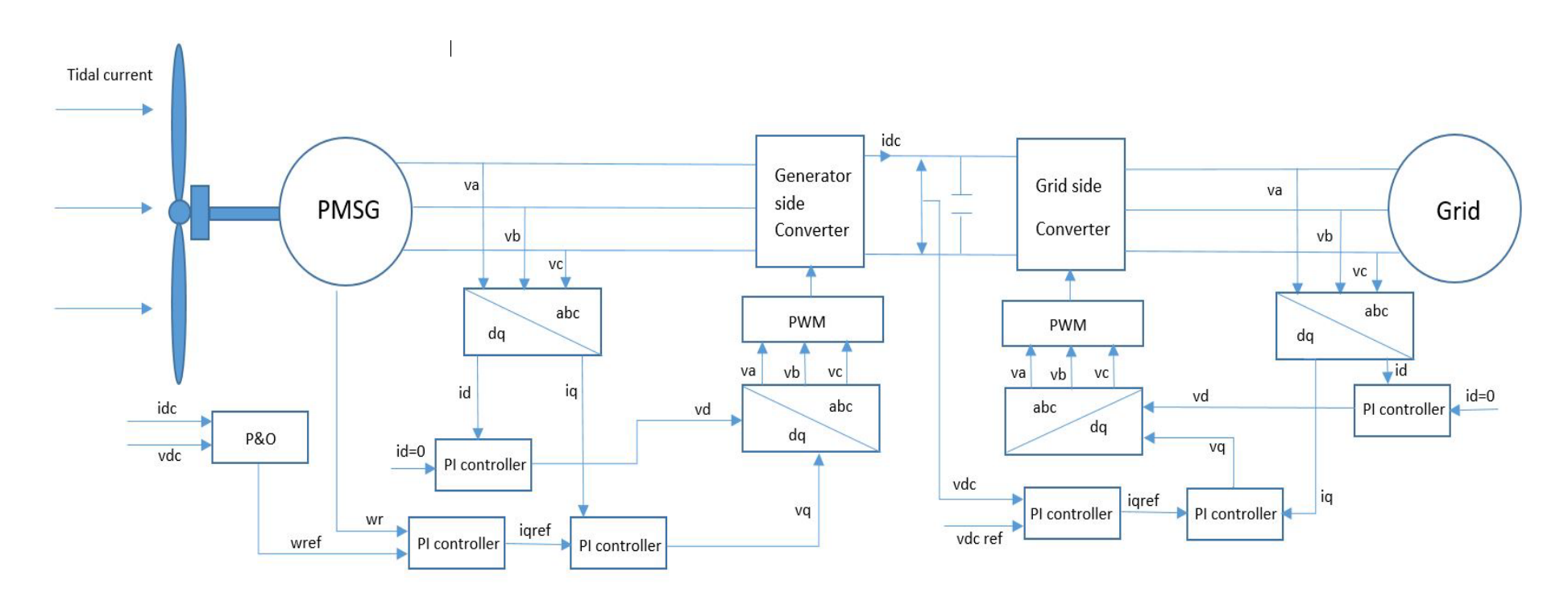


Figure 4.26 Conventional tidal current turbine system model with P&O control

4.5 Results and discussion

In order to test the P&O control performance, both step change tidal current input and ramp change tidal current inputs were tested in the grid connection model. The ramp input simulates a continuously changing tidal current velocity whilst the step tests the dynamic performance. The tidal current velocity step change input of the system is from 1.7m/s to 2.35m/s at 35s, with an overall whole simulation time of 100s, and the ramp change input also starts from 1.7m/s and begins increasing at 35s and reaches 2.35m/s at 55s simulation time. This will test the grid-connected system with P&O control under sudden change and continuously changing tidal current velocity states and how the step size and step time of P&O control affect the simulation results.

4.5.1 Step size and step time

Figure 4.27 illustrates the P&O control with different step size, it can be seen that the control with small step size needs more time to reach the optimal value: step size 0.4 reaches the optimal reference speed first, then step size 0.3, but for step size 0.1, 35s is not enough for this step size to reach the red line. However the small step size can have smaller fluctuations compared with the large step size. In this figure it can be seen that the step size 0.1 has the smallest fluctuations, while the fluctuations for step size 0.3 and step size 0.4 are much bigger, and during the steady state input phase, step size 0.4 overshoots the optimal value and then converges back, which means that the step size can affect the tracking speed and the fluctuations during steady states.

Figure 4.28 shows the P&O control with different step times. From this figure it can be seen that a smaller step time of the P&O control can provide shorter tracking time, as the P&O control with 0.75s step time in this figure reaches the optimal value first, while 1.75s step time is the last one to reach the red line. Also it can be seen that, the output of P&O control with smaller step time has more frequent fluctuations during steady state than larger step time. If the step time is too small, it will demand a faster response for the generator to follow the P&O output generator reference speed. From Figure 4.27 and Figure 4.28 it can be seen that

both step size and step time of P&O control can affect the system performance and simulation results, thus achieving an optimal performance of tidal current turbine generation system with P&O control needs the control strategy to have suitably tuned step size and step time.

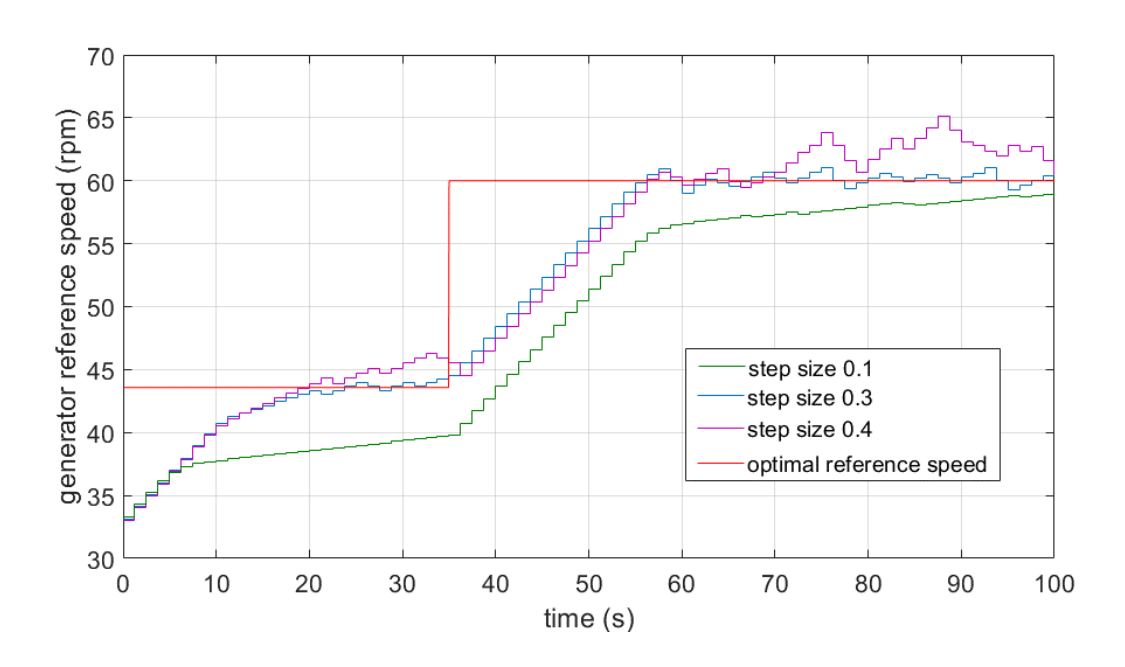


Figure 4.27 P&O control output with different step size

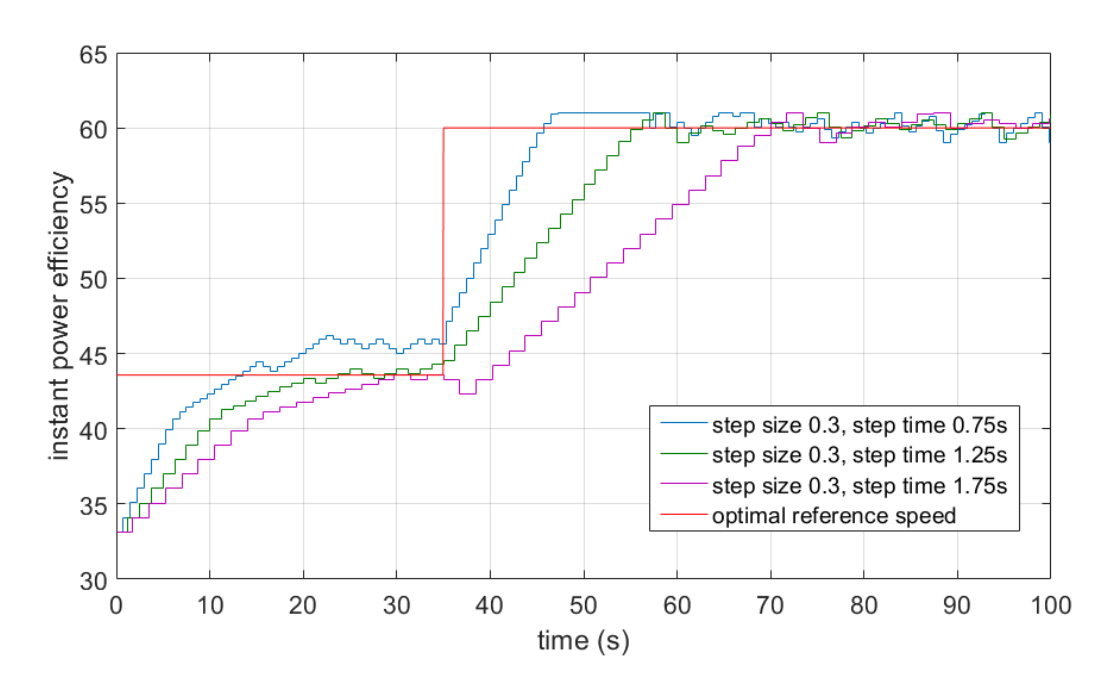


Figure 4.28 P&O control output with different step time

In order to tune the P&O control performance, not only is it necessary to consider the effect of the step size and step time, but it is also important to consider the tracking efficiency. The tracking efficiency of the MPPT algorithm is a criterion to compare each parameter, where the calculation of the average MPPT tracking efficiency is [155]:

$$\eta_{MPPT(average)}\% = \frac{\int P_{out}(t) dt}{\int P_{max}(t) dt} \times 100$$
 Equation 4.18

where P_{out} is the actual output power of the tidal current turbine and P_{max} is the theoretical calculated maximum power. The actual output power is calculated from the voltage and current sensors of the DC link. The theoretical maximum power is calculated by Equation 3.1. The actual power will be less than the theoretical power due to the losses in generator, converter and some other stray losses.

Table 4.1 shows the P&O control average power efficiency under the same step time with different step sizes.

Step size	Step input	Ramp input
0.1	86.02%	89.45%
0.2	86.94%	90.1%
0.3	88.85%	90.78%
0.4	88.8%	86.18%
0.5	89.12%	87.54%

Table 4.1 Average efficiency of P&O control with different step size under ramp and step change tidal current velocity input

Different step sizes will cause different performance and generally a large step size will make the system reach the MPP more quickly but with bigger fluctuations during steady state, as discussed above. Figure 4.29 and Figure 4.30 show the instantaneous power efficiency of the P&O control under step tidal current velocity input and ramp input respectively.

Figure 4.29 illustrates the instantaneous power efficiency of the P&O control with different step sizes under step change tidal current input. The instantaneous power efficiency is calculated as [155]:

$$\eta_{MPPT}\% = \frac{P_{out}(t)}{P_{max}(t)} \times 100$$
 Equation 4.19

It is clear that the efficiency for smaller step size tracking of the MPP is lower than with larger step sizes, such as step sizes 0.1 and 0.2 in this figure. This is because the tracking speed of small step sizes is slow, and sometimes cannot reach the optimal speed before the tidal current velocity input changes, but during the steady state, it is obviously that the fluctuation with large step sizes are bigger than with small step sizes, such as the step size of 0.5, which reaches the steady state first, but from 60s to the end, the fluctuation is the biggest.

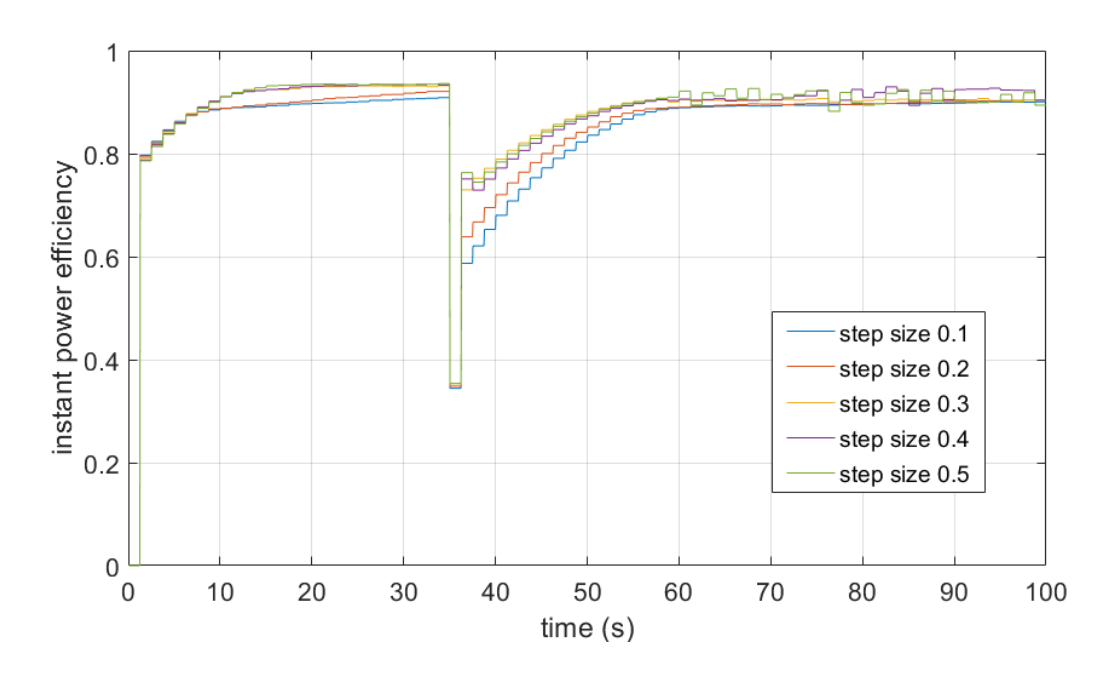


Figure 4.29 P&O control instantaneous power efficiency with different step size under step change tidal current velocity input

Figure 4.30 shows the P&O control instantaneous efficiency with different step sizes under ramp change tidal current input. Similar to the step change tidal current velocity input above, the large step size can reach the optimal value earlier, and with higher efficiency during the tidal current velocity increase period, but the fluctuation during the steady state will be bigger. It should also be noticed in this figure that the efficiencies of step sizes 0.4 and 0.5 have a significant drop when the input starts to increase, and after approximately 13s the efficiency starts to climb back to track the MPP. This drop of the generator reference speed sometimes happens in P&O control; this will be discussed later.

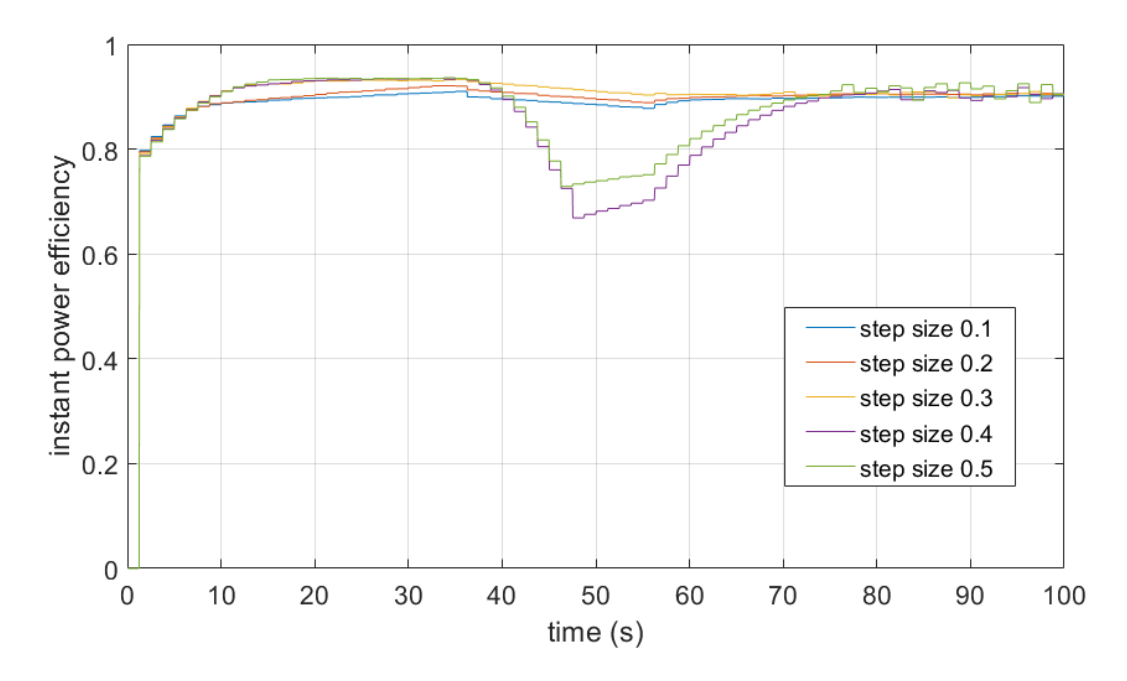


Figure 4.30 P&O control instantaneous power efficiency with different step size under ramp change tidal current velocity input

In P&O control, as mentioned above, it is not only the step size that can affect the MPPT efficiency, but also the step time can affect the tracking speed and the fluctuation during steady state. Table 4.2 shows the average tracking efficiency of P&O control with different step times under a step size of 0.3.

Perturb time	Step change	Ramp change
0.7s	89.6%	89.91%
1s	88.67%	86.87%
1.25s	88.85%	90.78%
1.5s	88.69%	90.61%
1.8s	88%	90.26%

Table 4.2 Average efficiency of P&O control with different perturb time under ramp and step change tidal current velocity input

Figure 4.31 illustrates the instantaneous power efficiency with different step times in response to a step change of tidal current velocity input, and from this figure, it can be seen that small step times can make the tracking time less, but the fluctuation during steady state will be more

frequent, while big step times will have small fluctuation during steady state but take more time to track the MPP. For example, the blue line in this figure, which is 0.7s step time: if this is compared with the green line (1.8s), after the tidal current velocity increased, the blue line reached steady state at about 52s, while the green line reached steady state at about 70s, and it is obvious that every 0.7s, the blue line will have an increase or decrease, but the green only increase or decrease every 1.8s

Figure 4.32 shows the instantaneous power efficiency with different step times under the ramp change tidal current velocity input. This is very similar to the results under step change input, and it is also obvious that the small step time has quick tracking time but comes with more frequent fluctuations. Notice again in Figure 4.32 that the step times of 0.7s and 1s have an efficiency drop problem, the reason for which is the same as in Figure 4.29. This is caused by the P&O control output generator reference speed drop, and this will be discussed in Section 4.5.2.

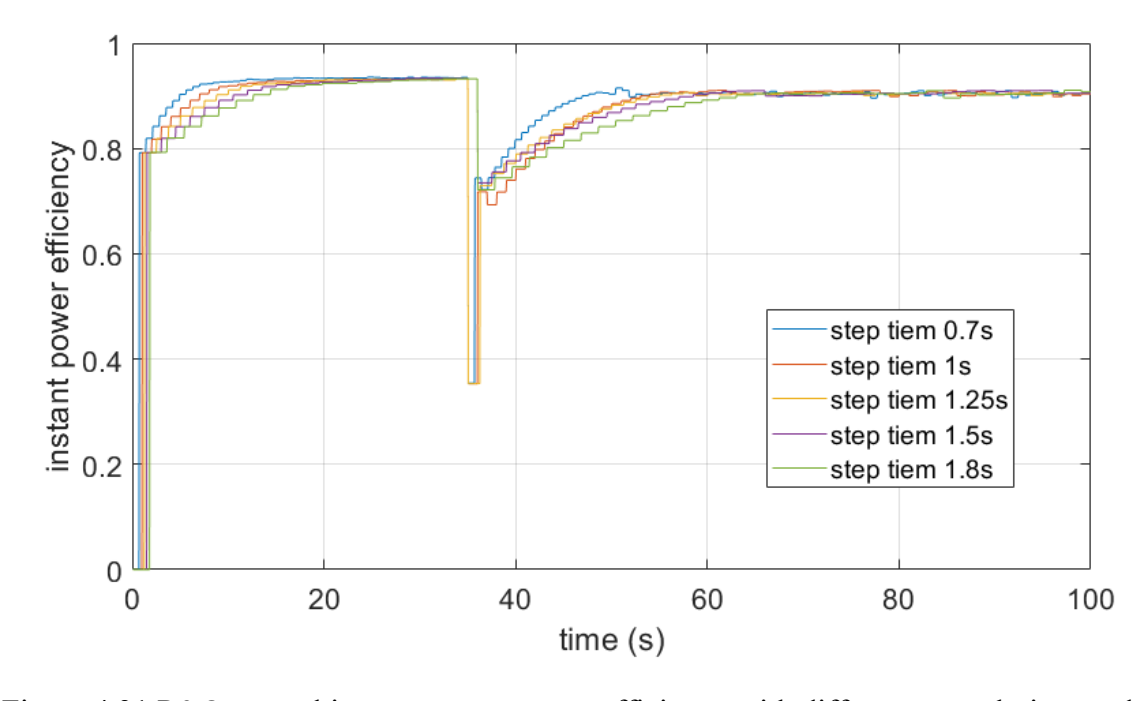


Figure 4.31 P&O control instantaneous power efficiency with different perturb time under step change tidal current input

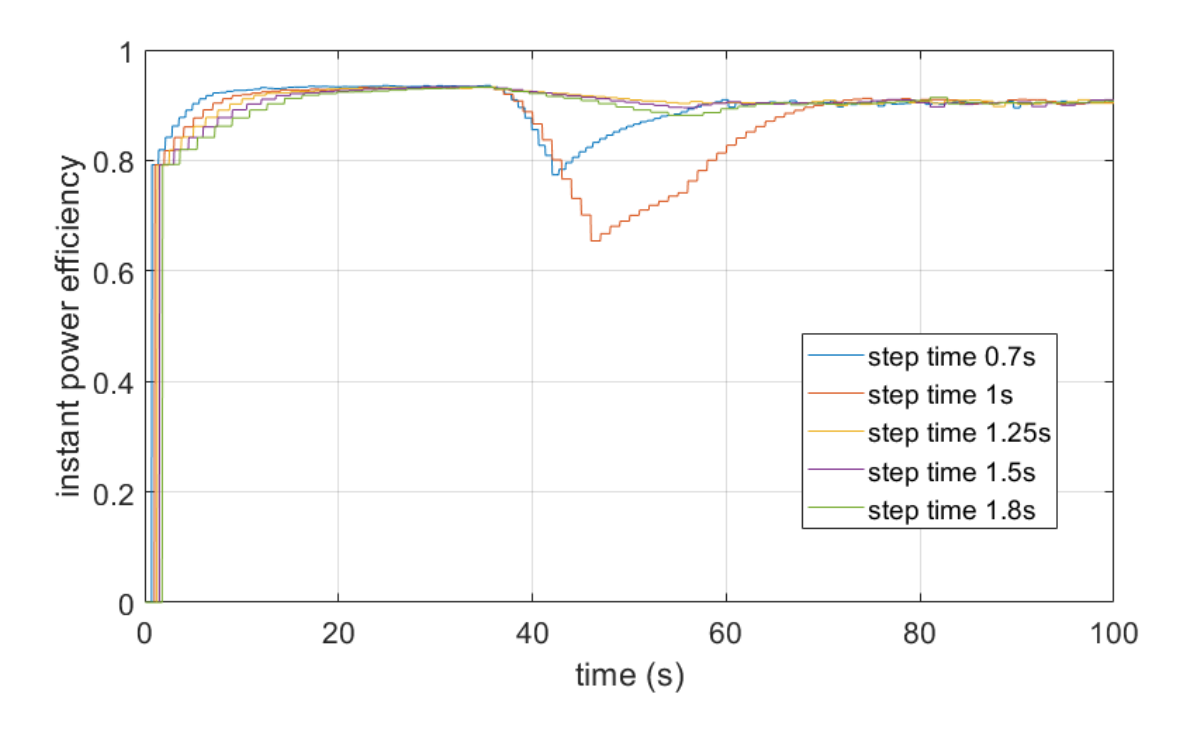


Figure 4.32 P&O instantaneous power efficiency with different perturb time under ramp change tidal current input

4.5.2 Drift problem discussion

Figure 4.33 presents the P&O control generator reference speed with a step size of 0.3 and step time of 1.75s. It can be seen that the generator reference speed increase in Figure 4.31 the P&O output speed decreases. This causes the instantaneous efficiency drop such as the green line in Figure 4.32. When the tidal current speed starts to change, the generator reference speed initially decreases and then increases to track the MPP. The control output generator reference speed goes in the wrong direction sometimes in P&O control, generally when then tidal current velocity input is rapidly changing, and this is referred to as the drift problem. The drift problem will affect the P&O control tracking efficiency, slowing down the MPP tracking speed.

The drift problem is caused by the P&O control searching process (shown in Figure 4.2 and Figure 4.3). In this process, the control algorithm first detects the change in power and rotor speed, and then gives an increase or decrease signal to the generator reference speed. According to the control flow chart Figure 4.3, if the change in power is positive and the change in rotor speed is negative, then the control signal will be negative, which means that

this control signal will result in a decreasing trend in the rotor speed control.

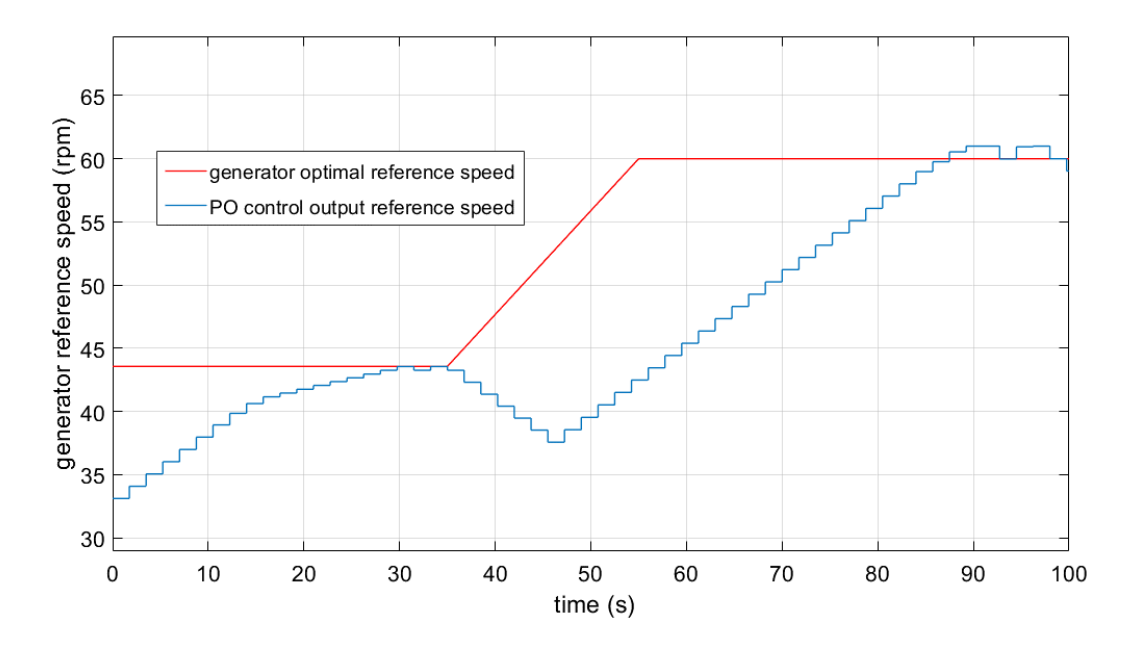


Figure 4.33 P&O control output generator reference speed with 0.3 step size and 1.75s step time

Figure 4.34 illustrates how the drift problem that may happen in the tidal current turbine system. In this figure, assume initially that the turbine is operating at point b under a tidal current velocity of 1.7m/s, the P&O control is tracking to the MPP on this curve and the previous step is point a. When the turbine is operating at point b, if the tidal current velocity increases from 1.7m/s to 1.9m/s, the turbine working point will change from b to b'. Thus, at turbine rotation speed ω_b the corresponding power under 1.9m/s tidal current velocity will be $P_{b'}$, and the P&O control output generator reference speed will be estimated following the rules: $P_{b'} - P_b > 0$ and $\omega_b - \omega_a < 0$. According to Figure 4.3, the change in power is positive and the change in speed is negative, so the P&O control will provide a negative change to the speed, thus for the 1.9m/s tidal current velocity the new operating will be point c, which is moving away from the MPP. Again, if the tidal current velocity keeps increasing form 1.9m/s to 2.1m/s, when the turbine is operating at point c, under 2.1m/s tidal current velocity with turbine rotation speed ω_c , the operating point will change from c to c', so the output of P&O control will be: $P_{c'} - P_c > 0$ and $\omega_c - \omega_d < 0$. This will again lead to a decrease in the turbine rotational speed, which is also moving away from the MPP under a tidal current velocity of 2.1m/s.

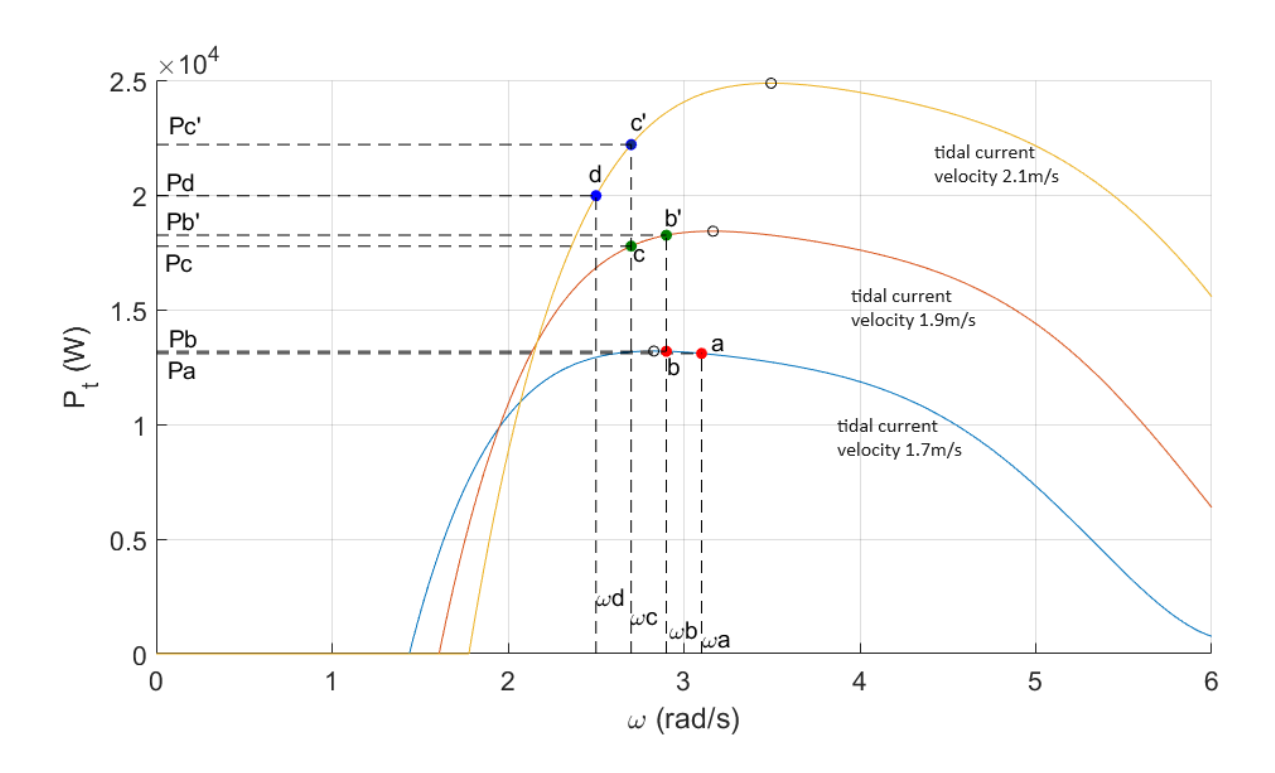


Figure 4.34 P&O control drift problem

As discussed above, the drift problem that happened with 0.3 step size and 1.75s step time can be explained. Figure 4.35 show the changes in power and in generator speed with 0.3 step size and 1.75s step time P&O control. From this figure it can be seen that when the tidal current speed input starts the ramp change at 35s, the change in power is negative, and the change in generator rotor speed is positive. According to Figure 4.3, this will lead to a decrease in the generator reference speed. At about 48s, the change in power is negative and the change in speed is also negative, and this situation makes the P&O control algorithm give an increasing change in the output. Thus, after 48s, the generator reference speed increases to track the MPP again. The drift problem is caused by the P&O control algorithm itself. It may happen in the P&O control tunning process, thus when choosing the P&O control parameters, the drift problem should be considered, as it can reduce the tracking efficiency and make the system slow in returning to the desired state.

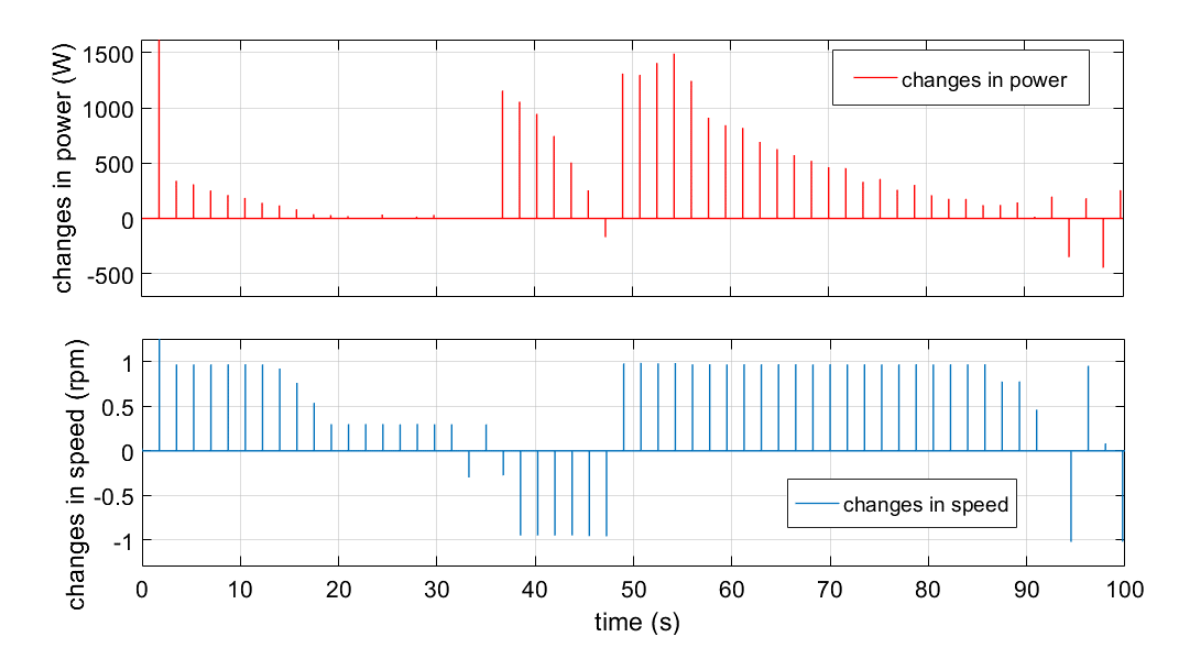


Figure 4.35 Changes in power and speed with P&O control with 0.3 step size and 1.75s step time

4.5.3 Performance analysis

According to the discussion above, the step size and step time can affect the P&O control performance and, based on the results in Tables 4.1 and 4.2 and Figure 4.29 to Figure 4.32, a group of parameters was selected with 0.3 step size and 1.25s step time. The P&O control with these parameters has a good average tracking efficiency and avoids the speed drift problems under both step change and ramp change tidal current input.

Figure 4.36 shows the generator reference speed with 0.3 step size and 1.25s step time under step change tidal current input. It can be seen from this figure that the P&O control output generator reference speed can track the desired value and varies around it. It first reaches the optimal speed at about 20s and then varies around it with maximum 0.7% error. When the tidal current velocity start increasing the P&O control output is also increased to converge to the optimal value, and at about 55s, the P&O control output reaches the optimal reference speed again and fluctuates around the optimal value with maximum 1.7% error. This means that the P&O control can give a generator reference speed signal without the tidal current speed sensor and can track the MPP with a small error.

Figure 4.37 presents the turbine output power and generator output electrical power of the

system under step change tidal current input. It can be seen that the mechanical power produced by the tidal current turbine has reached the theoretical calculated power, this means that the P&O control can make the turbine operate near MPP and capture maximum power under a given tidal current condition. Also, the output electrical power provided by generator follows the tidal current change and, as expected, due to the losses in the power transformation process and the losses in the generator (such as copper losses), the output electrical power is less than the mechanical power.

Figure 4.38 shows the active and reactive power that are injected into the grid. In this figure, the active power follows the tidal current speed change and due to the transmission loss and filter loss, the active power is a little bit lower than the generator output electrical power. During the whole simulation time, the reactive power remains at zero, this means the grid side converter control strategy can control the active and reactive powers that are injected into the grid.

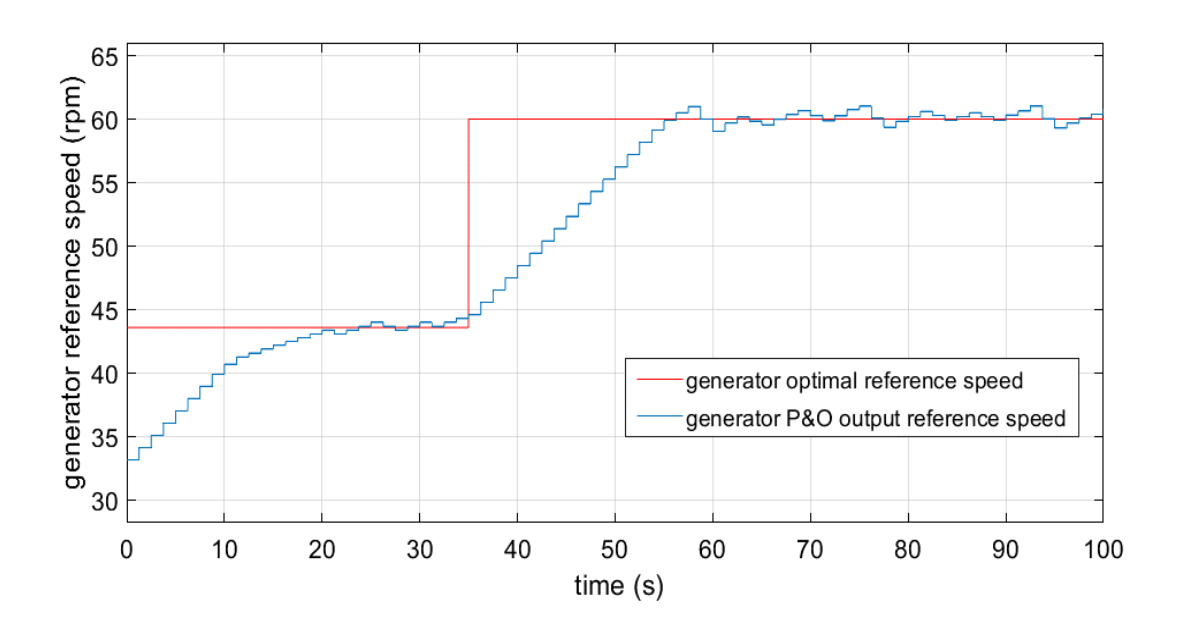


Figure 4.36 P&O control output generator reference speed under step change tidal current velocity input

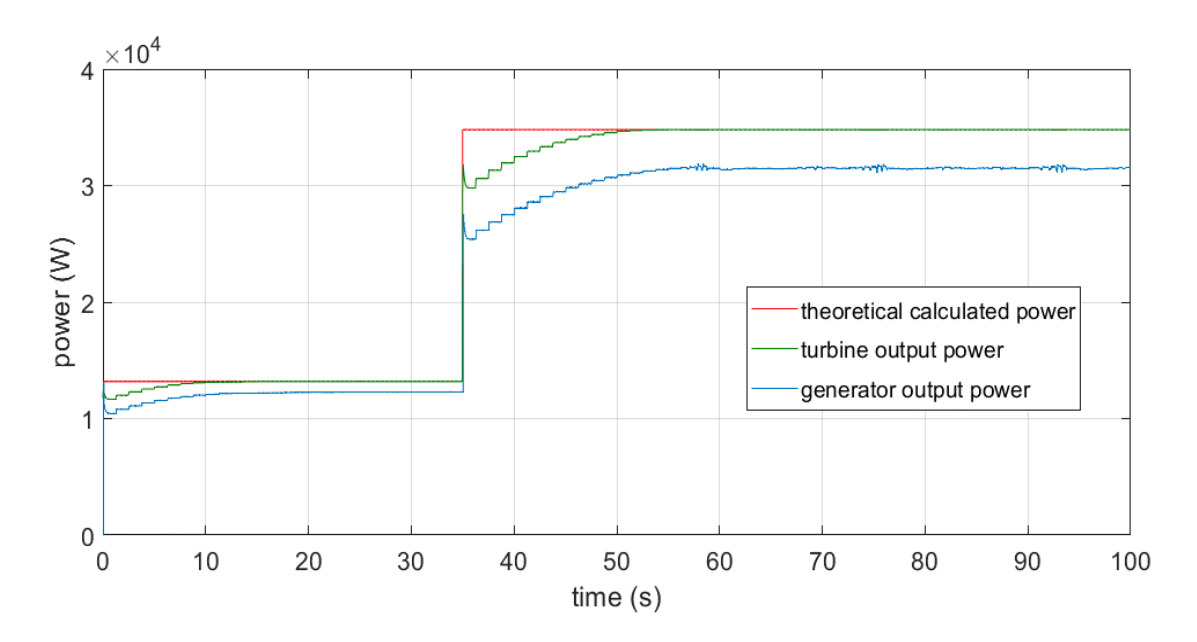


Figure 4.37 Turbine output power and generator output power under step change tidal current velocity input

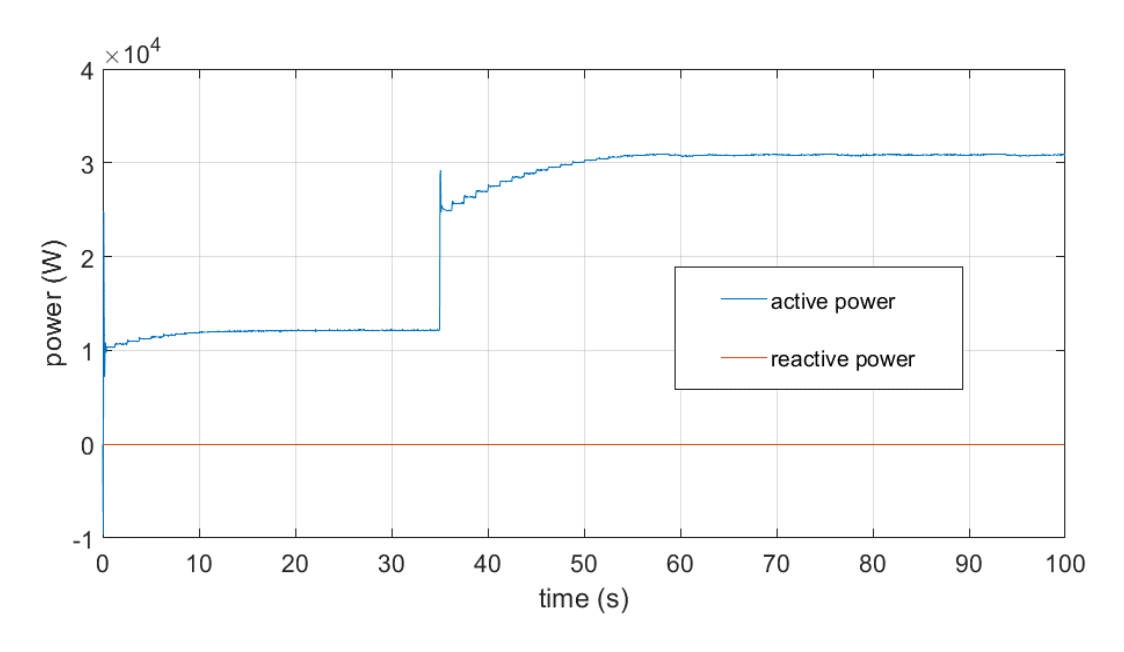


Figure 4.38 Active and reactive power under step change tidal current velocity input

Figure 4.39 shows the generator reference speed under ramp change tidal current input. The ramp change input can test the P&O control performance under continuously changing conditions, and from Figure 4.39 it can be seen that before the tidal current velocity starts the ramp increase, that is before 35s in the simulation, the P&O control output generator reference speed is the same as in Figure 4.35. When the tidal current velocity speed ramp starts to increase, it is clear that the generator reference speed can track the MPP during the ramp change and has a small fluctuation range (maximum 1.8% error) in the steady state. This

means that this group of parameters for the P&O control can control the system to track the MPP in an acceptable range both under the step change input and ramp change input without a signal from a tidal current speed sensor.

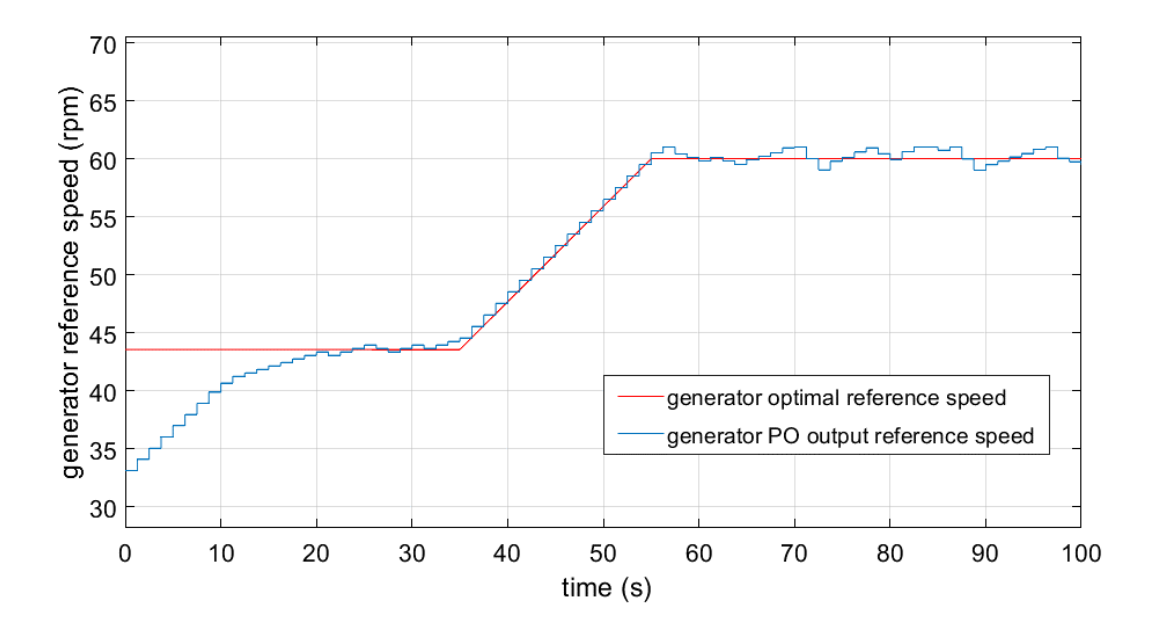


Figure 4.39 P&O control generator reference speed under ramp change tidal current input

Figure 4.40 illustrates the turbine output power and generator output electrical power, under the ramp change tidal current input. The tidal current turbine again provides mechanical power that matches the theoretical calculated power, and also due to losses in the system, the electrical power is slightly lower than the input mechanical power.

Figure 4.41 presents the active and reactive power that are injected into the grid under ramp change input conditions. Similar to the step change input, the active power is less than the generator electrical power due to the losses. The reactive power is also maintained at zero. This means that the grid side converter control strategy can control the active and reactive power injection both under step change tidal current input and ramp change tidal current input.

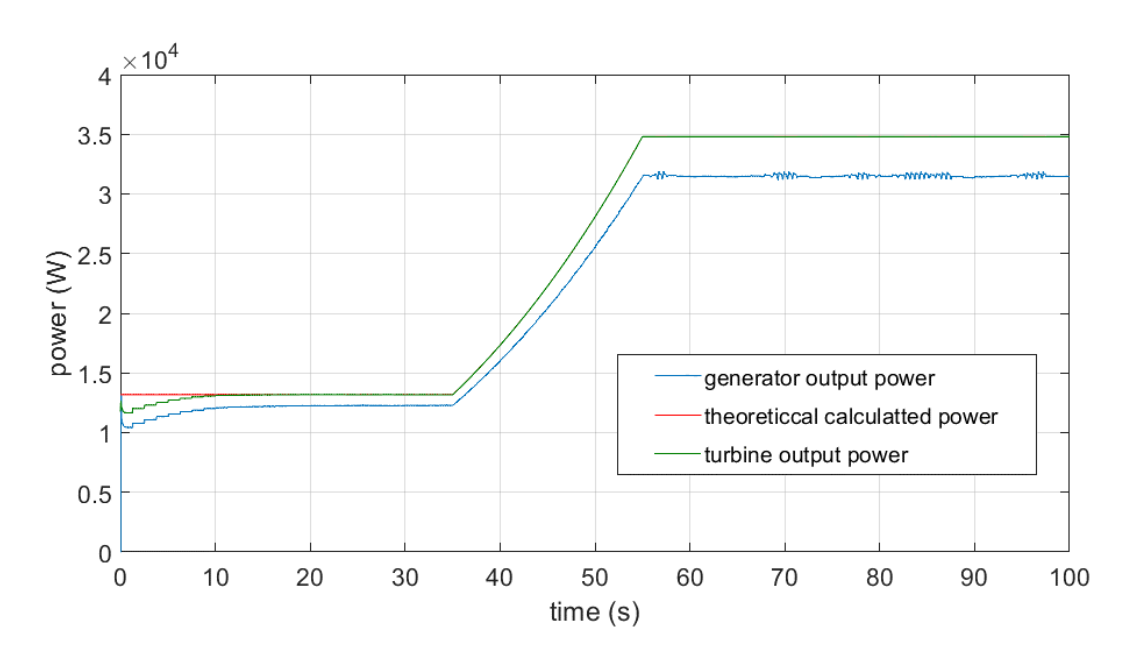


Figure 4.40 Turbine output power and generator output power under ramp change tidal current velocity input

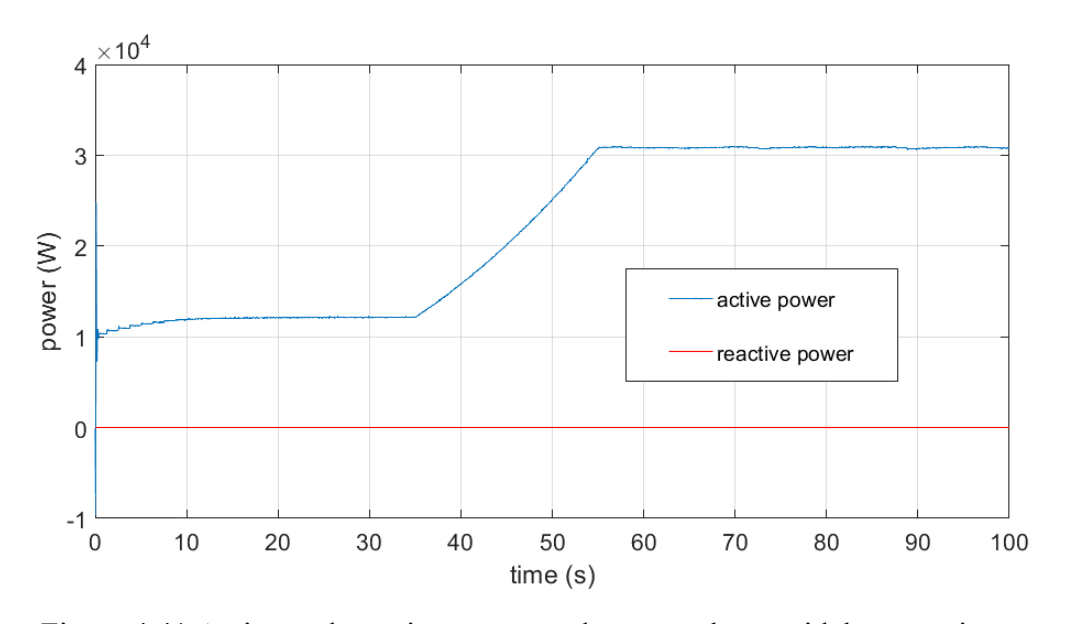


Figure 4.41 Active and reactive power under ramp change tidal current input

4.6 Summary

This chapter presented a stand-alone system model based on the model that built in Chapter 3 and tested the P&O control application with the stand-alone model, which was proved that to be able to work in the tidal current turbine generation system. Also, the grid-side converter control loop was developed in this chapter and combined with the generator side converter control model from Chapter 3 to produce a grid-connected model. Furthermore, P&O control

was redesigned to meet the requirements of the grid-connected model. The grid-connected model with P&O control to track the MPP was tested under both step and ramp change tidal current velocity input with an aim to investigate the performance of the system for both sudden and continuous changes. The results have shown that the P&O control can regulate the tidal current turbine generation system to operate close to the MPP under both step and ramp changes. This means that the P&O control provides the MPPT control without the tidal current speed sensor and has achieved the aim of the control strategy design. The results also show that P&O control can be applied both in a stand-alone system and a grid connection system. However, there is a drift problem which occurs periodically in P&O control. This mainly happens in PV and wind turbine systems when the solar radiation and wind speed change rapidly (as mentioned in Chapter 2), while the change in real tidal currents do not have rapid changes. However, considering the need for robustness in tidal current turbines, this is a limitation. Fuzzy Logic (FL) control is therefore investigated in Chapter 5 to address this limitation in the tidal current turbine generation system. FL control will be presented in Chapter 5 and tested in the same tidal current turbine system model and with the same tidal current velocity inputs. A comparison between P&O control and FL control will also be presented considering factors such as output value, generator power and efficiencies.

Chapter 5. Tidal current speed sensor-less MPPT control with Fuzzy Logic methodology

As presented in Chapter 4, P&O control is able to track the MPP without an input from a tidal current speed sensor in the conventional tidal current turbine system, but sometimes will face the drift problem. Another control algorithm that can track the MPP without a tidal current velocity sensor was introduced in Chapter 2, this is Fuzzy Logic (FL) control. FL control is a potential MPPT control strategy which can track the MPP without the knowledge of the tidal current turbine state. This chapter will use the conventional tidal current turbine generation system model developed in Chapter 4 and the same tidal current velocity inputs to test the FL control performance. FL control design for the conventional grid-connected system will be presented in this chapter and will be tested under both step change and ramp change tidal current velocity input. The results and discussion are presented and a comparison of the performance between P&O control and FL control will be analysed as well.

5.1 Fuzzy Logic Control

Fuzzy Logic control has been identified as a reliable and important control methodology in industrial engineering applications [156]. FL control is used in wind turbine generation systems and PV systems for MPPT control algorithms, and due to the similarities between wind turbine generation systems and tidal current turbine generation systems, FL control can be considered as a potential solution to deal with tidal current speed sensors failures.

In a wind turbine generation system, FL control can be used to track the MPP in different kinds of system topologies. In [157] and [158], a FL algorithm is used in stand-alone wind turbine systems to provide duty ratio as an output to control a boost converter or buck converter, while in [159] the FL algorithm was used to provide duty output in a grid connected wind turbine system with boost converter. In grid connected wind turbine generation systems which use back-to-back converters, a FL algorithm can also be used to implement the MPP tracking, such as in [160-162], where the FL control is used to provide the changes in generator reference speed. Alternatively, in [163] and [164], FL control gives

the electromagnetic torque as an output for wind turbine systems that operate in torque control mode. Just as FL control can be used in different wind turbine systems to provide different outputs, it can also be developed in tidal current turbine generation systems.

Compared with P&O control, FL control's theory is more complex. FL has a variable step size, which means that it will have smaller changes during the steady state than in dynamic conditions [160]. Similar to the P&O control, FL control also does not need knowledge of the system, which means that when the tidal current speed sensor is broken, the system can still operate to track the MPP.

The control structure of FL control can be implemented as three parts: fuzzification, rule based look up table and defuzzification [158, 163]. Figure 5.1 shows the block diagram of FL control. In this project, the inputs of the FL control are the change in power, ΔP and the change in generator speed, $\Delta \omega$, while the output is the generator reference speed, ω_{ref} . Then the speed control loop will control the generator speed to follow the reference speed to make the turbine operate at the MPP.



Figure 5.1 FL control diagram

5.1.1 Fuzzification

In the FL control algorithm, the first step is to convert the input variables to FL variables through membership functions (MFs). MFs can be defined in many types, such as monotonic, triangular and trapezoidal, with the subset degree from 0 to 1, and these three types of MFs are shown in Figure 5.2. When designing FL control, the MFs type chosen needs to be considered; each type of MFs has advantages and disadvantages. The number of MFs used can control the speed and accuracy of the FL control [165], with triangular and trapezoidal being the most commonly used MFs in FL control, due to the high dynamic variation in a short processing time [166].

In a FL control system, if the system has too few membership functions, then it is too simple which will lead to a short system processing time with variation in outputs. On the other hand, if the system has too many membership functions, it will become complex, and this will make the system processing time lengthy but it will have more accurate output results. So, in FL control design, the number of MFs also needs consideration.

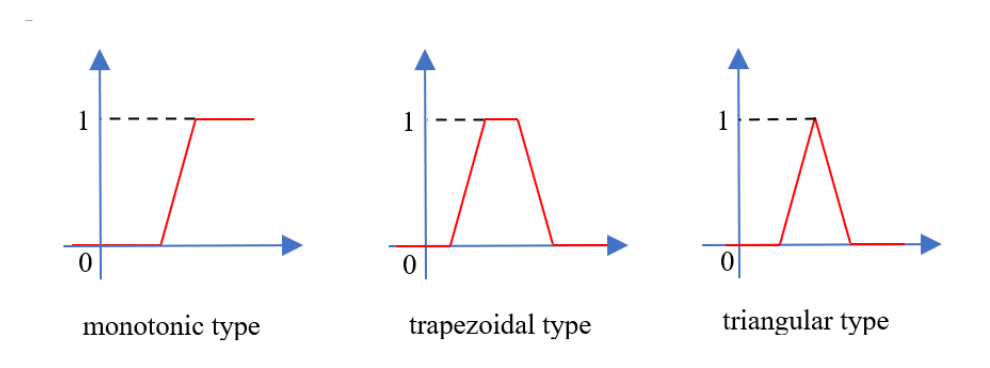


Figure 5.2 Types of membership functions

5.1.2 Fuzzy Rules

In FL control systems, after the fuzzification stage, based on "if-then" code, the input data are converted to the subset degree through MFs to describe the system changes, and then in the fuzzy rules stage, these subset degrees are compared with "and" or "or" code through a fuzzy rules lookup table which has to be designed. The design of the fuzzy rules in this project was similar to the searching process of the P&O control in Chapter 4, and the design will be illustrated in Section 5.2.

5.1.3 Defuzzification

In FL control systems, the defuzzification is the last step. In this stage, the signal will be transferred from subset degrees to normal output signals through the output MFs. Generally, the calculation of defuzzification has one of three forms: mean of maximum, height and the centre of gravity, and of these calculation methods, the centre of gravity is the most commonly used due to its smooth output value [167]. The centre of gravity is used to calculate the gravity centre point of the output membership functions. The calculation of the centre of gravity of the output MFs can be express as:

$$COG = \frac{\sum_{i}^{N} \mu_{i} x_{i}}{\sum_{i}^{N} \mu_{i}}$$
 Equation 5.1

where N is the number of fuzzy rules, μ_i is the membership value of the i_{th} rule, and the x_i is the centre value of the membership functions [168], and these will find the vertical line that divides the i_{th} corresponding area into two equal parts.

5.2 Fuzzy Logic Control Design

In this thesis, the FL control is used to provide the generator reference speed directly, to allow the generator to operate near this reference speed to reach the range of the maximum power point. The basic control theory is the same as P&O control in Chapter 4. Detecting the changes in the generator power and generator speed, the control can then predict the changes in tidal current speed and provide a generator reference speed signal for the generator to follow.

The difference between traditional P&O control and FL control is that the traditional P&O control is fixed step size while the FL control is of variable step size. In Figure 4.2, it can be seen that if the reference speed change is $\Delta\omega$, then in the tidal current turbine generation system, this will lead to a change ΔP in the output power, because the output power is proportional to the generator speed. In traditional P&O control the perturbation value that is given to the generator reference speed, $\Delta\omega$, is fixed. There is a gain value which can make it vary in the P&O control tested in Chapter 4, but the variation range is not big, and the range of variation of P&O control input is not determined, it can only detect whether the change is positive or negative and then give a corresponding signal to control the generator speed. In FL control, through the fuzzification stage, the variation range in the input signal can be determined, and in the defuzzification stage the output will be a variable value in the determined MFs across the variation range detected in the input.

Figure 5.3 shows the FL control searching process. It can be seen that under a certain tidal current speed, if the generator speed is ω_1 , the corresponding power will be P_1 . When the generator speed changes from ω_1 to ω_2 , the power changes from P_1 to P_2 , the FL control will

detect the speed change $\omega_2 - \omega_1$ and power change $P_2 - P_1$, if they are both positive then it will give a positive change $\Delta\omega_{2-1}$ in the output reference generator speed signal. Unlike the P&O control, the FL control will change the output value depending on the change in the speed as well as the power. In Figure 5.3, the changes in the power $P_2 - P_1$ and $P_3 - P_2$ are different, and the FL control will give different output signals, $\Delta\omega_{2-1}$ and $\Delta\omega_{3-2}$ respectively, while traditional P&O control would give a constant $\Delta\omega$ change value to the output reference speed signal.

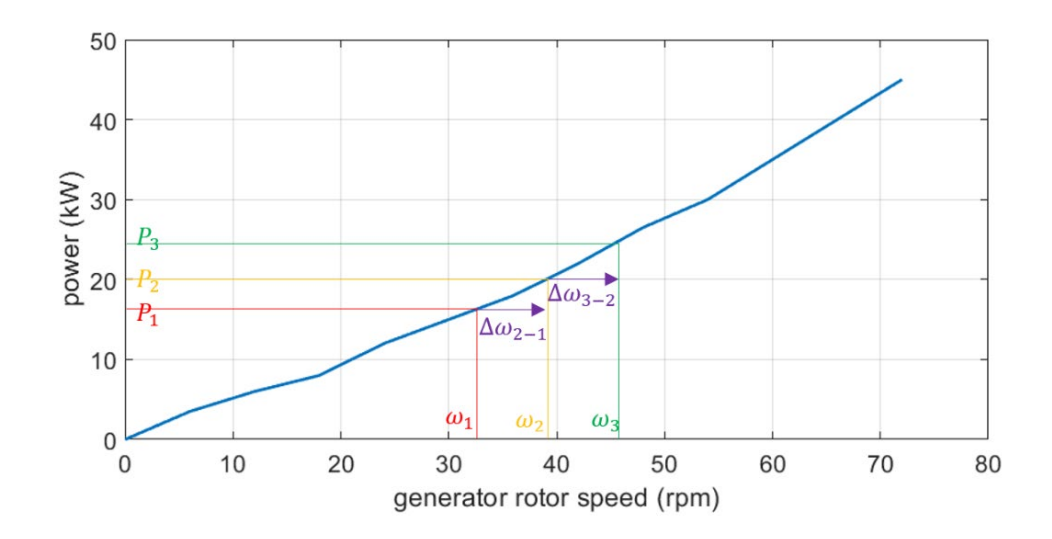


Figure 5.3 FL control detect searching process

From Equations 2.1 and 2.2, it can be seen that the turbine power P_t is proportional to the generator rotational speed ω_r . This can be considered in the FL control design, and in a TCT system, the relationship between turbine power P_t and generator rotational speed ω_r can be expressed in a P- ω curve [160]:

$$\begin{cases} dP_t/d\omega_r < 0, (\omega_r > \omega_{mpp}) \\ dP_t/d\omega_r = 0, (\omega_r = \omega_{mpp}) \\ dP_t/d\omega_r > 0, (\omega_r < \omega_{mpp}) \end{cases}$$
 Equation 5.2

The FL control in this thesis has two inputs, the change in power ΔP and the change in generator rotational speed $\Delta \omega$ respectively, and they can be express as:

$$\Delta P = P_n - P_{(n-1)}$$
 Equation 5.3

$$\Delta \omega = \omega_n - \omega_{(n-1)}$$
 Equation 5.4

the output of the FL control is the change in generator reference speed $\Delta\omega_{ref}$, and the signal that goes into the PI controller will be the new generator reference speed, as shown in Equation 5.5:

$$\omega_{ref} = \omega_{ref(n-1)} + \Delta\omega_{ref}$$
 Equation 5.5

The membership functions of FL control with the MATLAB fuzzy logic controller are illustrated in Figure 5.4. Nine MFs of power change input (ΔP) are defined: very big positive (P+), positive big (PB), positive medium (PM), positive small (PS), zero (ZE), negative small (NS), negative medium (NM), negative big (NB) and very big negative (N+). In order to simplify the system and increase the system processing time, the generator rotational speed input ($\Delta \omega$) will be defined three MFs: positive (P), zero (ZE) and negative (N). FL control input MFs can be viewed in Figure 5.4 (a) and (b) respectively. The output of the FL control is the change in generator reference speed ($\Delta \omega_{ref}$). Like the ΔP MFs, there are nine output MFs: very big positive (P+), positive big (PB), positive medium (PM), positive small (PS), zero (ZE), negative small (NS), negative medium (NM), negative big (NB) and very big negative (N+), and this is illustrated in Figure 5.4 (c).

The fuzzy rules are shown in Table 5.1, and the FL controller will follow this fuzzy rule table to adjust the output value. According to Figure 5.4, Equations 5.2 to 5.5 and Table 5.1, the fuzzy logic controller can be designed in the MATLAB fuzzy logic module. The FL control block diagram is illustrated in Figure 5.5. The fuzzy logic detailed model in MATLAB is illustrated in Appendix C.1, and the FL control MFs in the MATLAB module are shown from Appendix C.2 to C.4.

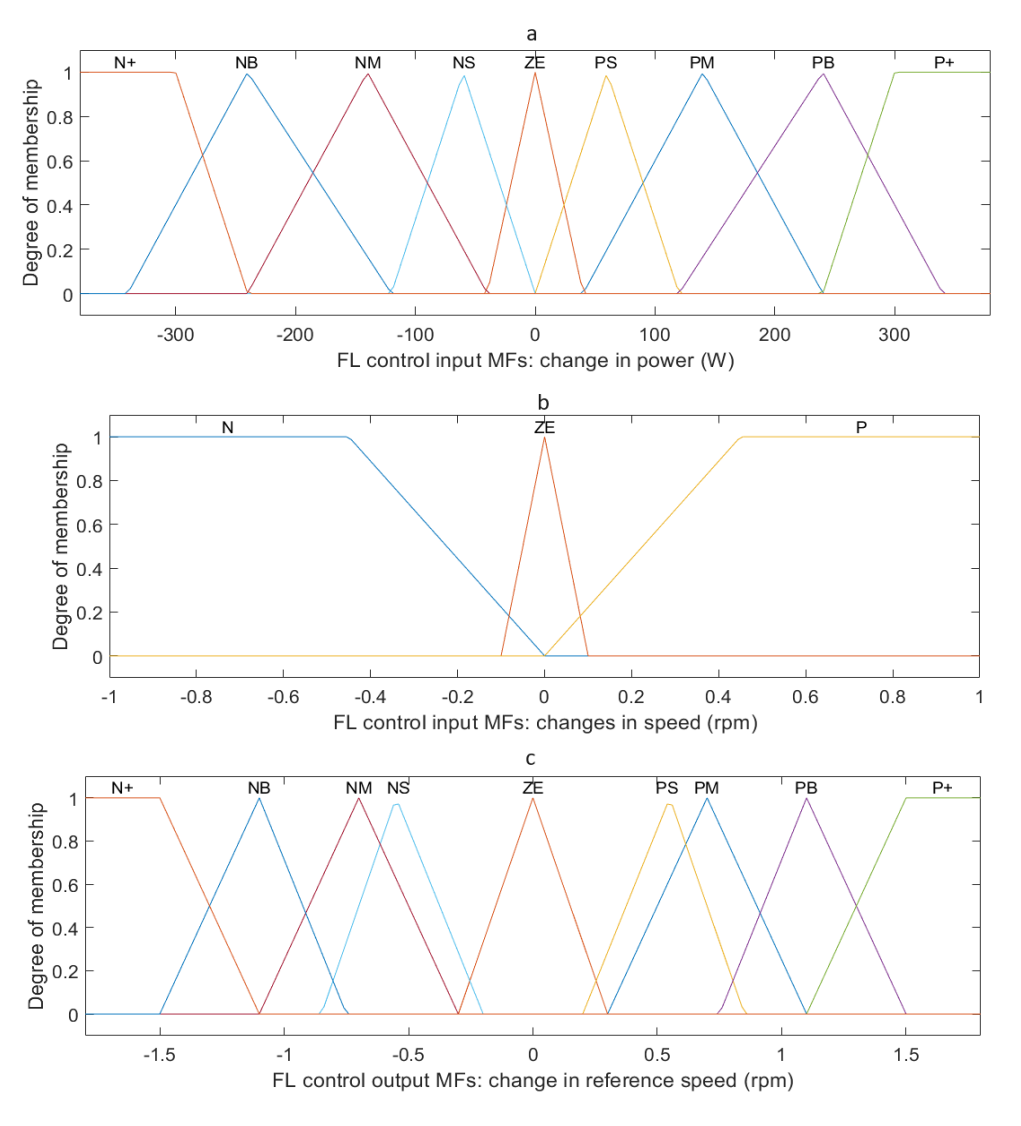


Figure 5.4 (a) MFs of FL input ΔP ; (b) MFs of FL input $\Delta \omega$; (c) MFs of FL output $\Delta \omega_{ref}$

$\Delta \omega_{ref}$		ΔΡ								
200	rej	N+	NB	NM	NS	ZE	PS	PM	PB	P+
	N	P+	PB	PM	PS	ZE	NS	NM	NB	N+
Δω	ZE	NB	NM	NS	NS	ZE	PS	PM	PM	PB
	P	N+	NB	NM	NS	ZE	PM	PM	PB	P+

Table 5.1 FL control fuzzy rules

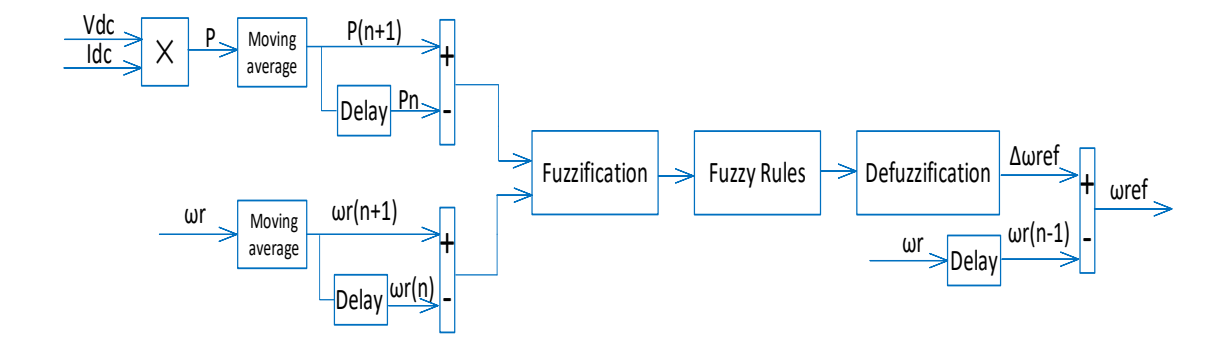


Figure 5.5 FL control block diagram

5.3 FL Control Application in Conventional Model

This section will present a TCT generation system with FL control. The basic system model is the same as for the P&O control in Section 4.4. FL control in this conventional TCT system model will give a generator reference speed signal to replace the traditional MPPT algorithm to help the system tracking of the MPP under the condition of loss of tidal current speed sensor signal. The change in generator output power and change in generator rotational speed go into the FL controller as the input, and the generator reference speed output signal goes into the speed PI controller to control the generator rotational speed to follow the reference speed. This will ensure that the TCT system operates near the MPP to extract the maximum power from the tidal current flow. Figure 5.6 illustrates the TCT system block diagram with FL control. It can be seen that the tidal current turbine system is the same as the model used in Chapter 4 in order to compare FL control and P&O control. The parameters of the conventional TCT model were controlled under the same conditions, such as the tidal current input and control method perturb time. The simulation model in MATLAB is illustrated in Appendix C.5.

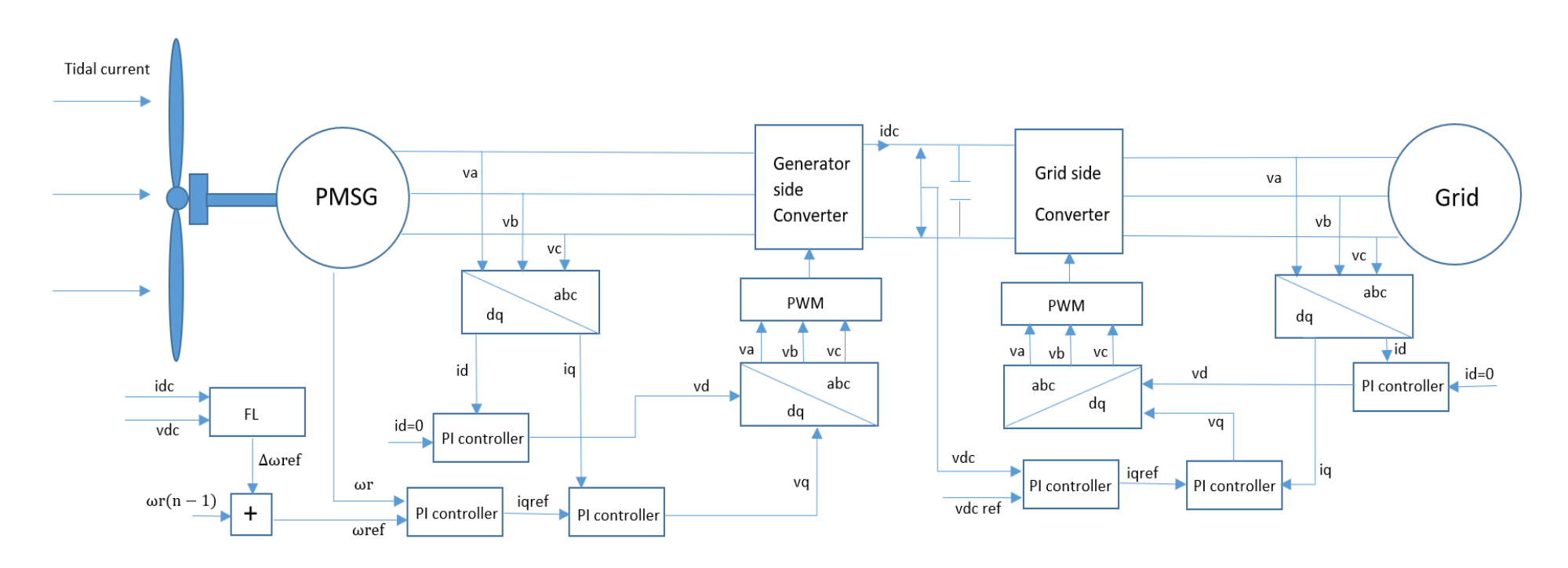


Figure 5.6 Conventional tidal current turbine system model with FL control

5.4 Results and discussion

This section will present the results of the FL control with the conventional grid-connected TCT system. With the aim to test the FL control performance, the control output generator reference speed, turbine output power, generator output power and tracking efficiency of the MPPT algorithm will be used to compare different FL control parameters, where the average MPPT tracking efficiency calculation is as given in Equation 4.16. Similar to the P&O control test, both step change and ramp change tidal current speed inputs were tested in this model. The tidal current step change input is from 1.7m/s to 2.35m/s, the step change happens at 35s into the 100s simulation time, and the ramp change input is also from 1.7m/s to 2.35m/s, where the ramp change happens at 35s and reaches 2.35m/s at 55s and the whole simulation is also 100s.

In FL control, the design of membership functions can lead to different output results. As mentioned in Section 5.2, the turbine power P_t is proportional to the generator rotational speed ω_t , but the power transferred from tidal current turbine is not unlimited, there is a rotational speed that can maximise the tidal current turbine power capture from the tidal current, thus the speed adjustment is necessary to make sure the turbine rotates in the maximum power point range. During the generator reference speed adjustment process, FL control can set step up and down limitations to limit the maximum value that can be added to the reference speed signal. Thus, in the FL control design, the relationship between power and generator speed can be considered as linear over the small range of the variation. In Section 3.2 the rated speed and power of the generator GDF-355L used in this thesis are given as 60rpm and 35kW respectively, and the rate of the linear relationship within the range of power and speed can be considered as around $\frac{35000}{60} \approx 584$. During the FL control design, the MFs can initially be set simply on this rate, and during the FL control tunning, this rate can be modified and the details in the MFs, such as each MFs' interval, can be varied until the parameters lead to the desired results.

For example, when tunning the FL control parameters initially, the maximum input value of ΔP can be set at 580W, the maximum input value of $\Delta \omega$ at 1 rpm, and maximum output value of $\Delta \omega_{ref}$ at 1.5rpm, and the MFs of the input and output may then be determined by triangular type. The process is then repeated until the output value tracks the optimal value and varies around it. During the tuning of the FL control parameters, the trail-and-error method was used, until the results presented were found. The results in this section will show

the FL with different MFs and step times to illustrate how they affect the output value, and the average efficiency and instantaneous efficiency of different combinations of FL control parameters are compared and discussed.

5.4.1 MFs and Step time

Similar to the P&O control, the MFs values and step time will also affect the performance of FL control. Figure 5.7 illustrates the FL control output generator reference speed with different MFs values, where MFs 5 has 2.25rpm maximum output value, MFs 3 has 1.8rpm maximum output and MFs 1 has 1.2rpm maximum output value. It is clear that MFs 5 can reach the optimal value first at about 11s before step change and around 50s after the step change, while MFs 1 is unable to reach the optimal value before step the change and reaches the optimal value at about 80s after step change. Also it is obvious that the fluctuations of the FL control output generator reference speed value of MFs 5 are bigger than for MFs1. Essentially, similar to P&O control in Chapter 4, FL control with bigger MFs output values leads to faster tracking speed but will also have bigger fluctuations during the steady state.

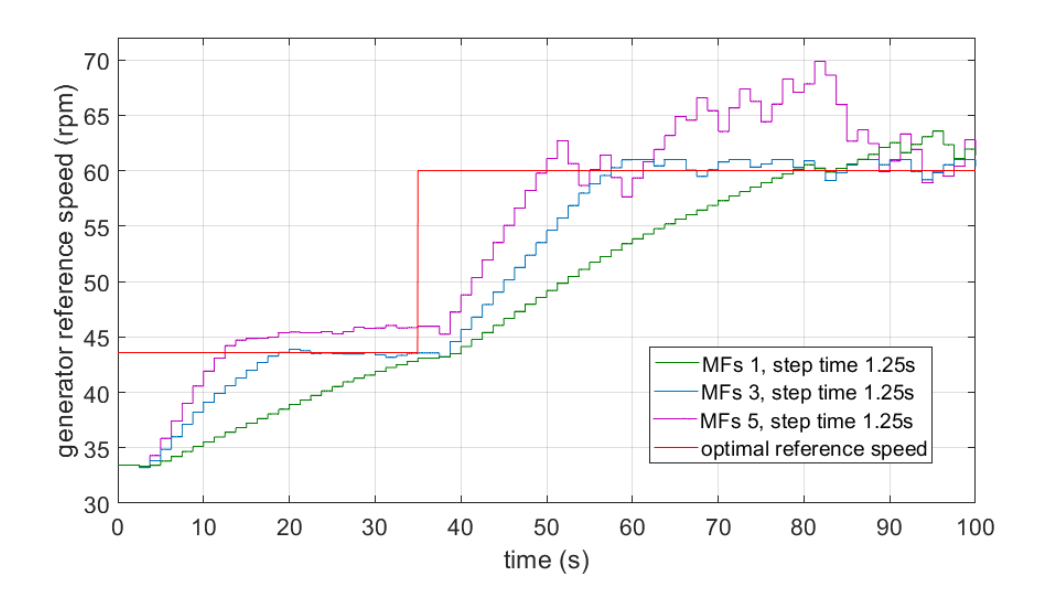


Figure 5.7 FL control output with different MFs

Figure 5.8 Figure 5.8 presents the FL control output generator reference speed with different step times. Also is similar to P&O control, it is obvious that the FL control with same MFs but smaller step time will have a quicker tracking speed. In the figure, a 0.75s step time reaches the optimal value at about 11s before the step change and at 47s after the step change, while FL control with 1.75s step time takes about 30s to reach the optimal value before the step change and reaches the red line at about 58s after the step change. Also, it can be seen that with the 0.75s step time the FL control output has more frequent fluctuations compared to

1.25s and 1.75s step times during steady state. Too high a fluctuation frequency will mean that the generator is constantly changing speed to follow the control output reference speed, which will reduce the system robustness. This is similar to the P&O control where a small step time will lead to a short tracking time but will come at the price of frequently fluctuating speed during the steady state.

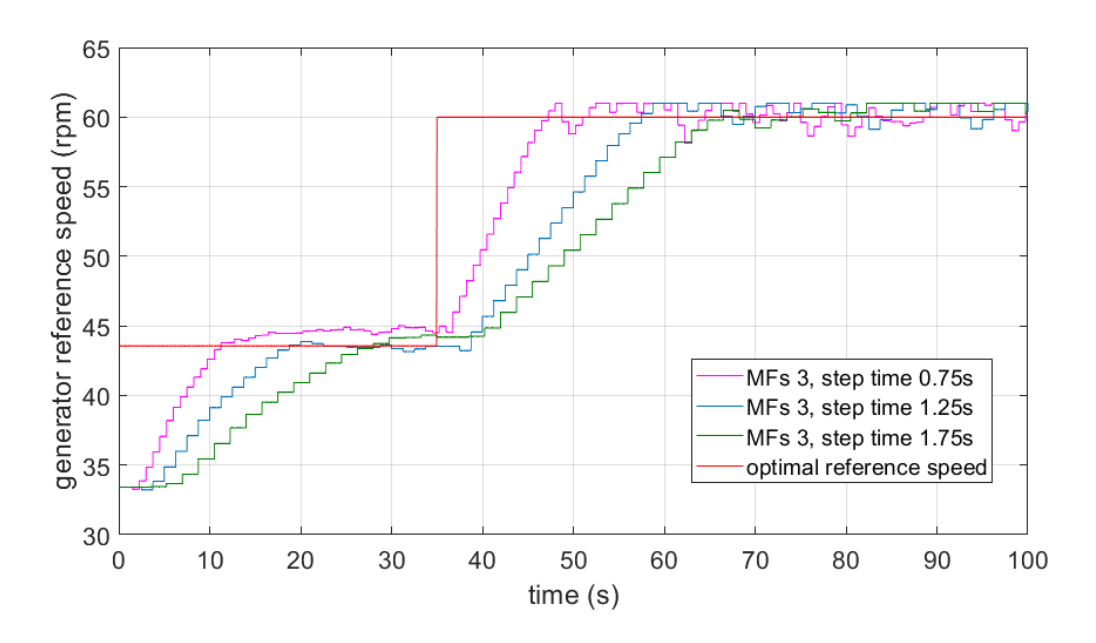


Figure 5.8 FL control output with different step time

5.4.2 Performance analysis

Table 5.2 shows the average MPPT efficiency of five selected FL control parameters. The differences between these parameters are the output MFs. Each of them has differences in the maximum value of output MFs so in order to compare with the P&O control in Chapter 4 they used the same step time which is 1.25s. Results with different step time will be presented later in this section. Average efficiency is an important standard for the choice of parameters, but the variation during steady state is important too. Figure 5.8 presents the instantaneous power efficiency of the FL control under the step change tidal current input and Figure 5.9 shows the instantaneous power efficiency for the ramp change input.

From Figure 5.9 it can be seen that FL control with small maximum output value MFs has obviously slower tracking speed than the high maximum output value MFs, as the green line in the figure below reaches the steady state first while the blue line is the last, but the larger MFs output value will lead to larger FL control output value fluctuations during steady state as discussed above, and this will also impact on the instantaneous power efficiency as, in Figure 5.9, the fluctuations of MFs with large output value such as MFs 5 is clearly larger

FL control MFs	Step change	Ramp change	
1 (1.2rpm)	86.59%	89.96%	
2 (1.5rpm)	87.87%	90.52%	
3 (1.8rpm)	87.98%	90.62%	
4 (2rpm)	88.34%	90.84%	
5 (2.25rpm)	89.66%	89.35%	

Table 5.2 Average power efficiency of FL control with different MFs under step and ramp change tidal current velocity input

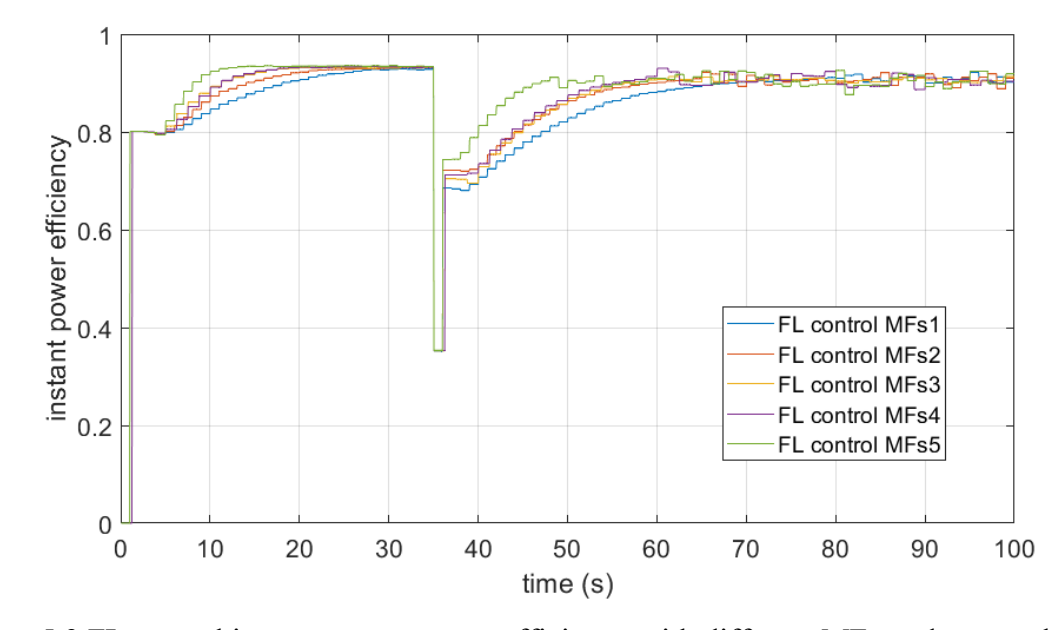


Figure 5.9 FL control instantaneous power efficiency with different MFs under step change tidal current input

Figure 5.10 shows the FL control instantaneous power efficiency with different MFs output values under ramp change tidal current velocity input. Similar to the instantaneous power efficiency under step change tidal current velocity input in Figure 5.9, the bigger output value of MFs will lead to quick tracking speed, but also will have larger fluctuations during steady state. Also, sometimes the FL control output will overshoot the optimal generator reference speed, such as the MFs 5 in Figure 5.10, where from 50s to 65s the instantaneous power efficiency drops before coming back to the steady state. This is because the MFs output value is too large and makes the FL control output generator reference speed overshoot the desired value resulting in reduced generator output power. The FL control output reference speed then

comes back to the optimal value and the generator output power increases again. This impacts the instantaneous power efficiency as shown by the green line (MFs 5) in Figure 5.10 from 50s to 65s. The performance of FL control with different MFs output values under both step change and ramp change tidal current velocity input are similar to the P&O control in Chapter 4, as bigger output values can lead to the shorter tracking time but with larger fluctuations during steady state in both P&O control and FL control.

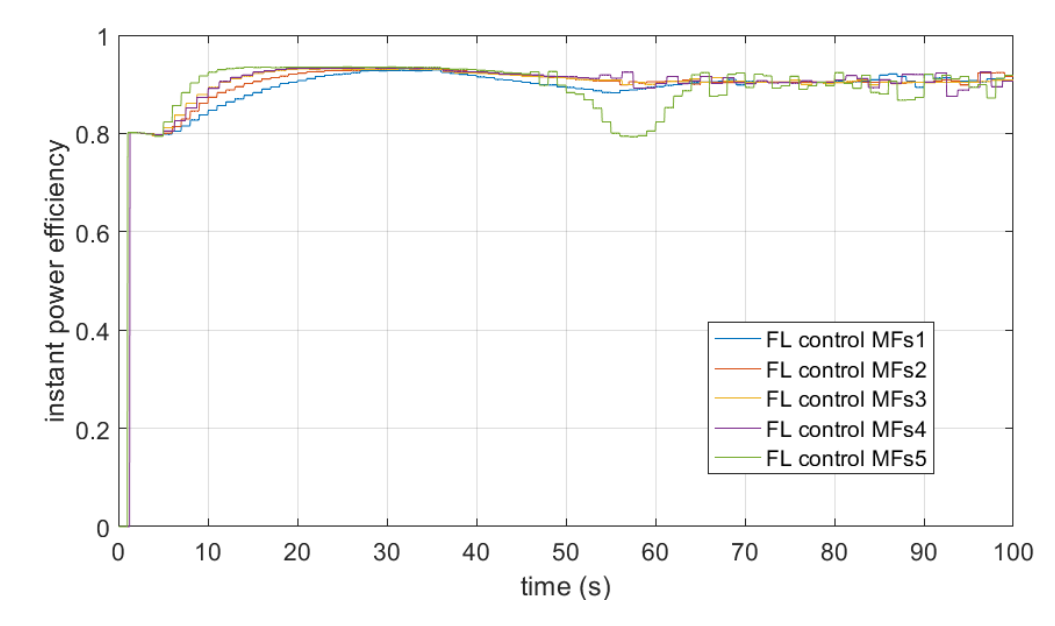


Figure 5.10 FL control instantaneous power efficiency with different MFs under ramp change tidal current input

From Table 5.2 and Figure 5.9 and Figure 5.10, it can be seen that among these FL control parameters, their average power efficiency values are very close, and the instantaneous power efficiencies all have the same trend. This is because in all cases the FL control output generator reference speed can track the MPP and varies around the optimal value. So, the chosen of FL parameter will consider the stability during the steady state. FL control with MFs 3 does not have the highest average power efficiency overall, but after entering the steady state, MFs 3 FL control has the smallest variations. In the average power efficiency table and instantaneous power efficiency figures, sometimes the FL control output generator reference speed overshoots the desired value, but it comes with a little bit higher efficiency. This is because the generator will follow the control output reference speed and will operate at higher rotation speed so the generator will generate higher power, but this is over the generator rated speed and working over the rated speed will cause damage to the generator. Thus, the chosen of control parameters not only consider the efficiencies, but also the FL control output value during steady state.

Table 5.3 shows the average power efficiency of FL control MFs 3 (maximum 1.8rpm) with different step times. Figure 5.11 and Figure 5.12 illustrate the instantaneous power efficiency of FL MFs 3 control under step change tidal current input and ramp change tidal current input respectively. Similar to the P&O control, the smaller perturb time will reduce the time in which the FL control output reaches the optimal value, but during the steady state, the small perturb time will lead to higher frequency of fluctuation near the MPP range. On the other hand, a larger perturb time will have relatively smooth variations during steady state, but the tracking time for the FL output to reach the desired value will be longer. Too big a step time will cause a lag in the FL control output and potentially it will be unable to follow the tidal current speed change in terms of generating a reference speed to reach the MPP.

FL control MFs	Step change	Ramp change	
0.7s	89.82%		
1s	89.19%	90.9%	
1.25s	87.98%	90.62%	
1.5s	87.87%	90.59%	
1.8s	87.38%	90.26%	

Table 5.3 Average efficiency of FL control with different perturb time under step and ramp input

From Figure 5.11 it can be seen that, FL MFs 3 control with 0.7s step can reach the first steady state at about 10s, while other step times need about 15s or even over 20s. Also, after step change happened, FL control with 0.7s step has the fastest tracking speed however, the fluctuations around the desired value will be at higher frequency compared with FL control with a bigger step time. This situation is the same as with P&O control under the step change input in Chapter 4.

Figure 5.12 presents the FL MFs 3 control with different step times under ramp change tidal current velocity input. As discussed for Figure 5.11, smaller step times will lead to shorter tracking time, but will also lead to higher fluctuation frequency. This is clear in Figure 5.12 with step times such as 1s and 1.8s. The FL control with 1s step time reaches steady state before the ramp change at about 17s while it takes the control with 1.8s step time about 25s, during the input ramp changing period and the steady state after the change, the control with 1s step time always reaches the optimal reference speed more quickly than the 1.8s step time.

This impact on the instantaneous power efficiency is shown in Figure 5.12. However, another situation may happen with a small step time, such as the blue line (0.7s step time) in this figure. In this case the instantaneous power efficiency from 50s to 65s first drops then rises again. The reason for this is similar to in Figure 5.10. In this case the step time is short, and this will lead to fast tracking but the FL control output generator reference speed may overshoot the desired value significantly, and then must track back. This is as opposed to Figure 5.10 where the overshoot of the FL output generator reference speed was caused by the large output value.

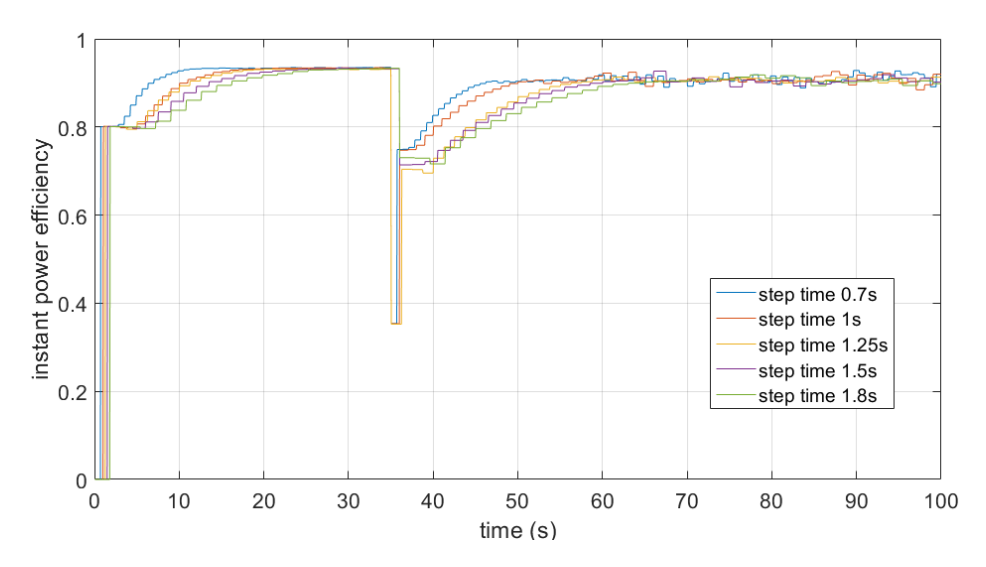


Figure 5.11 FL control instantaneous power efficiency with different perturb time under step change tidal current input

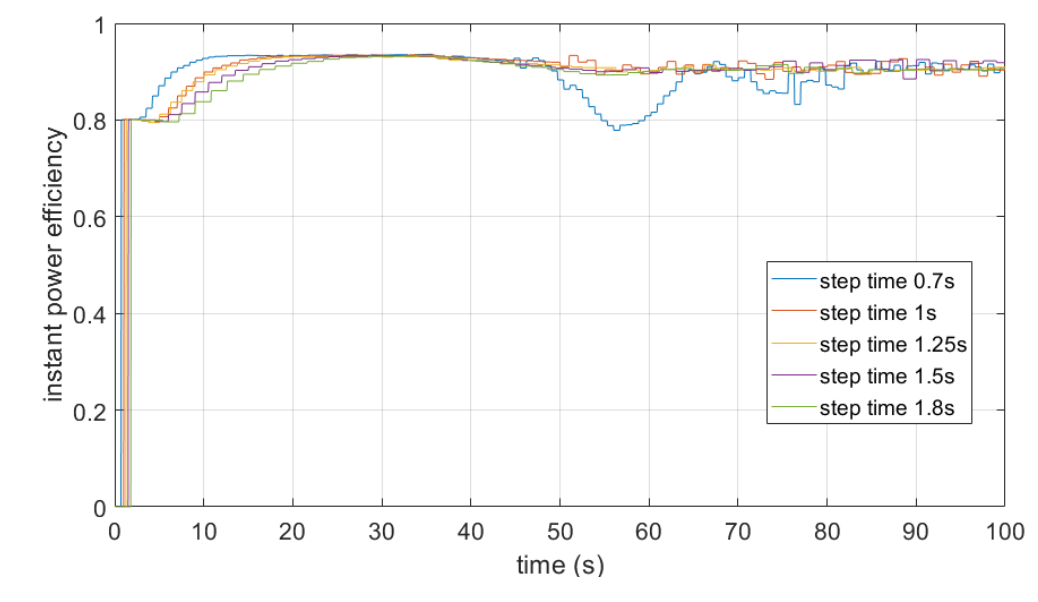


Figure 5.12 FL control instantaneous power efficiency with different perturb time under ramp change tidal current input

Essentially, the MFs maximum output value and the step time of the FL control can have similar effects on the control performance as for P&O control discussed in Chapter 4. Thus,

the choice of control parameters needs to consider the control output maximum value (step size for P&O, MFs for FL) and the step time and also needs to check the control performance: the control output generator speed and the tracking efficiencies.

Based on the discussion above, for the FL MFs 3 control, the 1s step time and 1.25s step time can be considered as the potential candidates for the TCT generation system in this thesis. Compared with the other step times, the tracking time is not too long when the tidal current input is changing, and the variations are not large during the steady state. In order to compare between P&O control and FL control, the perturb time needed to be in the same condition, thus FL MFs 3 with 1.25s step time was chosen.

Figure 5.13 shows the generator output reference speed of FL MFs 3 control with 1.25s step time under the step change input. From this figure it can be seen that the FL control output can track the optimal value after 20s from start-up and takes 25s to reach the desired value after the tidal current velocity input is changed and varies around it with an error of less than 1.7% during the steady state. This demonstrates that the FL control is able to control the system to operate near the MPP without a tidal current velocity sensor, and during the steady state (after the tidal current step or ramp change), the FL control output value does not go over the generator rated value significantly or over the rated speed for a long time. This ensures that the tidal current turbine and generator can operate in the rated condition and avoid damage caused by operating over the rated state. This means that the TCT generation system with FL control can realize the MPPT function without the tidal current speed sensor.

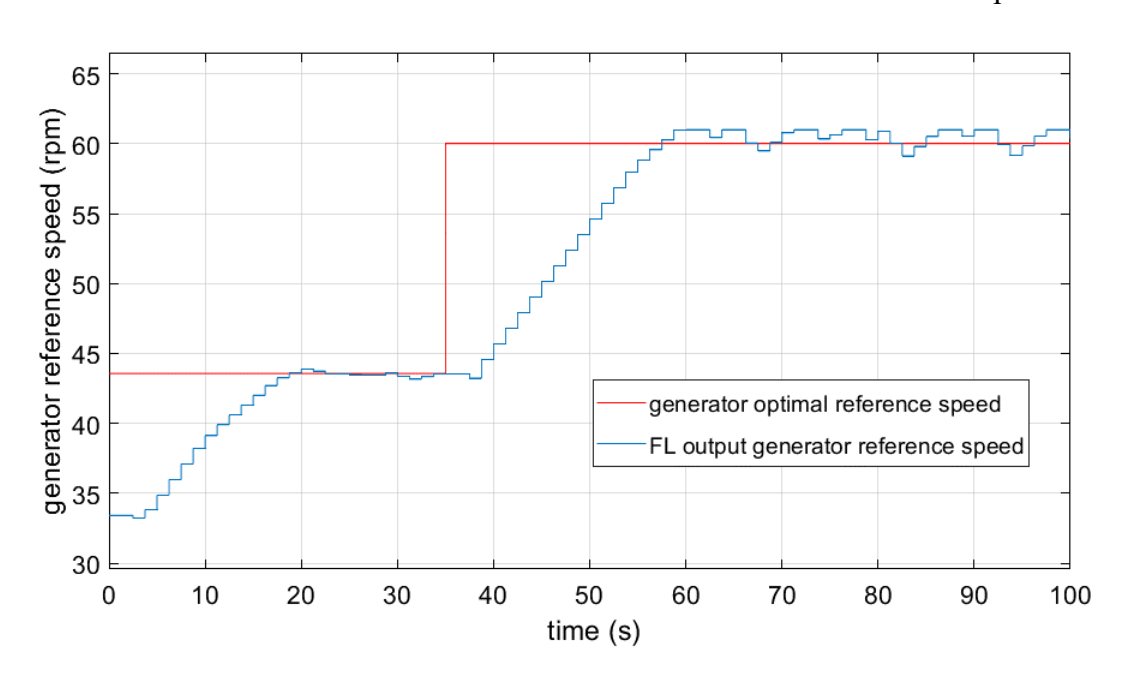


Figure 5.13 FL control generator output reference speed under step change tidal current velocity input

Figure 5.14 illustrates the turbine output power and generator output power of the TCT system under the step change tidal current input. In this figure, the tidal current turbine's mechanical output power has reached the theoretical calculated power, this means that the FL controls the tidal current turbine near to the MPP to capture maximum power under a given tidal current condition. The generator output power can follow the change of tidal current velocity and tidal current turbine output power, when the generator is operating under rated state, due to the losses in the power transformation and generator losses, the output electrical power of generator is less than the mechanical power provided by tidal current turbine. This is also similar to the P&O control performance in Chapter 4.

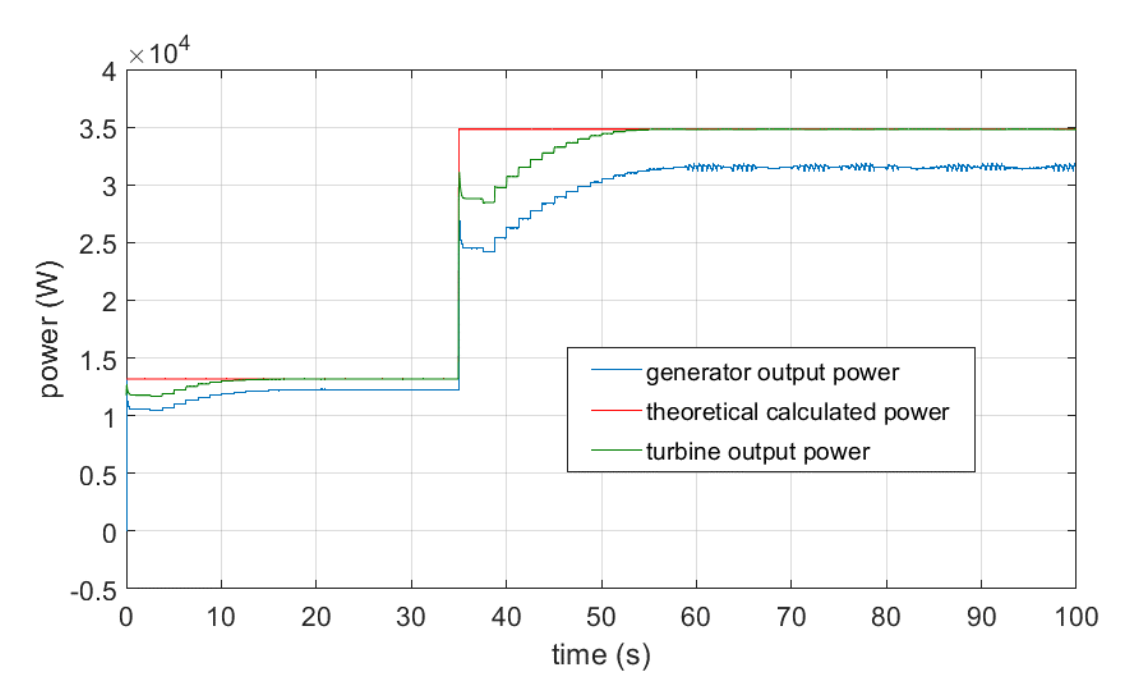


Figure 5.14 Turbine output power and generator output power under step change tidal current velocity input

Figure 5.15 shows the active and reactive power that are injected into the grid. In this figure, the active power follows the tidal current speed change and due to the power transmission loss and filter loss, the active power is lower than the generator output electrical power. The reactive power remains at zero for the whole simulation time. This means that the active and reactive power injected into the grid can be controlled by the grid side converter control strategy and that power captured by the tidal current turbine from the tidal current flow can be transferred to the grid efficiently.

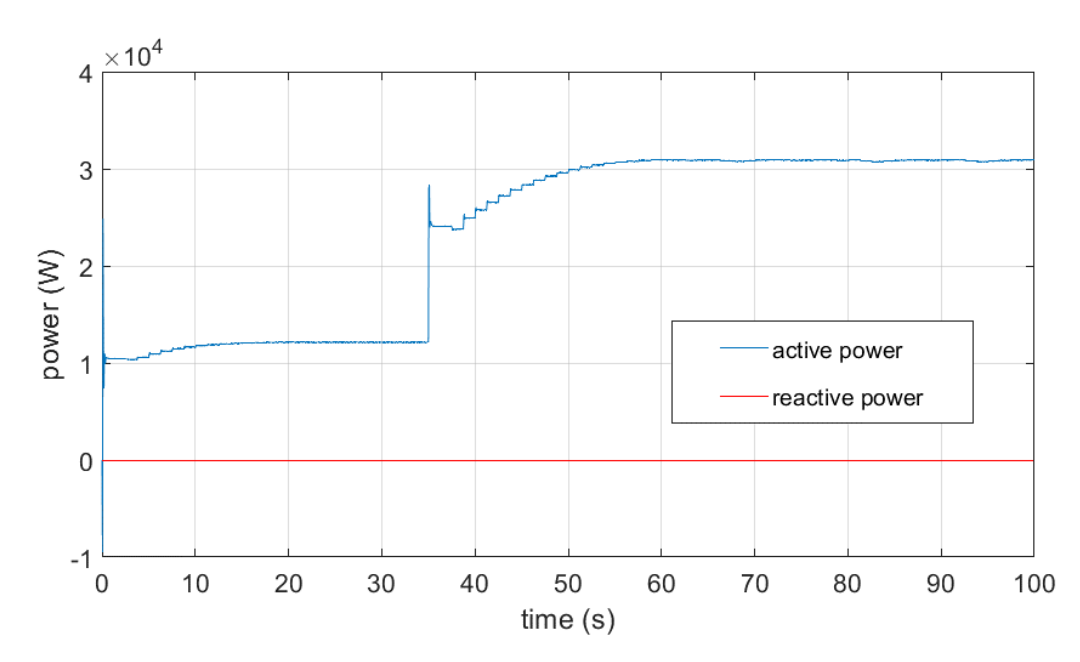


Figure 5.15 Active and reactive power under step change tidal current input

Figure 5.16 presents the generator reference speed of the FL MFs 3 control with 1.25s step time under the ramp change tidal current velocity input. The ramp change input is intended to test the FL control performance under continuously changing conditions. From Figure 5.16 it can be seen that before the ramp change starts, the control generator output reference speed is the same as it is in Figure 5.13. During the tidal current velocity ramp changing period, the FL control tracks the ramp change, but a little bit over the desired value with maximum 1.8% error. After the input becomes constant, the FL control output value varies around the optimal reference speed with small fluctuations (less than 0.3% error). From Figure 5.13 and Figure 5.16, it can be seen that the FL MFs 3 control is able to control the TCT generation system to track the MPP range to capture the maximum power from the tidal current flow under both step change and ramp change tidal current inputs without the tidal current speed sensor signal.

Figure 5.17 illustrates the tidal current turbine output mechanical power and generator output electrical power under ramp change tidal current input. Under ramp change input, the tidal current turbine can still provide mechanical output power that reaches the theoretical calculated maximum power, and again, due to losses in the system, the electrical output power is lower than the mechanical input power as expected.

Figure 5.18 shows the active and reactive power that are provided to the grid under the ramp change tidal current input. Similar to the step change input conditions, the active power is slightly lower than the generator electrical output power due to the losses, and the reactive power is maintained at zero, which means that the grid side converter control can control the power injected to the grid under the ramp change tidal current input.

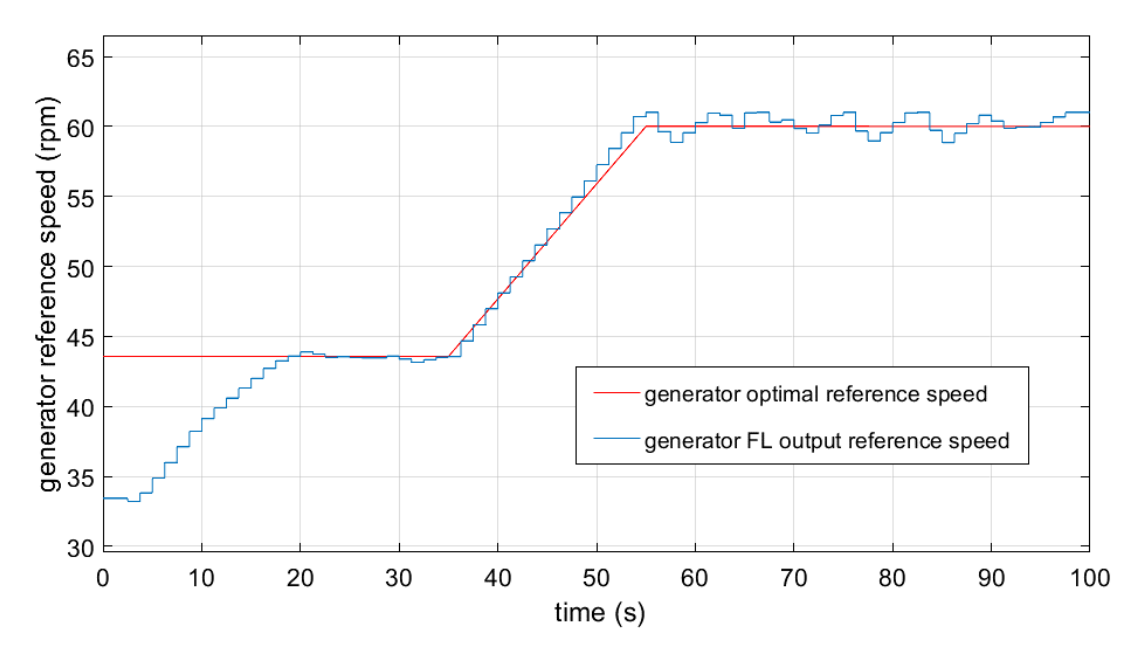


Figure 5.16 FL control generator output reference speed under ramp change tidal current velocity input

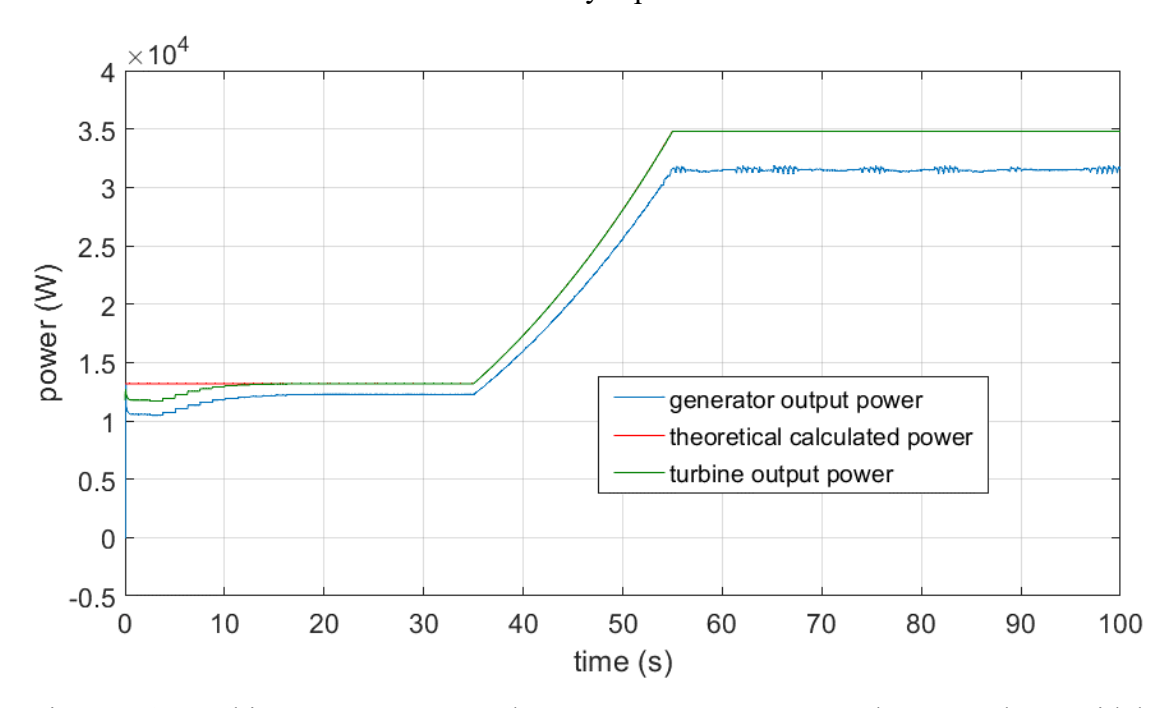


Figure 5.17 Turbine output power and generator output power under ramp change tidal current velocity input

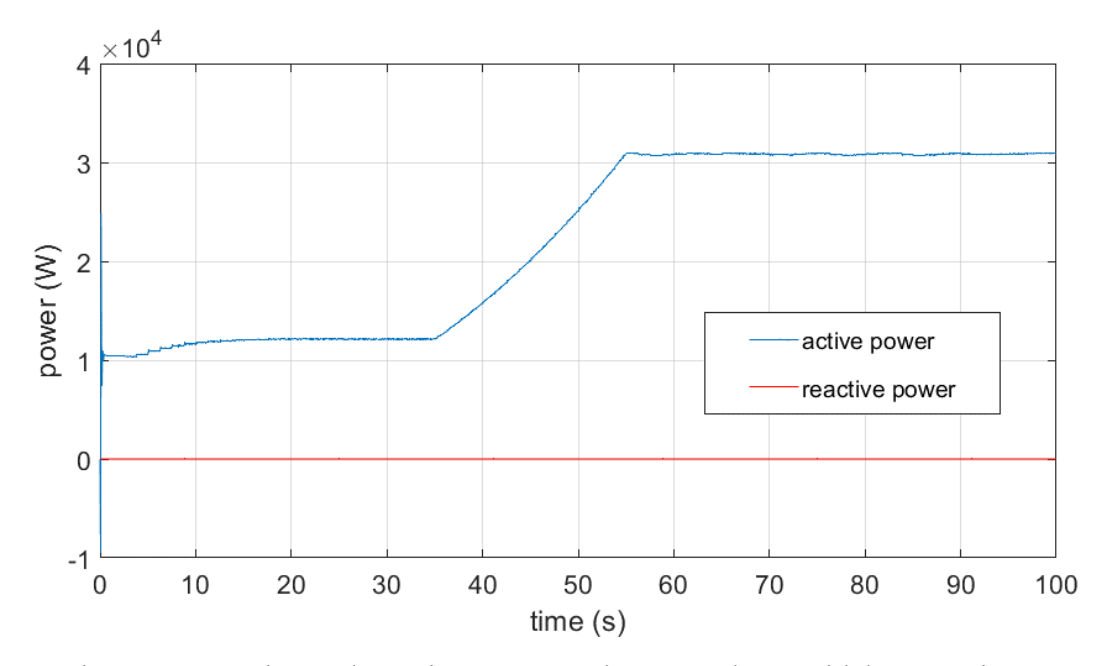


Figure 5.18 Active and reactive power under ramp change tidal current input

The results presented above have demonstrated that the FL control can adjust the tidal current turbine generation system to operate near the MPP range under both step change and ramp change tidal current inputs. The control output generator reference speed can track the optimal value and varies around it with a small error. The output power of the tidal current turbine and generator can reach the rated value with about 90% efficiency. The next section is going to compare the performance of P&O control and FL control in TCT system under the same conditions.

5.5 Comparison of P&O and FL control for the Conventional TCT Model

This section will compare the performance of P&O control and FL control applications in the same grid-connected TCT model. The comparison will be made under the same conditions, with the same tidal current turbine, generator, control step time, step change and ramp change tidal current velocity inputs. The average power efficiency, instantaneous power efficiency, generator reference speed, generator output power, and active and reactive power will be compared and discussed.

Table 5.4 shows the P&O control and FL control average efficiency values in the conventional grid-connected model with the same input conditions under both step change and ramp change tidal current inputs. For the selected parameters, the P&O control had slightly higher average efficiencies than the FL control.

	Step input	Ramp input		
P&O control	88.85%	90.78%		
FL control	87.98%	90.62%		

Table 5.4 Average power efficiency of P&O control and FL control

5.5.1 Under step change tidal current velocity input

Figure 5.19 illustrates the generator output reference speed of P&O control and FL control under step change tidal current velocity input with the same control step time (1.25s). In this figure it can be seen that initially P&O control output has a quicker response than FL control, but FL reaches the optimal value first, about 7s early than P&O control. After reaching the optimal value, both P&O control can FL control provide an output that varies around the optimal value with maximum error of less than 0.1%, and the fluctuations of FL control are slightly smaller than for P&O control during this period. When the tidal current velocity input starts the step change, the response of P&O control is still quicker than FL control and this time P&O control reaches the optimal value first while FL control is about 2s later. During the steady state after the tidal current input changed, both P&O control and FL control output values vary around the optimal generator reference speed with less than 0.2% error, and again the FL control has smaller fluctuations than P&O control.

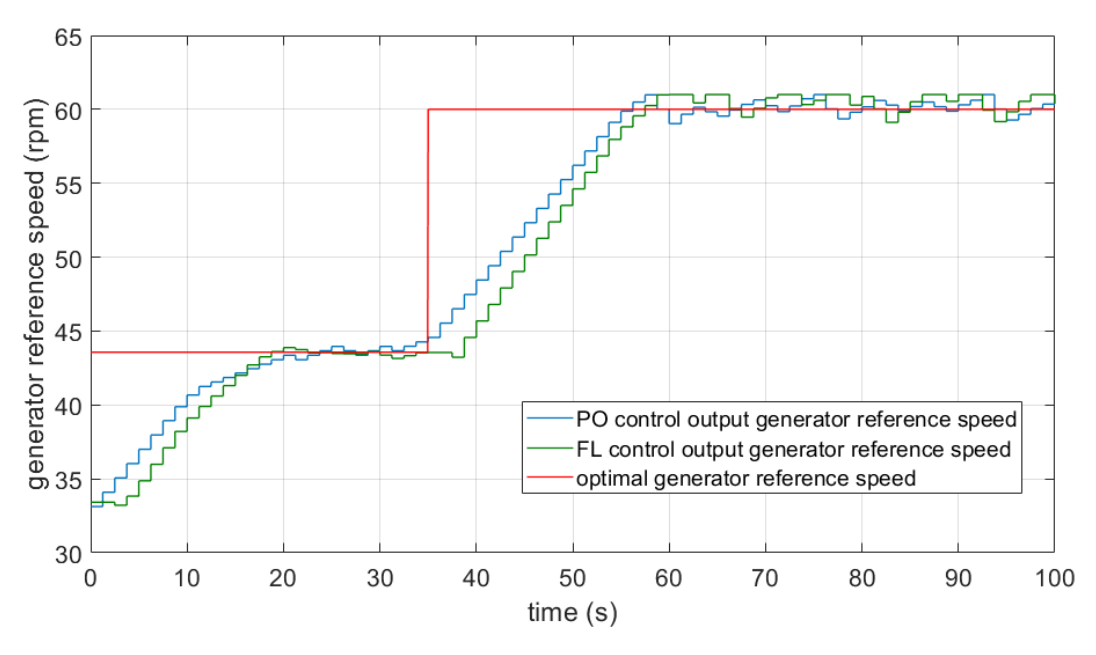


Figure 5.19 Generator reference speed of P&O control and FL control under step change tidal current input

Figure 5.20 presents the instantaneous power efficiency of P&O control and FL control under the step change tidal current input. It can be seen that from 0s to 17s and from 35s to 58s, the instantaneous power efficiency of P&O control is slightly higher than FL control. This is because, as shown in Figure 5.19, during these two periods the P&O control output is closer to the optimal value than FL control. During the steady state before the tidal current input changes, P&O control and FL control have the same efficiency, and after the input changes, the fluctuation of P&O control is larger than FL control but by a very small amount. This is because the P&O control output generator reference speed is bigger than that from the FL control in this period.

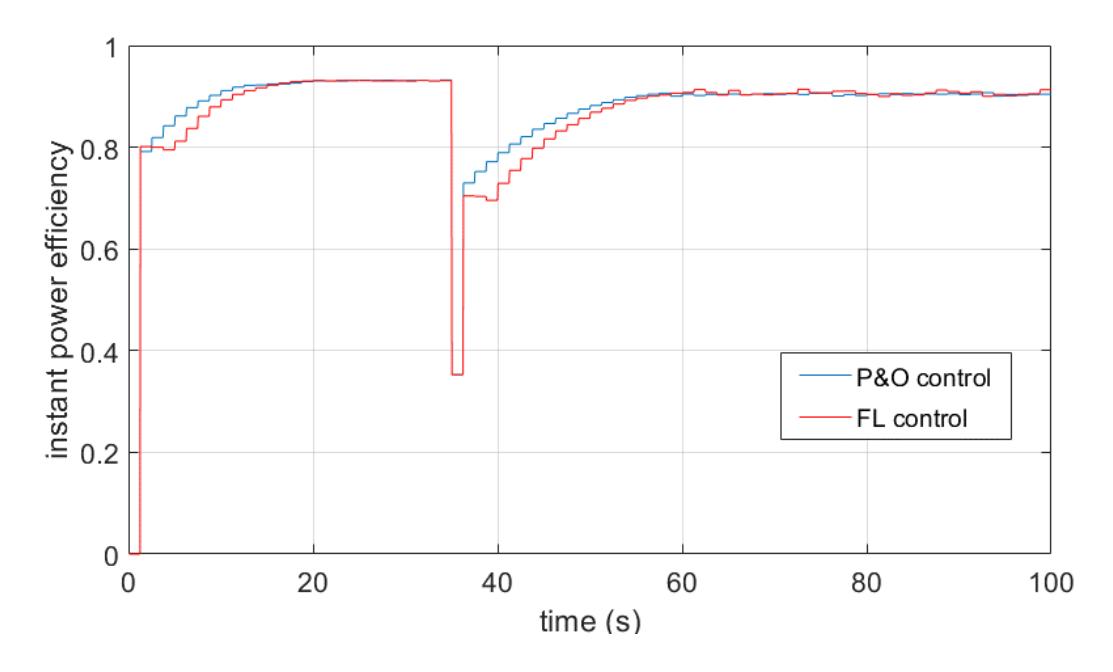


Figure 5.20 Instantaneous power efficiency of P&O and FL control under step change tidal current input

Figure 5.21 shows the generator output power of P&O control and FL control under step change tidal current velocity input. From 0s to 17s and 35s to 58s the P&O control has a slightly higher generator output power than FL, due to the higher speed it has during these periods. When the system enters the steady state, the generator output power is almost the same, even though the control generator reference speed output of P&O control and FL are different, and P&O control has bigger fluctuations than FL, these will not affect the generator power generation significantly.

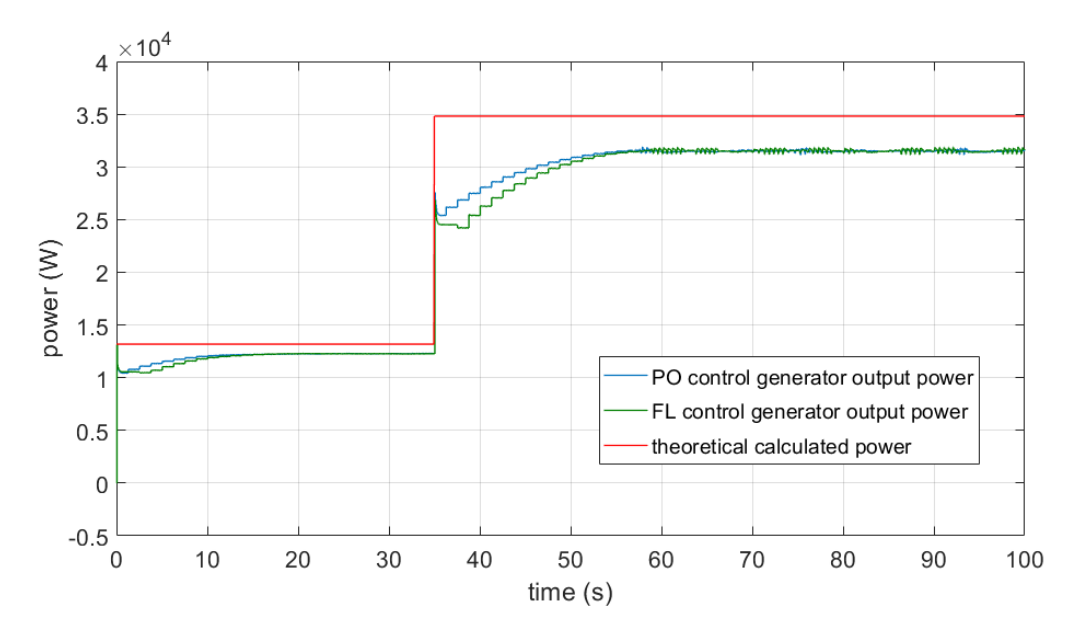


Figure 5.21 Generator output power of P&O control and FL control under step change tidal current velocity input

Figure 5.22 illustrates the active power that is transferred to the grid with P&O control and FL control. The active power curves in Figure 5.22 are similar to the generator output power in Figure 5.21. From 0s to 17s and 35s to 58s the P&O control has slightly higher power than FL control, and during the steady state, the active powers that are injected to the grid are the same, but due to the power transformation loss, the active power is lower than the generator output power in Figure 5.21.

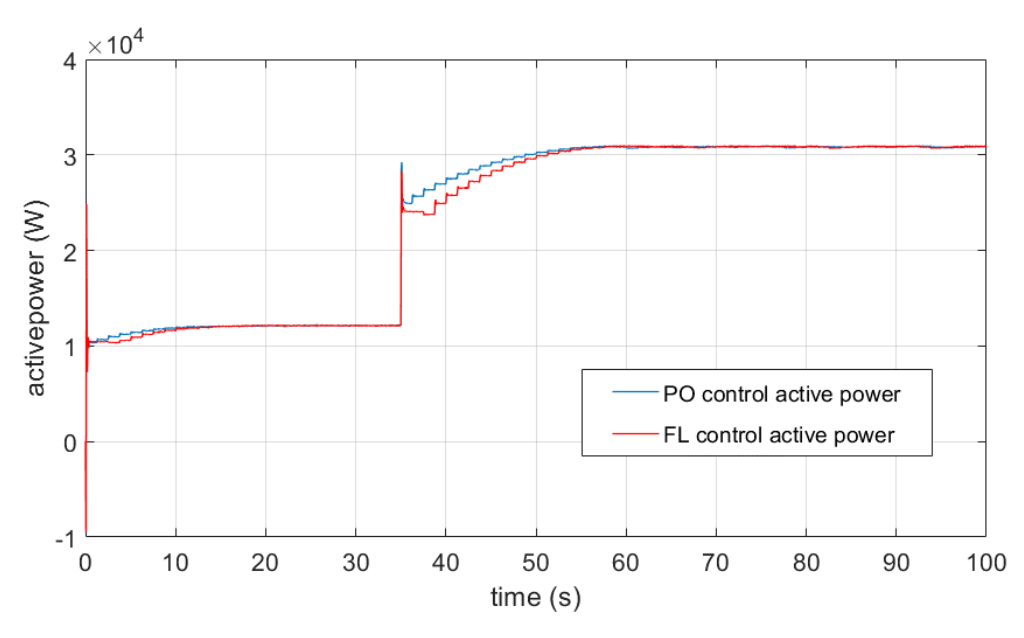


Figure 5.22 Active power of P&O control and FL control under step change tidal current input

5.5.2 Under ramp change tidal current velocity input

Figure 5.23 presents the control output generator reference speed of P&O control and FL control under ramp change tidal current velocity input. It can be seen from this figure that before the tidal current change happens (0s to 35s), the output reference speeds of the two control strategies are the same as it in Figure 5.19. From 35s, the tidal current velocity starts the ramp change and during the ramp changing period (35s to 55s), P&O control and FL can provide generator reference speeds that follow the optimal value and vary around it with a maximum error less of than 0.3%. The tracking speeds of the two control methods are almost the same and they reached the steady state at the same time. When the tidal current velocity becomes constant after the ramp change, the output reference speed of the P&O and FL control can maintain the optimal value with less than 1.8% error fluctuations. During this period, it can be seen that the fluctuations of P&O control and FL control are almost the same.

Figure 5.24 shows the instantaneous power efficiency of P&O control and FL control under ramp change input and that the efficiencies before the ramp change are the same as in Figure 5.20. During the ramp changing period and in the steady state after the ramp change, the instantaneous power efficiency of P&O control and FL control are almost the same, as the output reference speeds of the two control strategies are very close to each other in Figure 5.23.

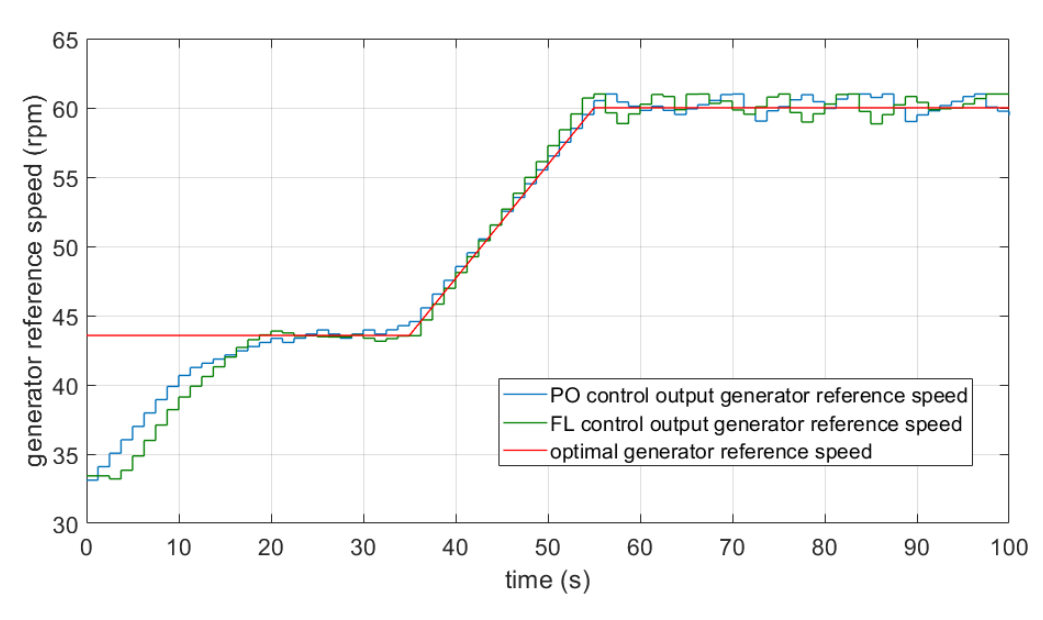


Figure 5.23 Generator reference speed of P&O control and FL control under ramp change tidal current input

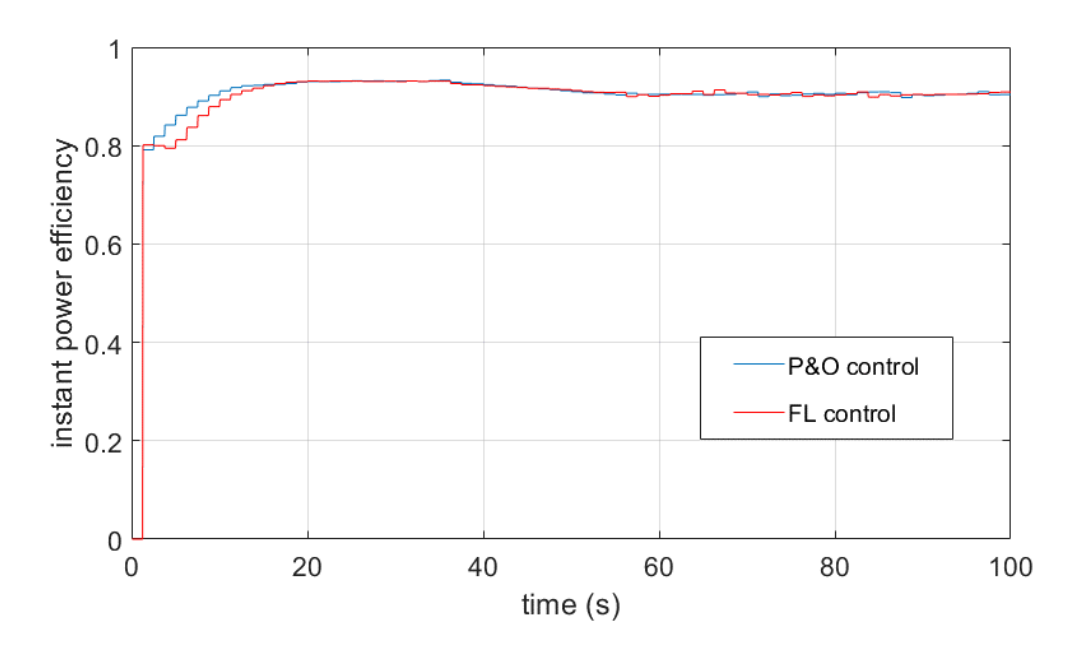


Figure 5.24 Instantaneous power efficiency of P&O and FL control under ramp change tidal current input

Figure 5.25 illustrates the generator output power of P&O and FL control under the ramp change tidal current input. From this figure it can be seen that before 35s the powers in Figure 5.25 are the same as those in Figure 5.21, and during the ramp changing period and the steady state period after 55s, the generator output power of P&O control and FL control can be considered to be the same. This is because there are no significant differences between the control output reference speeds, and this will lead to the generator output powers being almost the same, as well as the instantaneous power efficiency in Figure 5.24.

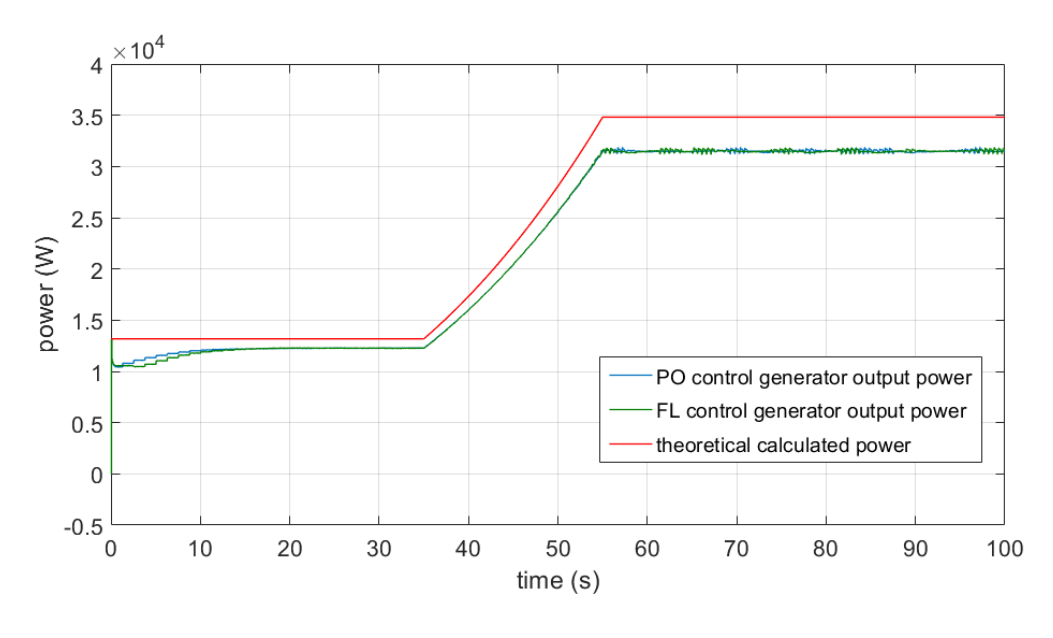


Figure 5.25 Generator output power of P&O control and FL control under ramp change tidal current velocity input

Figure 5.26 shows the active power that is injected into the grid for the P&O control and FL control with the ramp change input. In this figure, before 35s when the ramp change starts, the active power is the same as in Figure 5.22. From 35s to 55s during the ramping period, the active powers are following the ramp change, and when entering the steady state from 55s, the active power of P&O control and FL control are almost the same, as during this period, the generator output power in Figure 5.25 can be seen as the same. Due to the power transmission losses, the active power is lower than then generator output power in Figure 5.25.

From the figures in this section and those in section 5.4.2, it can be seen that the fluctuations of P&O control and FL control output generator reference speed will not greatly affect the generator output power and grid active power. Small fluctuations around the optimal value, which are less than 0.2%, will not cause significant generator output power changes or grid active power changes. Thus, when the P&O control and FL control track the optimal value with minor fluctuations, the system can be considered as operating steadily. But the control step size for P&O control, MFs value for FL control and step time for both control algorithms will affect the control performance. The system can tolerate minor fluctuations, but large or high frequency fluctuations will affect the system stability, as discussed in section 5.3.1 and Chapter 4. The similar performances between P&O control and FL control during the steady state mean there are no significant differences in the final control performance, but from Figure 5.19 it can be seen that P&O has relatively larger fluctuations than FL control during the steady state. This leads to slightly bigger fluctuations in Figure 5.20, but again, no significant differences are caused in generator power and active power.

Even though the performances of the two control strategies are very close to each other in Section 5.4, there are still differences between them that are caused by the control output reference speed, as the P&O control in this section has a slightly quicker transient response to step changes. This leads to the efficiency of P&O control being higher than FL control during these periods and is the reason why in Table 5.4 P&O control has 0.87% higher average efficiency than FL control under the step change input, while under the ramp change input, it is only 0.16% higher. This is because the tracking speeds of P&O control and FL control are almost the same, and the fluctuations during steady state are close, so there is no major error difference between the two.

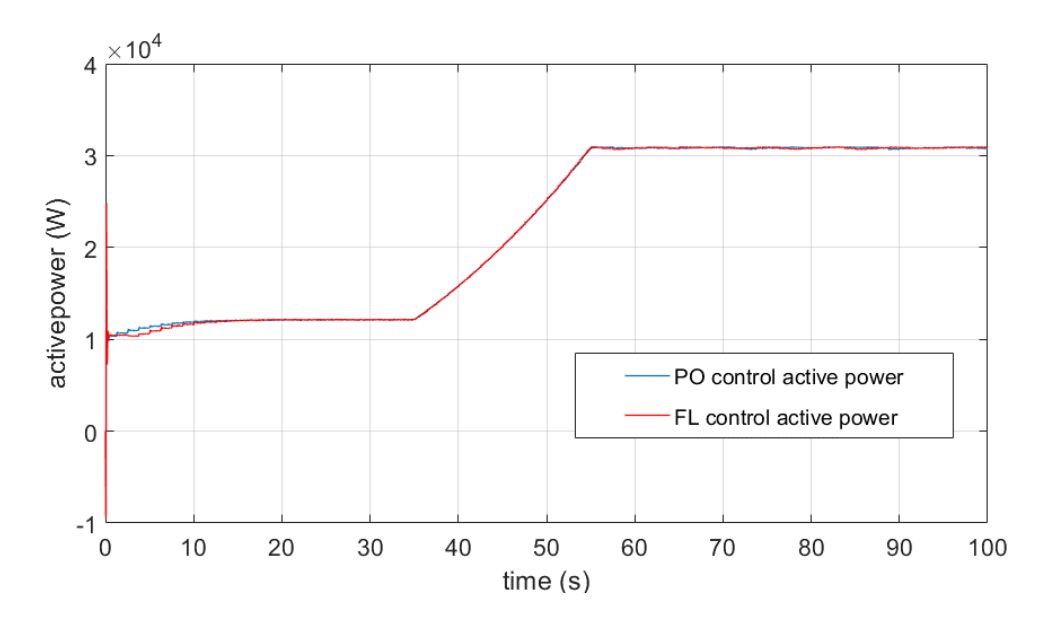


Figure 5.26 Active power of P&O control and FL control under step change tidal current input

5.5 Summary

This chapter presented the FL control application in a conventional grid-connected tidal current turbine generation system, which was developed in Chapter 4, illustrating the basic theory of FL control and the FL control design in the TCT control system. The results showed the effects on system performance of different MFs and step times of FL control in the conventional TCT model, and also that the FL control can provide the generator reference speed signal for the TCT system without a tidal current speed sensor and can regulate the system to operate close to the MPP under both step change and ramp change tidal current velocity inputs.

A comparison of P&O control and FL control is also presented in this chapter. Average power efficiency, instantaneous power efficiency, generator reference speed, generator output power and active powers have been compared to show the differences of the performance between P&O control and FL control. The comparison of results showed that the P&O control has a slightly higher average power efficiency than the FL control under a step change input, as the response of P&O control is about 2s quicker than FL control, but the FL control has higher tracking speed and smaller fluctuations. For the ramp change, during the tidal current changing period and steady state, P&O control and FL control have almost the same performance. Also, the small differences between P&O control and FL control performance will not lead to big differences in turbine output power, generator output power and active power injected into grid.

In conclusion, for test purposes in Chapter 4 and Chapter 5, P&O control and FL control can both provide efficient generator reference speed which varies around the optimal value with minor fluctuations, with the condition that there is no tidal current velocity signal provided, and the performance of two control strategies under step change and ramp change tidal current velocity input are similar to each other. The P&O control has slightly quicker response while FL control has smaller fluctuations during steady state. Another important condition mentioned in Chapter 4 is that the P&O control will face the speed drift problem sometimes due to the algorithm itself, but this problem did not occur with FL control.

Chapters 4 and 5 have demonstrated the potential of P&O control and FL control to be applied in TCT system without a tidal current velocity sensor. The TCT system with P&O control and FL control under real tidal current cycles also need to be evaluated, and the next chapter presents the simulation of the conventional TCT system with P&O and FL control under real tidal current velocity input. The results including control output generator reference speed, turbine and generator power will be presented and discussed, as well as the control performance comparison.

Chapter 6. Long term simulation test based on P&O and Fuzzy

Logic control strategies

Chapters 4 and 5 presented the P&O and Fuzzy Logic control under both step change and ramp change inputs to test their feasibility and their performance. The results have shown that under sudden and continuous change conditions, both of the control strategies have the ability to track the MPP without tidal current velocity information. In order to test the P&O and FL control performance in the tidal current turbine generation system in greater depth, this chapter presents details of a longer-term simulation model, using tidal current velocity data from the Pentland Firth, for which the results will be illustrated and discussed. From this chapter, for the applications of P&O and FL control strategies in a tidal current turbine system to deal with the loss of tidal current velocity, more intuitive conclusions will be drawn.

6.1 Model adjustments and tidal current velocity data

The model structure used in Chapters 4 and 5 is complex and the model sample times are very short. This brings challenges to the computer performance as when running the model, it will take a lot of time to finish, and the resulting data are too large to store on the disk. Under this situation, given the aim to investigate the control strategies' performance with long term input, it is necessary to modify the model to enable it to run for a long time.

6.1.1 Model adjustments

Generally, in MATLAB/SIMULINK, an aim to increase the simulation time requires an increase in the sample time but it cannot be too big, otherwise the results will become inaccurate or the model will not converge. The models developed in Chapter 3 and used in Chapters 4 and 5 are detailed models with very small sample time, in order to get accurate results to analyse P&O and FL control strategy performances in a tidal current turbine system. From Chapters 4 and 5, the results and discussions have proved that P&O control and FL control are able to provide a generator reference for the turbine and generator to track the maximum power point under the situation that there is no signal from tidal current velocity sensors. However, with the aim to consider the performance of P&O and FL control with long term real tidal current velocity input, this chapter investigates how to simplify the model and increase the sample time as well.

The P&O and FL control strategies are applied to provide the generator reference speed

through the power change on the generator side, thus the generator side converter control cannot be simplified, and in this chapter it is the grid side convertor that is simplified from a detailed model to an average model, which can reduce the time that is spent on switching calculations at very small sample time.

The detailed model of the grid side convertor is a three-phase three-level voltage source converter in which the grid side convertor control system has three control loops: one regulates the DC link voltage to the desired value, and the other two control loops regulate daxis and q-axis currents, the active and reactive current components. The reference value of daxis current is the output of the DC link voltage control loop, while the q-axis current reference is set to zero to maintain unity power factor.

For the simplified average model, the grid side voltage source converter is represented by equivalent voltage sources, which can generate AC voltage averaged over one cycle of the switch frequency. The model that uses equivalent voltage sources does not capture harmonics, but it maintains the dynamics that arise from the interaction between the control system and the power system. This will allow use of a larger sample time than the three-level voltage source converter model [169].

In the average model, the control of DC link voltage will be the same as it in the detailed model, the control loop of d-axis current and q-axis current in average model then can be expressed by:

$$v_{di} = v_{dg} + i_{dg} * (R_{LI} + R_{II}) - i_{qg} * (L_{LI} + L_{II}) + (k_1 + \frac{k_2}{S}) \Delta i_{dg}$$
 Equation 6.1

$$v_{qi} = v_{qg} + i_{dg} * (L_{LI} + L_{II}) + i_{qg} * (R_{LI} + R_{II}) + (k_1 + \frac{k_2}{S}) \Delta i_{dg}$$
 Equation 6.2

where R_{LI} and L_{LI} are the transformer leakage impedance, R_{II} and L_{II} are the inductor impedance, $\left(k_1 + \frac{k_2}{S}\right)$ is the transfer function of the PI controller, and the block diagram of the control loop is illustrated in Figure 6.1.

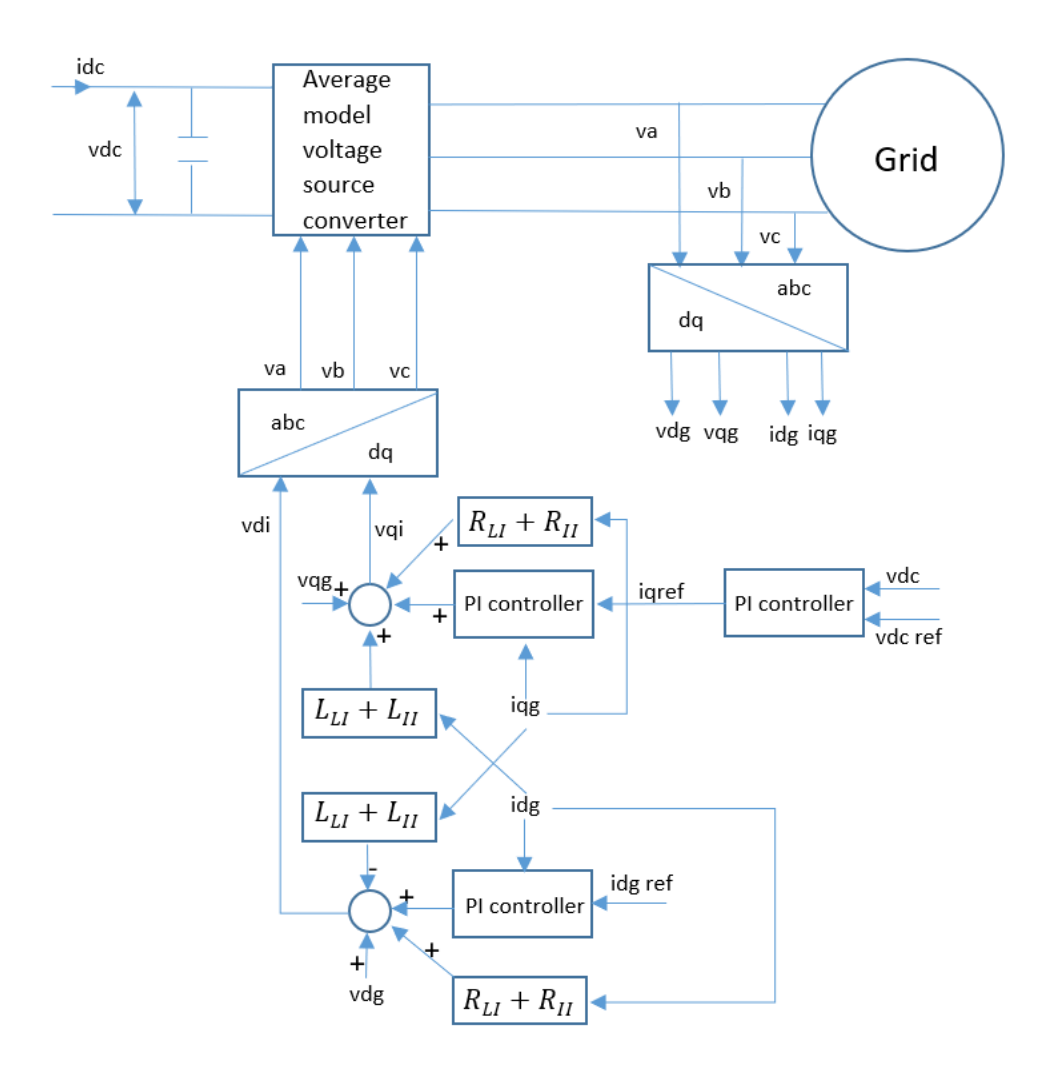


Figure 6.1 Block diagram of average model voltage source converter control

6.1.2 P&O control detailed model and average model comparison

Since the model was simplified from a detailed model to an average model, the validation of the average model needs to be investigated. This section will present P&O control and FL control with both the detailed model and the average model under the same conditions, compare the generator output reference speed and active power.

Figure 6.2 shows the P&O control generator output reference speed with detailed and average models under step change input. From this figure it can be seen that P&O control can track the maximum value and varies around it in both models. The differences between detailed and average models are small with maximum 3% error. Figure 6.3 illustrates the active power of P&O control in detailed and average models under step change input. In this figure, the average model active power is a little bit lower than the detailed model initially but after the step change, it becomes a little bit higher.

Figure 6.4 shows the differences in active power of P&O control with detailed and average models. It can be seen that the difference is less than 1kW (3%) during steady state. Figure 6.2 to Figure 6.4 proved that under step change tidal current input, P&O control can be applied in both detailed and average models, and the differences in the P&O control output values and active power are acceptable.

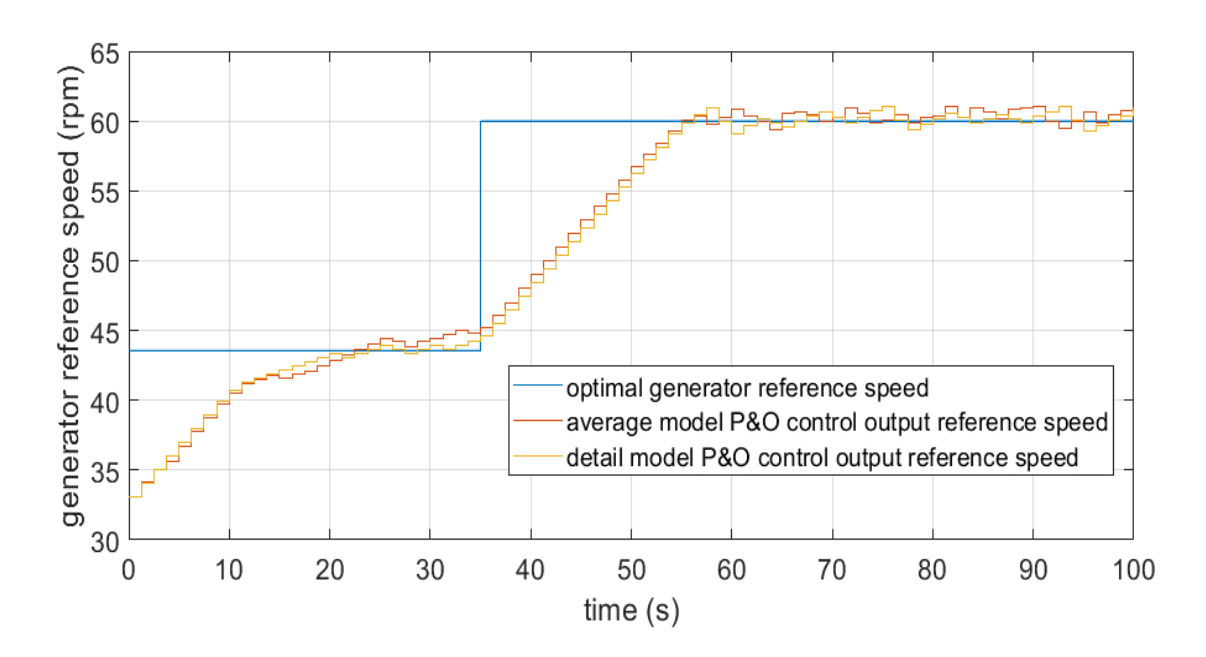


Figure 6.2 P&O control speed with detailed and average models under step input

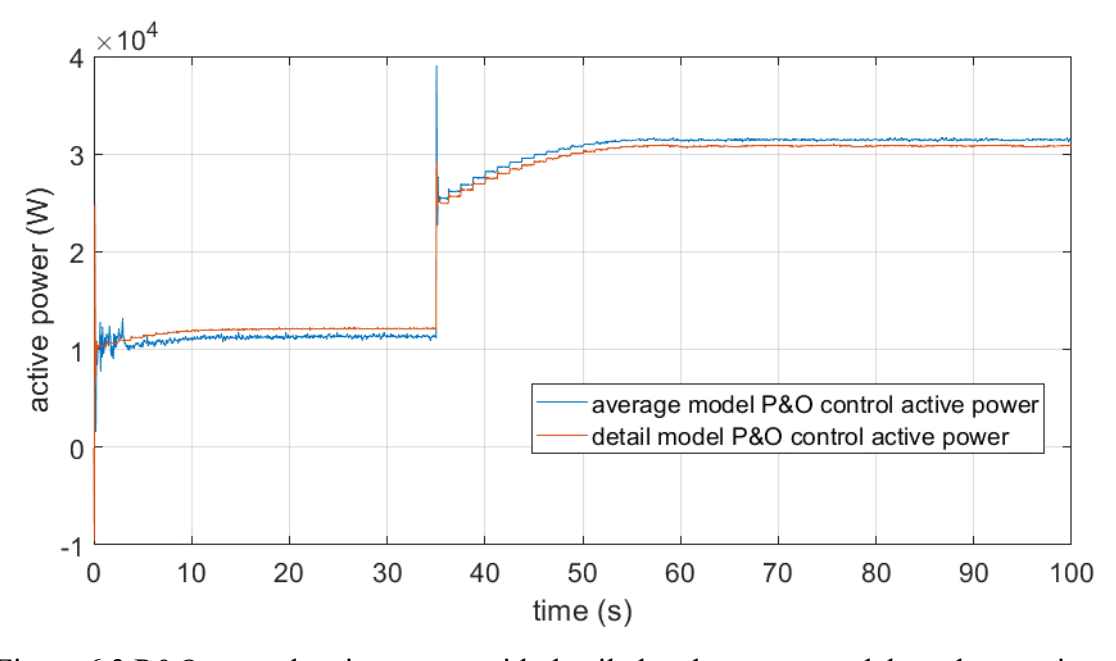


Figure 6.3 P&O control active power with detailed and average models under step input

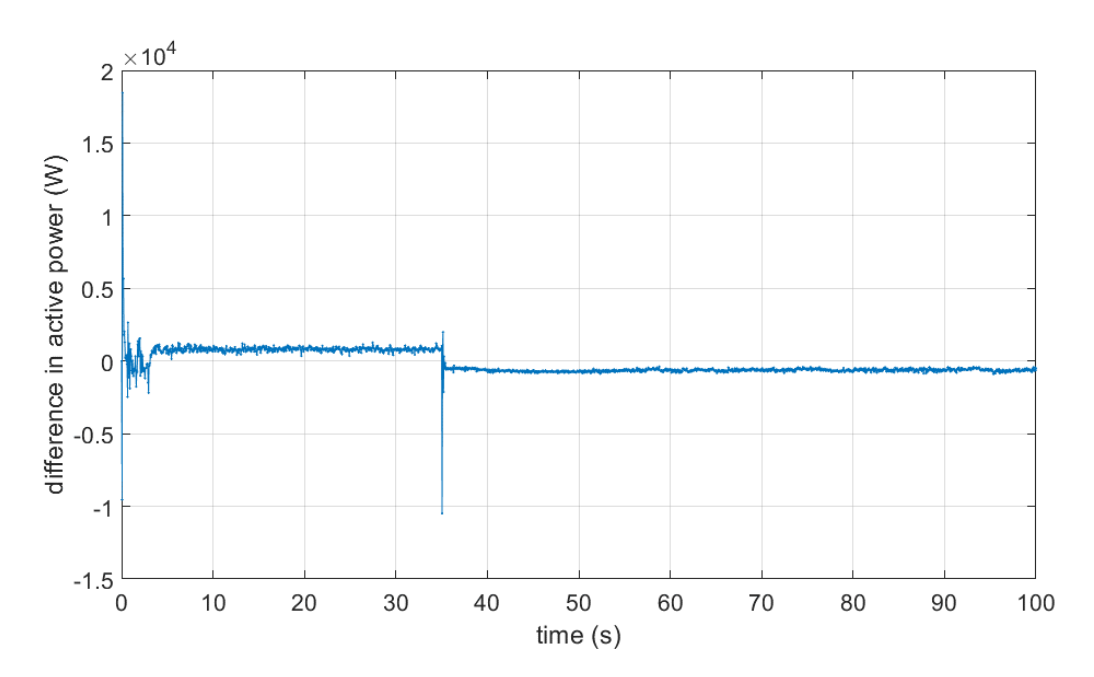


Figure 6.4 Differences in active power of P&O control under step input

Figure 6.5 illustrates the P&O control output generator reference speed under ramp change input. Similar to the step change figure, under ramp change, P&O in the average model can also track the maximum power points and varies around it during steady state with a maximum error of 3%. The active power of P&O control of the detailed and average models under ramp change input is presented in Figure 6.6. Again, the active power of the average model is slightly lower before the ramp change and then higher during steady state after the ramp change.

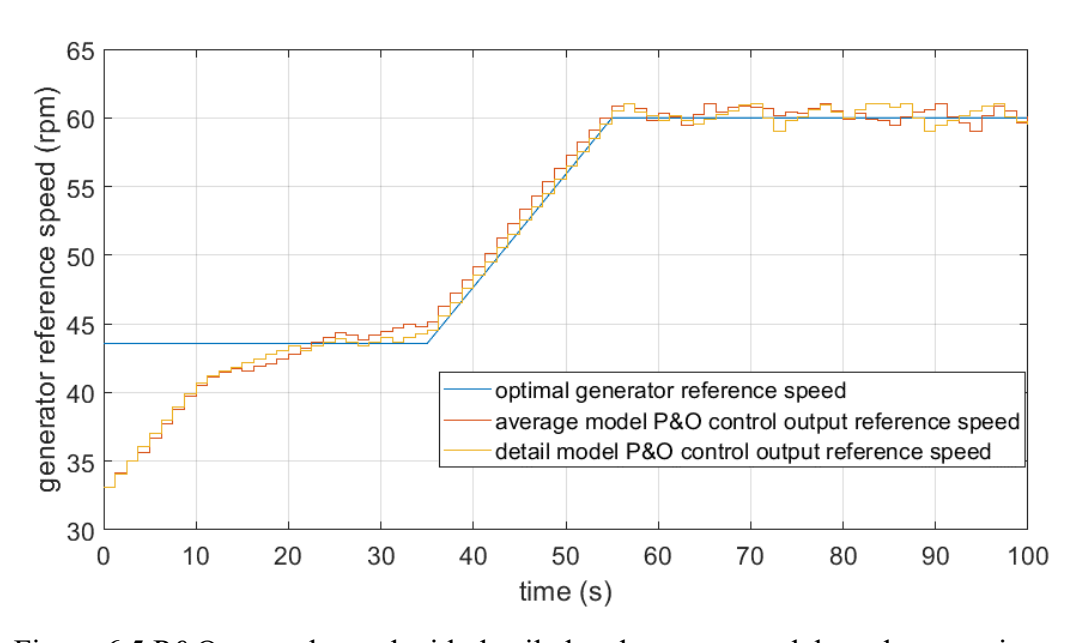


Figure 6.5 P&O control speed with detailed and average models under ramp input

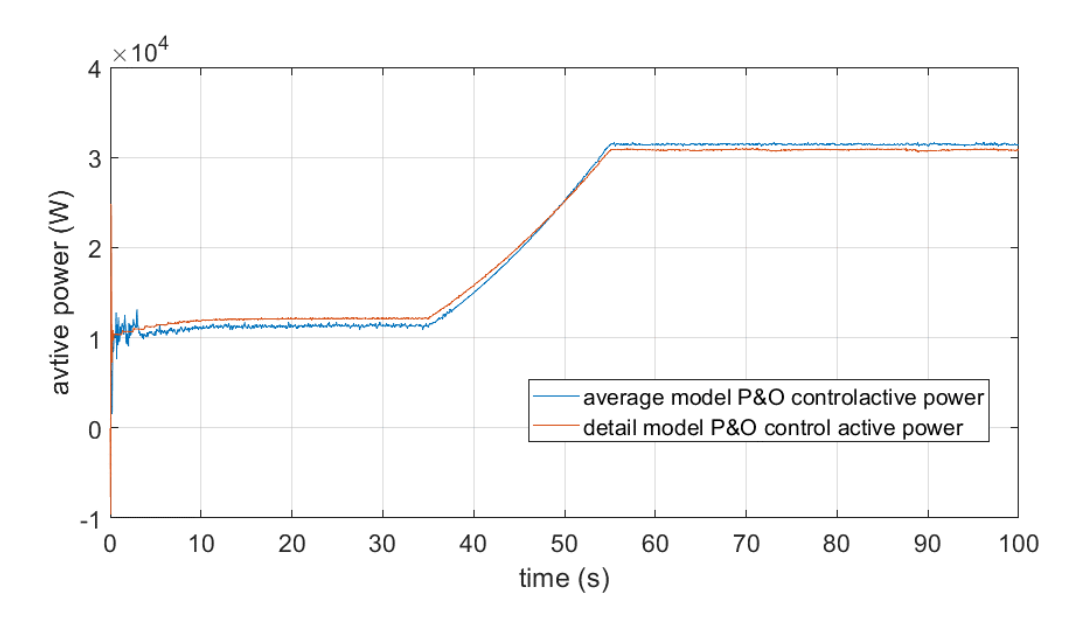


Figure 6.6 P&O control active power with detailed and average models under ramp input Figure 6.7 shows the differences in active power of the two models with P&O control under ramp change tidal input. In this figure, it can be seen that the differences between the average and detailed model are less than 1kW.

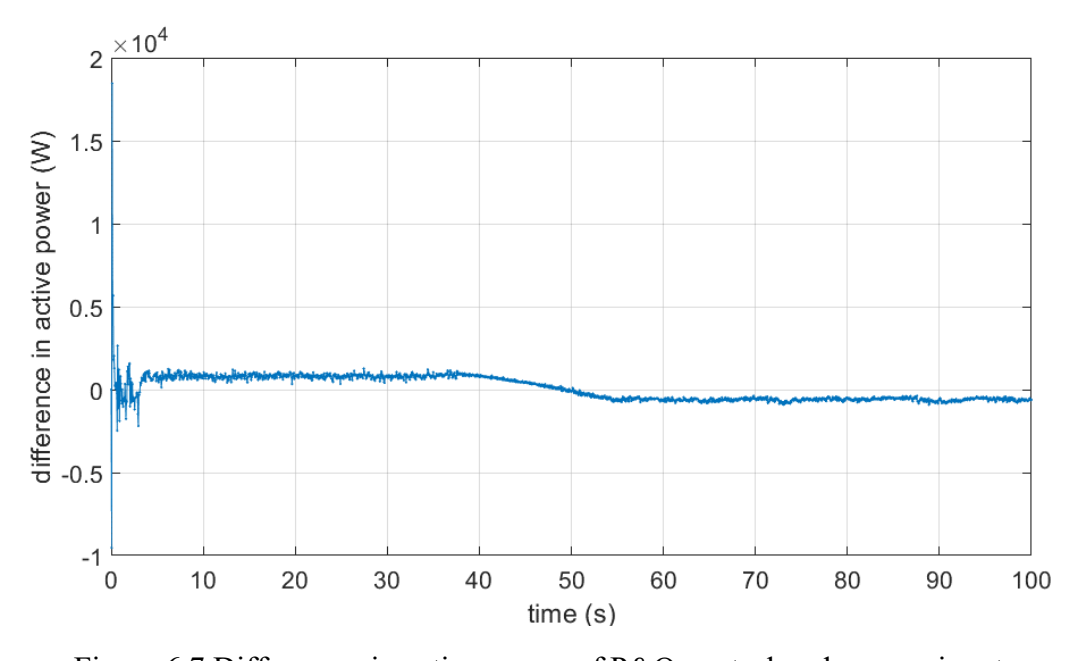


Figure 6.7 Differences in active power of P&O control under ramp input

From Figure 6.2 to Figure 6.7, it can be seen that for P&O control, the average model and detailed model have similar performance under both step change and ramp change tidal current input, and that the average model can therefore be used for the long-term simulation to test the P&O control performance.

6.1.3 FL control detailed model and average model comparison

The P&O control with the average model was validated in the previous section. This section is going to validate the FL control with the average model. Figure 6.8 shows the FL control with detailed and average models under step change tidal current input. It can be seen that FL control for the average model can track the optimal generator reference speed and varies around it during steady state, with the performance being similar to the detailed model, with maximum 3% error.

Figure 6.9 illustrates the active power of FL control. The active power of the average model is lower before the step change and higher after the step change, while Figure 6.10 shows the difference in active power of the average and detailed models with FL control. In this figure, it can be seen that the difference between the average and detailed models with FL control is less than 1.2kW.

From Figure 6.8 to Figure 6.10, the results proves that FL control with the average model has similar performance compared to FL control with the detailed model under step change tidal current input, which means that with average model under step change, FL control can be applied to track the maximum power points.

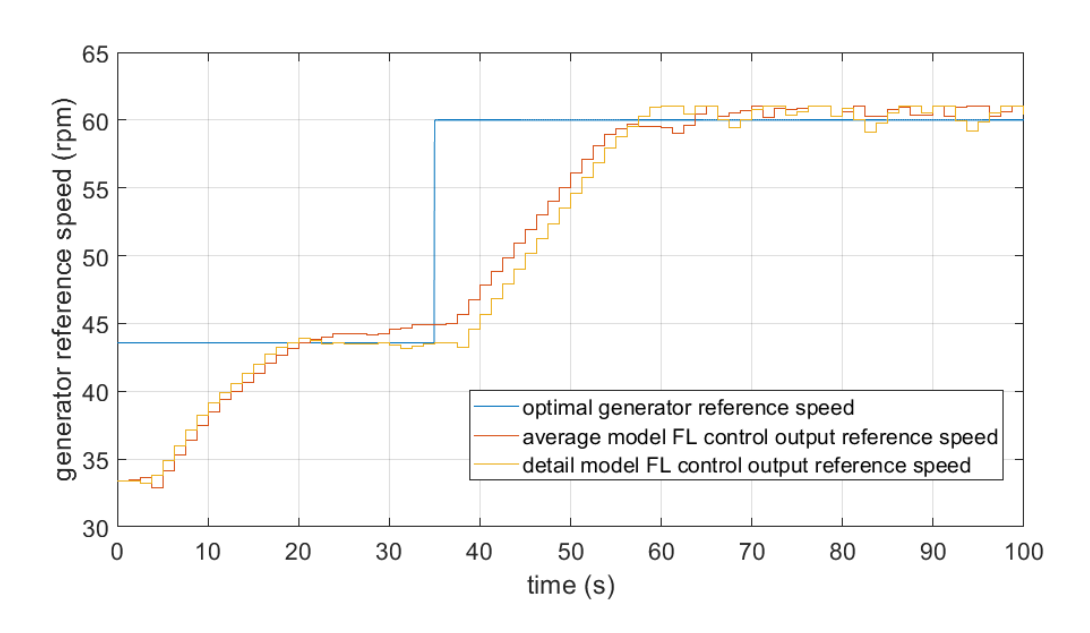


Figure 6.8 FL control speed with detailed and average models under step input

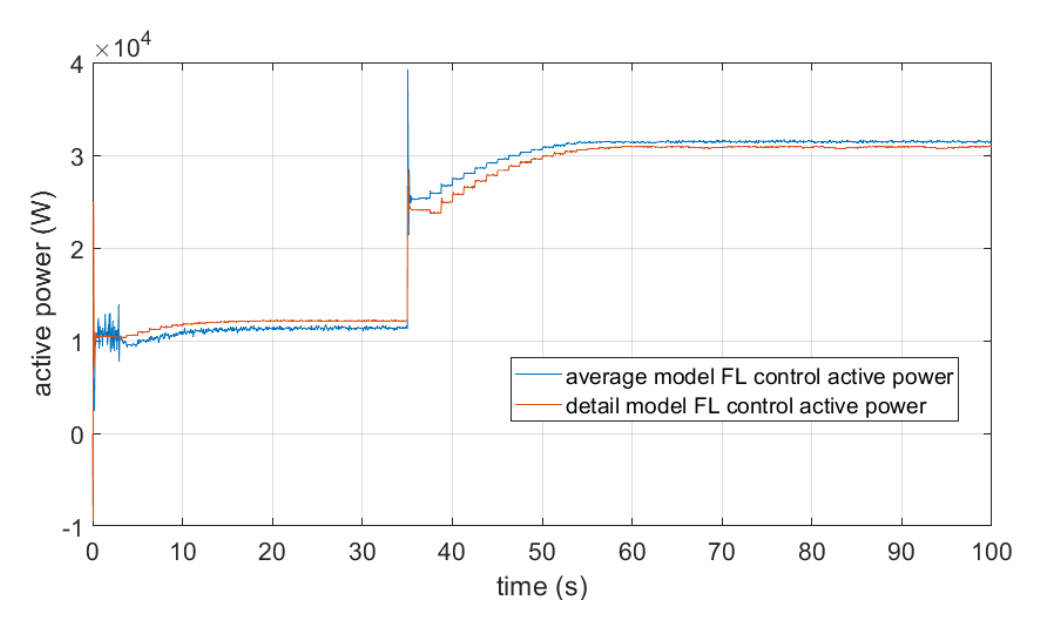


Figure 6.9 FL control active power with detailed and average models under step input

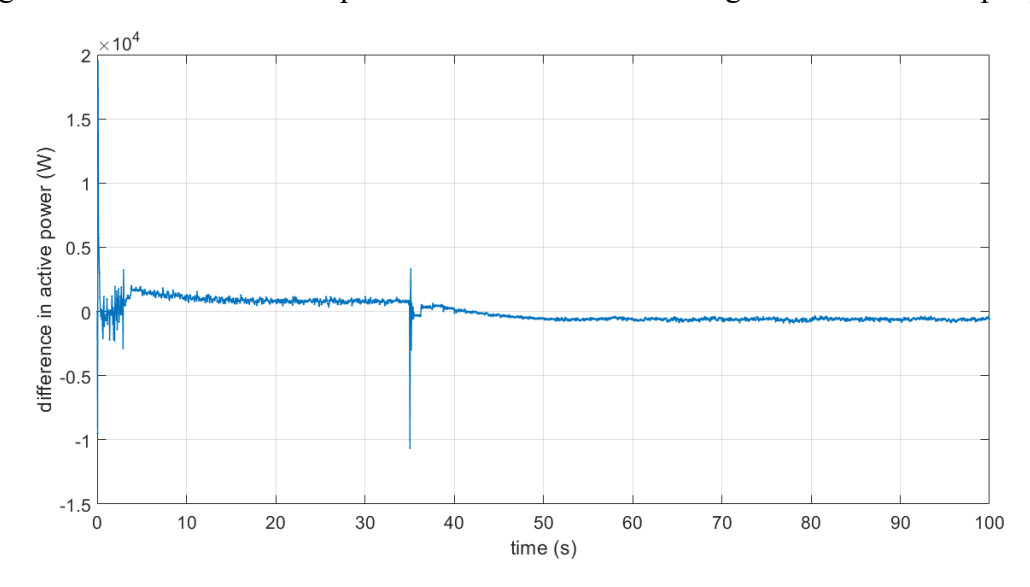


Figure 6.10 Differences in active power of FL control under step input

The performance of FL control with the average model under ramp change input are presented in Figure 6.11 to Figure 6.13. Figure 6.11 shows the FL control output generator reference speed of the average and detailed models under ramp change input. It can be seen from this figure that FL control in the average model can provide the reference speed that can track the maximum power points, fluctuating near it when the system enters the steady state, and that the difference between the average and detailed models is small at a maximum of 3%.

Figure 6.12 illustrates the active power of FL control with the two models under ramp change input. Similar to the step change input, the active power of the average model is slightly lower than that of the detailed model before the change and higher after the change.

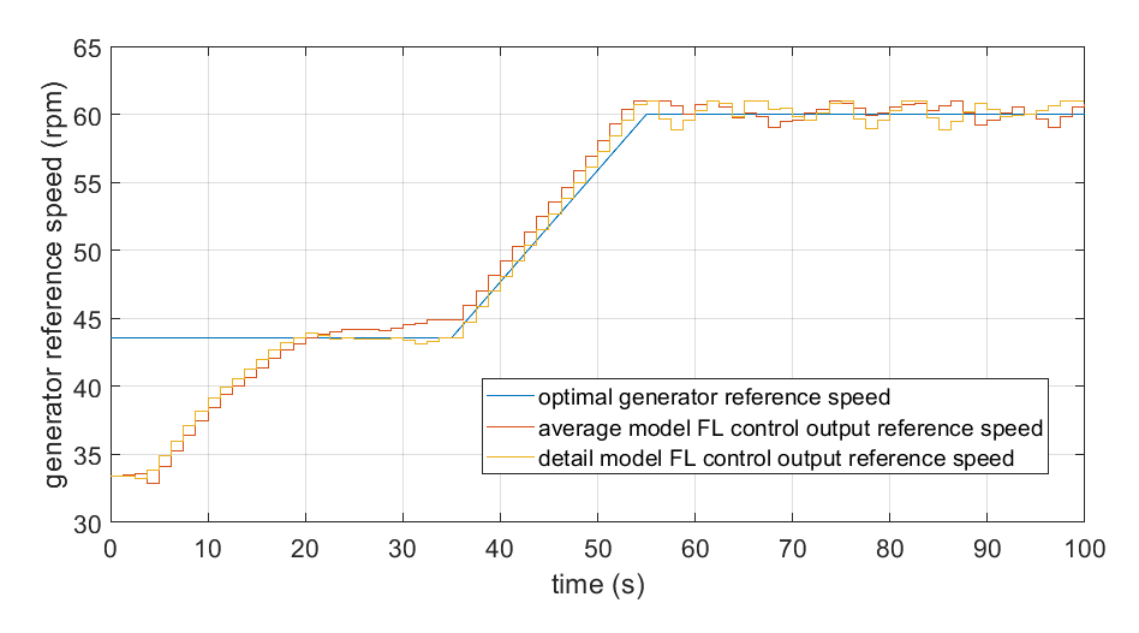


Figure 6.11 FL control speed with detail and average model under ramp input

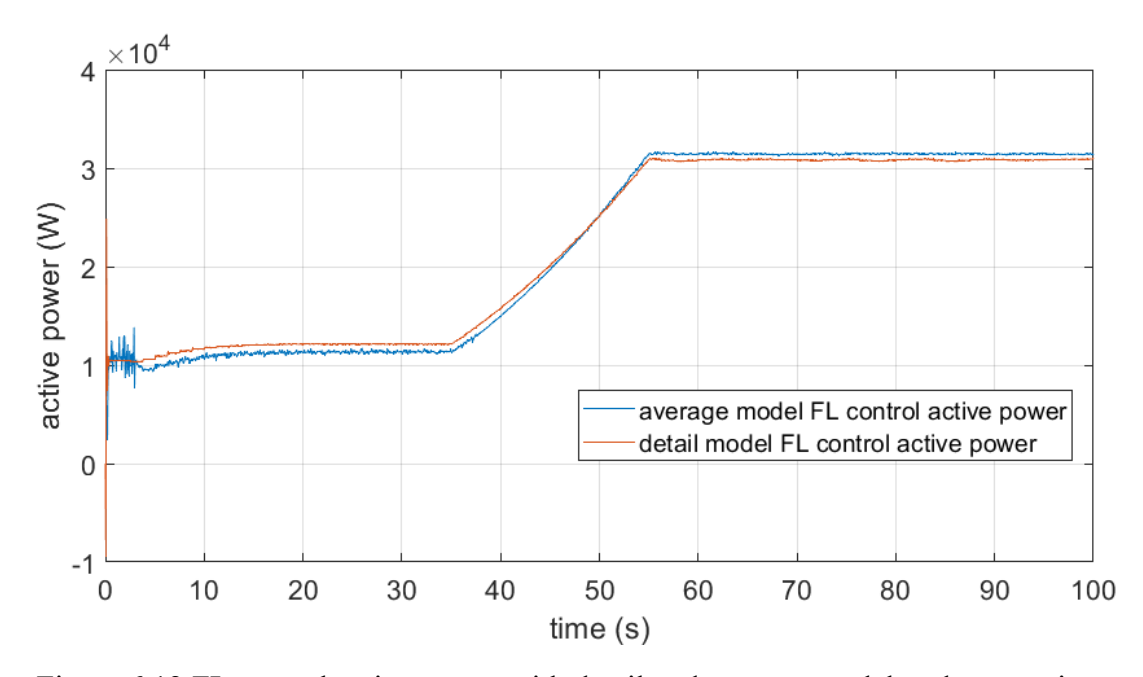


Figure 6.12 FL control active power with detail and average model under ramp input

Figure 6.13 presents the differences in active power between average and detailed models with FL control under ramp input. From this figure it can be seen that the difference between the two models is small, less than 1.3kW.

Form Figure 6.11 to Figure 6.13, the generator speed and active power differences of the two models with FL control under ramp change input have shown that the average model can provide similar performance compared to the detailed model. Combined with the results from Figure 6.8 to Figure 6.10, it has been shown that for the simplified average model, FL control can be applied to test the long term simulation.

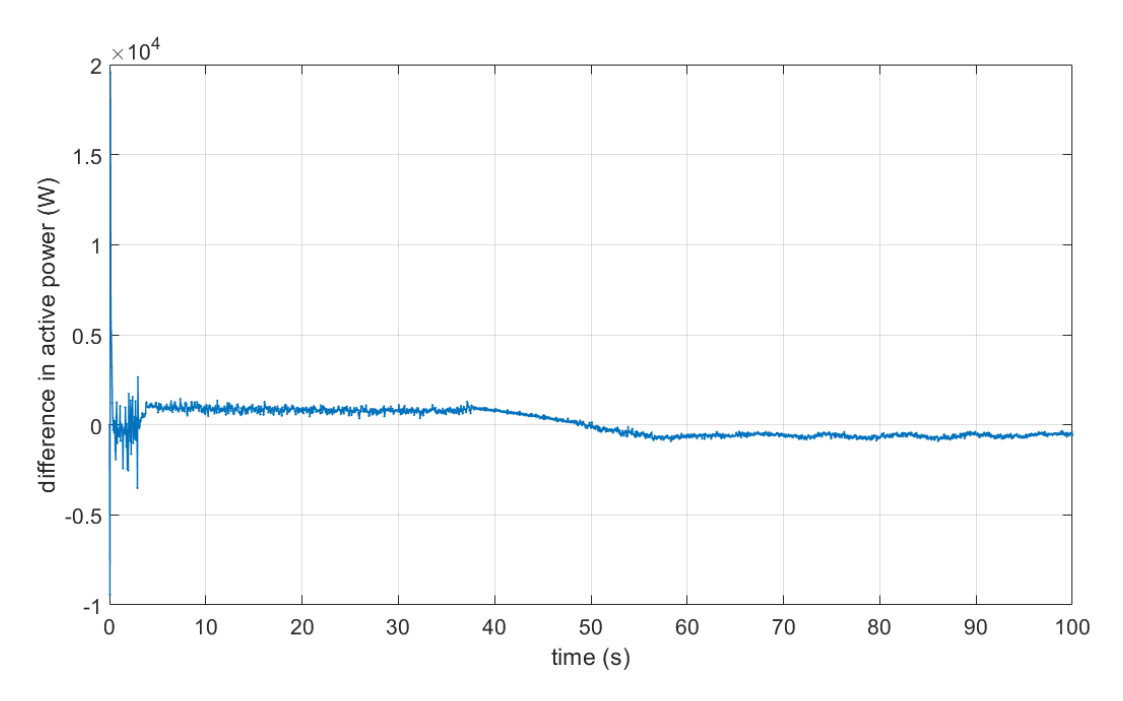


Figure 6.13 Differences in active power of FL control under step input

6.1.4 Tidal current velocity data

As mentioned in Chapter 3, the tidal current velocity data are taken from CMEMS, the location is Pentland Firth, and in order to avoid getting negative input, data in Figure 3.10 are rectified. Figure 6.2 shows the period of tidal current velocity data that is used as the input of the average model. This period contains the tidal current velocity from low tide to high tide and back to low tide again, with the maximum speed of 2.9 m/s, which is over the E35 turbine's rated speed (2.35 m/s). This provides a full speed range to investigate whether the P&O control and FL control can control the turbine and generator to follow the power range where below cut-in speed the output power is zero, and over rated speed the output power should remain at rated power as shown in Figure 3.11.

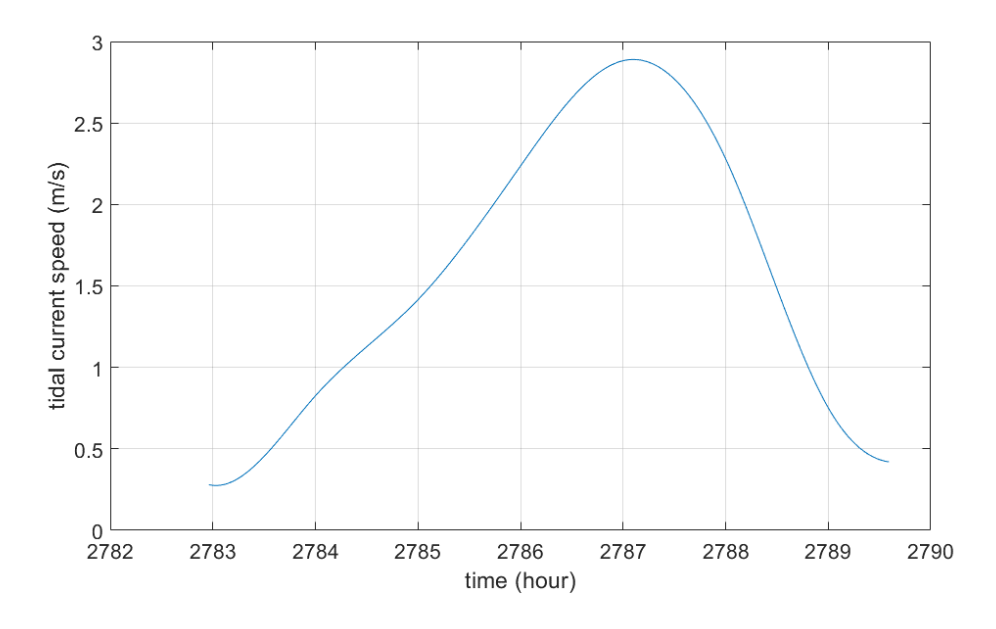


Figure 6.14 Tidal current velocity input for average model (from CMEMS)

6.1.5 Control parameter tuning

As mentioned above, the model was simplified to allow it to run for a longer period of time. As the model was changed, the control loops also needed to be adjusted to follow Equations 6.1 and 6.2, and Figure 6.1. In the new control arrangement, similar to the original control system illustrated in Section 4.4, there are still three loops, one DC-link voltage control loop and two dq-axis current control loops. The PI controller parameters thus need to be adjusted and the PI tuning processes were the same as mentioned in Section 3.3.5.

The tidal current velocity inputs in Chapters 4 and 5 are step change and ramp change inputs in order to test the P&O control and FL control performance under a tidal current velocity with sudden and continuous changes. The simulation time was short and the P&O control and FL control parameters were set to behave over the short simulation. As the input is to be changed to the real tidal current velocity for 6.5 hours, the control strategy parameters also needed to be tuned to meet the requirements of the long-term simulation. The step time of the P&O control and FL control were 1.25s in Chapters 4 and 5, and this is obviously too small for the 6.5 hours input, as it will lead to shorter tracking times but with big fluctuations during steady state or the output of the control strategies will overshoot the optimal speed with significant errors.

In order to test how different step times affect the simulation results and to choose a suitable step time for the control methods, a 3 hour simulation test was established to investigate the different step time effects, for both P&O control and FL control. Figure 6.15 shows the active power for FL control with different step times. The step times was increased from 1.25s (as

used in Chapters 4 and 5) to 160s.

It can be seen from Figure 6.15 that the active power was significantly affected by the step time. A smaller step time, such as step time 1.25s and 40s, may result in larger fluctuations during the tracking process, although most step sizes are capable of tracking the maximum power points effectively. On the other hand, larger step times, such as 160s, sometimes fail to track the maximum power points accurately.

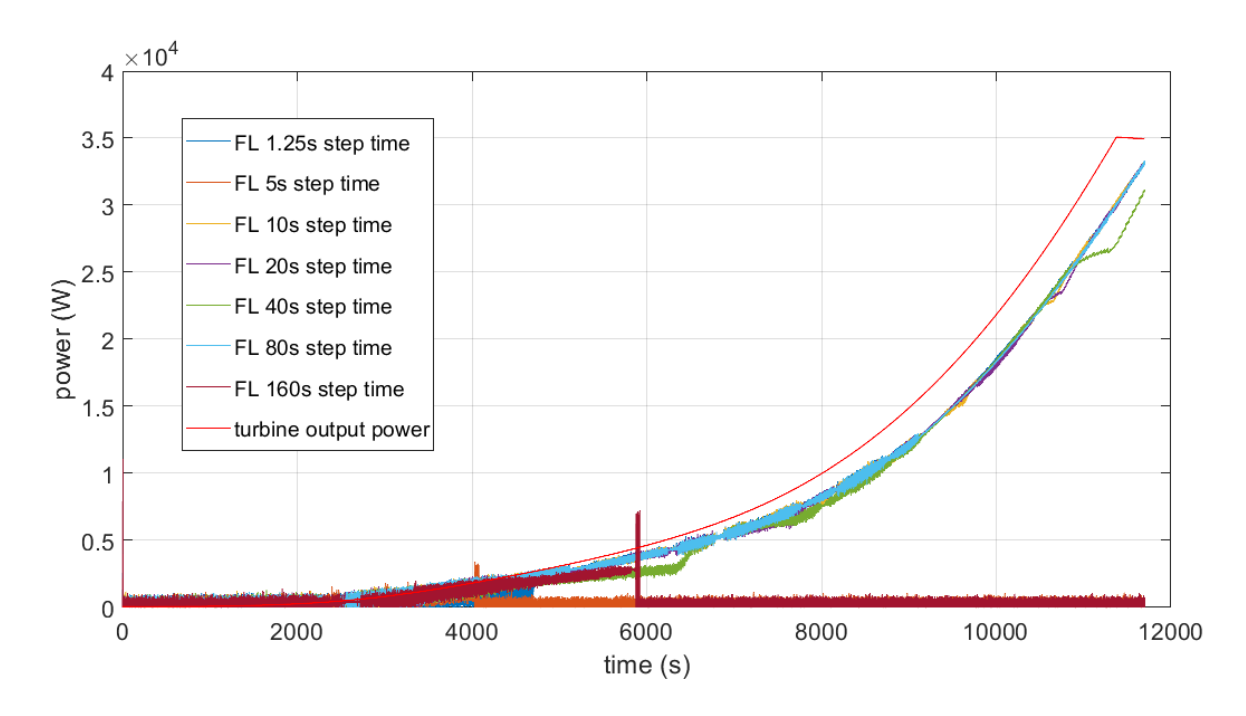


Figure 6.15 FL control active power with different step time

Figure 6.16 illustrates the active power of P&O control with different step times. Similar to Figure 6.15, a smaller step size can result in the oscillations near the optimal power value, such as step time 40s. While large step size, such as 160s, may lead to tracking failures.

From Figure 6.15 and Figure 6.16 it can be seen that an 80s step time has a good performance for both control methods, tracking the maximum power points with small fluctuations. The corresponding generator reference speeds are presented in Appendix D.1 and D.2 respectively. In the long term simulation, the step times were adjusted (from 1.25s in Chapters 4 and 5 to 80s) as well as the step sizes of P&O control and the membership functions of FL control being adjusted using the tuning methods introduced in Chapters 4 and 5. The basic performances of P&O and FL control were presented and discussed in Chapters 4 and 5, such as the relationships between different step sizes, step times and membership functions and how the control parameters affect the system operation. Thus, in this chapter, the results will only present the tidal current turbine generation system performance with discussions and

comparisons of the generator reference, output power and efficiencies.

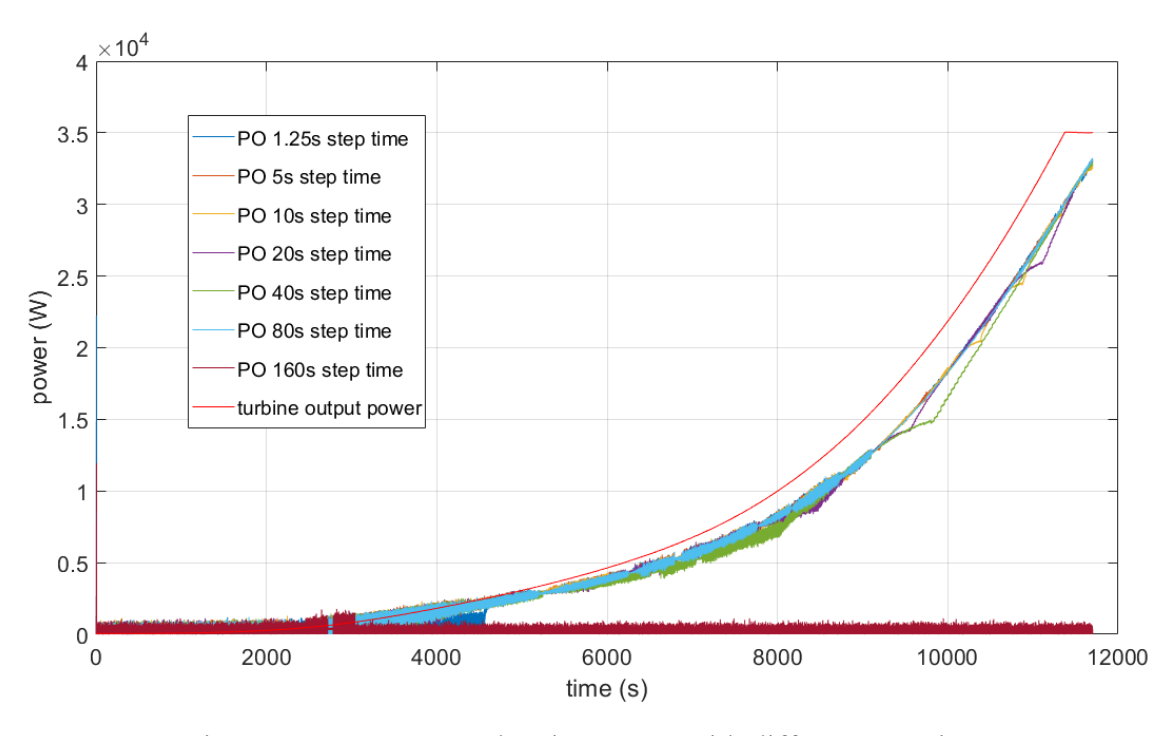


Figure 6.16 P&O control active power with different step time

6.2 Results and discussion

As shown in Figure 6.14, the input tidal current velocity takes approximately 6.5 hours to go from low tide to high tide then back to low tide. Even with the simplified average model and increased sample time, the 6.5 hours simulation still could not be completed in one run as the output data was still too large for the available computer memory. Thus, in this chapter, the input data is divided into two parts, which means that the first part of the simulation will start from time point 2783 and end at 2786.5 in Figure 6.14, and the second part will start from 2786.5 and run to the end of the input data. The model initial states for the second part were set to be the same as the final state of the first part of the simulation. The results presented in this chapter are all with the two parts combined together to show the complete performance of the control strategies in one tidal cycle.

6.2.1 Fuzzy Logic control results

Figure 6.17 illustrates the output of the Fuzzy Logic control strategy. The reference speed that is provided to the generator speed control loop is shown as the blue line in Figure 6.17, and the red line is the optimal reference speed for the 6.5 hours tidal current velocity input. From this figure it can be seen that when the tidal current starts to increase, the output of the FL control also increases to follow the speed change. The tracking process has a small delay period from 3000s to 8000s, with about maximum error of 3%. When the tidal current

velocity reaches the rated power speed, the generator reference speed provided by the FL control varies around 60rpm with a maximum error of also 3%. The figure of 60rpm is the rated speed of the generator, so that the generator operates in its rated state, and this means that the turbine is rotating at the rated speed even though the tidal current velocity is higher than the rated power point. After operating at the rated stated for about 6000s (from 12000s to 18000s, about 1.6 hours), the tidal current velocity starts to decrease below the rated power point and the FL output reference speed also starts to decrease. The decreasing period is not as smooth as the increasing period, this is because, from the control theory, as illustrated in Section 5.2, Figure 5.3 and Table 5.1, if the changes in power and changes in generator speed were both negative, the signal from the FL control is then positive. Thus, in Figure 6.17 when the speed decreases there will be small increases in the reference speed, but the decrease value is larger than the increase value, so that the overall trend is decreasing in this period and it can follow the optimal reference speed.

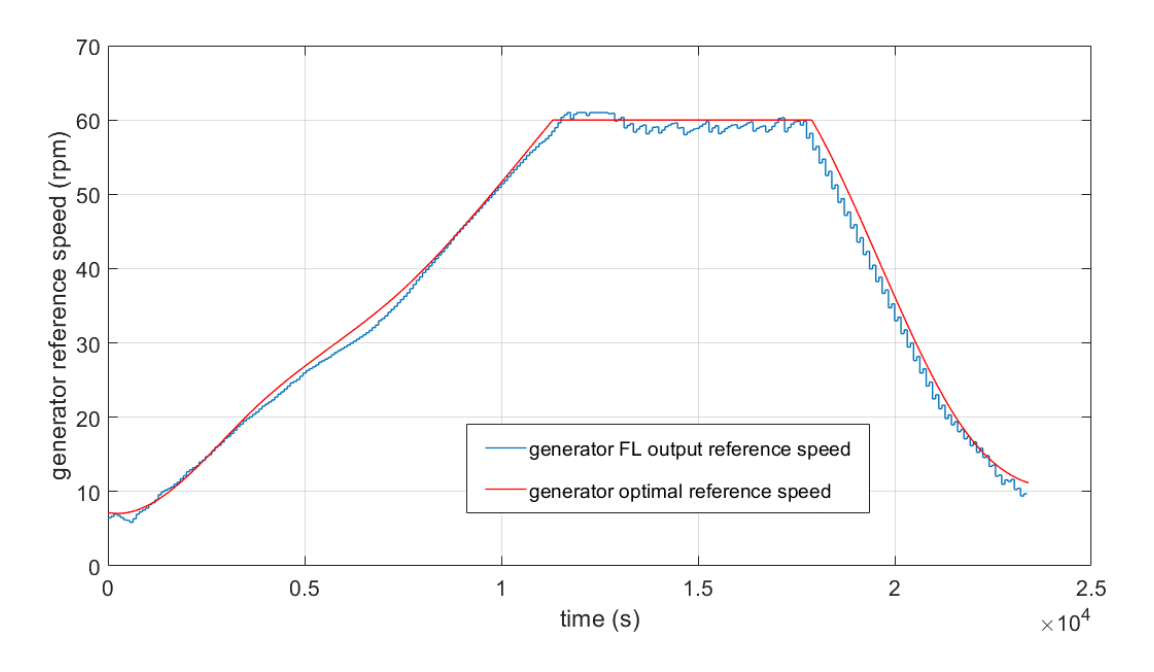


Figure 6.17 Fuzzy Logic control output reference speed

Figure 6.18 presents the output power of the tidal current turbine generation system with FL control, which includes the turbine output power, the generator output power, and the grid side active power. It can be seen that these power curves have the same trend, increasing at first, then maintaining at rated power then decreasing. The generator output power and active power curve are lower than the turbine output power, approximately 5% less, due to the losses in the turbine drive train and the losses in the generator (such as copper loss). During the tidal current velocity increasing period, before the turbine cut in speed (0.7m/s), it can be seen from Figure 6.18 that all three power curves are zero, then once the tidal current velocity

exceeds the cut in speed, the power can then start increasing. When the tidal current velocity reaches the rated power velocity (2.35m./s), the turbine and generator's rotational speed remains around the rated value. As shown in the figure, the turbine output power is maintained at 35kW, and the generator output power and grid active power are maintained at 33kW. This means that the turbine rotational speed is controlled at its rated speed and does not increase even though the tidal current velocity is still increasing. When the tidal current velocity decreased below the turbine rated power rotational speed, the output power of tidal current turbine, generator power and active power also decreased. Again, when the tidal current velocity is below the cut in speed, there is zero output power. The power curves in Figure 6.18 correspond to Equation 3.3, and the power verses tidal current velocity curve in Figure 3.11.

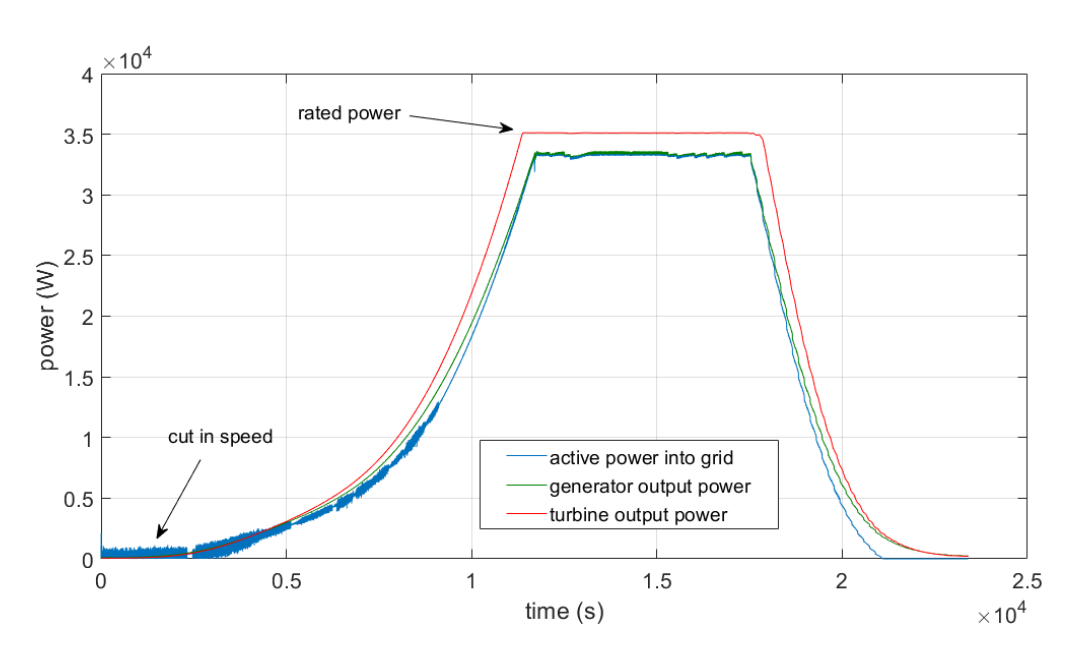


Figure 6.18 Power of Fuzzy Logic control

Figure 6.19 illustrates the power coefficient of the turbine with FL control. From this figure it can be seen that, during the increasing and decreasing period, the power efficiency has a relatively large error at the start and the end of the simulation. The maximum error during the whole simulation is about 5%, but when the tidal current velocity is over the cut-in speed and during the rated state, the power coefficient is very close to the optimal value. The fluctuation of power coefficient is larger in the decreasing period than the increasing period, this is due to the FL output generator reference speed having the characteristic mentioned above. The overall power coefficient is in an acceptable range with a maximum 5% error below cut-in speed and maximum 1.7% error when the tidal current velocity is over cut-in speed, and during the rated state, the maximum error is less than 0.2%.

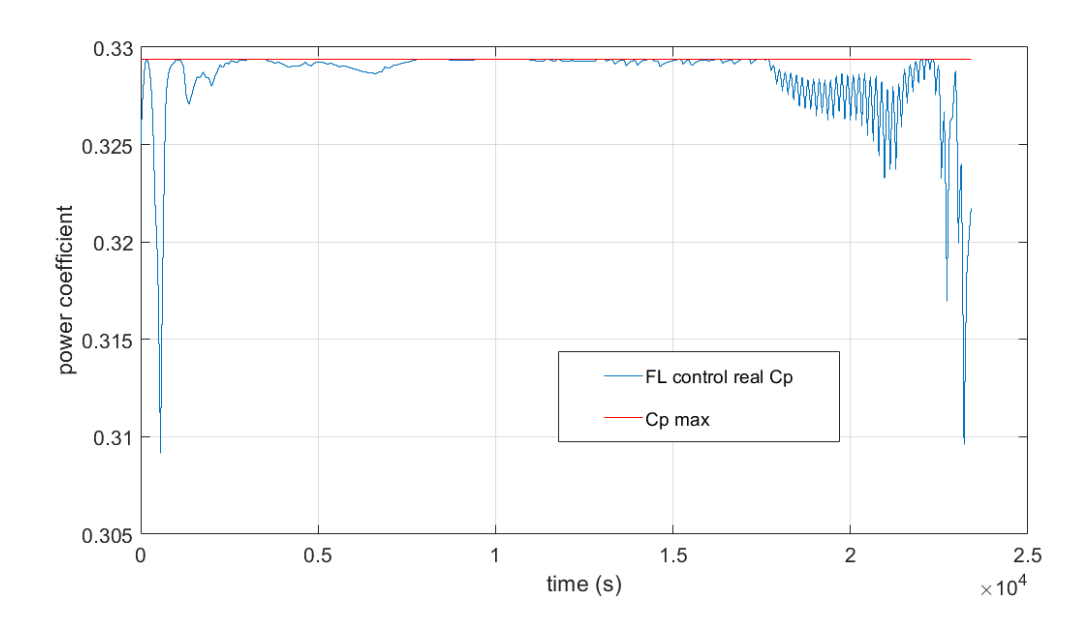


Figure 6.19 Fuzzy Logic control power coefficient

6.2.2 Perturb and observe control results

The previous section presented the performance of Fuzzy Logic control in the tidal current turbine generation system with the 6.5 hour tidal current velocity input. This section is going to illustrate the performance of P&O control under the same condition, with the same step time, which is 80s, as for the FL control above.

(1) Multiple Variable Step Size

As presented in Chapter 4, the variable step size P&O control has better performance in the grid-connect conventional tidal current turbine generation system under both step change and ramp change tidal current velocity inputs compared to traditional fixed step size P&O control. This is because, when the turbine and generator rotation speed is close to the optimal value, the changes in output power will become smaller. The variable step size can have a larger step size when the rotational speed is far from the optimal value and a smaller step size when the rotational speed is near to the optimal value. However, under the real tidal current velocity conditions, the tidal current velocity is always changing. In this situation, the variable step size P&O control cannot track the MPP efficiently, as illustrated in Figure 6.20. It can be seen that before about 2500s, the variable step size P&O control is tracking the optimal value, but from 2500s to 6000s, the P&O control output speed overshoots the optimal value then tracks back. Again from 6000s to 8500s it overshoots and tracks back, and so on.

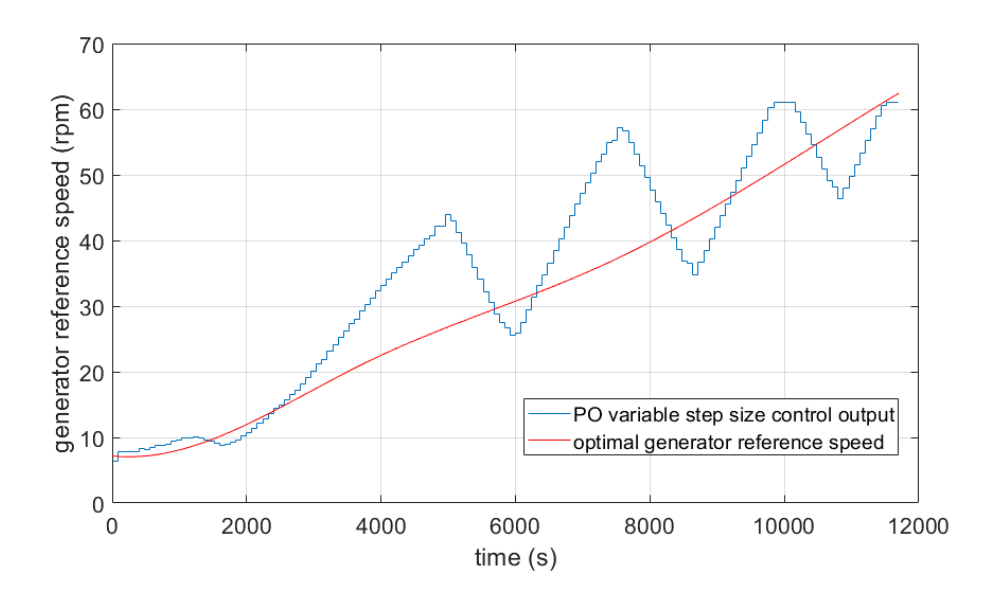


Figure 6.20 Variable step size P&O output reference speed

The reason that the variable step size P&O control output reference speed overshoots the optimal value and then tracks back, is because the tidal current velocity is constantly changing, which means that for every second there will be a new maximum power point, and so the changes in power will no longer be the same as in Chapter 4. Figure 6.21 shows the power changes in the MPP power curve with the same rotational speed change. It can be seen from this figure that, as the tidal current velocity increases, the MPP also changes. As illustrated in Section 2.3.2 on the power signal feedback control, the MPP power curve (blue line in Figure 6.21) can be expressed by Equation 2.3, from which the power can be expressed by $K_{opt}\omega_r^3$. Viewing this together with Figure 6.21, the tidal current turbine rotational speed will be changing following the tidal current velocity change, but a given change in tidal current turbine rotational speed, will lead to a different power change. For example in Figure 6.21, when the tidal current turbine rotational speed changes from 24rpm to 27rpm, or changes from 31rpm to 34rpm, the changes in power are significantly different. At higher rotational speed, same small change in speed will lead to much larger changes in power compared to the lower rotational speed.

This is the reason that the variable step size P&O control output in Figure 6.20 has a relatively poor performance under real tidal current velocity conditions. In this situation, the variable P&O control need to be adjusted to fit the realistic tidal current velocity input.

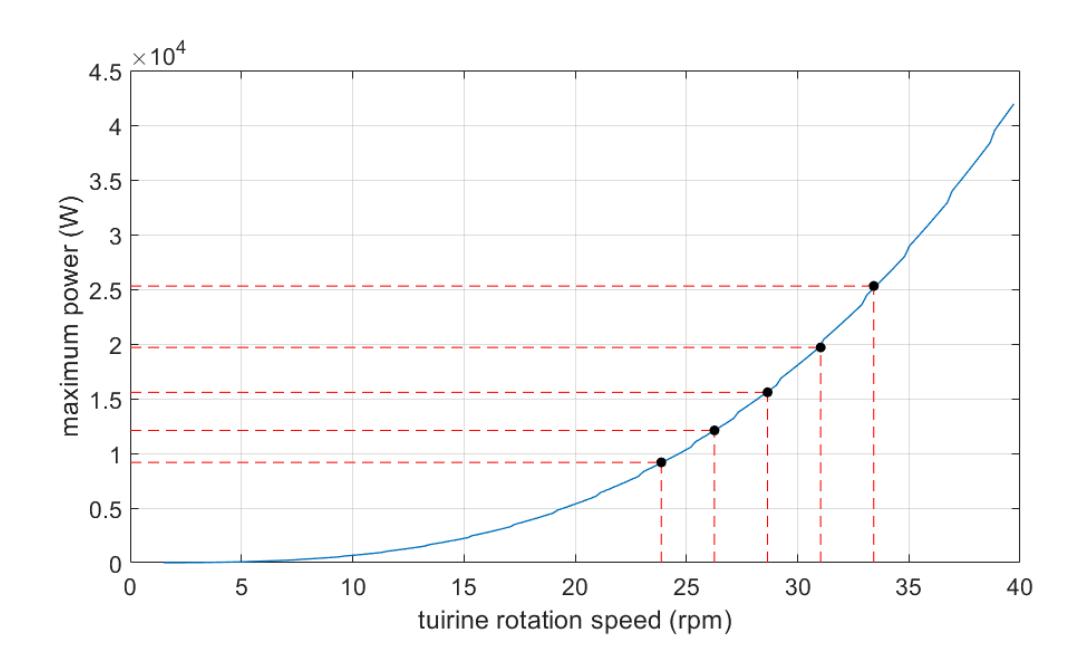


Figure 6.21 Changes in power with same rotation speed change

Figure 6.22 shows the changes in the power and changes in speed for P&O control under the output that is presented in Figure 6.20. It can be seen that the changes in power are larger when the tidal current velocity increases, as discussed above. In order to improve the accuracy of the control of the output generator reference speed, a new P&O control is established moving from a single variable step size to a multiple variable step size arrangement, and the $\Delta\omega_{ref}$ of the P&O control algorithm can then be express as follows:

$$\Delta\omega_{ref} = \begin{cases} \Delta P(n)K_1 & \Delta P \in A_1 \\ \Delta P(n)K_2 & \Delta P \in A_2 \\ \Delta P(n)K_3 & \Delta P \in A_3 \\ & \vdots \\ \Delta P(n)K_i & \Delta P \in A_i \end{cases}$$
 Equation 6.3

where K_i is the adjustment constant, which is the same as in Chapter 4 and A_i is the range of power changes. By determining the power change range, the multiple variable step size can be established. With the multiple variable step size P&O control, the control output can have different step sizes to fit different turbine speed and power changes under changing tidal current velocity. This can avoid the control output overshooting the desired value or oscillating below the optimal speed which had resulted from only having one adjustment parameter.

The key point of the multiple variable step size is the power range and adjustment constant. As can be seen from Figure 6.20 and Figure 6.22, the P&O control output overshoots the optimal speed from 2500s to 5800s and during this period the changes in power (from Figure

6.22) are approximately from 30W to 70W, and the desired speed range is about from 15rpm to 29rpm. As the P&O control output with 1%-2% differences from the optimal value can be considered acceptable and will not bring significant differences in the output power (as discussed in Chapter 4), thus, the adjustment constant K value could be between 0.005 to 0.0083 during this power range. Repeating this process, analysis of the single variable step size overshoot periods in Figure 6.20 again can define the power ranges and adjustment constant values. The control algorithm can then be tuned by running the simulation again to improve the performance; where there is overshoot or lag in the control output generator reference speed, the power range and adjustment constant can be tuned to improve the control performance.

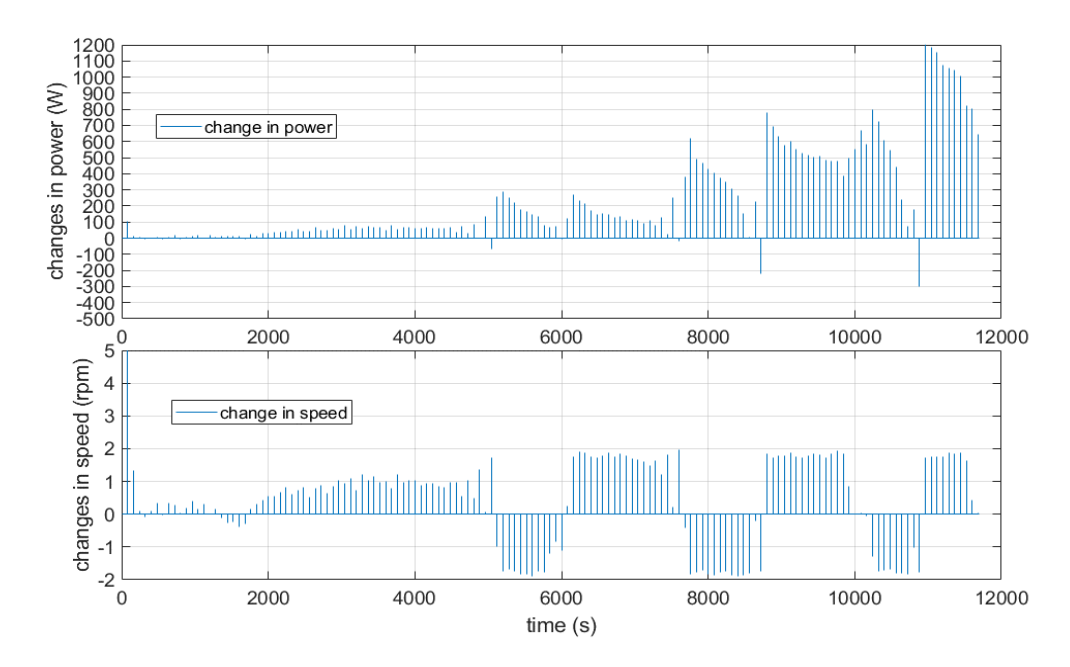


Figure 6.22 Changes in power and speed of variable step size P&O control

During the period when the tidal current velocity decreases, the single variable step size P&O control also has problems with the optimal value tracking, as shown in Figure 6.23 where the P&O control output generator reference speed cannot even track the optimal output value. The cause of this problem in the single variable step size P&O control is similar to the FL control in Section 6.2.1. Due to the control algorithm, during the decreasing period, there will be small increases in the output, and with single variable step size, the increase value will be large as the power change is large when the turbine is operating at high rotational speed. This will lead to the results presented in Figure 6.23 in which the increasing value is almost the same as the decreasing value. The multiple variable step size P&O control presented above can solve this problem by adjusting the power change range, *A*, in Equation 6.3. In addition, another slow adjustment factor also needed to be applied in the P&O control algorithm to

limit the increasing value which only happens when ΔP and $\Delta \omega$ are both negative. Thus the algorithm can be expressed as:

$$\omega_{ref} = \omega_{(n-1)} + sgn(\Delta\omega) \cdot \Delta P(n)K \cdot SAF(\Delta P, \Delta\omega)$$
 Equation 6.4

where *SAF* is the slowdown adjustment factor, which can control the increasing value of the P&O control output. By using the multiple variable step size and the slowdown adjustment factor in the P&O control algorithm, the P&O control is able to function in the conventional tidal current turbine system to track the MPP. The results will be illustrated in the following section.

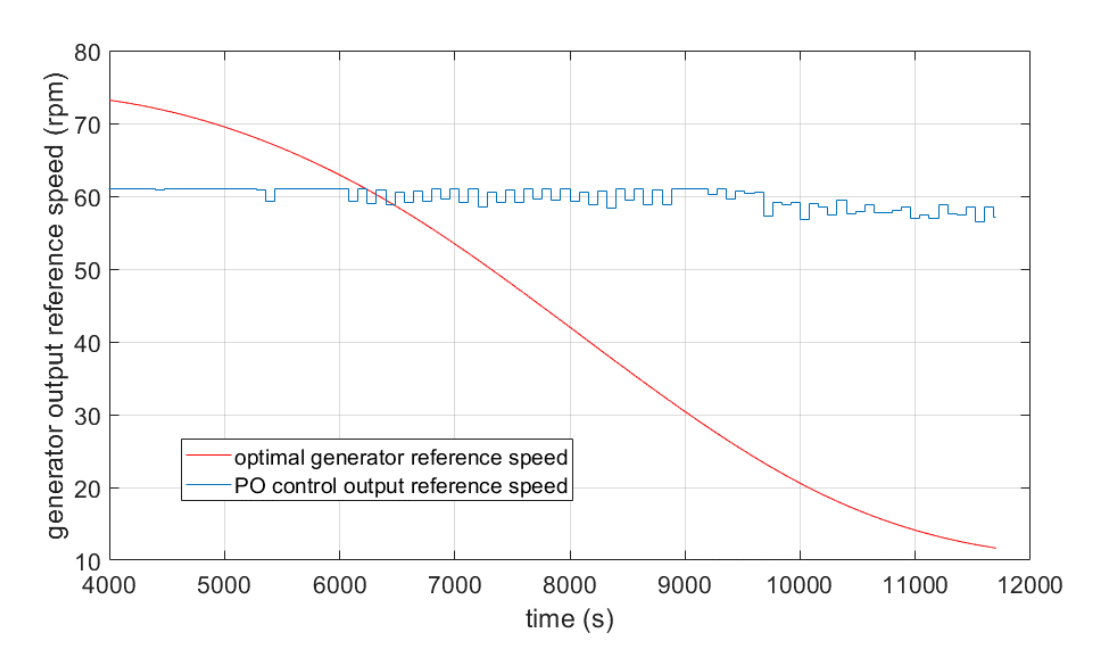


Figure 6.23 Variable step size P&O output reference speed with decreasing tidal current velocity

(2) P&O Control results with Multiple Variable Step Size

Figure 6.24 shows the generator reference speed provided by the P&O control. It can be seen that from 0s to 3500s the P&O output reference goes over the optimal reference speed with a maximum 3% error, and during the period from 3500s to 8000s the P&O control output speed is slower than the optimal reference speed with a maximum 5% error. From 8000s to the rated power period, the P&O output reference speed is able to track the optimal reference speed and stay very close to it, and during the rated state, the P&O output speed fluctuates around the rated power speed (60rpm) with maximum 3% error. While the tidal current velocity decreases below the rated power, the P&O output reference speed also decreased, and, similar to the FL control mentioned above, it has small increases during this period. This is also due to the control theory where the P&O control and FL control have the same basic searching

principle. From Figure 4.2 and Figure 4.3 it can be seen that when the change in power is negative and the change in generator rotation speed is positive, the P&O will then give a negative signal, but if both inputs of the P&O control are negative, the output of the P&O control will be positive, resulting in the small increases in speed during the tidal current decreasing period in Figure 6.24. However, during the tidal current velocity decreasing period, the overall tracking of the multiple variable step size P&O output reference speed is negative and it follows the optimal reference speed change. When the tidal current velocity starts to decrease, the output of the P&O control presents a slight delay with respect to the optimal value, and from 20000s to 22000s, the P&O output reference speed goes over the optimal speed and then tracks back to the optimal, the maximum error during this period is 2%, which is a small error and it's acceptable as it will not cause big changes in the output power and can meet the control requirements.

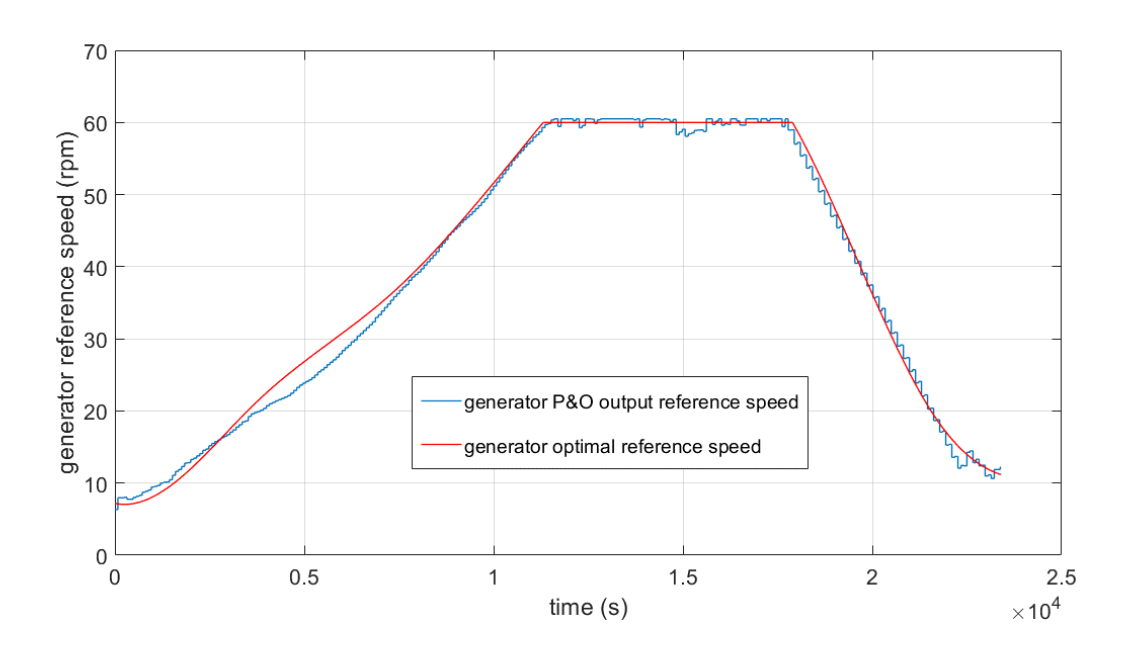


Figure 6.24 Perturb and observe multiple variable step size control output reference speed

Figure 6.25 illustrates the active power, generator output power and turbine output power of the system under 6.5 hours input with P&O control. Similar to the results with FL control in Section 6.2.1, the power curves have the same trend, and due to the losses in the drive train and generator, the green line and blue line in Figure 6.25 are lower than the red line. When the tidal current velocity is below the cut-in speed in this figure, during both the increasing and decreasing tidal current periods, all of the power are zero. When the tidal current velocity reaches the rated power speed, the turbine can provide rated power which is 35kW and maintains at this value, and the generator output power and grid active power are kept at this value with small fluctuations, even though during this period, the tidal current velocity is over

the turbine rate power rotational speed. During the tidal current velocity increasing and decreasing periods, the power curves follow the tidal current velocity change curve, which matches the turbine power verses tidal current velocity figure in Section 3.2.3 and Equation 3.3.

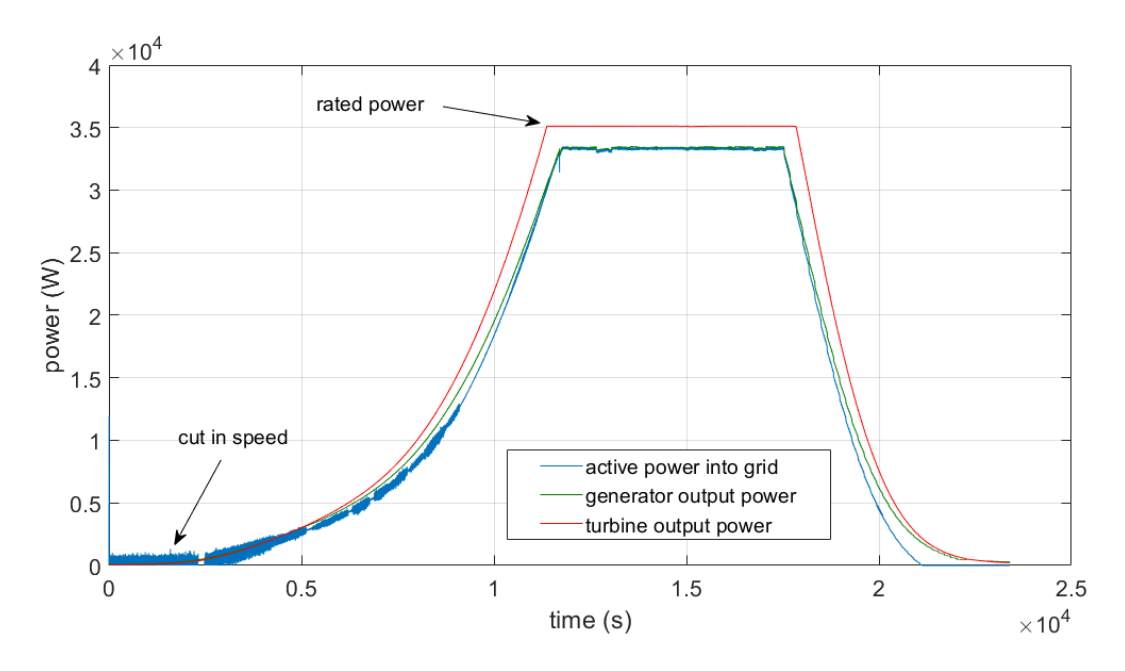


Figure 6.25 Power of Perturb and Observe multiple variable step size control

Figure 6.26 shows the power coefficient of the E35 turbine with multiple variable step size P&O control. It can be seen that from 0s to 8000s, the power coefficient has relatively big fluctuations, this is because, as shown in Figure 6.24, the generator reference speed during this period has maximum 3% error as mentioned above. From 8000s to 18000s, the turbine power coefficient is very close to the optimal value, as the reference speed in this period is more closely aligned to the calculated optimal value. Again, due to the small increases in speed during the decreasing tidal current period, even though the speed is close to the optimal value, the turbine coefficient is still affected by this, and this corresponds to fluctuations from 18000s to the end of the simulation.

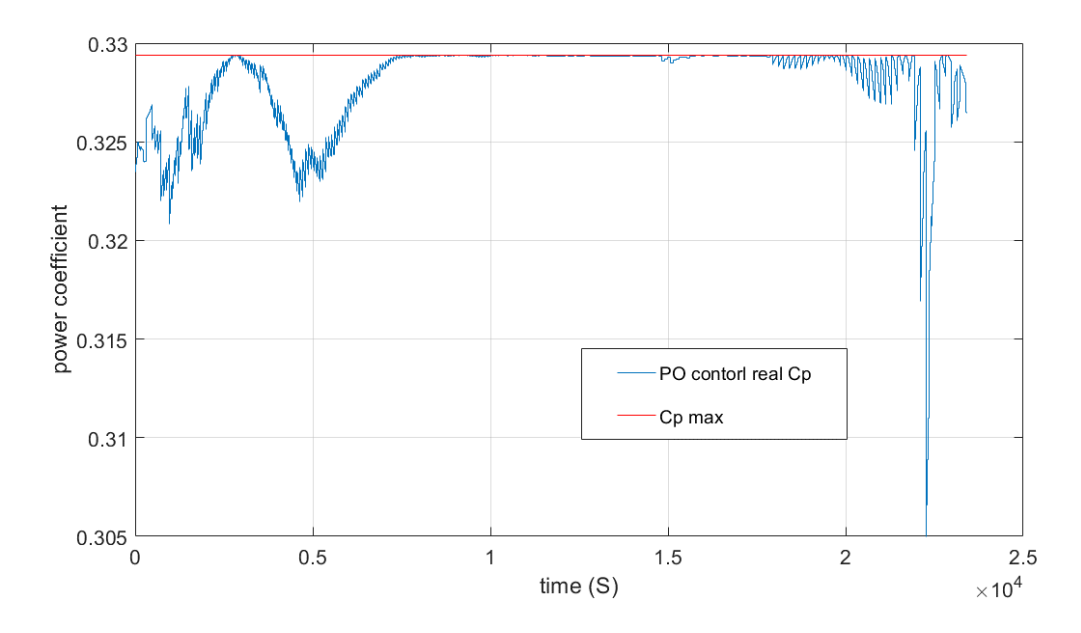


Figure 6.26 Perturb and observe multiple variable step size control power coefficient

6.2.3 Performance discussion

The outputs of FL control and multiple variable step size P&O control are illustrated above in terms of the generator reference speed for which both the FL and P&O control output can track the optimal value with maximum 5% error. Also, the output power of the turbine and generator, and the active power inject to the grid are presented. The turbine output power follows Equation 3.3 and Figure 3.11, discussed in Chapter 3, which ensures that the turbine is operating when tidal current velocity is above the cut-in speed and maintains at the rated power speed when tidal current velocity is larger than rated power speed. The generator output power of both control strategies can follow the turbine output change, but due to the losses in the system, is smaller than the turbine output power. The active power delivered to the grid is almost the same as the generator power, due to the losses in power transmission, the active power is lower than the generator output power (mentioned in Chapters 4 and 5).

Table 6.1 below shows the percentage energy yield and the energy production of FL, P&O and sensor (i.e. operation with the tidal current speed sensor) control. The percentage energy yield (Y_f) is defined as the energy produced by a system during a given period of time (E_{dc}) divided by the theoretical power (P_{max}) , which can be express as $Y_f = E_{dc}/P_{max}$ [170, 171].

From this table it can be seen that the percentage energy yield of FL control and P&O control are very similar. The energy yield of P&O control is slightly higher than FL control mainly because during the periods of increasing and decreasing tidal current speed, the P&O control's output value is closer to the optimal value than that of the FL control. The reason

that the average of P&O control and FL control are not as high as they were in Chapters 4 and 5 is because when the tidal current velocity is below the cut-in speed, the output power is zero.

Control strategy	Percentage Energy yield	Energy production (kWh)
Fuzzy Logic control	89.52%	90207
Perturb and Observe control	89.74%	90402
Sensor control	90.2%	90898

Table 6.1 Percentage Energy yield and energy production of FL and P&O control

Figure 6.27 presents the FL control, P&O control and sensor control output generator reference speed. It can be seen that the control output with the sensor has a good performance and the output reference speed is equal to the optimal speed. During the tidal current velocity increase period, at the start of the simulation (from 0s to about 7500s), the FL control's output is closer to the optimal reference speed than is the P&O control's output. After 8000s P&O control catches up and is slightly higher than the FL control. During the rated power period, the output of both FL control and P&O control is maintained at the optimal value and they have almost the same fluctuations. During the decreasing period, the P&O control has a slightly faster response than FL control, and this leads to the P&O control going slightly over the desired value, but the increasing steps in value of the P&O control are smaller than in the FL control case, which may lead to the FL control having larger fluctuations than P&O control in power efficiency (Figure 6.29) and turbine power coefficient (Figure 6.19 and Figure 6.26).

Figure 6.28 illustrates the active power of FL control, P&O control and sensor control, it can be seen from this figure that during the tidal current increase period, the three curve have almost the same performance, and during the steady state, compared to the sensor control, FL control and P&O control have slight fluctuations while sensor control is flat. When entering the tidal current decrease period, the active power of sensor control is slightly higher than FL control and P&O control. Compared to the sensor control, the FL control and P&O control do not have the same accuracy output reference as the sensor control, but the tracking efficiency and the power generated are very close to the sensor control (Table 6.1), which means that compared to the conventional sensor control, the FL and P&O sensor-less control have a good performance and can track the maximum power points effectively.

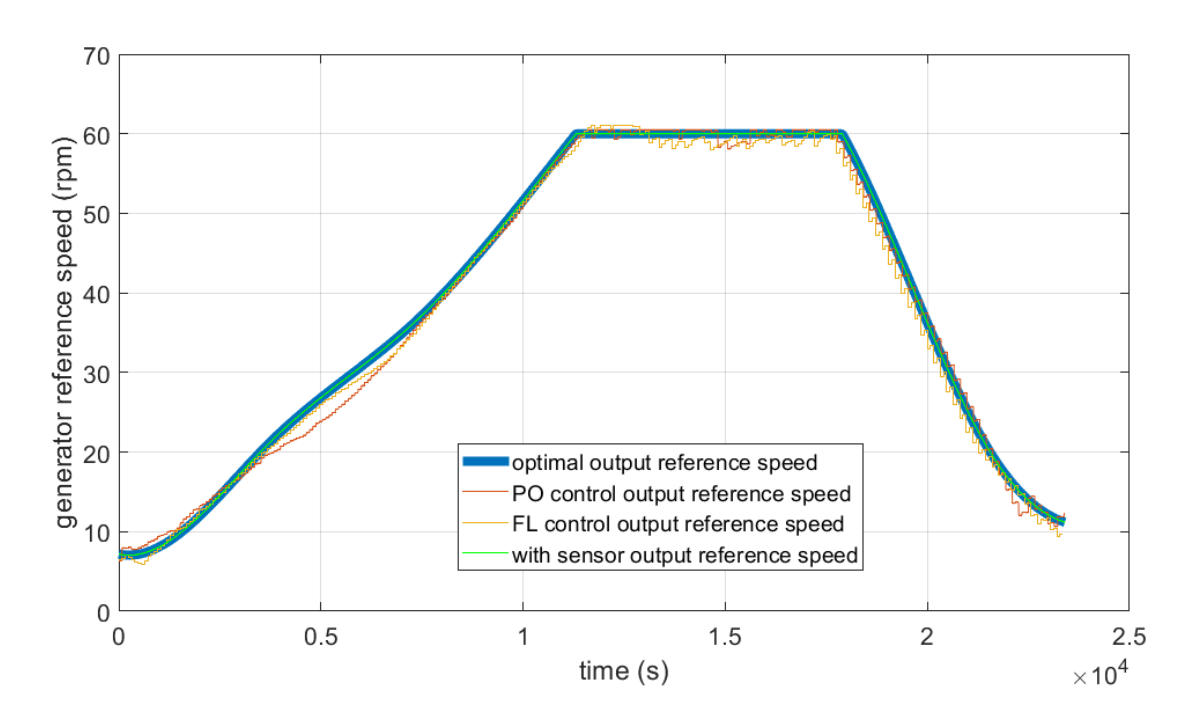


Figure 6.27 FL, P&O and sensor control output generator reference speed

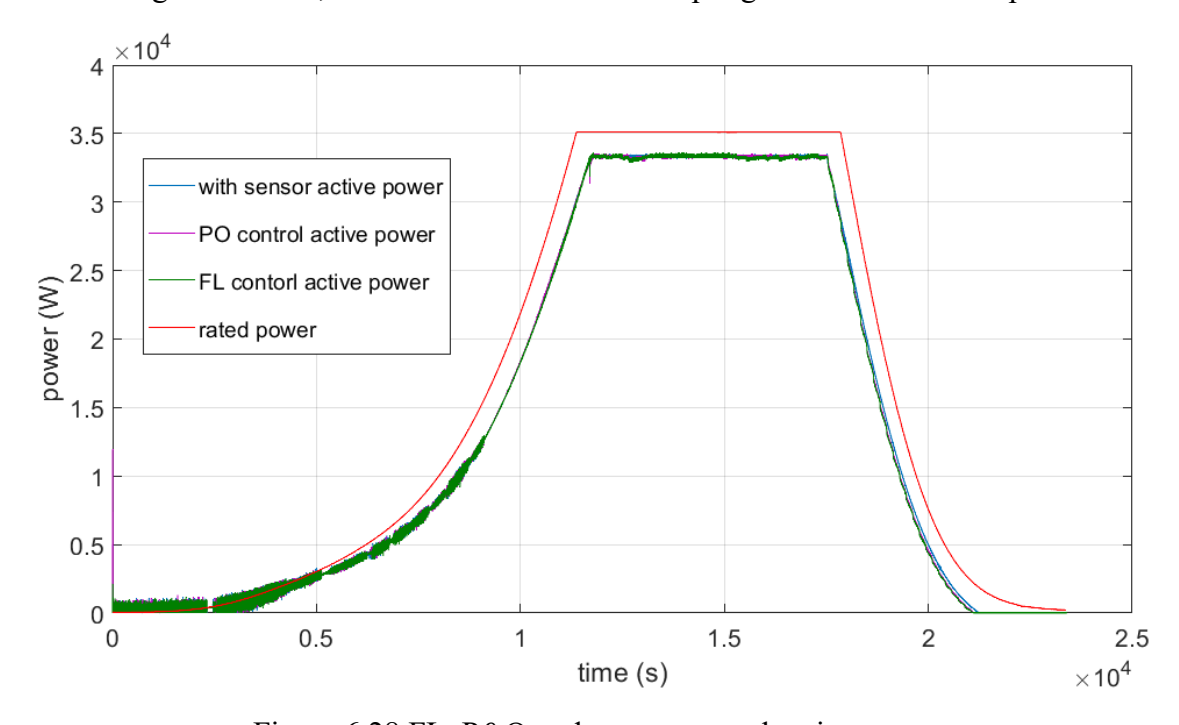


Figure 6.28 FL, P&O and sensor control active power

Figure 6.29 illustrates the instantaneous power efficiency of FL control and P&O control which is calculated by Equation 4.19. From this figure it can be seen that before the cut-in speed, the output power of the turbine and generator are both zero, thus the efficiency of the turbine will be zero, such as at the start and end of Figure 6.25. When the tidal current velocity is over the cut-in speed, the instantaneous efficiency becomes non-zero. During the increasing period, the instantaneous efficiency of FL control and P&O control are very close, but generally the P&O control is a little bit higher than the FL control, especially from 7500s

to the rated speed. This is because from about 7500s, the P&O control's output generator reference speed is closer to the optimal value than that of the FL control.

During the rated state, the efficiency of FL and P&O control are almost the same. The rapid increase and decrease of efficiency just before and after the rated state is because, when the theoretical power is at rated value, FL and P&O control are still tracking the MPP, and it takes approximately five steps (about 400s) for the turbine and generator to reach the rated power. Beyond the rated state, during the tidal current decreasing period, the P&O control's instantaneous efficiency is still higher than that of FL control, as in this period, as illustrated in Figure 6.27, the output generator reference speed of P&O control is closer to optimal than that of FL control until around 21500s after which the FL control has a smaller error from the optimal value than P&O control. Thus, in Figure 6.29, from 21500s the FL control's efficiency is higher than that of P&O control. After 21500s FL control presents a more stable efficiency than P&O control, and after the tidal current velocity drops below cut-in speed, the power efficiency becomes zero which can be seen at the end of the simulation in Figure 6.29.

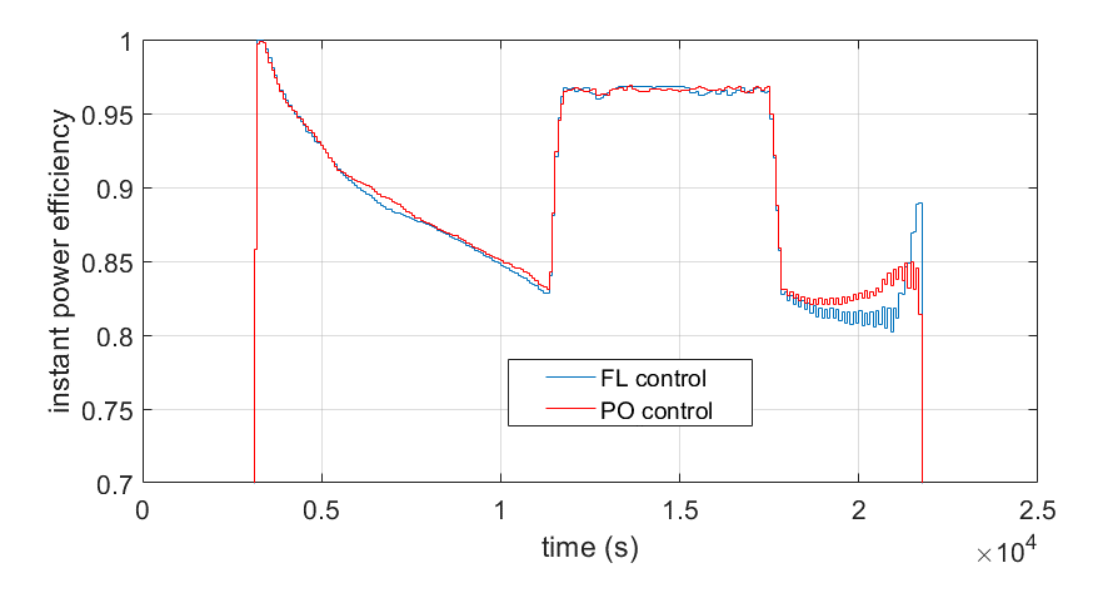


Figure 6.29 Instantaneous power efficiency of FL and P&O control.

Figure 6.30 presents the FL and P&O control generator output power. It can be seen that the blue line and red in this figure are almost the same, which is explained by the overall average efficiencies in Table 6.1 being also almost the same; the P&O control is only 0.07% higher than the FL control. The main differences in generator output power are zoomed in on in Figure 6.30. As mentioned above, from 7500s the output generator reference speed is higher for P&O than FL control in Figure 6.24, and this leads to the power in the left subfigure of Figure 6.30 having P&O control a little bit higher than FL control. It also leads to the

instantaneous power efficiencies in Figure 6.29 where from 7500s the P&O control has higher instantaneous power efficiency than FL control.

During the rated state period, P&O control and FL control have similar performance. The generator output power in Figure 6.30 is maintained at the same value with small fluctuations. This is because, as shown in Figure 6.27, the control strategies' output values are almost the same, leading to the instantaneous power efficiency values that are very close to each other, as mentioned above for Figure 6.29.

When the tidal current velocity starts decreasing, as shown in Figure 6.30, the generator output power of P&O and FL control have the same value until about 21500s. After this point, it can be seen from the right subfigure in Figure 6.30, the generator output power from FL control has larger fluctuations than P&O control, as mentioned above for Figure 6.27. The slight increases in speed of FL control are larger than for P&O control and this leads to the larger fluctuation of FL control in Figure 6.29. After 21500s, as the output generator reference speed of FL control is closer to the optimal value in Figure 6.27, this means that in Figure 6.30 right subfigure, the generator output power of FL control is higher than P&O control. This can also be seen from Figure 6.29, where from 21000s, the instantaneous power efficiency of FL control is higher than that of P&O control.

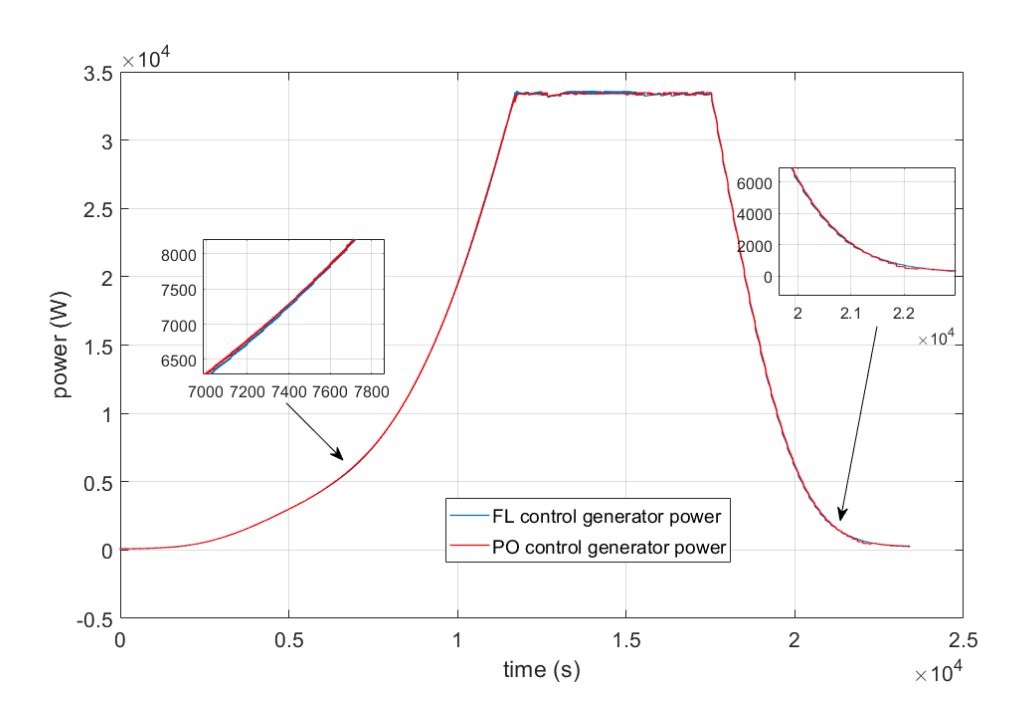


Figure 6.30 FL control and PO control generator output power

6.4 Extra long term simulation and energy production estimations

The sections above presented the FL control and P&O control for a single tidal cycle, in order to get more specific data of the control strategies' performances under real tidal current input. This section is going to illustrate longer-term simulation results of the control output generator reference speed and the active power, and based on the simulation results to estimate the energy yield and energy production for a year.

Figure 6.31 shows the 24 hour tidal current velocity input, representing a period between the neap tide and spring tide. This continuously changing real tidal current input under varying tidal conditions allows for a more comprehensive evaluation of the control strategies' performance.

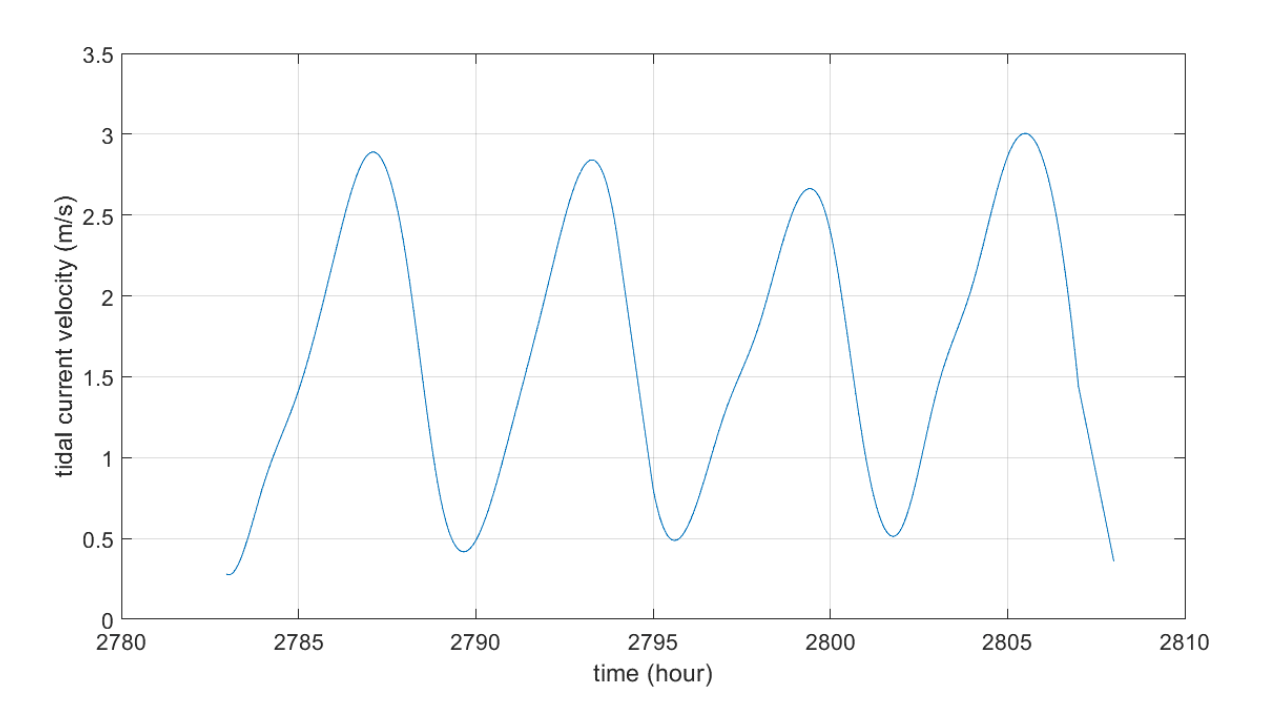


Figure 6.31 24 hour tidal current velocity input

Figure 6.32 illustrates the P&O control output generator reference speed under 24 hour tidal it current input. There are 4 tidal cycles in 24 hour simulation and from this figure it can be seen that the P&O control can track the optimal reference speed and varies around the rated value. When the tidal current cycles, the P&O control can provide the same trend in the output value to track the maximum power points.

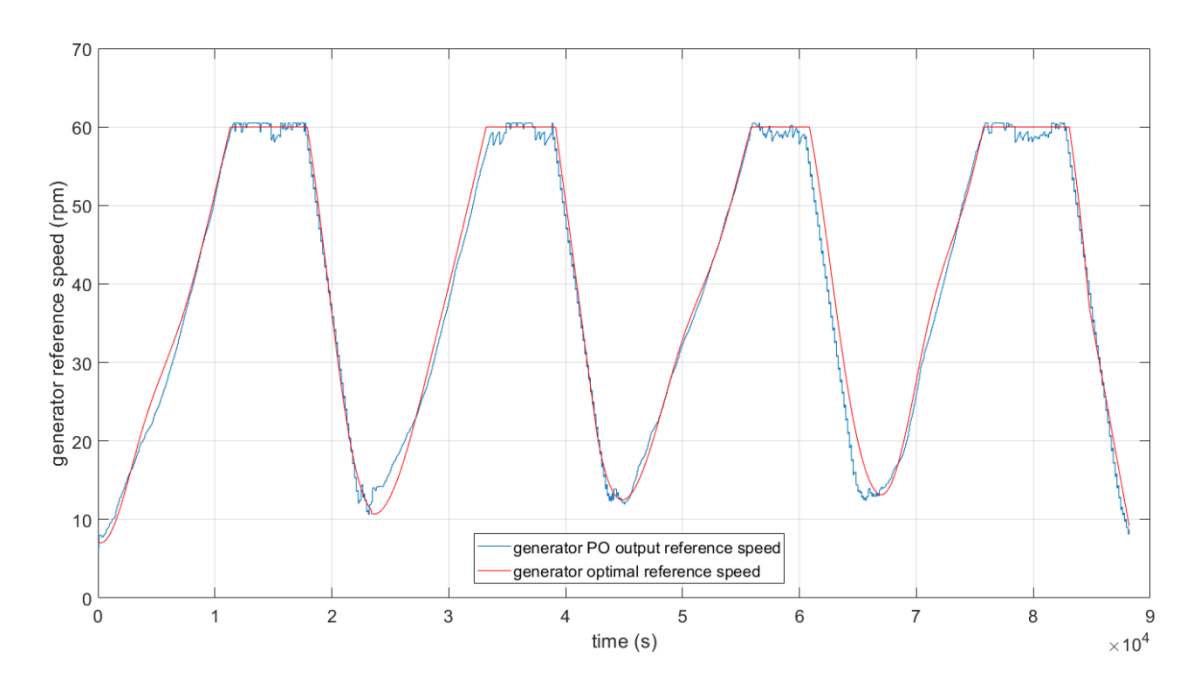


Figure 6.32 P&O control output reference speed under 24 hour tidal input

Figure 6.33 shows the active power of P&O control under 24 hour tidal current input. It can be seen from Figure 6.33 that the active power that is transferred to the grid is following the input change, and when the turbine reaches the rated power, the active power also maintains at the desired value.

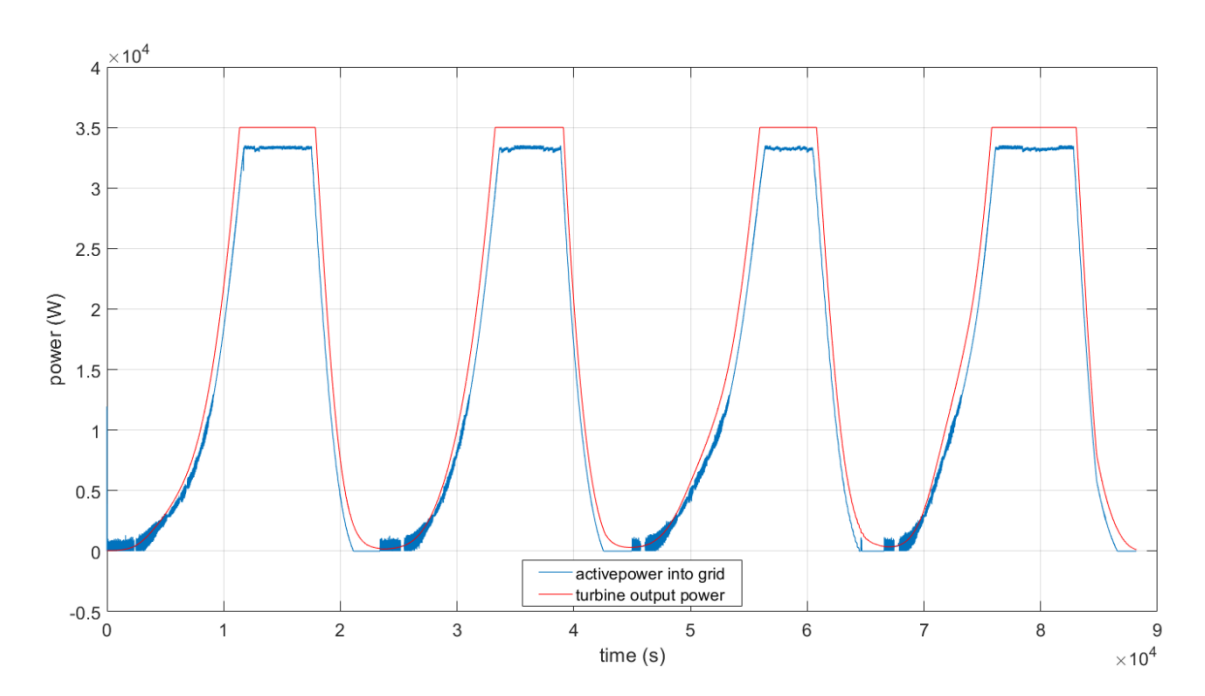


Figure 6.33 P&O control active power under 24 hour tidal input

Figure 6.34 presents the FL control output generator reference speed under 24 hours tidal current input. It can be seen from this figure that the FL control is able to track the maximum power points, essentially extending the cycle of Figure 6.17.

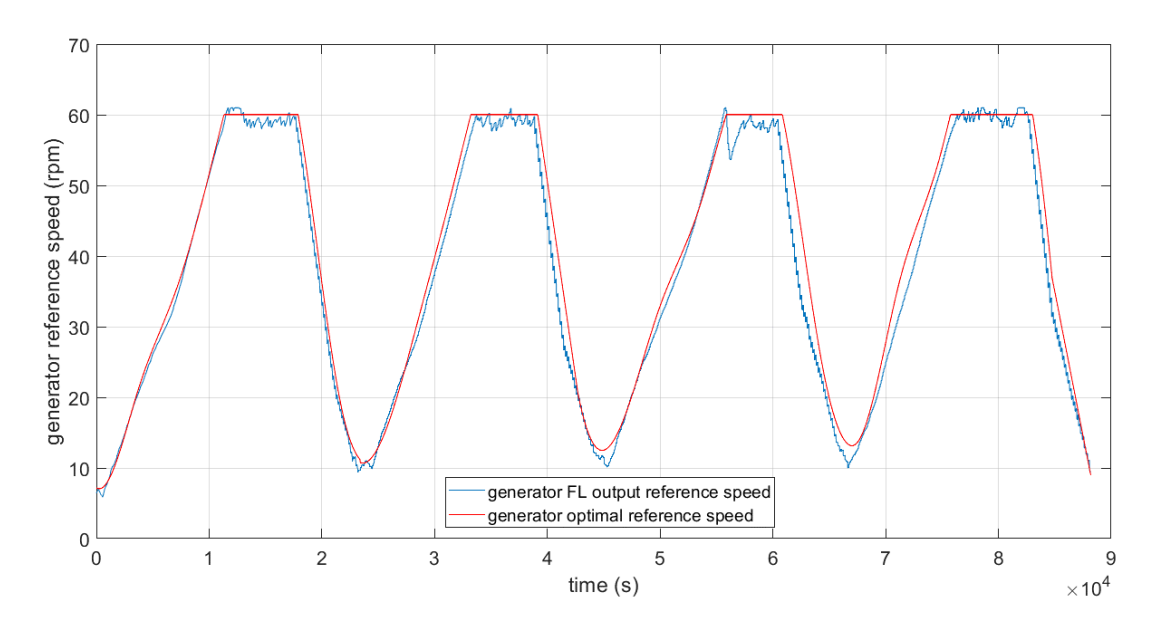


Figure 6.34 FL control output reference speed under 24 hour tidal input

Figure 6.35 illustrates the FL control active power under 24 hour simulation. From this figure it can be seen that, under different tidal cycles, the FL control can provide the desired power to the grid.

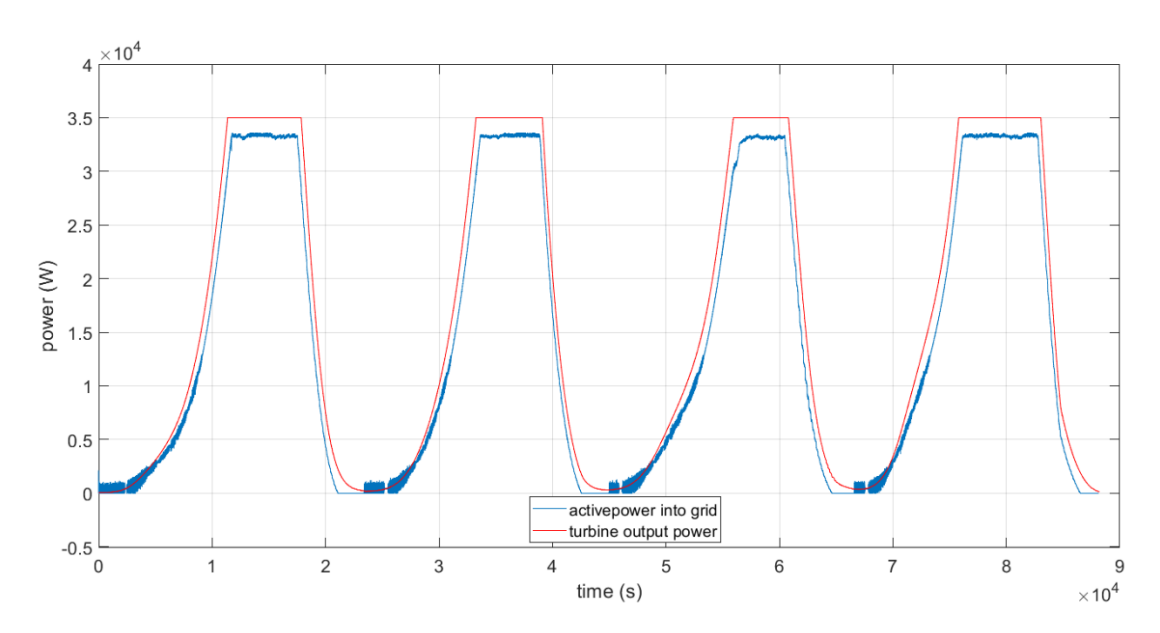


Figure 6.35 FL control active power under 24 hour tidal input

From Figure 6.32 to Figure 6.35, it is possible to estimate the full year energy production of the tidal turbine under the different control schemes. In order to validate the estimation accuracy, Figure 6.36 shows the difference between the estimated (i.e. ideal) power curve, P&O control and FL control power. It can be seen that the estimated power is higher than the other two as it is the ideal result.

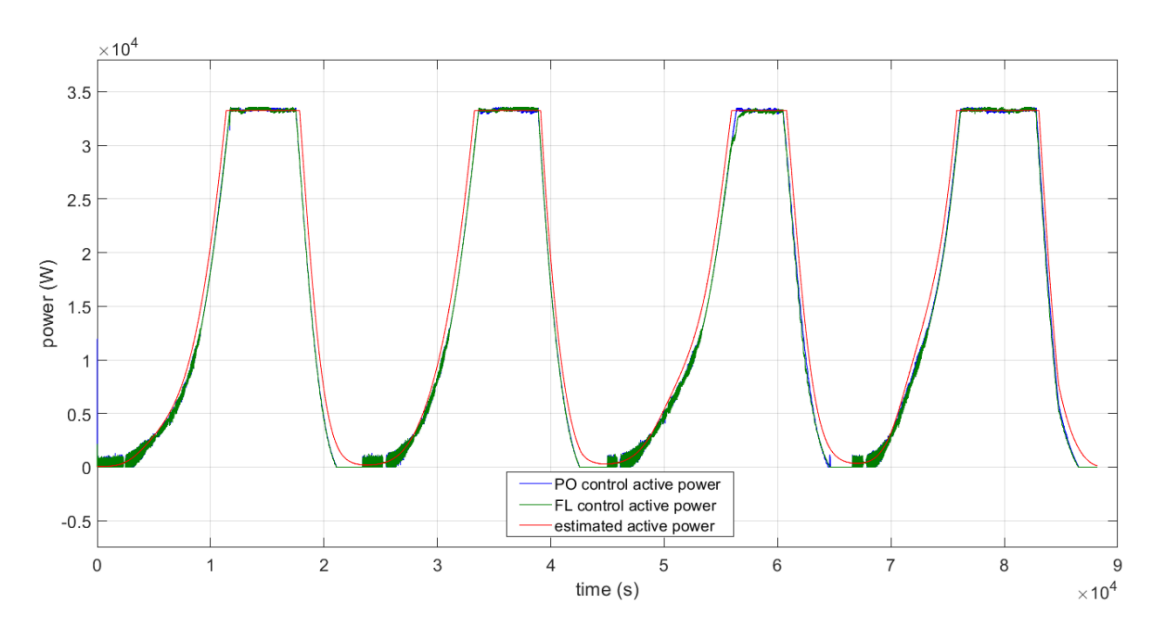


Figure 6.36 Estimated, P&O control and FL control active power

Tale 6.2 presents the percentage energy yield and energy production over the 24 hour simulation. The energy yield and energy production of P&O control and FL control are again similar, and both are below the estimated energy yield and production.

Control strategy	Percentage Energy yield	Energy production (MWh)
Perturb and Observe control	89.95%	352.77
Fuzzy Logic control	88.71%	350.72
Estimated	95%	376.85

Table 6.2 Energy yield and energy production for 24 hour tidal input

According to Figure 6.36 and Table 6.2, the energy production for a whole year is estimated to be 130 GWh (ideal). This is calculated from Equation 2.2, using the maximum turbine rated power as a limitation with 95% efficiency. Based on the estimation of the ideal condition, the FL control is estimated to produce 121GWh annual power output while multiple variable step size P&O control is estimated to generate 123GWh annual energy output.

From the generator reference speed, the powers and the energy yield illustrated above and the discussions, it can be seen that both FL control and P&O control can track the maximum power points effectively, and the active powers that are transferred to the grid are very close to the conventional sensor control, with the difference in percentage energy yield being less than 1% difference and the difference in energy production a maximum of 700kWh under a

tidal cycle. Comparing the FL control and P&O control, the performances are even closer, with only 0.22% difference in the percentage energy yield and less than 200kWh difference in the energy production.

Under this situation, with similar performance between FL control and P&O control, the choice of control strategy will not only focus on the percentage energy yield or energy production but will also need to consider the control strategy complexity, stability and operability. Both FL control and P&O control have been widely applied in real world wind and PV systems. The reliability and feasibility of the control strategies have been proved. However, for the tidal current generation systems, due to the high cost of maintenance work, the requirements of reliability and robustness of the system are fundamental, thus the choice for the developers also needs to consider the cost.

For FL control, during the control parameter tunning process, the fuzzy inference part needs significant work and experience, i.e. it requires experts' knowledge. Also, when the input variables increase aiming to get more accurate results, the complexity of FL control will rise sharply. This happens during the parameter tunning process, and more MFs result in greater computational requirements, which limits the improvement of FL control's efficiency. The high real-time processing computational resource requirements of a FL controller may lead to system delays and increase the cost.

For P&O control, when adjusting the control parameters, it was found that it sometimes faces the output drift problems (discussed in Section 4.5.2), this mainly happens in the system when there are sudden changes in the inputs, for example in this thesis, the drift problem is only found when using the step change input, while using the ramp change input and the real tidal current input data, because these inputs change slowly, the drift problem does not occur. Similar to the FL control, the parameter tunning also requires expert knowledge, but due to its simple calculation process, the computational requirements are not as high as FL does, this will lead to a faster response and lower energy cost.

In summary, from the results for percentage energy yield and energy production, both P&O control and FL can have similar performances, even compared to the conventional sensor control system. However, considering the cost savings and real applications, the author recommends the multiple variable step size P&O control as the potential solution for tidal current turbine generation system sensor-less control, due to its simple structure, low requirements in terms of computational resource and lower cost.

6.5 Summary

This chapter has investigated the performance of FL control and P&O control applications in the tidal current turbine generation system over an extended period of tidal current velocity input. The results have proved that both of the control strategies are able to track the MPP without a signal from a tidal current velocity sensor. The FL and P&O multiple variable step size control can provide the reference speed signal for the generator, with the average efficiencies of the two control strategies being over 90%. The turbine output power follows the theoretical power (Equation 3.3 and Figure 3.11). From the control strategies' output reference speed, power curves and efficiencies, it has been demonstrated that both FL control and P&O control have quality of performance for the system operating with the real tidal velocity data (tidal current velocity rise from low tide to high tide and back to low tide). Also, the detailed performance and relationships in reference speed, generator power and efficiencies have been discussed and analysed. The comparison of P&O control and FL control performance are presented, and from the results and figures it can be seen that the P&O control and FL control have very similar performance. The detailed conclusions of P&O control and FL control are presented in the next chapter, as well as recommendations for future work to further investigate the performance of P&O control and FL control strategies in tidal current turbine generation systems to eliminate the need for a tidal current velocity sensor.

Chapter 7. Conclusions and Recommendations for Further Work

7.1 Conclusions

Tidal current turbine generation systems are subjected to the harsh underwater environment and suffer from a high rate of failures in the electrical side. The tidal current turbine system operation will be interrupted and require unplanned maintenance if one electrical or control system failure occurs. Human intervention needs significant planning, and the maintenance work may need to be conducted on land, which will lead to a long power transmission interruption, significantly decreasing the power generation reliability and increasing the cost. In this context, in order to avoid unscheduled maintenance work, improve the power conversion efficiency and increase the tidal current turbine system reliability and robustness, tidal current velocity sensor-less MPPT control strategies were implemented in this thesis to eliminate the tidal current velocity sensor. The proposed sensor-less MPPT control strategy can improve the system reliability, ensuring continuous operation of the system without the tidal current velocity sensor, and tracking the maximum power point as well.

To evaluate the performance of the proposed strategies, a detailed comparison between P&O and FL control methods was conducted under different conditions.

7.1.1 Comparison of P&O and FL under step change and ramp change input

The comparisons between P&O control and FL control were illustrated, through power efficiency, generator speed, turbine output power, generator output power, active and reactive power to compare the control performance.

From the results, both P&O and FL based MPPT sensor-less control can track the MPP without the tidal current velocity sensor signals. The P&O control has a slightly higher average power efficiency than FL control, due to the faster response at the beginning of the simulation. For the turbine output power and generator output power, the fluctuations of generator speed during steady states will not affect the turbine and generator output power significantly, as well as the active power that injected to the grid. The overall performance of P&O control and FL control do not have big differences. The P&O control has a slightly quicker response at the beginning while the FL control has smaller fluctuations during the steady state. However, the P&O control can have a drift problem while this was not found in FL control.

7.1.2 Control performance with real tidal current velocity input

The feasibility of P&O control and FL control was initially tested and analysed under both step change and ramp change tidal current velocity inputs. The conventional grid-connected tidal current turbine generation system with P&O and FL control was then tested under the realistic tidal current velocity condition, to evaluate the performance of the system for a tidal cycle.

The variable step size P&O control that was developed in Chapter 4 could not track the MPP efficiently. Thus, multiple variable step size P&O control was implemented, by determining different power change ranges to allow the P&O to have different output values, which can fit the realistic tidal current velocity change.

Both multiple variable step size P&O control and FL control were simulated under real tidal current velocity input and the results are illustrated and discussed in Chapter 6. From the results, in terms of the energy yield and energy production, multiple variable step size P&O control and FL control have very similar performance. The simulation results of multiple variable step size P&O control and FL control have illustrated the possibility of the control strategies applied in conventional grid-connected TCT system to eliminate the tidal current velocity sensor.

In addition to conducting a quantitative evaluation of the results, the author also carried out a qualitative assessment to identify the strengths and weaknesses of various control methods. Taking multiple factors into account, the author recommended the multi-variable step size P&O control as an effective solution for sensor less control.

7.1.3 Discussion of wider issues

The model built in this thesis was based on the turbine Evopod E35, which is a ¼ scale test turbine. The conventional control system developed in this thesis is used in many large capacity tidal current turbine systems, such as the MeyGen and O2 projects suggesting that system built in this thesis could readily be scaled up.

Generally, in tidal current turbine generation systems, the turbines are designed and located to avoid flow speeds exceeding the cut-out speed, to ensure the safety of the equipment, extend the lifespan and maximize the energy capture. Based on this premise, it would be expected that the turbine system would not face a cut-out situation frequently, for example, the MeyGen turbines' cut-out speed is 5m/s, while the environment maximum flow speed in the

installation area is approximately 4m/s. Thus in this thesis, when designing the sensor-less control systems the cut-out problem has not been considered. In practice, one potential solution for sensor-less control to deal with the cut-out problem will be a time-base estimation. As the tidal current resource is highly predictable, when the tidal current flow reaches the cut-out speed, the brake can be applied to stop the turbine, and after a calculated period of time, the brake can be released for the turbine to operate again.

7.1.4 Generalisation and limitations of proposed control strategies

The P&O and FL based MPPT sensor-less control strategy can provide continuous operation of the conventional tidal current turbine generation system without a tidal current speed sensor, and does not require any system changes in terms of the generator or the converter structure.

For horizontal-axis tidal current turbines, PMGs and with conventional grid-connected control loops (such as O2 project mentioned in Chapter 3), with both seabed mounted or floating systems, the multiple variable step size P&O control and FL control will be able to be applied to operate the system without a tidal current velocity sensor. For the systems with DFIGs, the generator side control is slightly different from PMGs, but conventionally they still need a tidal current velocity signal to calculate the optimal generator reference speed. Thus, the P&O control and FL control would be able to be applied in a horizontal-axis TCT system with a DFIG.

The way that vertical axis tidal current turbines capture energy is similar to the horizontal axis turbines, thus, for every tidal current velocity, there still an optimal rotation speed for the vertical turbine to capture maximum power through the tip-speed-ratio. Thus, for the vertical turbine system, with PMGs or DFIGs, P&O control and FL control can still be applied to realize tidal current velocity sensor-less MPPT control.

In Chapter 6, in order run the simulation model for a long time, the grid side converter detailed model was replaced by an average model with equivalent voltage sources. The AC voltage will not contain the harmonics that arise from the converter switching, but the dynamics of control system and power system are modelled.

Both the proposed P&O control with multiple variable step size and the FL control require iterative tuning of the parameters. The control strategies both require tuning for a specific turbine and generator and the control parameters would require adjustment if the system was used on a different TCT arrangement. Other research has been conducted into sensor-less

control for tidal current turbine systems, such as in paper [172] where the adaptive Extreme Learning Machine (ELM) is applied to realize the sensor-less control to track the maximum power points. This methodology requires a substantial amount of initial data to train the ELM model. The system presented in this paper also uses a control structure based on a hydraulic transmission system rather than a traditional electric power converter. In comparison, the FL and P&O control do not require detailed knowledge of the turbine and generator characteristics beyond the initial tuning, and can be applied to conventional tidal current turbines electrical systems.

7.1.5 Thesis contributions

The main contributions of this thesis are as follow:

- 1. A variable step size P&O MPPT control has been implemented in the conventional tidal current system and compared with traditional fixed step size P&O control, showing that the variable step size P&O control offers higher efficiency and smaller error (less than 2%).
- The FL and P&O control in conventional grid-connected TCT systems have been developed to provide generator reference speed signal directly instead of providing the PWM switching signals of traditional systems and as demonstrated in the stand alone system.
- 3. Long term simulation of conventional grid-connected TCT system under real tidal current velocity (one tidal cycle) has been demonstrated. The multiple variable step size P&O control strategy has been developed to solve the P&O control tracking problem under realistic tidal current velocity. Both the multiple variable step size P&O and FL control have been developed to provide tidal current velocity sensor-less MPPT control performance under realistic conditions.

7.2 Recommendations for further work

This thesis has presented P&O and FL based MPPT sensor-less control to deal with a tidal current speed sensor fault for conventional grid-connected system. In tidal current turbine generation systems, subject to the harsh subsea environment, it is not only the tidal current speed sensor that may be damaged. In order to address a series of issues, fault tolerant control strategies need to be applied to deal with the tidal current system electrical failures.

For the control strategy used in this thesis, if a fault detection system can be applied together

with the control strategy, then when the detection system identifies that either the tidal current velocity sensor signal is unusual or lost, it could switch to the tidal current velocity sensor-less control. This will help to improve the system power transmission efficiency, make the system more reliable, and also improve the system robustness and fault tolerance.

If other faults happen in the tidal current turbine system, a single fault tolerant control strategy will not typically be able to solve all of the problems. A fault tolerant control strategy which can combine some common electrical and control system failures needs to be employed to improve the system fault tolerance.

When several failures occur at once, a fault detection and isolation system would be helpful to recognize which part of the system has a problem and isolate the fault from the main system and, if available, start a spare equipment item to maintain the system operation and wait for human intervention to make a decision as to whether offshore maintenance is needed. This will improve the system reliability and robustness significantly.

Reference

- [1] Z. Zhang, Y. Zhang, Q. Huang, and W.-J. Lee, "Market-oriented optimal dispatching strategy for a wind farm with a multiple stage hybrid energy storage system," *CSEE Journal of power and energy systems*, vol. 4, no. 4, pp. 417-424, 2018.
- [2] K. Umoh and M. Lemon, "Drivers for and barriers to the take up of floating offshore wind technology: a comparison of Scotland and South Africa," *Energies*, vol. 13, no. 21, p. 5618, 2020.
- [3] H. Chen, T. Tang, N. Aït-Ahmed, M. E. H. Benbouzid, M. Machmoum, and M. E.-H. Zaïm, "Attraction, challenge and current status of marine current energy," *IEEE Access*, vol. 6, pp. 12665-12685, 2018.
- [4] T. Xie, T. Wang, Q. He, D. Diallo, and C. Claramunt, "A review of current issues of marine current turbine blade fault detection," *Ocean Engineering*, vol. 218, p. 108194, 2020.
- [5] J. Forslund, A. Goude, and K. Thomas, "Validation of a Coupled Electrical and Hydrodynamic Simulation Model for a Vertical Axis Marine Current Energy Converter," *Energies*, vol. 11, no. 11, p. 3067, 2018.
- [6] J. N. Goundar and M. R. Ahmed, "Marine current energy resource assessment and design of a marine current turbine for Fiji," *Renewable Energy*, vol. 65, pp. 14-22, 2014.
- [7] Z. Ren, Y. Wang, H. Li, X. Liu, Y. Wen, and W. Li, "A coordinated planning method for micrositing of tidal current turbines and collector system optimization in tidal current farms," *IEEE Transactions on Power Systems*, vol. 34, no. 1, pp. 292-302, 2018.
- [8] M. C. Sousounis, J. K. Shek, and M. A. Mueller, "Modelling, control and frequency domain analysis of a tidal current conversion system with onshore converters," *IET Renewable Power Generation*, vol. 10, no. 2, pp. 158-165, 2016.
- [9] Z. Liu, A. Houari, M. Machmoum, M.-F. Benkhoris, and T. Tang, "An active FTC strategy using generalized proportional integral observers applied to five-phase PMSG based tidal current energy conversion systems," *Energies*, vol. 13, no. 24, p. 6645, 2020.
- [10] MeyGen. https://saerenewables.com/tidal-stream/meygen/ (accessed 26/03, 2024).
- [11] N. Energy. "MeyGen Tidal Power Project, Pentland Firth." https://www.nsenergybusiness.com/projects/meygen-tidal-power-project/ (accessed 26/03, 2024).
- [12] A. Al Ameri, A. Payman, B. Dakyo, and M. B. Camara, "Control Strategy for Orbital O2 Tidal System Based on EMR Model," in *International Conference of the IMACS TC1 Committee*, 2021: Springer, pp. 85-96.
- [13] O. M. Power. "Orbital Marine Power O2 at EMEC." https://tethys.pnnl.gov/project-sites/orbital-marine-power-o2-emec (accessed 2024, 26/03).
- [14] O. M. Power. "Obtial Marine Power." https://www.orbitalmarine.com/technology/ (accessed 26/03, 2024).
- [15] Seetao. "Zhejiang Zhoushan tidal energy power station successfully launched." https://www.seetao.com/details/141111.html (accessed 26/03, 2024).
- [16] N. O. T. Center. http://www.notcsoa.org.cn/cn/index/show/3520 (accessed 26/03, 2024).
- [17] O. E. Systems. "ANNUAL REPORT 2018." https://report2018.ocean-energy-systems.org/ (accessed 260/03, 2024).
- [18] G. Deng, Z. Zhang, Y. Li, H. Liu, W. Xu, and Y. Pan, "Prospective of development of large-scale tidal current turbine array: An example numerical investigation of Zhejiang,

- China," Applied energy, vol. 264, p. 114621, 2020.
- [19] F. Mekri, S. Benelghali, M. Benbouzid, and J. F. Charpentier, "A fault-tolerant multiphase permanent magnet generator for marine current turbine applications," in 2011 IEEE International Symposium on Industrial Electronics, 2011: IEEE, pp. 2079-2084.
- [20] Y. Amirat, M. E. H. Benbouzid, E. Al-Ahmar, B. Bensaker, and S. Turri, "A brief status on condition monitoring and fault diagnosis in wind energy conversion systems," *Renewable and sustainable energy reviews*, vol. 13, no. 9, pp. 2629-2636, 2009.
- [21] Y. Li, W. Jiang, G. Zhang, and L. Shu, "Wind turbine fault diagnosis based on transfer learning and convolutional autoencoder with small-scale data," *Renewable Energy*, vol. 171, pp. 103-115, 2021.
- [22] H.-T. Pham, J.-M. Bourgeot, and M. E. H. Benbouzid, "Comparative investigations of sensor fault-tolerant control strategies performance for marine current turbine applications," *IEEE Journal of Oceanic Engineering*, vol. 43, no. 4, pp. 1024-1036, 2017.
- [23] S. E. B. Elghali, M. E. H. Benbouzid, T. Ahmed-Ali, and J. F. Charpentier, "High-order sliding mode control of a marine current turbine driven doubly-fed induction generator," *IEEE Journal of Oceanic Engineering*, vol. 35, no. 2, pp. 402-411, 2010.
- [24] F. Mekri, S. B. Elghali, and M. E. H. Benbouzid, "Fault-tolerant control performance comparison of three-and five-phase PMSG for marine current turbine applications," *IEEE Transactions on sustainable Energy*, vol. 4, no. 2, pp. 425-433, 2012.
- [25] S. Djebarri, J.-F. Charpentier, F. Scuiller, and M. Benbouzid, "Influence of fixed-pitch tidal turbine hydrodynamic characteristic on the generator design," in *11th European Wave and Tidal Energy Conference*, 2015: EWTEC, pp. 8A2-2-1 8A2-2-10.
- [26] M. Leijon, H. Bernhoff, M. Berg, and O. Ågren, "Economical considerations of renewable electric energy production—especially development of wave energy," *Renewable Energy*, vol. 28, no. 8, pp. 1201-1209, 2003.
- [27] R. Gao and Z. Gao, "Pitch control for wind turbine systems using optimization, estimation and compensation," *Renewable Energy*, vol. 91, pp. 501-515, 2016.
- [28] C.-N. Wang, W.-C. Lin, and X.-K. Le, "Modelling of a PMSG wind turbine with autonomous control," *Mathematical Problems in Engineering*, vol. 2014, 2014.
- [29] A. Z. Mohamed, M. N. Eskander, and F. A. Ghali, "Fuzzy logic control based maximum power tracking of a wind energy system," *Renewable energy*, vol. 23, no. 2, pp. 235-245, 2001.
- [30] E. Omerdic, D. Toal, S. Nolan, H. Ahmad, and G. Duffy, "Design & development of assistive tools for future applications in the field of renewable ocean energy," in *OCEANS 2011 IEEE-Spain*, 2011: IEEE, pp. 1-6.
- [31] Y. Li and H. K. Florig, "Modeling the operation and maintenance costs of a large scale tidal current turbine farm," in *OCEANS 2006*, 2006: IEEE, pp. 1-6.
- [32] M. Muenchhof, M. Beck, and R. Isermann, "Fault-tolerant actuators and drives—Structures, fault detection principles and applications," *Annual reviews in control*, vol. 33, no. 2, pp. 136-148, 2009.
- [33] D. Campos-Delgado, D. Espinoza-Trejo, and E. Palacios, "Fault-tolerant control in variable speed drives: a survey," *IET Electric Power Applications*, vol. 2, no. 2, pp. 121-134, 2008.
- [34] M. A. Parker, C. Ng, and L. Ran, "Fault-tolerant control for a modular generator—converter scheme for direct-drive wind turbines," *IEEE Transactions on Industrial Electronics*, vol. 58, no. 1, pp. 305-315, 2010.
- [35] K. Rothenhagen and F. W. Fuchs, "Doubly fed induction generator model-based sensor fault detection and control loop reconfiguration," *IEEE Transactions on*

- Industrial Electronics, vol. 56, no. 10, pp. 4229-4238, 2009.
- [36] K. Rothenhagen and F. W. Fuchs, "Current sensor fault detection, isolation, and reconfiguration for doubly fed induction generators," *IEEE Transactions on Industrial Electronics*, vol. 56, no. 10, pp. 4239-4245, 2009.
- [37] S. Benelghali, F. Mekri, M. Benbouzid, and J. F. Charpentier, "Performance comparison of three—and five-phase permanent magnet generators for marine current turbine applications under open-circuit faults," in *2011 International Conference on Power Engineering, Energy and Electrical Drives*, 2011: IEEE, pp. 1-6.
- [38] F. Baudart, B. Dehez, E. Matagne, D. Telteu-Nedelcu, P. Alexandre, and F. Labrique, "Torque control strategy of polyphase permanent-magnet synchronous machines with minimal controller reconfiguration under open-circuit fault of one phase," *IEEE Transactions on Industrial Electronics*, vol. 59, no. 6, pp. 2632-2644, 2011.
- [39] H. Guo and J. Xu, "Fault tolerant control with torque limitation based on fault mode for ten-phase permanent magnet synchronous motor," *Chinese Journal of Aeronautics*, vol. 28, no. 5, pp. 1464-1475, 2015.
- [40] Z. Zhou, F. Scuiller, J. F. Charpentier, M. E. H. Benbouzid, and T. Tang, "Power control of a nonpitchable PMSG-based marine current turbine at overrated current speed with flux-weakening strategy," *IEEE journal of oceanic engineering*, vol. 40, no. 3, pp. 536-545, 2014.
- [41] Y. Dong, Y. Zhao, W. Zhu, X. Zhang, and J. Guo, "Development of a simple power controller for horizontal-axis standalone tidal current energy generation system," *International Journal of Global Energy Issues*, vol. 40, no. 1-2, pp. 117-127, 2017.
- [42] M. Hannachi and M. Benhamed, "Modeling and control of a variable speed wind turbine with a permanent magnet synchronous generator," in 2017 International conference on green energy conversion systems (GECS), 2017: IEEE, pp. 1-6.
- [43] A. Honarbari, S. Najafi-Shad, M. Saffari Pour, S. S. M. Ajarostaghi, and A. Hassannia, "MPPT Improvement for PMSG-Based Wind Turbines Using Extended Kalman Filter and Fuzzy Control System," *Energies*, vol. 14, no. 22, p. 7503, 2021.
- [44] K. Xiahou and Q. Wu, "Fault-tolerant control of doubly-fed induction generators under voltage and current sensor faults," *International Journal of Electrical Power & Energy Systems*, vol. 98, pp. 48-61, 2018.
- [45] H.-T. Pham, J.-M. Bourgeot, and M. Benbouzid, "Performance comparison of sensor fault-tolerant control strategies for PMSG-based marine current energy converters," in *IECON 2015-41st Annual Conference of the IEEE Industrial Electronics Society*, 2015: IEEE, pp. 003417-003422.
- [46] C. Johnstone, K. Nielsen, T. Lewis, A. Sarmento, and G. Lemonis, "EC FPVI coordinated action on ocean energy: A European platform for sharing technical information and research outcomes in wave and tidal energy systems," *Renewable Energy*, vol. 31, no. 2, pp. 191-196, 2006.
- [47] A. Von Jouanne and T. K. Brekken, "Ocean and geothermal energy systems," *Proceedings of the IEEE*, vol. 105, no. 11, pp. 2147-2165, 2017.
- [48] T. Ravens, K. Cunningham, and G. Scott, "Assessment and mapping of the riverine hydrokinetic energy resource in the continental United States," *Electric Power Research Institute, Palo Alto, CA, Retrieved:* http://water. energy. gov/pdfs/riverine hydrokinetic resource assessment and mapping. pdf, 2012.
- [49] X. Yang, K. A. Haas, and H. M. Fritz, "Evaluating the potential for energy extraction from turbines in the gulf stream system," *Renewable energy*, vol. 72, pp. 12-21, 2014.
- [50] S. B. Elghali, M. E. H. Benbouzid, and J.-F. Charpentier, "Modelling and control of a marine current turbine-driven doubly fed induction generator," *IET Renewable Power Generation*, vol. 4, no. 1, pp. 1-11, 2010.
- [51] D. Magagna and A. Uihlein, "Ocean energy development in Europe: Current status

- and future perspectives," *International Journal of Marine Energy*, vol. 11, pp. 84-104, 2015.
- [52] G. Cada *et al.*, "Potential impacts of hydrokinetic and wave energy conversion technologies on aquatic environments," *Fisheries*, vol. 32, no. 4, pp. 174-181, 2007.
- [53] M. Nachtane, M. Tarfaoui, I. Goda, and M. Rouway, "A review on the technologies, design considerations and numerical models of tidal current turbines," *Renewable Energy*, vol. 157, pp. 1274-1288, 2020.
- [54] L. Kitzing, C. Mitchell, and P. E. Morthorst, "Renewable energy policies in Europe: Converging or diverging?," *Energy policy*, vol. 51, pp. 192-201, 2012.
- [55] L. Blunden and A. Bahaj, "Initial evaluation of tidal stream energy resources at Portland Bill, UK," *Renewable Energy*, vol. 31, no. 2, pp. 121-132, 2006.
- [56] D. Coles *et al.*, "A review of the UK and British Channel Islands practical tidal stream energy resource," *Proceedings of the Royal Society A*, vol. 477, no. 2255, p. 20210469, 2021.
- [57] O. R. E. Catapult, "Tidal stream and wave energy cost reduction and industrial benefit," Technical report. Glasgow, UK: ORE Catapult, 2018.
- [58] M. R. Barakat, B. Tala-Ighil, H. Chaoui, H. Gualous, Y. Slamani, and D. Hissel, "Energetic macroscopic representation of a marine current turbine system with loss minimization control," *IEEE Transactions on Sustainable Energy*, vol. 9, no. 1, pp. 106-117, 2017.
- [59] H. H. Aly and M. El-Hawary, "Small signal stability analysis comparison of tidal current energy using DFIG and DDPMSG," in *2012 IEEE Electrical Power and Energy Conference*, 2012: IEEE, pp. 229-232.
- [60] H. H. Aly, "Dynamic modeling and control of the tidal current turbine using DFIG and DDPMSG for power system stability analysis," *International Journal of Electrical Power & Energy Systems*, vol. 83, pp. 525-540, 2016.
- [61] G. Li and W. Zhu, "A Review on Up-to-Date Gearbox Technologies and Maintenance of Tidal Current Energy Converters," *Energies*, vol. 15, no. 23, p. 9236, 2022.
- [62] J. Faiz and A. Nematsaberi, "Linear electrical generator topologies for direct-drive marine wave energy conversion-an overview," *IET Renewable Power Generation*, vol. 11, no. 9, pp. 1163-1176, 2017.
- [63] F. O. Rourke, F. Boyle, and A. Reynolds, "Tidal energy update 2009," *Applied energy*, vol. 87, no. 2, pp. 398-409, 2010.
- [64] L. Blunden and A. Bahaj, "Tidal energy resource assessment for tidal stream generators," *Proceedings of the Institution of Mechanical Engineers, Part A: Journal of Power and Energy,* vol. 221, no. 2, pp. 137-146, 2007.
- [65] T. E. M. E. Centre. "OPEN HYDRO." https://www.emec.org.uk/about-us/our-tidal-clients/open-hydro/ (accessed 27/03, 2024).
- [66] S. Toumi, E. Elbouchikhi, Y. Amirat, M. Trabelsi, M. Benbouzid, and M. F. Mimouni, "Marine current turbine system post-fault behavior under an open circuit fault," *Advances in Electrical and Electronic Engineering*, vol. 16, no. 3, pp. 279-287, 2018.
- [67] S. Toumi, S. B. Elghali, M. Trabelsi, E. Elbouchikhi, M. Benbouzid, and M. F. Mimouni, "Robustness analysis and evaluation of a PMSG-based marine current turbine system under faulty conditions," in 2014 15th International Conference on Sciences and Techniques of Automatic Control and Computer Engineering (STA), 2014: IEEE, pp. 631-636.
- [68] S. Toumi, Y. Amirat, E. Elbouchikhi, M. Trabelsi, M. Benbouzid, and M. F. Mimouni, "A comparison of fault-tolerant control strategies for a pmsg-based marine current turbine system under generator-side converter faulty conditions," *Journal of Electrical Systems*, vol. 13, no. 3, pp. 472-488, 2017.

- [69] L. Myers and A. Bahaj, "Power output performance characteristics of a horizontal axis marine current turbine," *Renewable energy*, vol. 31, no. 2, pp. 197-208, 2006.
- [70] K. Ghefiri, S. Bouallègue, I. Garrido, A. J. Garrido, and J. Haggège, "Complementary power control for doubly fed induction generator-based tidal stream turbine generation plants," *Energies*, vol. 10, no. 7, p. 862, 2017.
- [71] A. Habibic. "DeepOcean performs offshore maintenance on MeyGen tidal energy project." https://www.offshore-energy.biz/deepocean-performs-offshore-maintenance-on-meygen-tidal-energy-project/ (accessed 27/03, 2023).
- [72] O. M. Power. https://www.orbitalmarine.com/o2/ (accessed 2024, 27/03).
- [73] Y. Zhao, C. Wei, Z. Zhang, and W. Qiao, "A review on position/speed sensorless control for permanent-magnet synchronous machine-based wind energy conversion systems," *IEEE Journal of Emerging and Selected Topics in Power Electronics*, vol. 1, no. 4, pp. 203-216, 2013.
- [74] R. Datta and V. Ranganathan, "A method of tracking the peak power points for a variable speed wind energy conversion system," *IEEE Transactions on Energy conversion*, vol. 18, no. 1, pp. 163-168, 2003.
- [75] J. Hui, A. Bakhshai, and P. K. Jain, "An adaptive approximation method for maximum power point tracking (MPPT) in wind energy systems," in *2011 IEEE Energy Conversion Congress and Exposition*, 2011: IEEE, pp. 2664-2669.
- [76] J. Shen, Z. Zhu, and D. Howe, "Improved speed estimation in sensorless PM brushless AC drives," *IEEE Transactions on Industry Applications*, vol. 38, no. 4, pp. 1072-1080, 2002.
- [77] A. B. Kulkarni and M. Ehsani, "A novel position sensor elimination technique for the interior permanent-magnet synchronous motor drive," *IEEE Transactions on Industry Applications*, vol. 28, no. 1, pp. 144-150, 1992.
- [78] S. Fan, P. Wang, and C. Wen, "A new sensorless control strategy used in direct-drive PMSG wind power system," in *The 2nd International Symposium on Power Electronics for Distributed Generation Systems*, 2010: IEEE, pp. 611-615.
- [79] S. Chi, Z. Zhang, and L. Xu, "Sliding-mode sensorless control of direct-drive PM synchronous motors for washing machine applications," *IEEE Transactions on Industry Applications*, vol. 45, no. 2, pp. 582-590, 2009.
- [80] W. Gao and Z. Guo, "Speed sensorless control of PMSM using model reference adaptive system and RBFN," *Journal of networks*, vol. 8, no. 1, p. 213, 2013.
- [81] I. Jlassi, S. K. El Khil, and N. M. Bellaaj, "Power switch and current sensor fault-tolerant control of PMSG drives for wind turbine systems," in 2015 IEEE 10th International Symposium on Diagnostics for Electrical Machines, Power Electronics and Drives (SDEMPED), 2015: IEEE, pp. 401-407.
- [82] S. Toumi *et al.*, "Modeling and simulation of a PMSG-based marine current turbine system under faulty rectifier conditions," *Electric Power Components and Systems*, vol. 45, no. 7, pp. 715-725, 2017.
- [83] S. Benelghali, M. E. H. Benbouzid, J. F. Charpentier, T. Ahmed-Ali, and I. Munteanu, "Experimental validation of a marine current turbine simulator: Application to a permanent magnet synchronous generator-based system second-order sliding mode control," *IEEE Transactions on Industrial Electronics*, vol. 58, no. 1, pp. 118-126, 2010.
- [84] W. Qiao, X. Yang, and X. Gong, "Wind speed and rotor position sensorless control for direct-drive PMG wind turbines," *IEEE Transactions on Industry Applications*, vol. 48, no. 1, pp. 3-11, 2011.
- [85] J. Liu, J. Hu, and L. Xu, "Sliding mode observer for wide speed range sensorless induction machine drives: Considerations for digital implementation," in *IEEE International Conference on Electric Machines and Drives*, 2005., 2005: IEEE, pp.

- 300-307.
- [86] S.-H. Moon, B.-G. Park, J.-W. Kim, and J.-M. Kim, "Maximum power-point tracking control using perturb and observe algorithm for tidal current generation system," *International Journal of Precision Engineering and Manufacturing-Green Technology*, vol. 7, no. 4, pp. 849-858, 2020.
- [87] B.-G. Kim, C.-J. Yang, and M.-S. Choi, "A study on the performance of an 100 kW class tidal current turbine," *Journal of the Korean Society of Marine Environment & Safety*, vol. 18, no. 2, pp. 145-152, 2012.
- [88] A. Bahaj and L. E. Myers, "Fundamentals applicable to the utilisation of marine current turbines for energy production," *Renewable energy*, vol. 28, no. 14, pp. 2205-2211, 2003.
- [89] N. S. D'Souza, L. A. Lopes, and X. Liu, "Comparative study of variable size perturbation and observation maximum power point trackers for PV systems," *Electric Power Systems Research*, vol. 80, no. 3, pp. 296-305, 2010.
- [90] F. Paz and M. Ordonez, "Zero oscillation and irradiance slope tracking for photovoltaic MPPT," *IEEE Transactions on Industrial electronics*, vol. 61, no. 11, pp. 6138-6147, 2014.
- [91] M. Munoz, M. C. Alonso-García, N. Vela, and F. Chenlo, "Early degradation of silicon PV modules and guaranty conditions," *Solar energy*, vol. 85, no. 9, pp. 2264-2274, 2011.
- [92] S. B. Kjær, "Evaluation of the "hill climbing" and the "incremental conductance" maximum power point trackers for photovoltaic power systems," *IEEE Transactions on Energy Conversion*, vol. 27, no. 4, pp. 922-929, 2012.
- [93] M. A. Elgendy, B. Zahawi, and D. J. Atkinson, "Assessment of perturb and observe MPPT algorithm implementation techniques for PV pumping applications," *IEEE transactions on sustainable energy*, vol. 3, no. 1, pp. 21-33, 2011.
- [94] S. Lalouni, D. Rekioua, K. Idjdarene, and A. Tounzi, "Maximum power point tracking based hybrid hill-climb search method applied to wind energy conversion system," *Electric Power Components and Systems*, vol. 43, no. 8-10, pp. 1028-1038, 2015.
- [95] A. A. Chhipa *et al.*, "Adaptive neuro-fuzzy inference system-based maximum power tracking controller for variable speed WECS," *Energies*, vol. 14, no. 19, p. 6275, 2021.
- [96] A. C.-C. Hua and B. C.-H. Cheng, "Design and implementation of power converters for wind energy conversion system," in *The 2010 International Power Electronics Conference-ECCE ASIA*-, 2010: IEEE, pp. 323-328.
- [97] N. Femia, D. Granozio, G. Petrone, G. Spagnuolo, and M. Vitelli, "Predictive & adaptive MPPT perturb and observe method," *IEEE Transactions on Aerospace and Electronic Systems*, vol. 43, no. 3, pp. 934-950, 2007.
- [98] H. R. Chamorro, I. Riano, R. Gerndt, I. Zelinka, F. Gonzalez-Longatt, and V. K. Sood, "Synthetic inertia control based on fuzzy adaptive differential evolution," *International Journal of Electrical Power & Energy Systems*, vol. 105, pp. 803-813, 2019.
- [99] A. Elfergani, M. A. Elsharif, R. H. Hamd, S. M. Saad, N. El Naily, and F. A. Mohamed, "Advanced self-tuned pitch angle control based on fuzzy logic for grid connected variable-speed wind turbine system," in 2018 9th International Renewable Energy Congress (IREC), 2018: IEEE, pp. 1-6.
- [100] W. Ayrir, M. Ourahou, B. El Hassouni, and A. Haddi, "Direct torque control improvement of a variable speed DFIG based on a fuzzy inference system," *Mathematics and Computers in Simulation*, vol. 167, pp. 308-324, 2020.
- [101] F. Mazouz, S. Belkacem, S. Ouchen, Y. Harbouche, and R. Abdessemed, "Fuzzy control of a wind system based on the DFIG," in *International Conference in Artificial Intelligence in Renewable Energetic Systems*, 2017: Springer, pp. 173-181.

- [102] E. Chavero-Navarrete, M. Trejo-Perea, J. C. Jáuregui-Correa, R. V. Carrillo-Serrano, G. Ronquillo-Lomeli, and J. G. Ríos-Moreno, "Hierarchical pitch control for small wind turbines based on fuzzy logic and anticipated wind speed measurement," *Applied Sciences*, vol. 10, no. 13, p. 4592, 2020.
- [103] H. Slah, D. Mehdi, and S. Lassaad, "Advanced control of a PMSG wind turbine," *International Journal of Modern Nonlinear Theory and Application*, vol. 5, no. 1, pp. 1-10, 2016.
- [104] M. Kesraoui, S. A. Lagraf, and A. Chaib, "Aerodynamic power control of wind turbine using fuzzy logic," in 2015 3rd international renewable and sustainable energy conference (IRSEC), 2015: IEEE, pp. 1-6.
- [105] M. Ben Smida and A. Sakly, "Pitch angle control for grid-connected variable-speed wind turbine system using fuzzy logic: A comparative study," *Wind Engineering*, vol. 40, no. 6, pp. 528-539, 2016.
- [106] A. S. Al-Toma, G. A. Taylor, and M. Abbod, "Intelligent pitch angle control scheme for variable speed wind generator systems," in 2017 52nd International Universities Power Engineering Conference (UPEC), 2017: IEEE, pp. 1-6.
- [107] A. Slimen, H. Tlijani, M. Dhaoui, and R. B. Younes, "Intelligent control of wind pump based on PMSG using pitch control," in 2017 14th International Multi-Conference on Systems, Signals & Devices (SSD), 2017: IEEE, pp. 59-64.
- [108] H. Habibi, H. Rahimi Nohooji, and I. Howard, "Power maximization of variable-speed variable-pitch wind turbines using passive adaptive neural fault tolerant control," *Frontiers of Mechanical Engineering*, vol. 12, no. 3, pp. 377-388, 2017.
- [109] X.-m. Zheng, D.-m. Ding, and P. Li, "Power stable regulation of direct-drive permanent magnet wind power system using pitch and torque control," in *International Conference on Renewable Power Generation (RPG 2015)*, 2015: IET, pp. 1-6.
- [110] S. Narasimalu and B. Chellaiah, "Pitch angle control for horizontal axis wind turbine: A comparative study," in 2017 Asian Conference on Energy, Power and Transportation Electrification (ACEPT), 2017: IEEE, pp. 1-6.
- [111] R. Tiwari, N. Ramesh Babu, and P. Sanjeevikumar, "Fuzzy logic-based pitch angle controller for PMSG-based wind energy conversion system," in *Advances in Smart Grid and Renewable Energy*: Springer, 2018, pp. 277-286.
- [112] T. L. Van, T. H. Nguyen, and D.-C. Lee, "Advanced pitch angle control based on fuzzy logic for variable-speed wind turbine systems," *IEEE Transactions on Energy Conversion*, vol. 30, no. 2, pp. 578-587, 2015.
- [113] T. Renuka and P. Reji, "Frequency control of wind penetrated hydro-dominated power system," in 2015 International Conference on Technological Advancements in Power and Energy (TAP Energy), 2015: IEEE, pp. 316-321.
- [114] M. A. Zeddini, R. Pusca, M. N. Mansouri, and M. F. Mimouni, "TSK fuzzy controller of wind-turbine self-excited induction generator for remote site applications," in 2015 16th International Conference on Sciences and Techniques of Automatic Control and Computer Engineering (STA), 2015: IEEE, pp. 499-506.
- [115] C. B. Salah and M. Ouali, "Comparison of fuzzy logic and neural network in maximum power point tracker for PV systems," *Electric Power Systems Research*, vol. 81, no. 1, pp. 43-50, 2011.
- [116] S. Ozdemir, N. Altin, and I. Sefa, "Fuzzy logic based MPPT controller for high conversion ratio quadratic boost converter," *International Journal of Hydrogen Energy*, vol. 42, no. 28, pp. 17748-17759, 2017.
- [117] T. H. Kwan and X. Wu, "Maximum power point tracking using a variable antecedent fuzzy logic controller," *Solar Energy*, vol. 137, pp. 189-200, 2016.
- [118] M. A. A. M. Zainuri, M. A. M. Radzi, A. Che Soh, and N. A. Rahim, "Development

- of adaptive perturb and observe-fuzzy control maximum power point tracking for photovoltaic boost dc–dc converter," *IET Renewable Power Generation*, vol. 8, no. 2, pp. 183-194, 2014.
- [119] Y. Soufi, M. Bechouat, and S. Kahla, "Fuzzy-PSO controller design for maximum power point tracking in photovoltaic system," *International Journal of hydrogen energy*, vol. 42, no. 13, pp. 8680-8688, 2017.
- [120] O. Guenounou, B. Dahhou, and F. Chabour, "Adaptive fuzzy controller based MPPT for photovoltaic systems," *Energy Conversion and Management*, vol. 78, pp. 843-850, 2014.
- [121] B. N. Alajmi, K. H. Ahmed, S. J. Finney, and B. W. Williams, "Fuzzy-logic-control approach of a modified hill-climbing method for maximum power point in microgrid standalone photovoltaic system," *IEEE transactions on power electronics*, vol. 26, no. 4, pp. 1022-1030, 2010.
- [122] T. L. Kottas, Y. S. Boutalis, and A. D. Karlis, "New maximum power point tracker for PV arrays using fuzzy controller in close cooperation with fuzzy cognitive networks," *IEEE Transactions on Energy conversion*, vol. 21, no. 3, pp. 793-803, 2006.
- [123] C. Larbes, S. A. Cheikh, T. Obeidi, and A. Zerguerras, "Genetic algorithms optimized fuzzy logic control for the maximum power point tracking in photovoltaic system," *Renewable energy*, vol. 34, no. 10, pp. 2093-2100, 2009.
- [124] N. Gupta and R. Garg, "Tuning of asymmetrical fuzzy logic control algorithm for SPV system connected to grid," *international journal of hydrogen energy*, vol. 42, no. 26, pp. 16375-16385, 2017.
- [125] S.-a. Blaifi, S. Moulahoum, R. Benkercha, B. Taghezouit, and A. Saim, "M5P model tree based fast fuzzy maximum power point tracker," *Solar Energy*, vol. 163, pp. 405-424, 2018.
- [126] S. Subiyanto, A. Mohamed, and M. Hannan, "Intelligent maximum power point tracking for PV system using Hopfield neural network optimized fuzzy logic controller," *Energy and Buildings*, vol. 51, pp. 29-38, 2012.
- [127] M. Nabipour, M. Razaz, S. G. Seifossadat, and S. Mortazavi, "A new MPPT scheme based on a novel fuzzy approach," *Renewable and Sustainable Energy Reviews*, vol. 74, pp. 1147-1169, 2017.
- [128] O. F. Energy, "Evopod ¼-Scale Tidal Energy Converter: Decommisioning Programme Sanda Sound, Kintyre, Scotland," ODL-P10-003-G5217-DOC, 17/02/2017 2017. [Online]. Available: http://www.oceanflowenergy.com/documents/Sanda%20Sound%20Decommissioning%20Programme.pdf
- [129] D. Mohamad, "The Evopod marine current turbine MSc thesis in renewable energy (REFLEX)," Newcastle University, 2006.
- [130] A. Pacheco and Ó. Ferreira, "Hydrodynamic changes imposed by tidal energy converters on extracting energy on a real case scenario," *Applied Energy*, vol. 180, pp. 369-385, 2016.
- [131] O. F. Energy. "E35 completes over 1 year continuous deployment." https://www.oceanflowenergy.com/news26.html (accessed 27/03, 2024).
- [132] R. Martin-Short, J. Hill, S. Kramer, A. Avdis, P. Allison, and M. Piggott, "Tidal resource extraction in the Pentland Firth, UK: Potential impacts on flow regime and sediment transport in the Inner Sound of Stroma," *Renewable Energy*, vol. 76, pp. 596-607, 2015.
- [133] T. A. Adcock, S. Draper, G. T. Houlsby, A. G. Borthwick, and S. 臺. oğluSena, "The available power from tidal stream turbines in the Pentland Firth," *Proceedings of the Royal Society A: Mathematical, Physical and Engineering Sciences*, vol. 469, no.

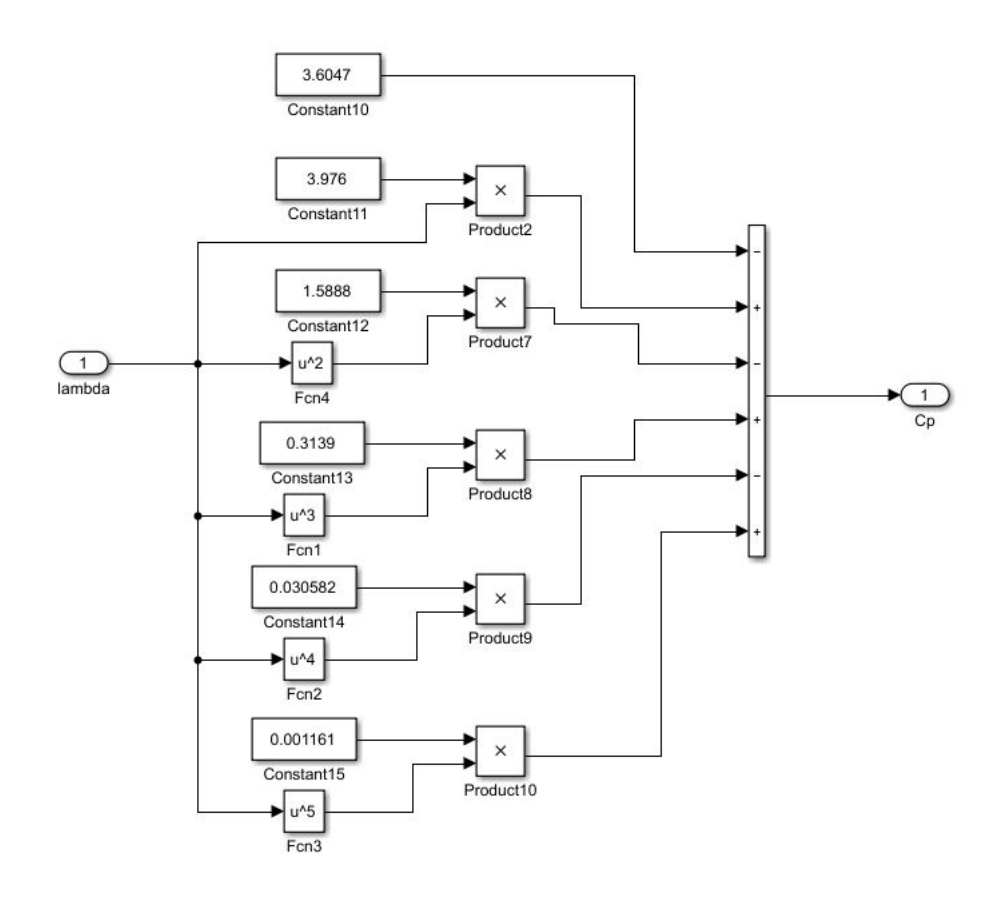
- 2157, p. 20130072, 2013.
- [134] G. J. Allan *et al.*, "Concurrent and legacy economic and environmental impacts from establishing a marine energy sector in Scotland," *Energy Policy*, vol. 36, no. 7, pp. 2734-2753, 2008.
- [135] S. P. Neill *et al.*, "The wave and tidal resource of Scotland," *Renewable energy*, vol. 114, pp. 3-17, 2017.
- [136] L. Goddijn-Murphy, D. K. Woolf, and M. C. Easton, "Current patterns in the inner sound (Pentland Firth) from underway ADCP data," *Journal of Atmospheric and Oceanic Technology*, vol. 30, no. 1, pp. 96-111, 2013.
- [137] L. Stevens. "ORKNEY TIDAL TURBINE BREAKING ENERGY GENERATION RECORDS." https://www.scotland.org/. https://www.scotland.org/inspiration/orkney-tidal-turbine-breaking-energy-generation-records (accessed 27/03, 2024).
- [138] E. U. C. M. S. I. a. D. S. (MDS). "Global Ocean Physics Analysis and Forecast." https://doi.org/10.48670/moi-00016 (accessed 15/03, 2024).
- [139] L. Furgerot, P. B. Du Bois, Y. Méar, M. Morillon, E. Poizot, and A.-C. Bennis, "Velocity profile variability at a tidal-stream energy site (Aldemey Race, France): from short (second) to yearly time scales," in 2018 OCEANS-MTS/IEEE Kobe Techno-Oceans (OTO), 2018: IEEE, pp. 1-8.
- [140] J. I. Encarnacion, C. Johnstone, and S. Ordonez-Sanchez, "Design of a horizontal axis tidal turbine for less energetic current velocity profiles," *Journal of Marine Science and Engineering*, vol. 7, no. 7, p. 197, 2019.
- [141] M. Lewis, S. Neill, P. Robins, M. R. Hashemi, and S. Ward, "Characteristics of the velocity profile at tidal-stream energy sites," *Renewable Energy*, vol. 114, pp. 258-272, 2017.
- [142] S. Toumi, Y. Amirat, E. Elbouchikhi, Z. Zhou, and M. Benbouzid, "Techno-Economic Optimal Sizing Design for a Tidal Stream Turbine–Battery System," *Journal of Marine Science and Engineering*, vol. 11, no. 3, p. 679, 2023.
- [143] S. Benelghali, "On multiphysics modeling and control of marine current turbine systems," Université de Bretagne occidentale-Brest, 2009.
- [144] B. Wu, Y. Lang, N. Zargari, and S. Kouro, *Power conversion and control of wind energy systems*. John Wiley & Sons, 2011.
- [145] N. Huang, "Simulation of power control of a wind turbine permanent magnet synchronous generator system," 2013.
- [146] Z. M. Fan, "Mathematical modelling of grid connected fixed-pitch variable-speed permanent magnet synchronous generators for wind turbines," University of Central Lancashire, 2012.
- [147] D. K. Porate, S. Gawande, A. Munshi, K. Porate, S. Kadwane, and M. Waghmare, "Zero direct-axis current (ZDC) control for variable speed wind energy conversion system using PMSG," *Energy Procedia*, vol. 117, pp. 943-950, 2017.
- [148] T. N. A. Nguyen, D. C. Pham, C.-T. Pham, and N. H. C. Thanh, "D-axis Stator Current Control Methods Applied to PMSG-based Wind Energy Systems: A Comparative Study," *WSEAS Transactions on Systems and Control*, vol. 14, pp. 239-246, 2019.
- [149] A. Clément *et al.*, "Wave energy in Europe: current status and perspectives," *Renewable and sustainable energy reviews*, vol. 6, no. 5, pp. 405-431, 2002.
- [150] M. Mueller and R. Wallace, "Enabling science and technology for marine renewable energy," *Energy policy*, vol. 36, no. 12, pp. 4376-4382, 2008.
- [151] S. D. A. Al-Majidi, "Efficient Maximum Power Point Tracking Techniques for a Gridconnected Photovoltaic System using Artificial Intelligence," Brunel University London, 2020.
- [152] M. Mahdavian, N. Wattanapongsakorn, G. Shahgholian, S. Mozafarpoor, M.

- Janghorbani, and S. Shariatmadar, "Maximum power point tracking in wind energy conversion systems using tracking control system based on fuzzy controller," in 2014 11th International Conference on Electrical Engineering/Electronics, Computer, Telecommunications and Information Technology (ECTI-CON), 2014: IEEE, pp. 1-5.
- [153] B. Whitby, "Control of an axial flow tidal stream turbine," Cardiff University, 2013.
- [154] S. M. Parida and P. K. Rout, "A comparative analysis of the performance of a grid connected permanent magnet synchronous generator with PI and DE optimized PI controller," in 2015 IEEE Power, Communication and Information Technology Conference (PCITC), 2015: IEEE, pp. 36-42.
- [155] R. Bründlinger, N. Henze, H. Häberlin, B. Burger, A. Bergmann, and F. Baumgartner, "prEN 50530–The new European standard for performance characterisation of PV inverters," in *24th EU PV Conf., Hamburg, Germany*, 2009: WIP-Renewable Energies Munich.
- [156] M. Cirstea, A. Dinu, J. Khor, and M. McCormick, "Neural and fuzzy logic control of drives and power systems, Newnes," *An imprint of Elsevier Science First published*, vol. 412, 2002.
- [157] M. Zerouali, M. Boutouba, A. El Ougli, and B. Tidhaf, "Control of variable speed wind energy conversion systems by fuzzy logic and conventional P&O," in 2019 International Conference on Intelligent Systems and Advanced Computing Sciences (ISACS), 2019: IEEE, pp. 1-5.
- [158] R. I. Putri, F. Ronilaya, M. Rifa'i, L. Jasa, A. Priyadi, and P. M. Hery, "Sensorless Optimum Power Extraction for Small Scale Stand Alone Wind Turbine Based on Fuzzy Controller," in 2018 2nd International Conference on Applied Electromagnetic Technology (AEMT), 2018: IEEE, pp. 44-49.
- [159] J. Lee and Y. S. Kim, "Sensorless fuzzy-logic-based maximum power point tracking control for a small-scale wind power generation systems with a switched-mode rectifier," *IET Renewable Power Generation*, vol. 10, no. 2, pp. 194-202, 2016.
- [160] X.-P. Li, W.-L. Fu, Q.-J. Shi, J.-B. Xu, and Q.-Y. Jiang, "A fuzzy logical MPPT control strategy for PMSG wind generation systems," *Journal of Electronic Science and Technology*, vol. 11, no. 1, pp. 72-77, 2013.
- [161] M. G. Simoes, B. K. Bose, and R. J. Spiegel, "Design and performance evaluation of a fuzzy-logic-based variable-speed wind generation system," *IEEE Transactions on Industry Applications*, vol. 33, no. 4, pp. 956-965, 1997.
- [162] A. M. Eltamaly and H. M. Farh, "Maximum power extraction from wind energy system based on fuzzy logic control," *Electric Power Systems Research*, vol. 97, pp. 144-150, 2013.
- [163] S. Marmouh, M. Boutoubat, and L. Mokrani, "MPPT fuzzy logic controller of a wind energy conversion system based on a PMSG," in 2016 8th International Conference on Modelling, Identification and Control (ICMIC), 2016: IEEE, pp. 296-302.
- [164] A. Uehara *et al.*, "Output power smoothing of PMSG-based wind energy conversion system," in *2010 Conference Proceedings IPEC*, 2010: IEEE, pp. 128-133.
- [165] J. Zhao and B. K. Bose, "Evaluation of membership functions for fuzzy logic controlled induction motor drive," in *IEEE 2002 28th Annual Conference of the Industrial Electronics Society. IECON 02*, 2002, vol. 1: IEEE, pp. 229-234.
- [166] M. Seyedmahmoudian *et al.*, "State of the art artificial intelligence-based MPPT techniques for mitigating partial shading effects on PV systems—A review," *Renewable and Sustainable Energy Reviews*, vol. 64, pp. 435-455, 2016.
- [167] A. Daoud and A. Midoun, "Maximum power point tracking techniques for solar water pumping systems," *Journal of Renewable Energies*, vol. 13, no. 3, pp. 497–507-497–507, 2010.

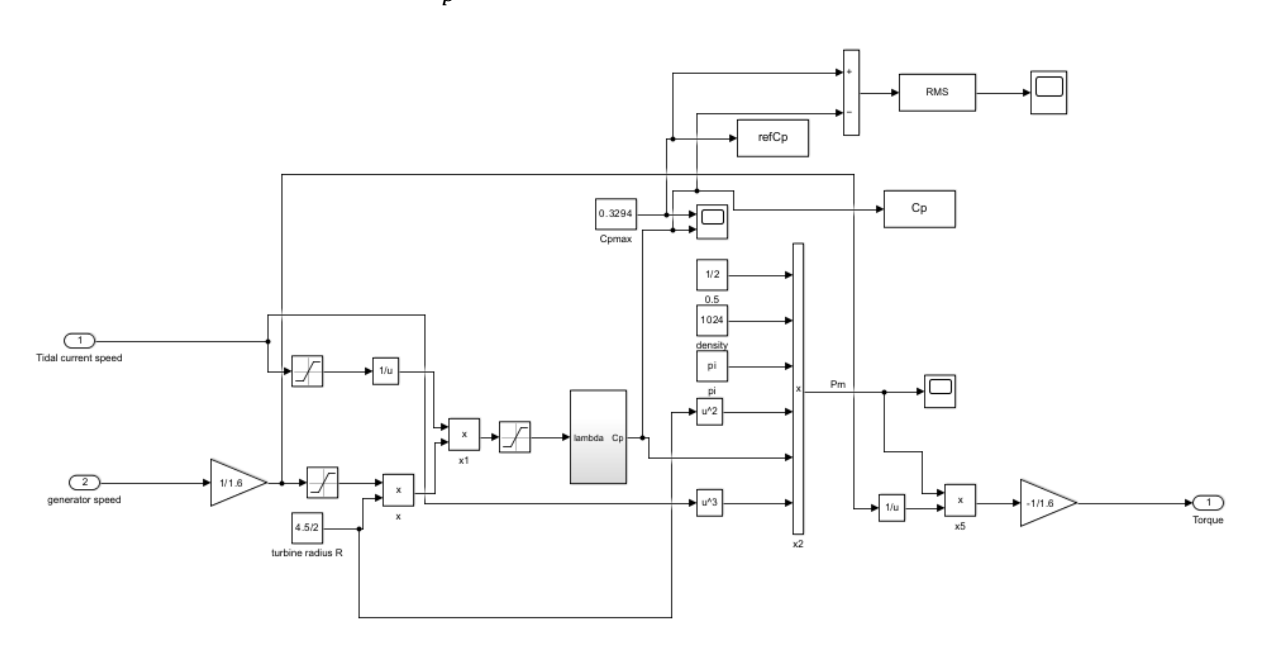
- [168] M. A. Soliman, H. M. Hasanien, H. Z. Azazi, E. E. El-Kholy, and S. A. Mahmoud, "An adaptive fuzzy logic control strategy for performance enhancement of a grid-connected PMSG-based wind turbine," *IEEE Transactions on Industrial Informatics*, vol. 15, no. 6, pp. 3163-3173, 2018.
- [169] P. Giroux, G. S. C. Osorio, and S. Chandrachood, "Average Model of a 100-kW Grid-Connected PV Array," *MathWorks. Available:* https://uk.mathworks.com/help/sps/ug/average-model-of-a-100-kw-grid-connected-pv-array.html, 2014.
- [170] P. Ferrada, F. Araya, A. Marzo, and E. Fuentealba, "Performance analysis of photovoltaic systems of two different technologies in a coastal desert climate zone of Chile," *Solar Energy*, vol. 114, pp. 356-363, 2015.
- [171] M. Mussard and M. Amara, "Performance of solar photovoltaic modules under arid climatic conditions: A review," *Solar Energy*, vol. 174, pp. 409-421, 2018.
- [172] X. Yin and X. Zhao, "Sensorless maximum power extraction control of a hydrostatic tidal turbine based on adaptive extreme learning machine," *IEEE Transactions on Sustainable Energy*, vol. 11, no. 1, pp. 426-435, 2019.

Appendices

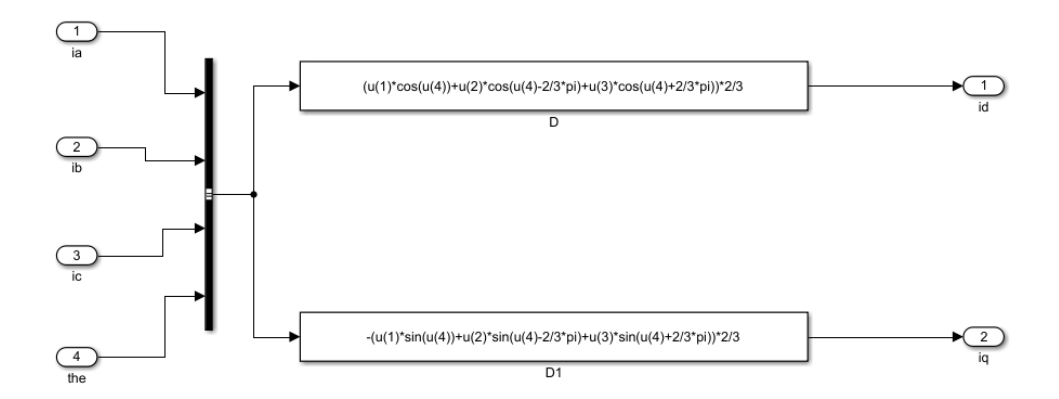
Appendix A



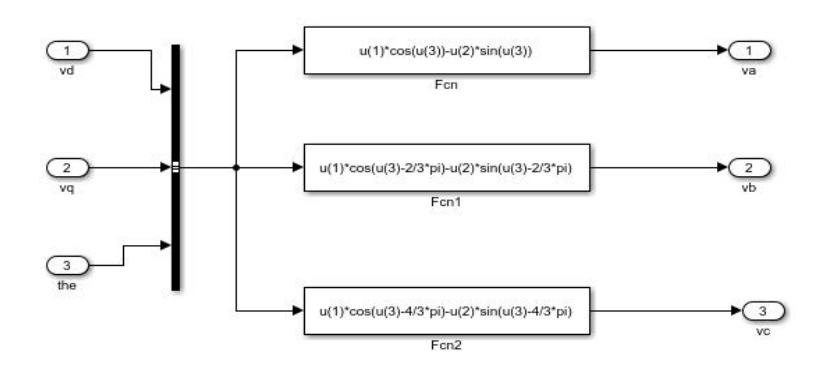
A.1 C_p and λ relation in MATLAB model



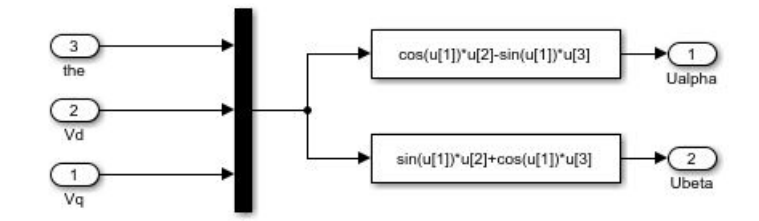
A.2 Tidal current turbine simulation model in MATLAB



A.3 abc/dq axis reference frame transformation module

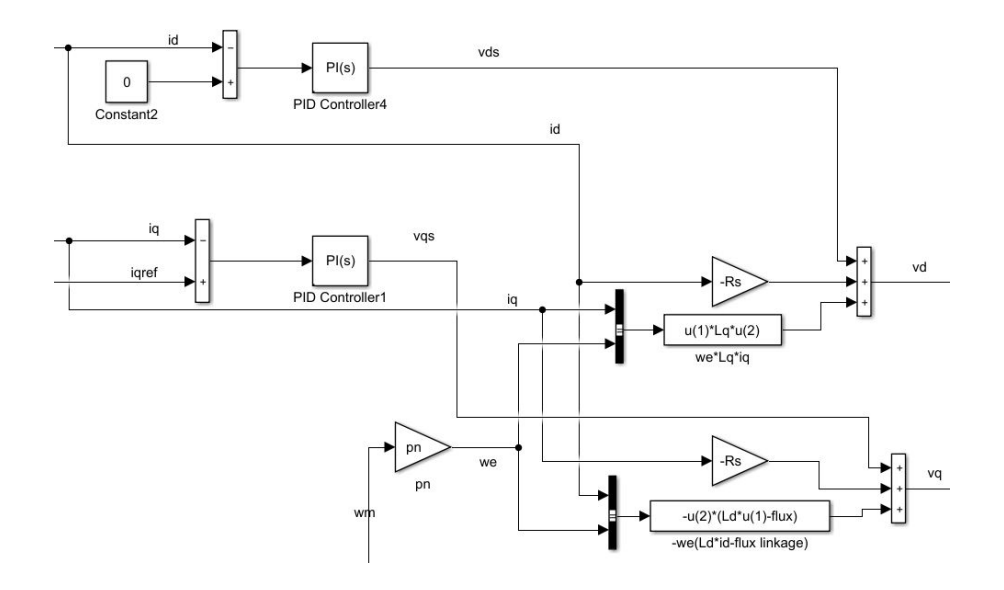


A.4 dq/abc axis frame transformation module

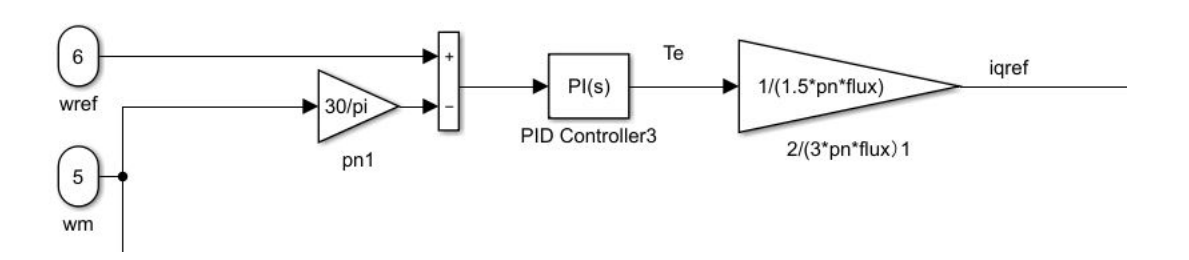


A.5 $dq/\alpha\beta$ axis transformation module

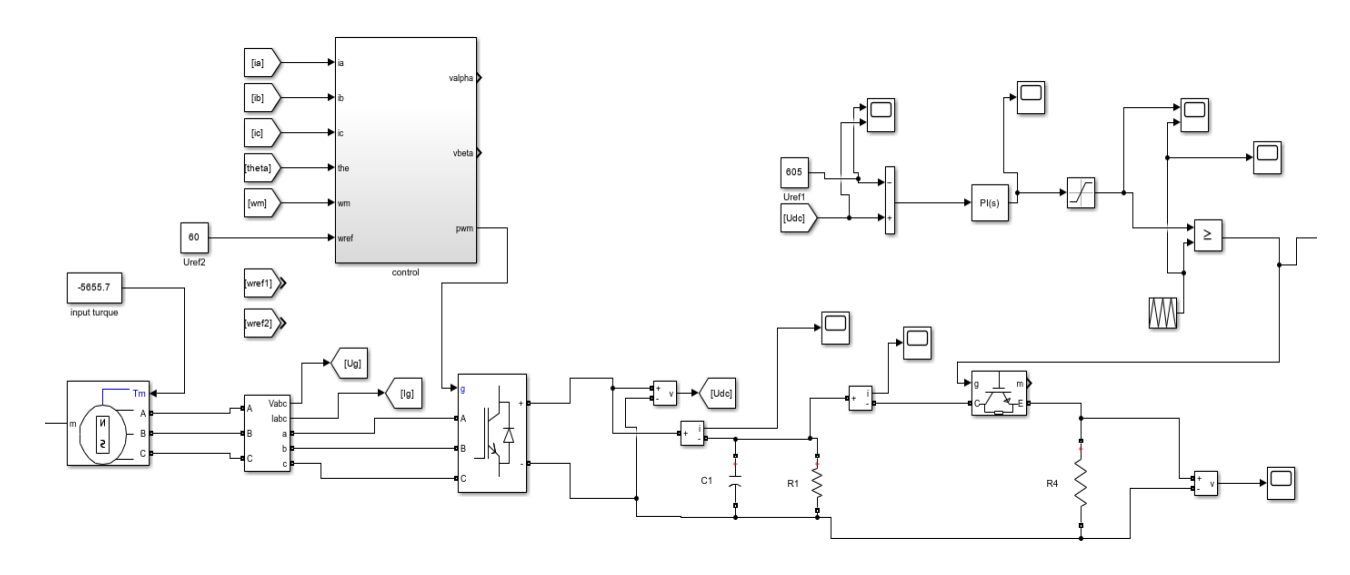
170



A.6 Current control loop in MATLAB

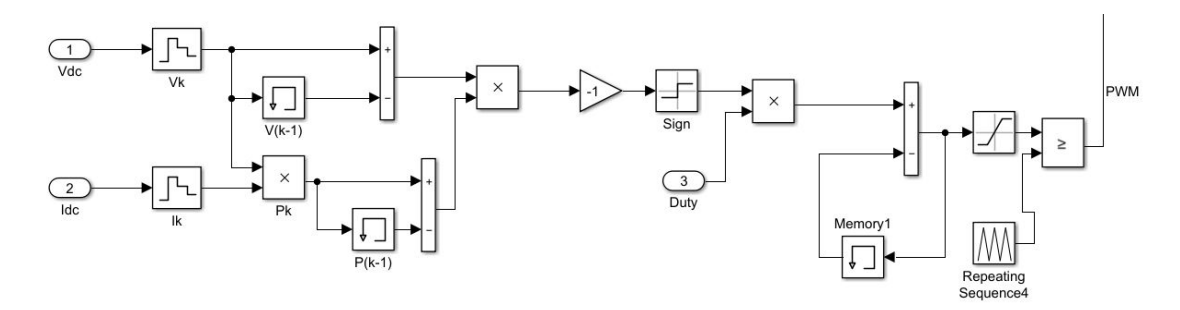


A.7 Speed control loop in MATLAB

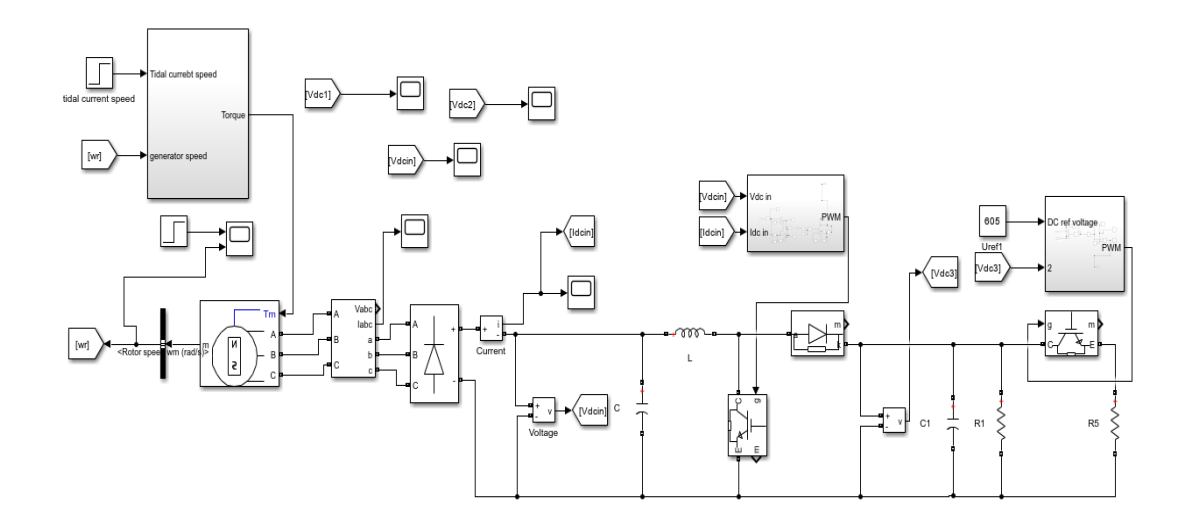


A.8 Tidal current turbine generator side control simulation in MATLAB

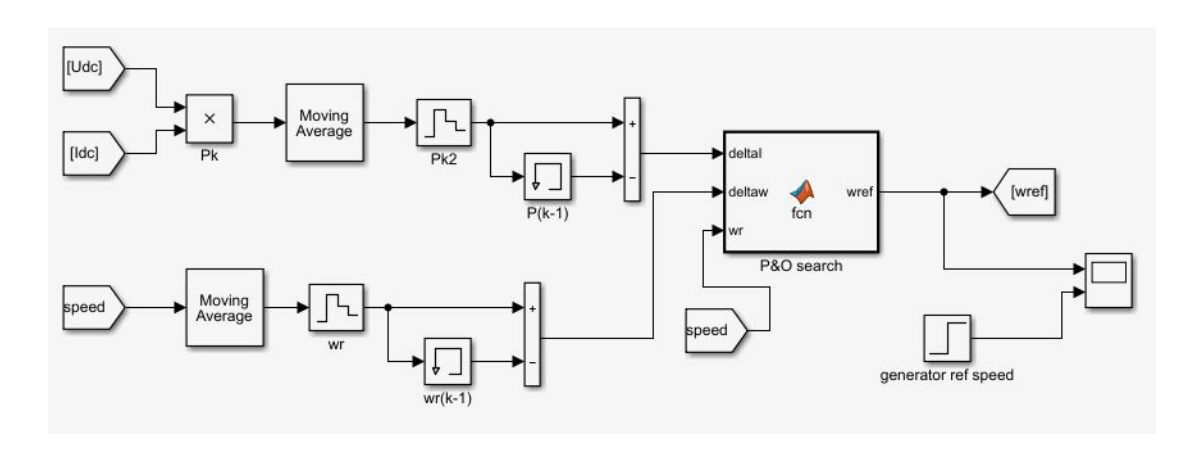
Appendix B



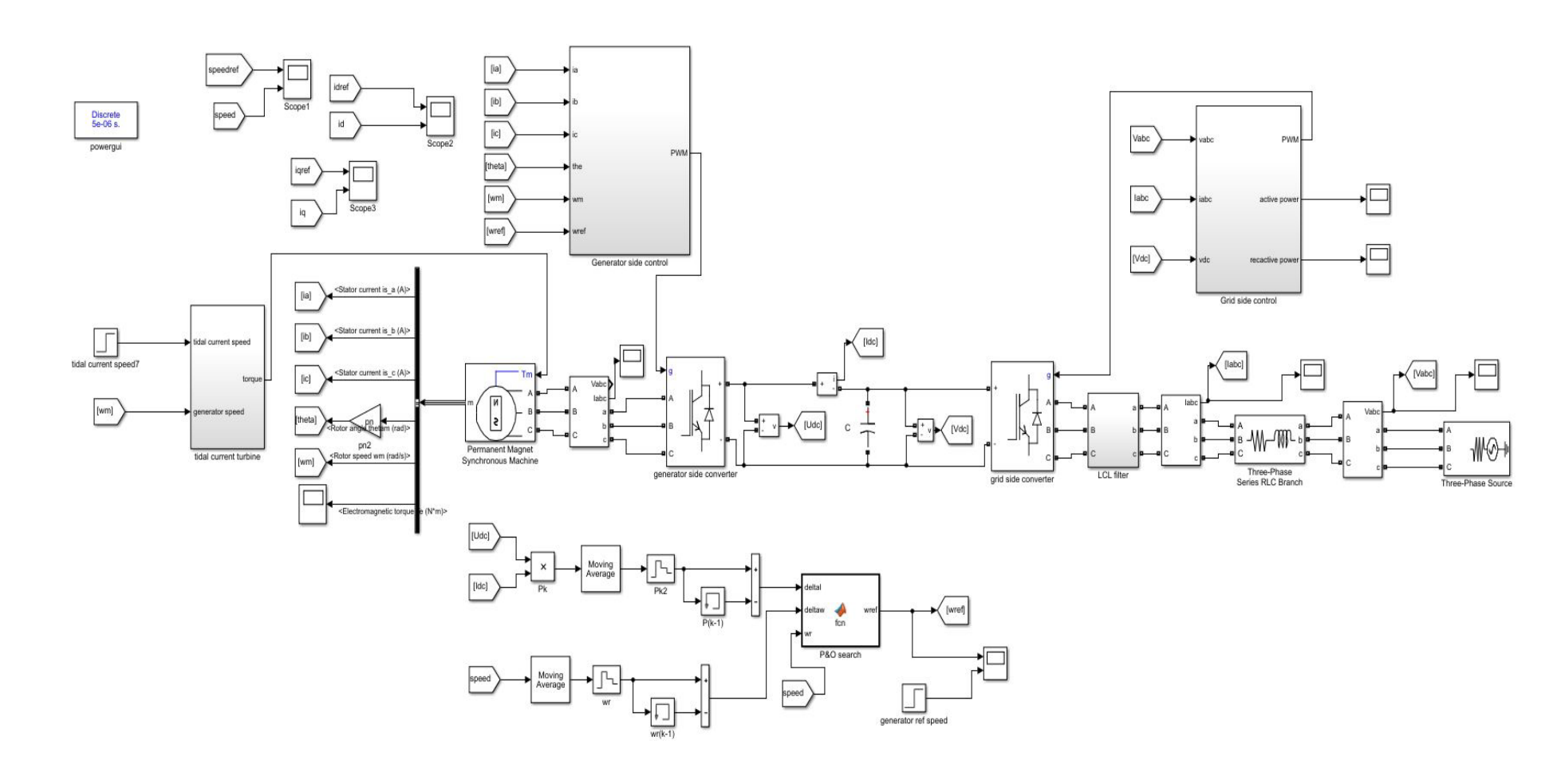
B.1 P&O stand-alone system P&O control in MATLAB



B.2 Stand-alone tidal current turbine system simulation model in MATLAB

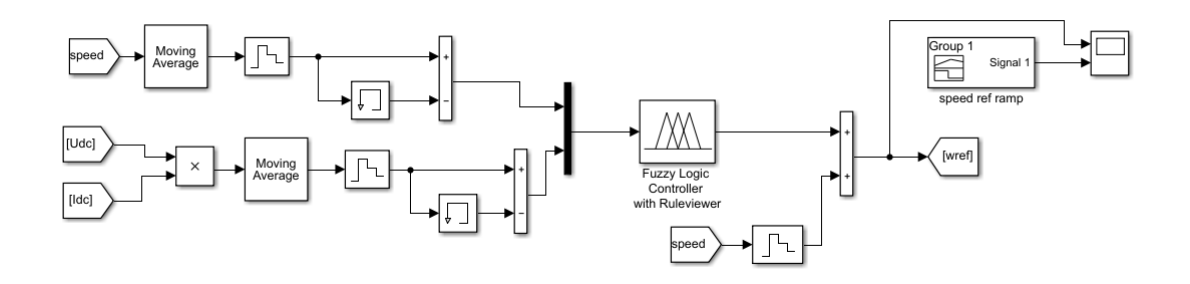


B.3 P&O control model in MATLAB

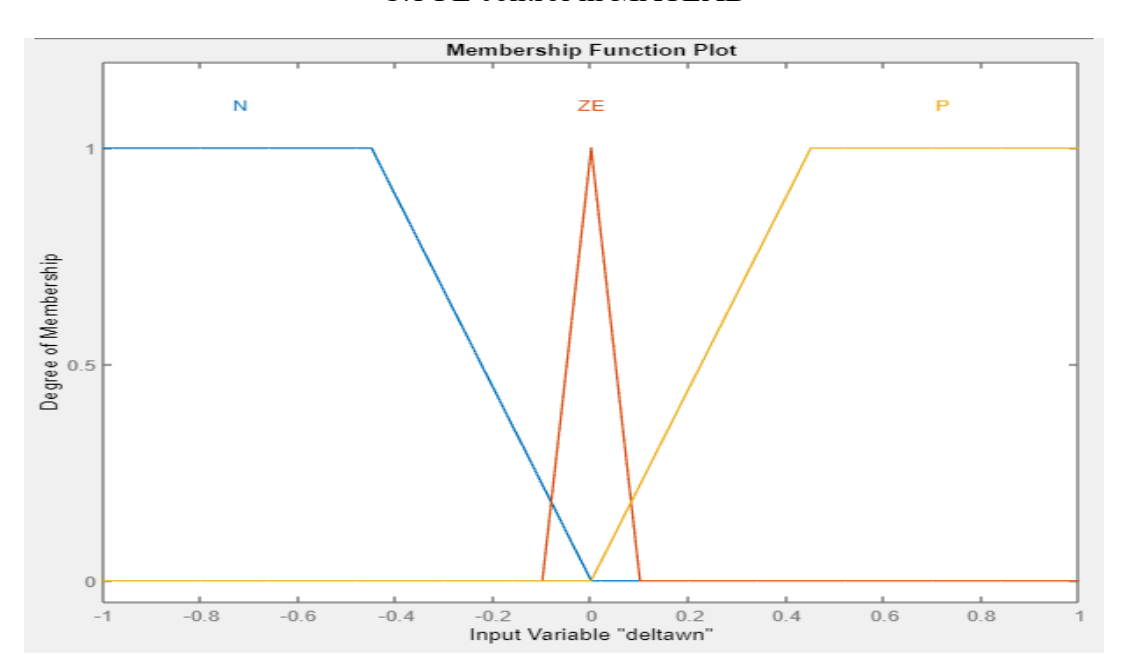


B.4 conventional tidal current turbine system simulation model in MATLAB

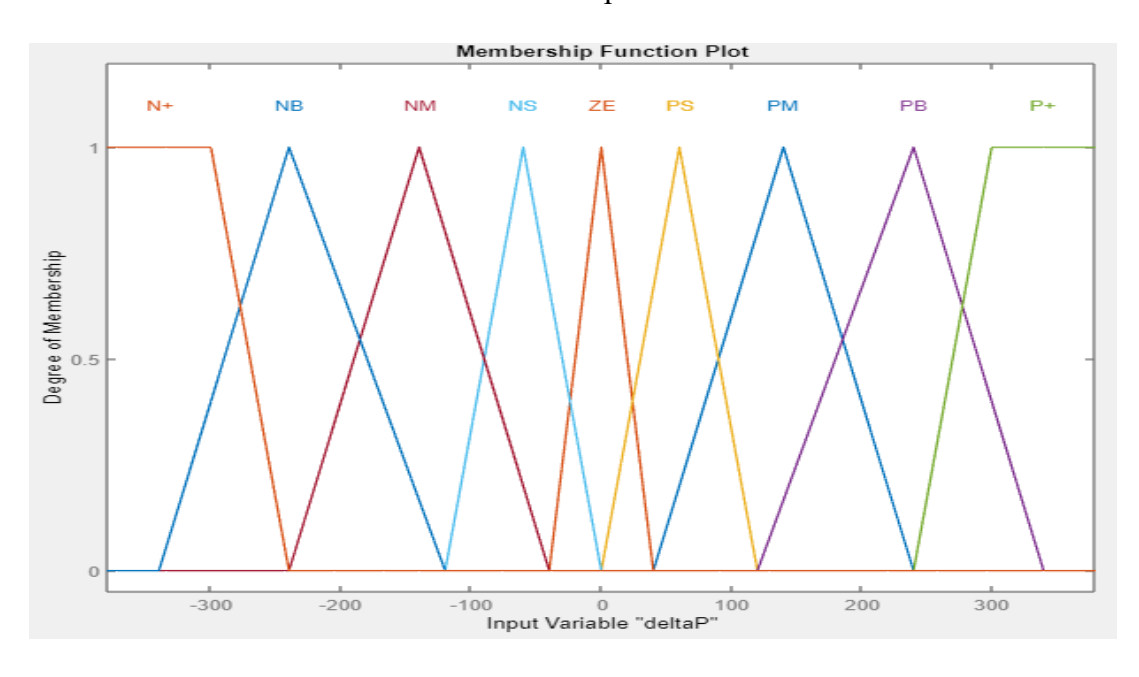
Appendix C



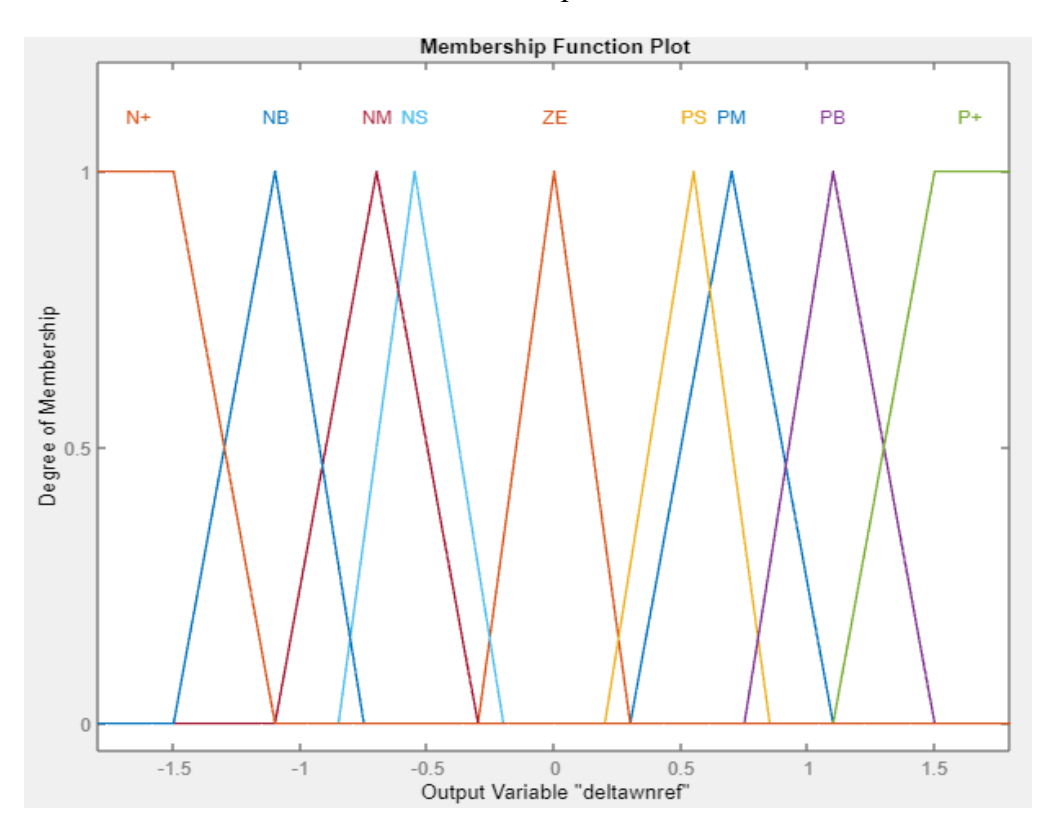
C.1 FL control in MATLAB



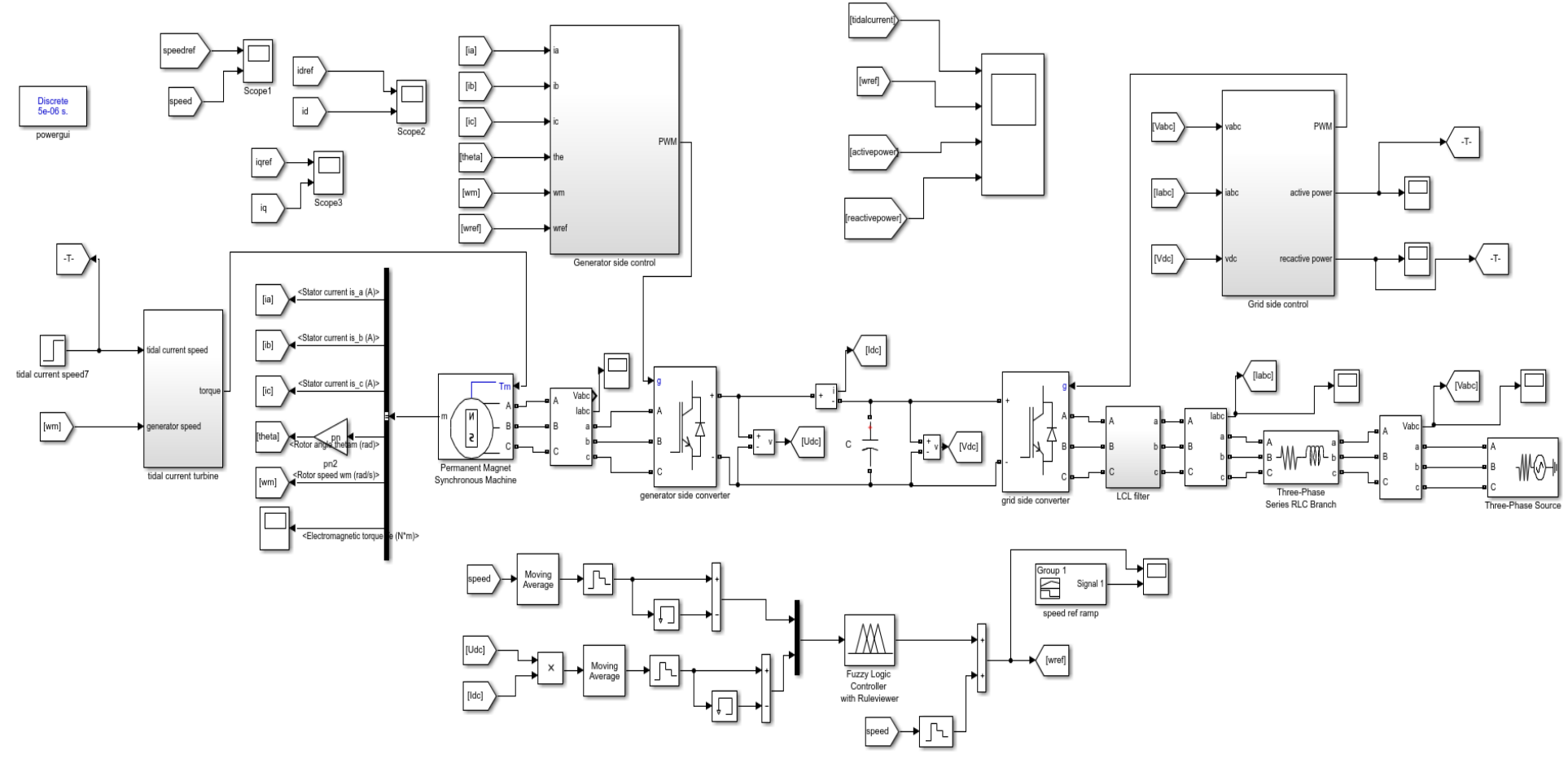
C.2 FL control input $\Delta\omega$ MFs



C.3 FL control input ΔP MFs

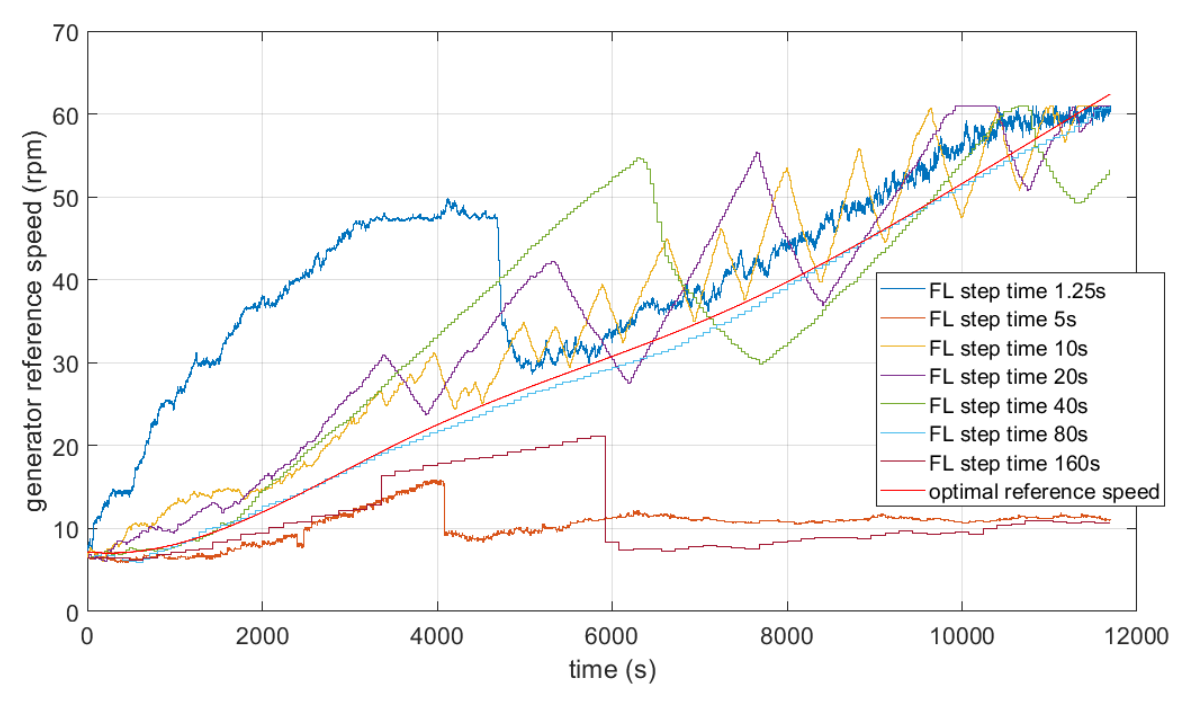


C.4 FL control output $\Delta\omega_{ref}$ MFs

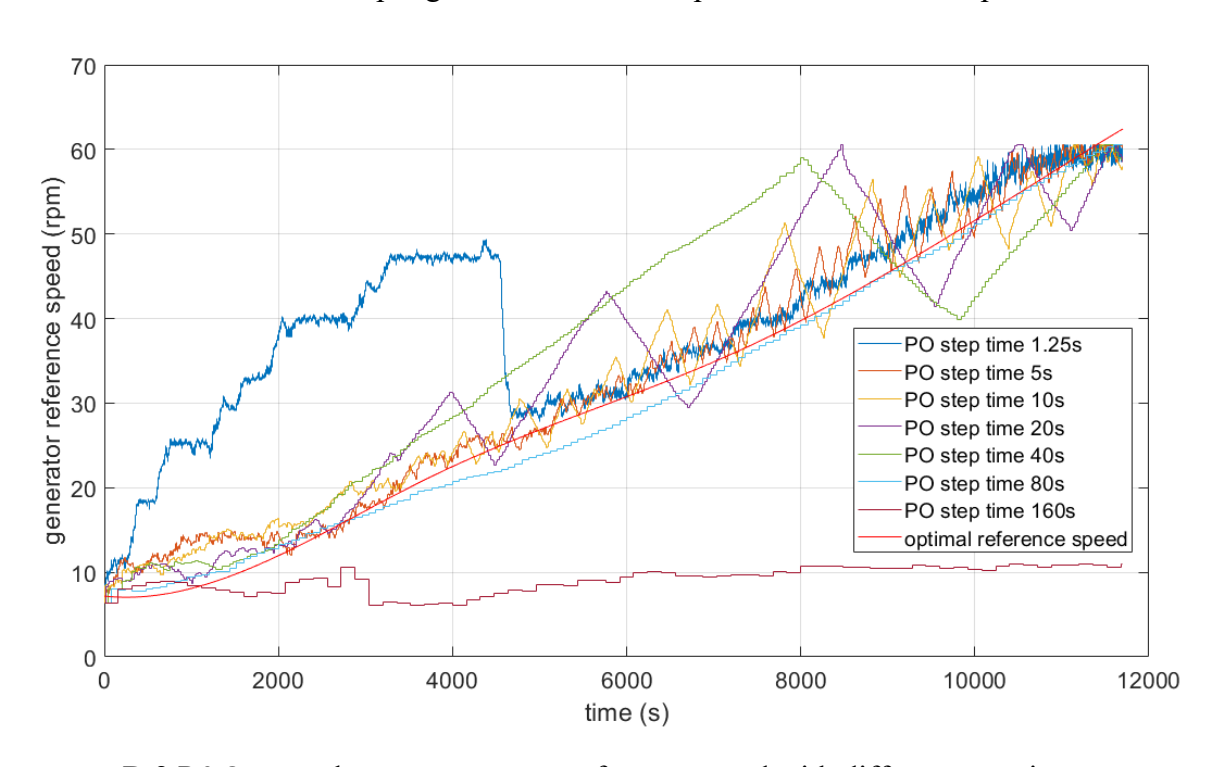


C.5 Conventional tidal current turbine system simulation model with FL control in MATLAB

Appendix D



D.1 FL control output generator reference speed with different step time



D.2 P&O control output generator reference speed with different step time